Design, Analysis and Optimization of a Cherenkov radiation based sub-mm/THz BWO

by

Ahmed Ibrahim Nashed

A thesis
presented to the University of Waterloo
in fulfillment of the
thesis requirement for the degree of
Doctor of Philosophy
in
Electrical and Computer Engineering

Waterloo, Ontario, Canada, 2015

AUTHOR'S DECLARATION

I hereby declare that I am the sole author of this thesis. This is a true copy of the thesis, including any required final revisions, as accepted by my examiners.

I understand that my thesis may be made electronically available to the public.

Abstract

The Terahertz (THz) radiation –also known as "*T-ray and THz gap*"– refers to a certain band of the electromagnetic spectrum whose frequency extends between 0.1THz and 10THz. Compared to the microwave band, the THz radiation has higher frequency. Therefore, it can be used for high capacity wireless communication and high resolution imaging application. Furthermore, several applications – such as biomedical imaging and spectroscopy – can be designed to use the unique material response to the THz radiation. The lack of an appropriate (stable, compact, high power and reasonably inexpensive) THz radiation source has held up the progress in these THz potential applications.

Powered by the advance in the modern micro-fabrication techniques along with the huge progress in the computational resources/tools, several THz radiation sources have been introduced. These sources can be classified as; vacuum sources, solid state source and laser and photonic sources. Among these sources, the Vacuum Electronic Devices (VEDs) demonstrate the highest average power. Therefore, it can be used to accomplish both the compact size and the sufficient generated power requirements for the THz source. Since the parameters of the VED –such as the operating frequency, the power conversion efficiency and the bandwidth– are defined from the Slow Wave Structure (SWS) design, the SWS is considered as the key element in the VED radiation source. The design of the VED source is performed in two steps; the cold analysis and the hot analysis. While, the design of the SWS is performed in the cold analysis, the hot test deals with the electron beam-wave interaction and the electromagnetic field generation.

In this work, the Photonic Crystal (PC) structure is used to design a novel Double Defected PC (DD-PC) based SWS. Compared to other SWSs, the DD-PC structure has no axial discontinuity, which facilitates the fabrication of the SWS. Additionally, the generated THz radiation is extracted from the defects, which is located away from the electron beam. Hence, the electron beam-wave interaction process is not affected. Moreover, since the DD-PC based SWS is a metallic structure, it can be used for high THz power radiation. Taking advantage of non-uniform Finite Difference Frequency Domain (FDFD) method, the design of a DD-PC based SWS operating at 130GHz was performed.

Due to the complexity of the SWS and electron beam-wave interaction, the hot analysis was carried out using a numerical analysis. The numerical simulation can be divided into two connected sub-simulations; the electromagnetic field simulation and the particle simulation. While, the Finite

Difference Time Domain (FDTD) analysis is used as the electromagnetic field simulator, the physical parameters of the electron beam were calculated using the Particle In Cell (PIC) simulation. The FDTD/PIC simulation was used to analyze the performance of several Backward Wave Oscillators (BWO) designed using the DD-PC based SWS. Furthermore, the FDTD/PIC was used to optimize the BWO parameters for maximum THz radiation. To reduce the simulation time, a parallel Open Multi-Processing (OpenMP) version of the FDTD/PIC tool was created and implemented.

To alleviate the high acceleration voltage required for the electron beam in the BWO using the DD-PC based SWS, the Axial loaded Double Defected Photonic Crystal (ADD-PC) based SWS was implemented at 200GHz. Starting from the band gap diagram, the ADD-PC based SWS was designed. Then using the High Frequency Structural Simulator (HFSS), an optimization of the SWS was performed. Then, the design of the SWS was verified using the HFSS probe-wheel experiment. The performance of the BWO using the ADD-PC based SWS was investigated using the FDTD/PIC simulation. Finally, to show the potential of the proposed SWS, a BWO operating at 650GHz was presented using the ADD-PC based SWS. The FDTD/PIC simulation results, of the proposed BWO, indicate that an output power of almost 8W at 650GHz with 1.8% conversion efficiency can be achieved.

Acknowledgements

I would like to thank all those who helped me reach this point. Foremost, I would like to express my deepest gratitude to my advisors, Professor Sujeet K Chaudhuri and Prof. Safieddin Safavi-Naeini, for their mentorship, continual guidance, and for the numerous opportunities they gave to me. All of my successes and achievements in research are owed to their patience and insightful guidance. Even when achieving progress was difficult, I was inspired by their ability to see a light at the end of the tunnel. Their kindness and personalities have made it an honor to work with them.

I would also like to thank the members for my dissertation committee; Professor Hamed Majedi, Professor Simarjeet Saini, Prof. James Martin and Professor Frank Wilhelm-Mauch, for their support, helpful discussions and invaluable comments.

Also, I would like to thank the members of our group (CIARS) for their helpful discussions. Special thanks to Ahmed Shehata for helping in the setup and testing of my structures.

Dedication

This work is dedicated to my wife *Reem* for her continuous support and encouragement.

Table of Contents

List of Figures

List of Tables

Chapter 1

Introduction

Covering the gap between the microwave band and the optical band in the electromagnetic spectrum, the Terahertz (THz) radiation is an electromagnetic radiation whose frequency extends from 0.1 to 10THz [1]. Although the THz radiation is naturally available in everyday life, it is considered as the least explored region in the electromagnetic spectrum. The main reason of this is the lack of appropriate THz radiation source. Due to technical difficulties involved in the design, analysis, optimization and realization of a compact THz source, the term "*THz gap*" is used to define this frequency band.

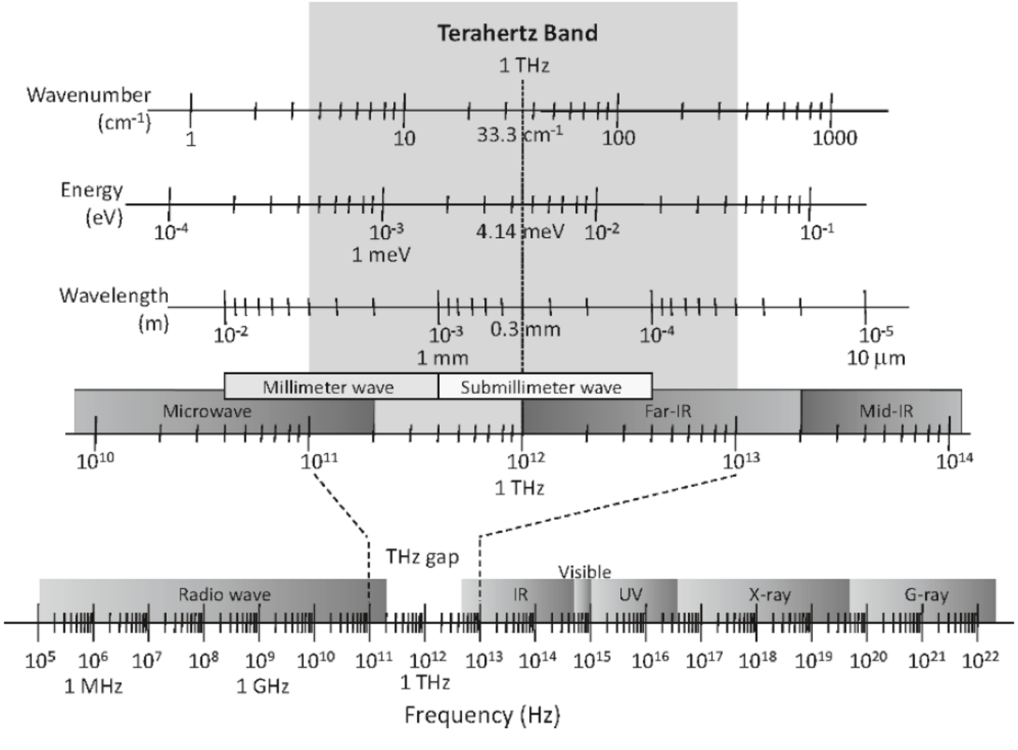

Figure 1-1 The THz radiation band in the electromagnetic spectrum [1].

Since several physical processes have unique spectral features in THz band such as; energy gaps in superconductors, rotational transition in molecules, and intra-band transitions in semiconductors, and powered by the advance of micro-fabrication techniques and micro-electronics, research in the THz frequency regime has become an important research topic within the last two decades. In addition to the high data rate communication offered in this frequency band, several applications are designed to use these particular characteristics of material responses to THz radiation [2-7].

1.1 Motivation and Methodology

In most of the sub-millimeter (sub-mm)/THz application, the radiation source is the keystone element. There are two types of THz radiation; the pulsed radiation, and the Continuous Wave (CW) radiation. At present, the bottle neck in the development of commercial THz applications is the lack of a compact THz radiation source. The main challenges in the THz source are the generated power, the source efficiency and the compactness of the source. Since the THz radiation is highly attenuated, the THz source should be powerful enough to overcome it. Also, The source should be compact enough to be deployed in the system [8- 10].

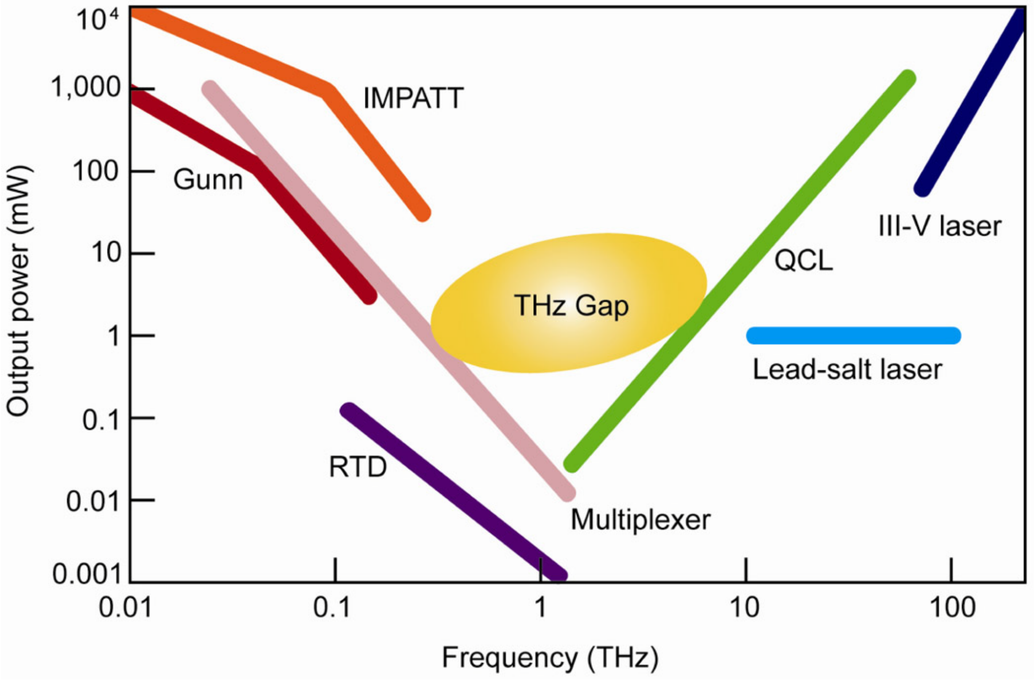

Figure 1-2 THz-power performance of different sources around the THz gap [14].

RTD: Resonant tunnel diode. IMPATT: Impact ionization avalanche transit-time diode. Gunn: Gunn laser. QCL: Quantum-cascade laser. III–V: Denotes groups III and V in the periodic table of elements.

In the last decade, powered by the advance in the optical technology and the fast growth of the microwave technology, the THz gap has rapidly shrunk. However, neither the optical source nor the microwave devices were able to fully exploit the THz gap. For the microwave frequency end (low frequency side - Figure 1-2) the electronic-based sources are able to cover the THz gap, up to 0.8THz, but their output power falls down rapidly as the frequency increases [11-12]. On the other side of the gap, the fundamental physical limitation of the laser source ($kT \approx 26\ meV$, where k is Boltzmann constant) bounds its use as a compact, room temperature and powerful source at this band [13]. The THz power performance of both the solid state sources and the optical sources are presented in Figure 1-2.

While, the Vacuum Electronic Devices (VEDs) are known as efficient, stable and high power microwave energy sources [15-18], realization of the VED source in THz band faces different challenges (Figure 1-3). These challenges include; the electron beam, thermal management, source fabrication and the efficiency. To have a reliable source, an electron beam with a cathode life time > 10^4 hour is required. Also, the efficiency of the proposed VED source should be high enough such that the generated power is larger than 1mW. Depending on the source efficiency, a powerful and compact cooling system is required. Besides, the dimensions of the proposed source should be realizable using modern micro-fabrication techniques.

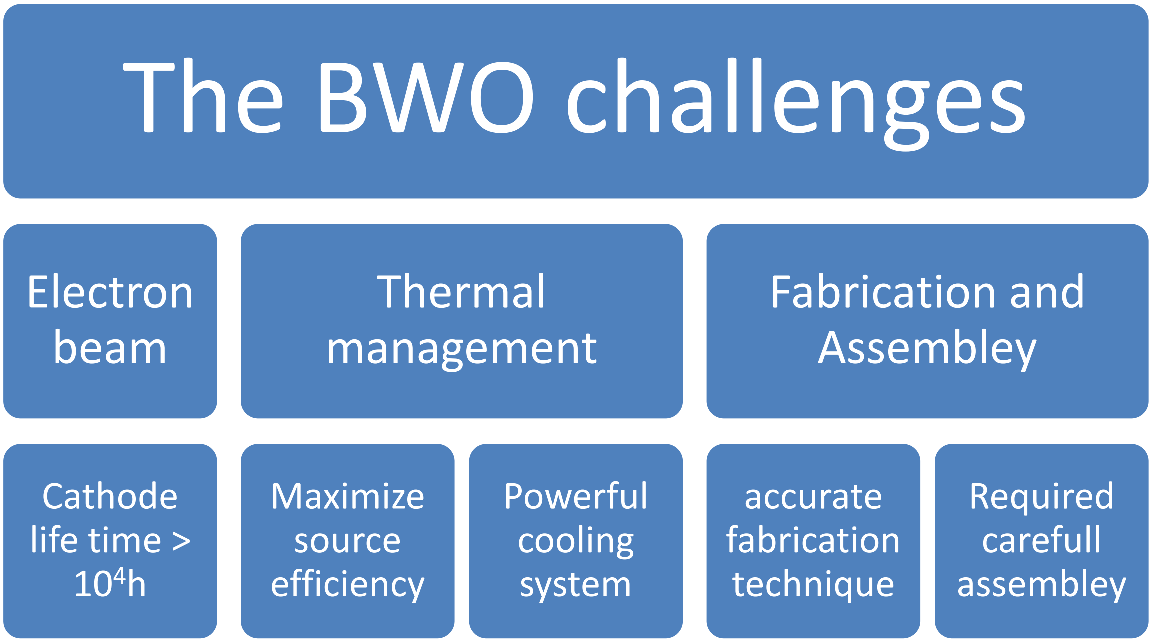

Figure 1-3 The Sub-mm/THz VED source challenges

Since the parameters of the VED source (such as; the operating frequency, operational bandwidth and the efficiency) are defined by the proper selection of the Slow Wave Structure (SWS), it is considered as the key element in designing VED source. The SWS is an electromagnetic device that allows the propagation of an electromagnetic wave with a phase velocity lower than the speed of light in the medium. Thus, this electromagnetic wave can interact with an electron beam travelling with the same velocity. Although different SWS designs were reported such as; the folded waveguide, the coupled cavity, the vane loaded waveguide, and the double corrugated waveguide, they suffer from different drawbacks (limited power handling capability, fabrication and assembly of the source and tunability problems).

The Backward Wave Oscillator (BWO) is considered as the most promising VED source for THz radiation [18-19]. Therefore, the main goal of this thesis is to design a BWO operates in this frequency band. Since the performance of the BWO is defined by the SWS, a major part of this work was dedicated to design it. The project consists of two main phases; the cold analysis and the hot analysis (Figure 1-4). Within the cold analysis, novel SWS were designed using the metallic Photonic Crystal (PC) structure. To test the suggested structure, a proof of concept prototypes were fabricated using both the CNC machining and the 3D print technology. During the hot analysis, a numerical Computer Aided Design (CAD) tool was implemented to simulate the electron beam-wave interaction problem. Hence, the performance of the BWO was investigated. To illustrate the potential of the proposed BWO, the design procedure and optimization of two BWO operating at 200GHz and 650GHz are provided (Figure 1-4).

The first phase, the cold analysis, deals mainly with the design of the SWS using a rigorous electromagnetic numerical method. In this work, the main idea is to combine both the excellent mode selectivity of the PC structure along with the high power handling capabilities of the metallic structure in designing the Double Defected Photonic Crystal (DD-PC) based SWS. In order to verify the existence of the slow wave mode in the DD-PC based SWS, two main verifications were proposed; numerical verification and a simple proof of concept experiment.

The electron beam-wave interaction is carried out in the second part of this research (hot analysis). Due to the complexity of the SWS and the electron beam-wave interaction, a numerical model was used to analyze the performance of the THz radiation source. The simulation can be divided into two timely interactive sub-simulations; the field simulation and the particle simulation. Taking advantage of the timely update of the electromagnetic fields in the Finite Difference Time Domain (FDTD) method, the field simulation was carried out. On the other hand, the Particle In Cell (PIC) simulation was used to calculate the physical parameters of the electron beam particles (particle momentum, acceleration, velocity, and position) [21- 23]. Both sequential 2D and 3D version of the FDTD/PIC simulation was first implemented, and then a parallel 3D version of the code was realized using Open Multi-Processing (OpenMP). Furthermore, using the FDTD/PIC simulation as an optimization tool, the optimum values of both the electron beam current and the applied axial magnetic fields were obtained.

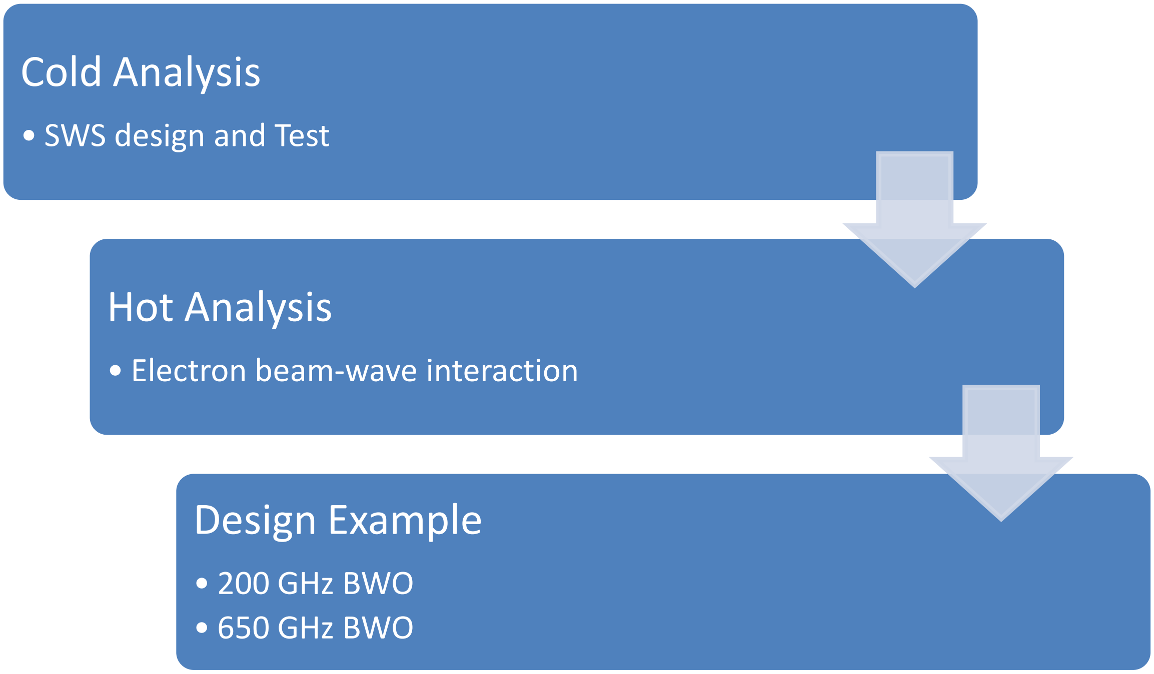

Figure 1-4 A Hierarchy of the research plan

To show the potential of the proposed BWO, the operating frequency of the proposed BWO was extended to 200GHz and 650GHz. To fulfill this task, the Axial loaded Double Defected Photonic Crystal (ADD-PC) based SWS was introduced. Compared to the DD-PC based SWS, the ADD-PC based SWS supports a slow wave mode with lower phase velocity. Thus, the required electron beam velocity (and acceleration voltage) is significantly reduced and the overall performance of the BWO is enhanced.

1.2 Organization of the thesis

The thesis is organized as follows:

In chapter 2, an overview of the current progress in the THz radiation sources is introduced. Also, a literature review on both the available SWS as well as a brief discussion on electron beam sources is provided.

Chapter 3 provides the modal analysis of the SWS using the FDFD. First, an introduction to the FDFD method is provided. Using the multi-level meshing and the implementation of the finite conductivity, a non-uniform FDFD was established. After that, the design of the DD-PC based SWS is introduced. The geometrical parameters of the PC structure were calculated from the band gap diagram. Then using the non-uniform FDFD method, the modal analysis of the DD-PC based SWS was performed. To provide a verification of the existence of the slow wave mode, a scaled model of the SWS was fabricated and tested.

In Chapter 4, the interaction between the electron beam and the electromagnetic fields is carried out using the FDTD/PIC tool. First the physics of the FDTD/PIC CAD tool is briefly introduced. Several aspects of the CAD tools were discussed in details. Then, a BWO –designed using the DD-PC based SWS– was analyzed using the FDTD/PIC tool. The parameters of the BWO (the generated electromagnetic fields, the average calculated power and the particle physical parameters) are discussed in details. Furthermore, the FDTD/PIC tool was used to optimize the generated electromagnetic power.

A full design of 200GHz BWO radiation source was presented in chapter 5. The design was performed using two types of SWS; the DD-PC and the ADD-PC structure. A full study of the performance and optimization of the proposed BWO was carried-out using FDFD, HFSS and FDTD/PIC simulations. Following the same procedure, the operating frequency of the BWO was extended to 650GHz. A brief introduction to the design of the SWS and the performance of the BWO – at this frequency– was highlighted.

Finally, a summary, conclusions and topic for both the current and the future research are presented in chapter 6

Chapter 2

Background

2.1 Introduction

THz radiation –also known as near millimeter or sub-millimeter radiation– refers to electromagnetic fields and waves in the frequency ranges from 0.1 THz to 10 THz. Since THz frequency band extends between microwave and infrared bands, so it can be considered as a bridge connecting electronics to optics. The THz radiation sources can be categorized into three main categories (Figure 2-1); vacuum devices, solid state devices and laser based devices (Figure 2-2). Since the Vacuum Electronic Devices (VEDs) are known for its high efficiency and power [10], the proposed source was selected to be a vacuum source. Taking advantage of the excellent mode selectivity, ease of fabrication and high thermal conductivity of the metallic Photonic Crystal (PC) structure, The PC was selected as the building device of the proposed VED device. The coupling between the vacuum technology and the PC devices may result in development of a compact and efficient THz power source.

The main concept of the Vacuum Electronic Devices (VEDs) is to convert the kinetic energy of the electron beam into electromagnetic energy. The electromagnetic radiation is generated from a time varying current, which can be achieved either by electron beam velocity modulation, electron beam density modulation or both of them. Using static magnetic field or high frequency electric field, the time varying current can be done. The mathematical background of the electromagnetic radiated power can be explained from Larmor formula [24]. The relativistic expression for the radiated power from a single particle:

$$\boldsymbol{P} = \frac{2}{3}\frac{q^2}{v_c}\gamma^6\left[\left(\frac{\dot{v}}{v_c}\right)^2 - \left(\frac{v}{v_c}\times\frac{\dot{v}}{v_c}\right)^2\right] \tag{2-1}$$

And for non-relativistic case:

$$\boldsymbol{P} = \frac{2}{3}\frac{q^2}{v_c}\left(\frac{\dot{v}}{v_c}\right)^2 \tag{2-2}$$

where “q” is the charge of the particle, “v_c” is the speed of light in the vacuum, “γ” is the relativistic Lorentz parameter and “v” is the velocity vector of the particle.

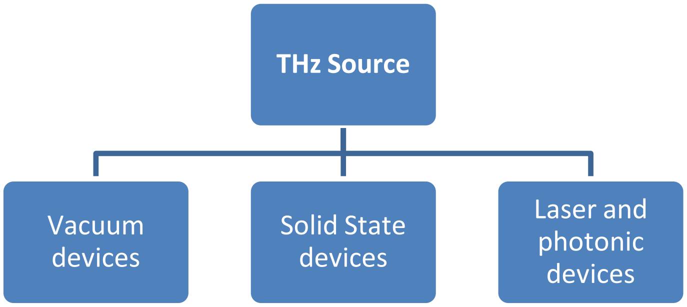

Figure 2-1 Available THz source

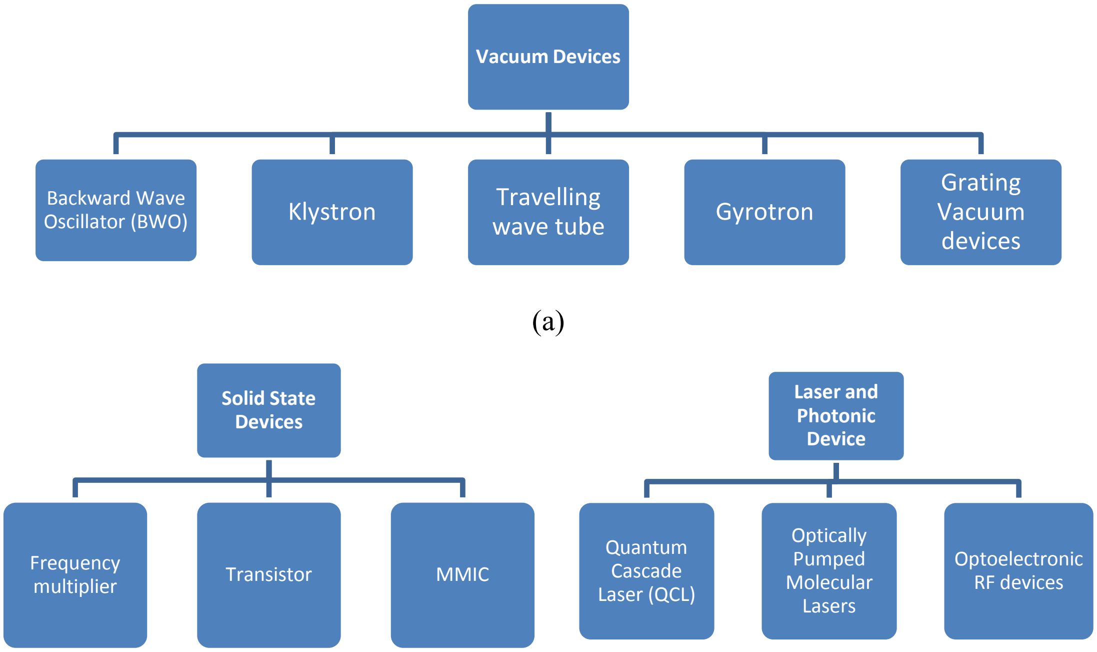

(a)

(b)

(c)

Figure 2-2 Different THz Source Technologies; (a) Vacuum device, (b) Solid state devices, and (c) Laser and photonic device

Since the parameters of the VED source (the operating frequency, the power conversion ratio and the bandwidth) are defined by the SWS. It considered as the main element in the VED. Therefore, research for SWS suitable for work in sum-millimeter (sub-mm)/THz band and the fabrication/realization of such structure is considered as an active research topic.

Thus, this chapter is divided into three main parts; the VEDs, the SWS, and the electron emission devices. First, a short introduction to the different VEDs is presented. Among the different vacuum devices, it was found that the BWO is considered as the most promising source for the THz band. After that, different designs of the SWSs are discussed in the next section. Since the electron emission is the driving force of the VED device, the last part in this chapter outlines the different types of electron guns.

2.2 The Vacuum Electronic Devices

Modern microwave VEDs are known for their power efficiency, cost effective, reliability, and thermal robustness. They relay on the coherent electromagnetic radiation of electron beam [25-26]. The coherent electromagnetic radiation generated by the accelerated electron beam can be classified into three types (Figure 2-3); Cerenkov radiation, transition radiation and Bremsstrahlung. The Cerenkov radiation is generated if a charged particle travels in a medium that can support the propagation of an electromagnetic field with a phase velocity less than the speed of the light in this medium.

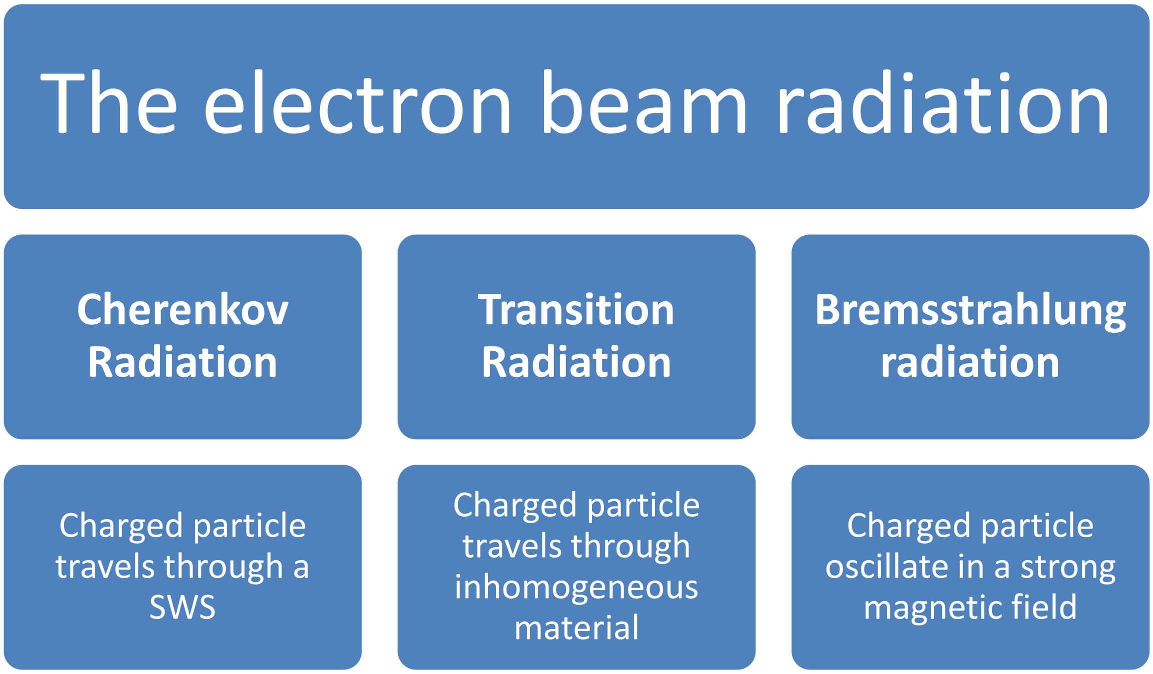

Figure 2-3 Coherent Electron beam radiation

While the radiation associated with the oscillation of a charged particle in a strong magnetic field is defined as Bremsstrahlung radiation, transition radiation happens when a charge particle travels between two different medium [10], [27-33].

In this section, an introductory of the different VED devices, such as; the Travelling Wave Tube (TWT), the Backward Wave Oscillator (BWO), the klystron and the magnetron, will be presented. The introduction highlights the operation principles and potential use in sub-mm/THz regime.

2.2.1 The Travelling Wave Type (TWT)

The TWT is an essential component in communication system [15],[27]. It consists of; an electron gun, electron beam-wave interaction medium, electron beam collector and RF output (Figure 2-4). Its operation principle is based on the density modulation. First, the electron gun is used to generate the required electron beam with a circular cross section (pencil beam - Pierce gun). As the electron beam travels through the SWS, the velocity of the electron beam is bunched, thus the electromagnetic radiation is formed. The maximum gain of the TWT is obtained at the synchronization condition:

$$v_{ph} = v_e - v_{sc} = v_{bunch} \tag{2-3}$$

where "v_{ph}" is the electromagnetic field phase velocity, "v_e" is the speed of the electron beam, "v_{sc}" is the speed of the decelerated particles and "v_{bunch}" is the bunch velocity.

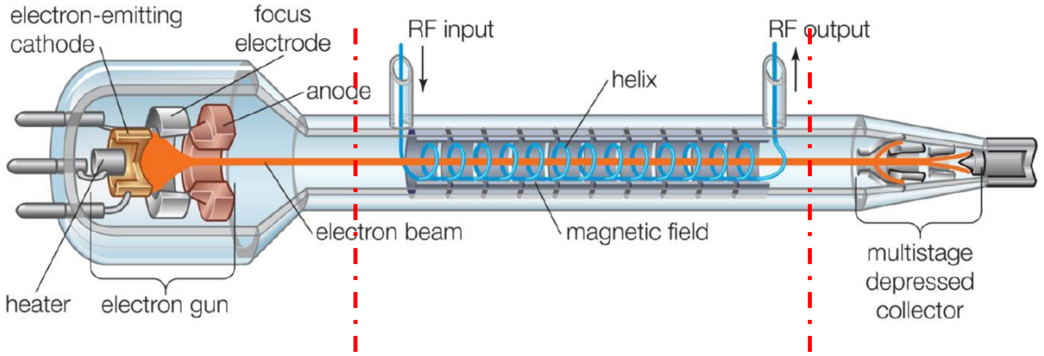

Electron gun	SWS	Collector
Electron beam generation	Electron beam-wave interaction	Exhaust electron beam collector

Figure 2-4 Schematic diagram of the TWT [34]

The advantages of the TWT include; compact size, good linearity, and good bandwidth [15]. For the sub-mm/THz TWT, there are two main challenges; the fabrication of the SWS and the TWT assembly. Due to the long length of the interaction medium (SWS) and its small diameter, a careful manufacturing is required to build it. In addition, a careful design of the focusing network of the electron beam is required to align the electron beam inside the SWS [35]. Also, an accurate assembly of the TWT is required.

2.2.2 The Klystron

The klystron operation is based on the velocity modulation of the electron beam [32],[36-37]. A schematic diagram of two cavity klystron is presented in Figure 2-5. The first cavity "*buncher*" is used to modulate the electron velocity by the input RF signal. Then, as the electron beam travels through the drift tube – drift space –, the electron beam bunched. The RF signal is collected from the second cavity "*collector*". The main drawback of the klystron is its limited bandwidth.

Taking advantage of the high output power and efficiency of the klystron, and the extended bandwidth of the TWT, the Extended Interaction Klystron (EIK) amplifier is introduced. Alike the cavity design in the klystron, a ladder circuit is added to the cavity in the EIK amplifier [37]. Compared to a klystron, the EIK has a higher gain per unit length. Therefore, the length of the EIK is smaller, and the required magnetic focusing circuit is less complicated [38-39]. Furthermore, by removing the input cavity, an Extended Interaction Oscillator (EIO) was built as an oscillator.

Although klystron, EIO and EIK are efficient microwave sources/amplifiers, the migration to sub-mm/THz band has some limitations. These limitations are mainly due to the electron beam, thermal dissipation and the accuracy of the assembly [10]. As the SWS dimensions decreased, the radius of the electron beam is reduced which leads to increase both the space-charge effect and the transverse velocity. Therefore the overall performance of the EIK will be limited. Moreover, due to the small dimensions of the SWS and the power dissipation, an efficient cooling system may be required to avoid thermal breakdown.

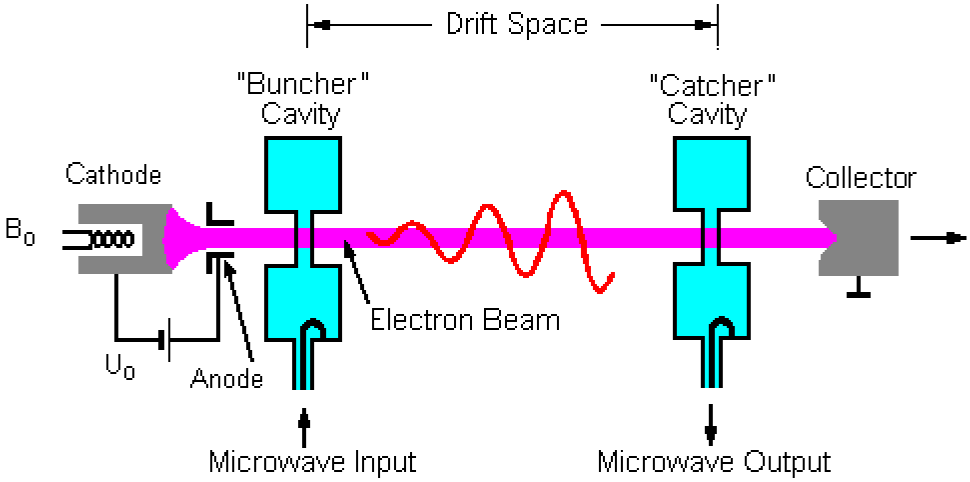

Figure 2-5 A schematic diagram of a two cavity klystron [37]

2.2.3 The Backward Wave Oscillator (BWO)

Currently, the BWO is considered the most established VED source in the THz regime [2], [15-18], [40]. There are two main types of the BWO; the O-type BWO and the M-type BWO. In the O-type, the electron beam and the applied magnetic fields are parallel, while in M-type the magnetic field is perpendicular on the electron beam. The main difference between the BWO and the TWT is the operating mode. In the TWT, the electron beam interacts with the forward electromagnetic wave. While in the BWO the electron beam interacts with the backward wave. Therefore, the electromagnetic wave is collected at the electron beam entrance point. Since, the maximum electromagnetic wave is located at the point of the minimum electron beam bunching; the efficiency of the BWO is limited. To increase the efficiency, a cascade BWO is introduced (Figure 2-6). In the cascaded BWO, the first SWS is used to modulate the electron beam, while the second SWS is used as the main beam-wave interaction devices [44-45].

The BWO is a tunable device. The improvement in the fabrication techniques, the slow wave structure design and the beam-wave interaction software had led to increase of the operating frequency, and the efficiency of the BWO. A list of the available BWO sources are listed in Table 2-I [41-44]. All the devices listed in this table required both external DC voltage source (high voltage / current) and external water cooling system. Furthermore, the actual dimensions of most of them are not listed.

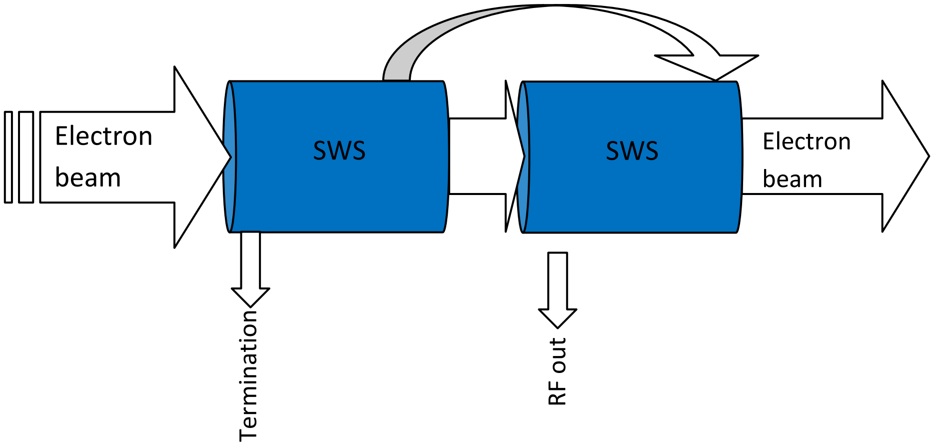

Figure 2-6 A schematic diagram of the cascaded BWO

Manufacture		Operating Frequency	Power	Notes	
Microtech [42]	QS1 - 260	160 - 260 GHz	20 mW	-Water cooled system. -Consist of a BWO followed by several frequency multipliers	All Sources requires an external power source / sweeper
	QS1 – 370	180 – 370 GHz	10 mW		
	QS1 – 900	550 – 950 GHz	3 mW		
	QS1 – 1000	700 – 1000 GHz	1 mW		
	QS1 – 1100	950 – 1200 GHz	3mW		
Insight Products [41]	36 – 178 GHz	36 – 178 GHz	20 – 80 mW	- Water cooled system	
	179 – 1250 GHz	179 – 1250 GHz	0.5 – 30 mW		
L3 – Communications [44]	Q – band	43.5 – 50 GHz	70 – 160 W	No details about the cooling system	
	Ka – band	26.5 – 40	150 – 300 W		
	K – band	18 – 26.5 GHz	150 – 190 W		

Table 2-I Available BWO operates at sub-mm/THz band

2.2.4 The Magnetron

The magnetron is considered as the smallest, robust, cheapest and the most power efficient VED radiation source [46-47]. Since it is used mainly in microwave heating, it considered as the most widely used VED. Comparing to the previous VEDs, the magnetron is a transverse current modulation device. It consists of a coaxial cathode surrounded by copper cavity anodes (Figure 2-7(a)). Due to both the applied uniform magnetic field and the electromagnetic wave of the cavity, the velocity of the electron beam modulated and the wheel of electron formed (Figure 2-7(b)).

Although there is an effort to extend the operation of the magnetron to the THz band, there are two main challenges; the short life time and the lack of high precision tuning mechanism [48-50]. Currently, the Micro-Electro-Mechanical System (MEMS) technology is used to design a THz reveres magnetron [49], but no further details about the experiments were published.

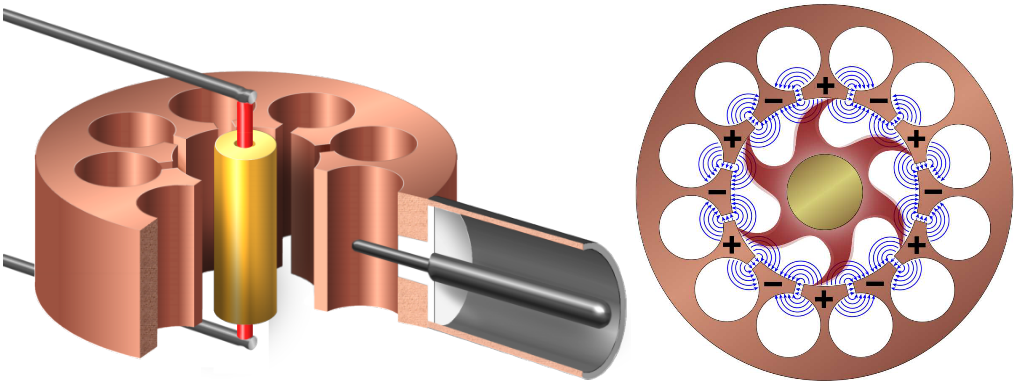

(a) (b)

Figure 2-7 (a) A schematic of the magnetron, and (b) picture of the electron beam velocity modulation [34]

2.3 The Slow Wave Structure (SWS)

The Slow Wave Structure (SWS) is defined as a guiding structure which supports the propagation of an electromagnetic wave with a phase velocity lower than the velocity of the light in the medium. This electromagnetic wave is called the Slow Wave (SW) mode. As a key element, most of the VED performance parameters (the power conversion ratio, the operating bandwidth, the tunability of the device, the attenuation and the heat dissipation) are determined from the SWS. For example the helix SWS has a wide bandwidth, but its thermal capacity limits its usage as a higher power source.

Alternatively, although the metallic couple cavity structure solves the problem of the thermal capacity, its operational bandwidth is almost 5%. In this section a brief description of state of art SWS is presented and discussed.

2.3.1 The Helical Waveguide (HGW)

The Helical Groove Waveguide (HGW) has two main configurations; either a rectangular cross-section with a helical groves, or a circular cross section with a helix installed inside it [52]. Its main advantage is the large transverse dimensions. Therefore, its fabrication is feasible [52]. Moreover, since the HGW is an all metallic structure, it has good heat dissipation. Therefore, it can be used for high power VEDs. On the other hand, both the limited bandwidth and efficiency of the HGW restrict its use. In addition, due to the dispersive nature of the HGW, the electron velocity spread degrades the performance of the SWS [53].

2.3.1.1 The rippled HGW

The helical corrugation waveguide consists of a cylindrical waveguide with a helical corrugation of the inner surface (Figure 2-8). Compared to the conventional HGW, the rippled HGW have higher band width and efficiency [54-55].

2.3.1.2 The ridge loaded HGW

Although the ridge loaded HGW has a narrow bandwidth, the power handling capability and the circuit fabrication tolerance provide significant advantage of the SWS. Therefore it can be considered as a low cost SWS for millimeter (mm) TWT devices [53]. For example, an output power of 163W with an efficiency of 6.2% was achieved at a frequency of 42GHz. The bandwidth of this device was measured to be 1.3% [53].

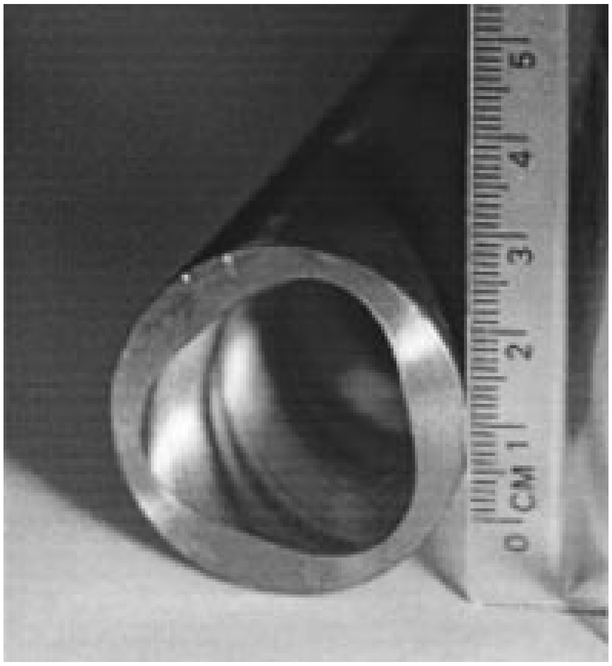

Figure 2-8 A picture of x-band helical corrugation waveguide [55]

2.3.2 The Helix Waveguide

Although the helix SWS has several advantages for mm-TWT (high bandwidth, low electron beam voltage and the relatively high power capabilities) [56], its realization in sub-mm/THz band is difficult. Due to the extremely small dimensions of the helix SWS, it fabrication becomes more complex. Moreover, the difficulty of passing a meaningful current through the structure arises. A novel fabrication technique for a 650GHz helix slow wave structure was introduced [57-58]. Although the actual fabrication of the waveguide was done using the lithography (Figure 2-9), no RF power was detected at the output port due to misalignment. Another prototype of the helix waveguide scaled to operate at 95GHz was introduced, and analyzed using CST studio suite [59-60]. The simulation shows that a gain of 5.8dB can be achieved at this frequency range, as far as the author knowledge, no fabrication and testing results are published.

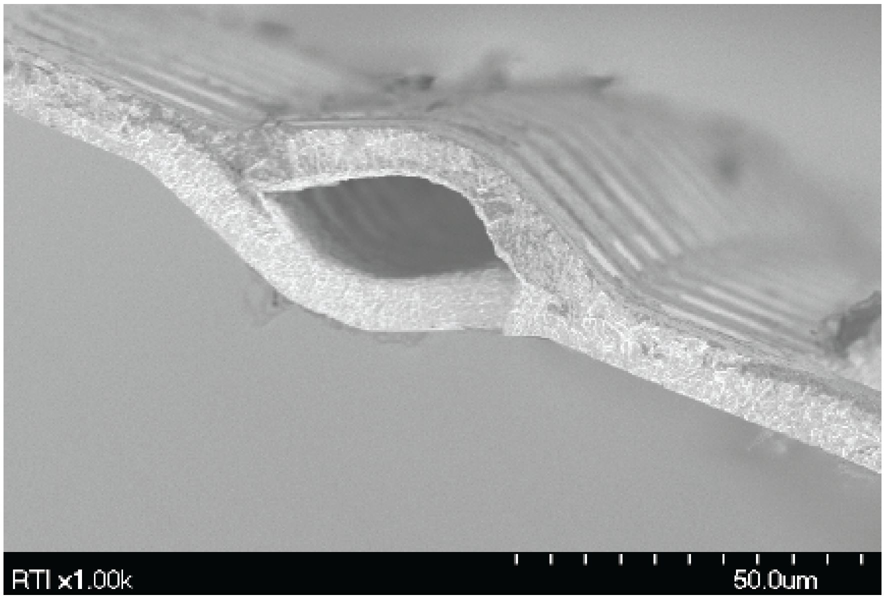

Figure 2-9 A helix slow wave structure operates at 650GHz [57]

2.3.3 Microstrip meander-line SWS

To overcome the complex fabrication process of the helix slow wave structure, the microstrip meander-line SWS was introduced. It consists of a periodic microstrip meander line placed on a partially filled rectangular waveguide is show in Figure 2-10 [61]. Since a single period looks like the letter “U”, this mender line may be called the U-shape microstrip meander-lines.

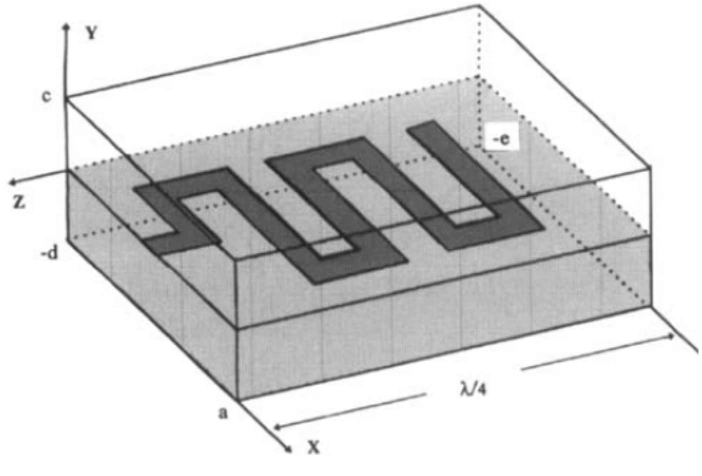

Figure 2-10 A microstrip meander line place in a rectangular waveguide [61]

Since the microstrip meander line SWS has the low interaction impedance, the efficiency of the oscillator is limited. To overcome this, the raised microstrip meander line SWS is introduced. A SEM picture of the raised microstrip meander line is shown in Figure 2-11. The figure shows that the dielectric was removed beneath the meander line [62].

Figure 2-11 A SEM picture of the meander line [62]

In order to reduce the operating beam-voltage, A V-shaped microstrip meander line SWS was introduced (Figure 2-12) [63]. It consists of; a metal shielding cavity, a dielectric substrate, and a V-shape metal mender line. Within a frequency range 75 – 100GHz, simulation results indicates that the V-shape microstrip meander line SWS required 25% less electron beam-voltage compared to the U-shaped microstrip mender line SWS.

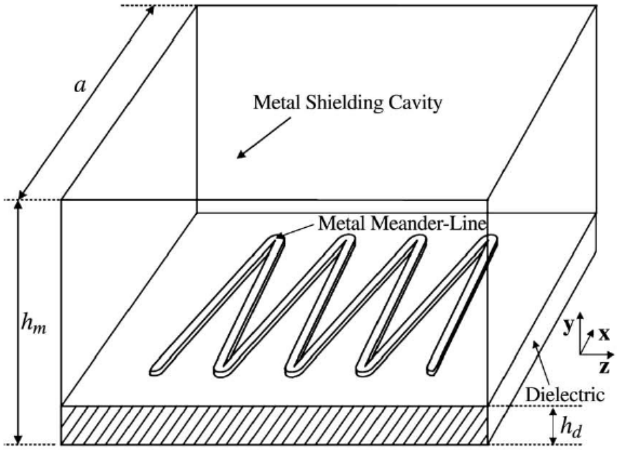

Figure 2-12 A V-shaped microstrip meander line [63]

The main limitations of the meander line SWS is its limited power capabilities. Moreover, the sensitivity the SWS to fabrication and assembly tolerance limits its use in the sub-mm/THz band.

2.3.4 The Folded Waveguide (FDW)

The Folded Waveguide (FDW) has become a promising SWS for sub-mm/THz wave devices [64]. The FDW is a serpentine waveguide folded back, multiple times, around itself. The beam tunnel is located at the center of the structure (Figure 2-13). The dominant mode (TE_{10}) propagates forward and backward across the electron beam, with its forward axial propagation slowed down. Thus this wave has a phase velocity matched to the phase velocity of the axial electron beam. Therefore, a good interaction between the electromagnetic wave and electron beam can be achieved. The FDW has a moderate bandwidth, high power handling capability and it is compatible with the planar fabrication using the MEMS technologies [64-68].

Depending on the cross-sectional dimensions, there are two main types of the FDW; the E-plane, and H-plane (Figure 2-13). In E-plane FDW, the electric field direction is parallel to the electron beam movement, while the electron beam movement is perpendicular to the electric field direction in the H-plane FDW. The E-plane FDW has a higher power conversion efficiency[70], while the disturbance in the field distribution is significantly reduced in the H-plane FDW [71].

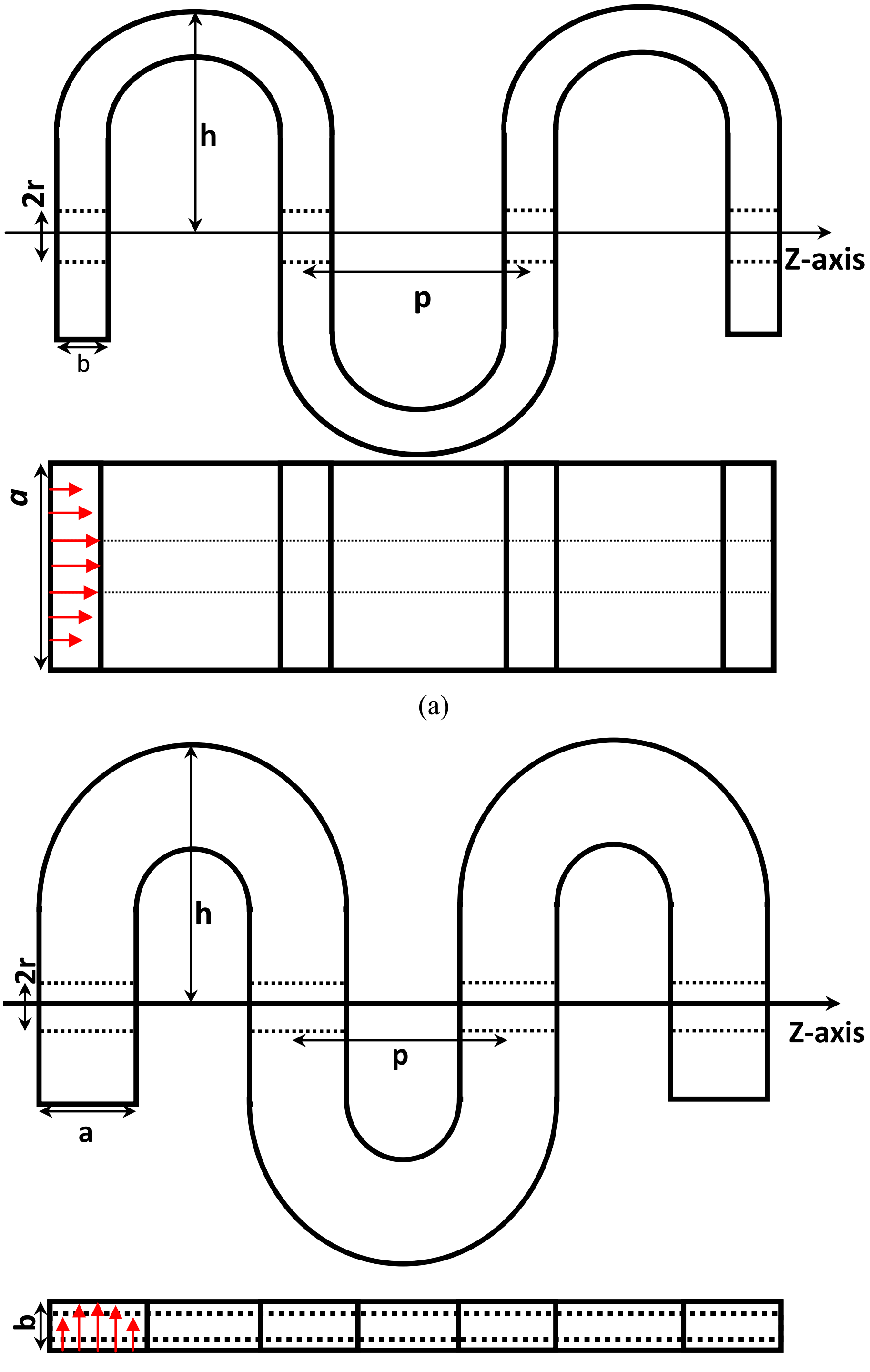

(a)

(b)

Figure 2-13 A schematic diagram of the FDW, (a) E-plane and (b) H-plane

Recently, different shapes of FWG were introduced. In [72] a folded frame SWS for millimeter TWT is proposed. The SWS, shown in Figure 2-14, consists of a series of metal frames connected to each other by a V-shape connector. The simulation results indicates that using a sheet electron beam (6 KV and 0.2A) produce an average power of 196W with an electron efficiency up-to 16.3%.

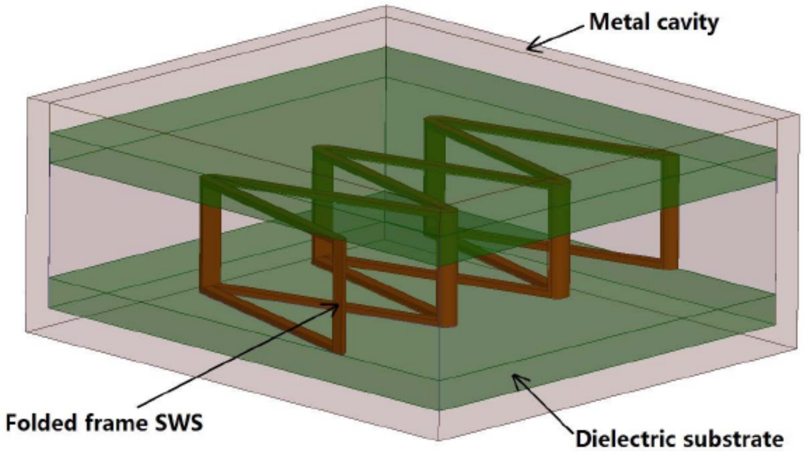

Figure 2-14 The Folded Frame SWS

The Meander-Line (ML) is an alternative type of the FDW. Figure 2-15 shows the schematic diagram of a 3D U-shaped microstrip ML SWS. It consists of two arrays of conductors, connected using a series of vias. Compared to the V-shaped ML, the U-shaped ML provides lower circuit attenuation and higher gain [73].

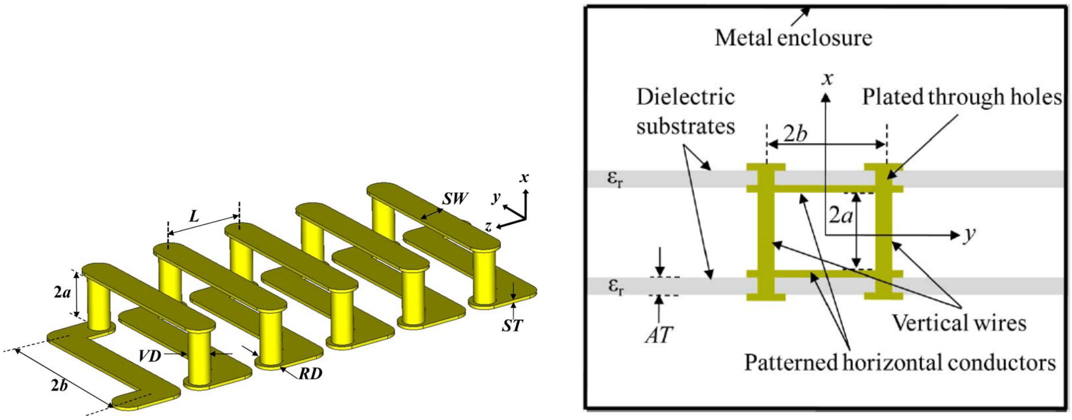

Figure 2-15 Schematic diagram of a U-shape meander line (a) 3D view and (b) cross sectional view [73]

There are several drawbacks for the FDW. Complex micro-fabrication is required to realize the FDW. Moreover, the conduction losses of the FDW are defined by the sidewall surface roughness. It was found that when characterizing a LIGA fabricated FWD to work as a SWS for upper mm-wave regime (100 – 300 GHz), it is almost impossible to have a smooth sidewalls [74-75].

2.3.5 The Periodic Loaded Waveguide (PLW)

The Periodic Loaded Waveguide (PLW) is considered as the ideal SWS for the Cherenkov based devices [51]. There are two main PLW structures; the disk loaded waveguide and the rippled waveguide.

2.3.5.1 The Disk Loaded Waveguide (DLW)

The disk loaded waveguide (DLW) is SWS for relativistic electron beam devices. Depending on the device, there are two types of excitation fields; the E-fields (TM-mode), and the H-fields (TE-mode). The TWT, BWO and the accelerators devices uses the axial electric fields (TM-mode) to interact with the electron beam. For the gyro-TWT, the electron beam interacts with the transverse electric fields (TE-mode). A schematic diagram of the DLW is presented in Figure 2-16. It consists of a circular waveguide loaded with several disks. By controlling the structure parameters (R_D is the disk hole radius, R_W is the waveguide radius, T is the disk thickness and L is the period length), the dispersion diagram of the DLW can be tailored [76-79].

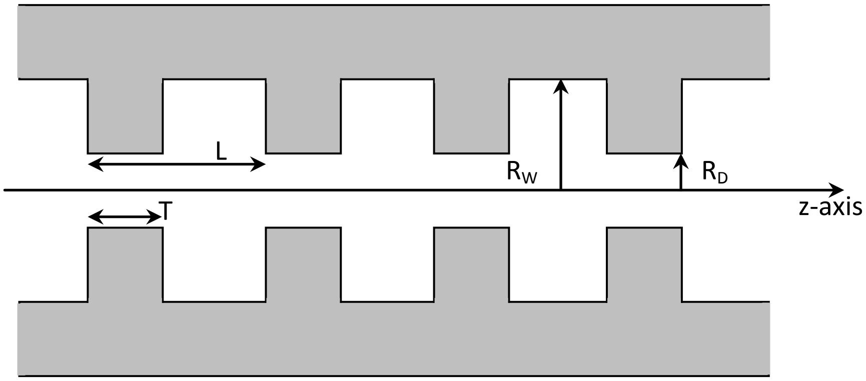

Figure 2-16 A schematic diagram of the DLW

2.3.5.2 The Ripple Waveguide (RW)

Instead of having a coaxial disc loaded at several distance across the waveguide, the ripple waveguide have a corrugated waveguide walls (Figure 2-17). Compared to the DLW, the ripple waveguide has two main advantages; it can handle higher breakdown field (voltage) and it has better beam modulation efficiency compared to the DLW. Several ripple waveguide was used a SWS in BWO [79]. A simulation result of a sine ripple waveguide structure was able to generate 1W of power at 220GHz [80]. Using dimensions scaling, the sine ripple SWS generated the same amount of power at 1THz [81].

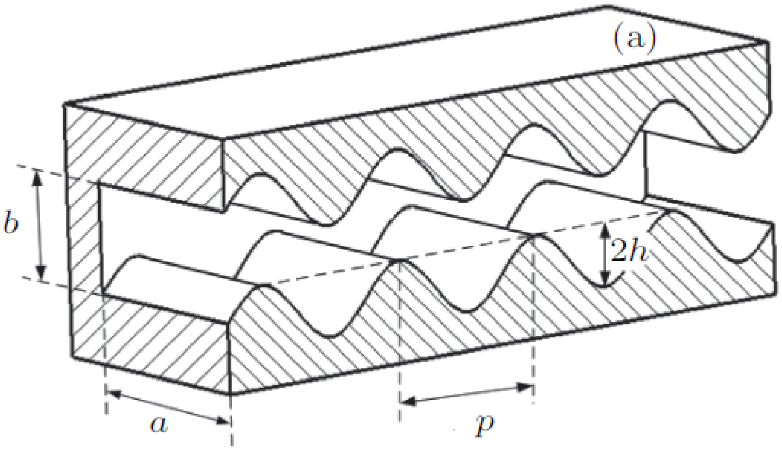

Figure 2-17 A schematic diagram of the Ripple Waveguide [80]

2.4 The Electron Beam

Since the VED is based on converting the electron beam energy to an electromagnetic energy, the electron gun is an essential component of the VED. Based on the electron emission, the electronic gun can be categorized as; thermionic gun, field emission gun and photo-electric gun. Although the thermionic gun is the most common on, several devices are designed to operate using the field emission gun. In this section a brief introduction to the both the thermionic gun and the field emission gun is provided.

2.4.1 The Thermionic Gun

In thermionic gun, the thermal energy is used to free the electron from the surface. Typical current density for a thermionic gun is 10 – 30 A/cm^2 [82-83]. Since most material melt if heated, the materials that can be used in the thermionic gun are either having a high melting point (refractory metals), or those have a low work function. Table 2-II presents the work function and the melting point for common thermionic gun materials.

Material	Work function (eV)	Melting temperature (˚K)	Richardson constant (A/cm^{2}K^2)
Tungsten (W)	4.5	3695	60
Lanthanum hexaboride (LaB$_6$)	2.7	2500	29
Cerium hexaboride (CeB$_6$)	2.65	2825	3.6

Table 2-II List of work function and melting temperature of selected materials

The thermionic gun consists of three main parts; filament (cathode), anode and the Wehnelt (grid), Figure 2-18(a). The electron beam emission is directly proportional to the heating current. It can be increase by increasing the heating current till the electron beam reaches saturation point (Figure 2-18(b)). The tungsten cathode is usually consists of a wire bent into hairpin (Figure 2-19(a)), in order to increase the efficiency of the generated beam, a disk attached to the wire bent (Figure 2-19(b)) is heated by the wire and emit electrons from the disk.

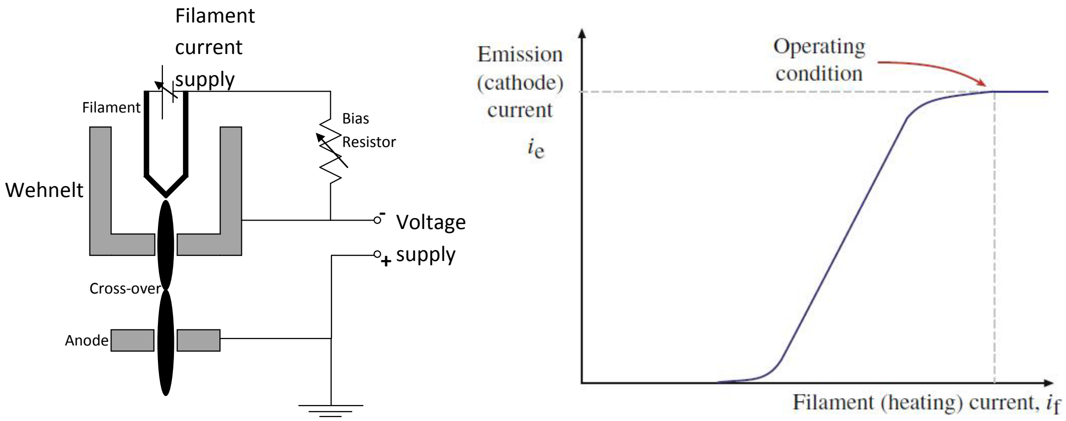

(a) (b)

Figure 2-18 (a) Schematic of a thermionic gun and (b) the saturation condition [84]

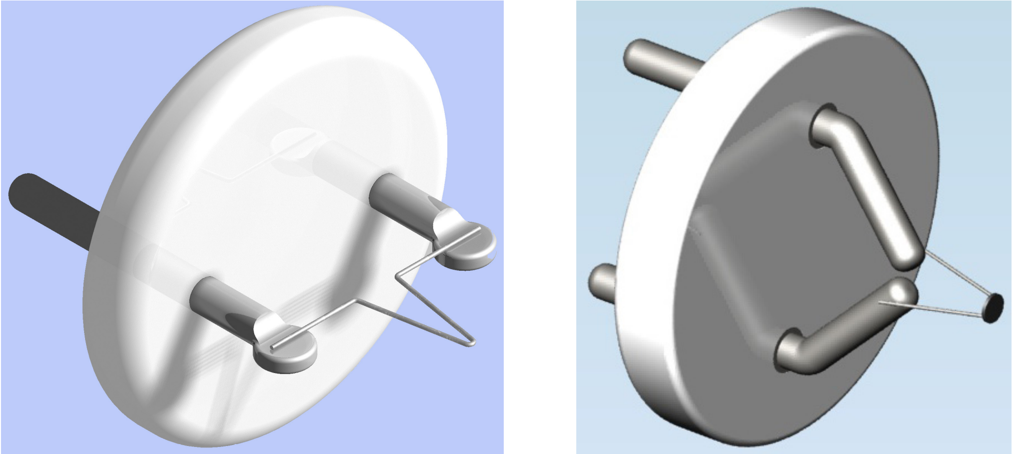
(a) (b)

Figure 2-19 A tungsten cathode (a) bent wire and (b) disk loaded bent wire

2.4.2 The Field Emission Gun (FEG)

Electron emission from material under the influence of strong electric field is called the field emission (cold emission). The field emission is usually occurring from the sharp needles, called Field Emission Gun (FEG) tip (Figure 2-20). A schematic of the FEG circuit is shown in Figure 2-20(b). The figure shows that the gun has two different anodes. The first anode has a voltage of few kV to tunnel the voltage from the gun tip. While the second anode, which is connected to higher voltage, is used to accelerate the electron beam to the desired velocity. The companied field of the two anodes produces an electromagnetic lens that forms the cross-over. Another magnetic lens is required to provide more control to the electron beam parameters.

To overcome the contamination of the FEG, the FEG is usually kept in vacuum. Since the FEG emits electrons from a very small tip, the generated beam is extremely small [85-86]. Using an array of FEGs, a high average current requirement can be achieved [87].

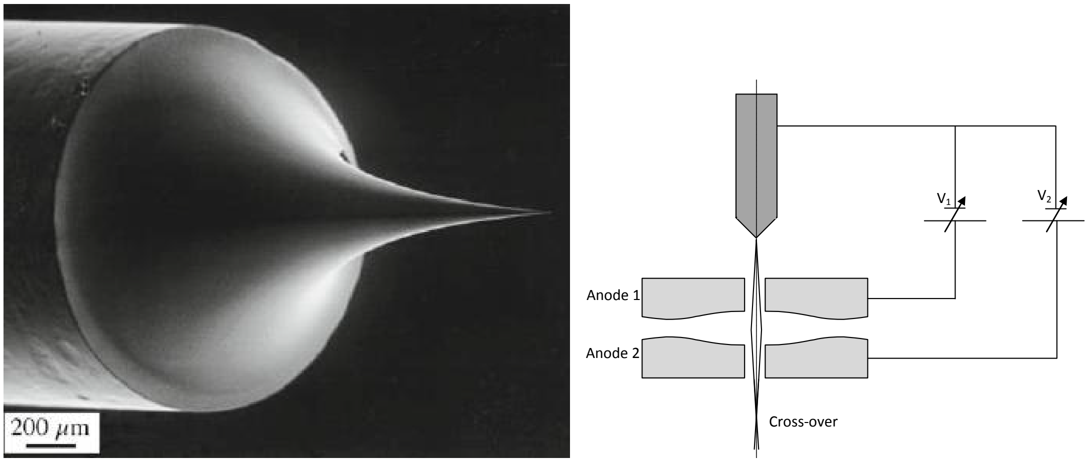

(a) (b)

Figure 2-20 (a) A FEG tip and (b) Schematic of FEG [84]

2.4.2.1 The Field Emitter Array (FEA)

Since the Field Emitter Array (FEA) – the cold cathode – has several applications. It attracts a lot of attention. The FEA consists of a large number of identical small field emitter organized in a 2D array (Figure 2-21). The FEAs has higher beam current, good beam quality and spatial uniform emission can be achieved. The main limitation in micro-fabrication of the FEAs is their reliability and the efficiency. The Transfer Mold Technique (TMT) is considered as the main fabrication method for the FEA. An FEA with different emitter materials such as; Molybdenum (Mo), Lanthanum Hexaboride (LaB6), Titanium Nitride (TiN), amorphous Carbon (a-C) and diamond, has been reported [88-90].

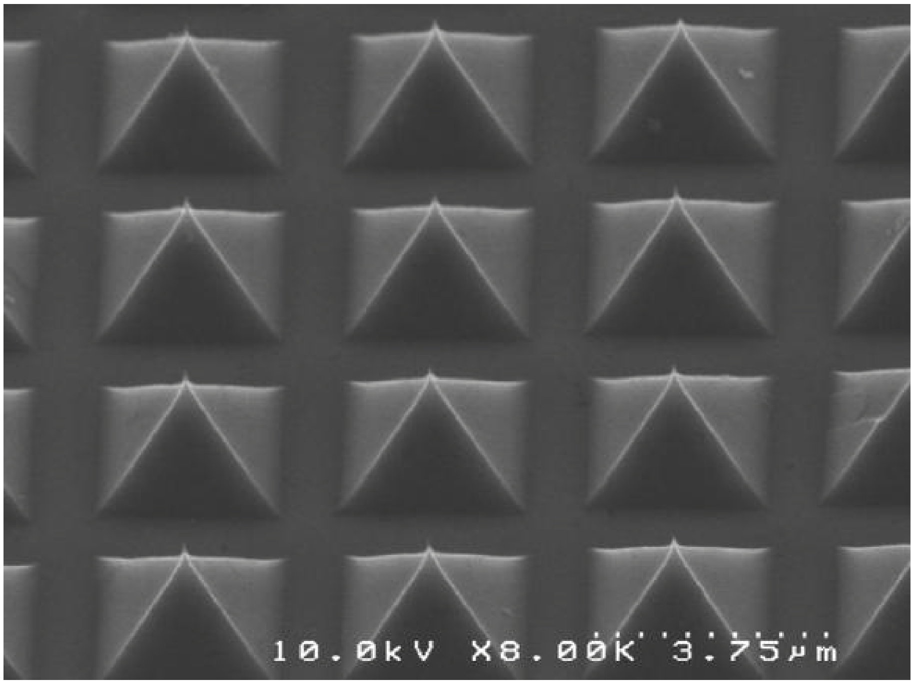

Figure 2-21 An SEM image of an FEA [88]

2.5 Conclusion

The above discussion shows that although the VEDs sources can be considered as a promising high power sub-mm/THz source, there are several problems and challenges in realizing it. For the SWS part, while currently there are several SWS under research and investigation, they have several drawbacks. Realization and fabrication problems, limited power handling capabilities, limited efficiency are examples for the current challenges in the SWS. On the other hand, although the advance in the FEA source fabrication and realization makes it a good choice for VEDs operating in THz regime, the complex focusing network requirements limits its use in the VED.

Starting from the SWS part, using the metallic based Photonic Crystal (PC) based SWS may alleviate the above problems. The power handling of the metallic structure, the robust fabrication techniques and the good mode selectivity of the PC structure provide an answer to the SWS problem in this band. Furthermore, coupling the FEA beam with such structure may result in solving the THz source problem.

Chapter 3

Design and Analysis of the SWS

3.1 Introduction

The first step in designing a photonic device is the design of a Photonic Crystal (PC) based waveguide. The accurate determination of the modal parameters of the PC waveguide such as; field distribution, attenuation constant, phase constant, and phase velocity is a critical part in analyzing of such devices. Therefore in this chapter, the non-uniform FDFD method will be introduced to define these modal parameters. Then using the non-uniform FDFD method, a novel non-axial slow wave structure (the Double Defected Photonic Crystal (DD-PC)) will be proposed and analyzed.

The chapter will outline the design/analysis of the SWS. First, the FDFD method is established highlighting both; the multi-level meshing and the material coefficient implementation. After that, the DD-PC based SWS is introduced and analyzed using the proposed FDFD method. Finally, the existence of the slow wave mode inside the proposed DD-PC structure was verified using both numerical and experimental verifications.

3.2 The non-uniform FDFD method

Starting from Maxwell's equation [24], assuming all fields vary in longitudinal and time in the form $e^{j(\beta z-\omega t)}$, and scale the electric field by the free space wave impedance:

$$\nabla \times \vec{\boldsymbol{E}} = j\omega \vec{\boldsymbol{B}} \qquad \text{(3-1a)}$$

$$\nabla \times \vec{\boldsymbol{H}} = -j\omega \vec{\boldsymbol{D}} \qquad \text{(3-1b)}$$

Convert from the vector form to the component form:

$$jk_0 H_x = \frac{\partial E_z}{\partial y} - j\beta E_y \qquad \text{(3-2a)}$$

$$jk_0 H_y = -\frac{\partial E_z}{\partial x} + j\beta E_x \qquad \text{(3-2b)}$$

$$jk_0 H_z = \frac{\partial E_y}{\partial x} - \frac{\partial E_x}{\partial y} \qquad \text{(3-2c)}$$

Where “ $\vec{\boldsymbol{E}}$ ” and “ $\vec{\boldsymbol{H}}$ ”” are the vector form of electromagnetic fields, “β” is the phase shift constant and “k_0” is the free space wavenumber.

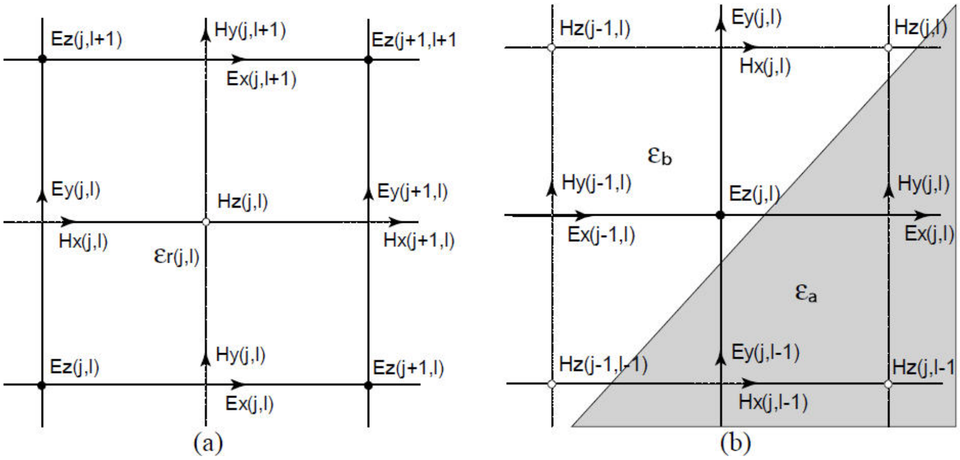

Figure 3-1 (a) 2-D Yee mesh based, (b) mesh handle in curved structure [97]

Then, by applying the central difference algorithm on the 2D Yee mesh discretization (Figure 3-1) the eigenvalue problem can be expressed as:

$$\beta^2 \begin{bmatrix} E_x \\ E_y \end{bmatrix} = \begin{bmatrix} P_{xx} & P_{xy} \\ P_{yx} & P_{yy} \end{bmatrix} \begin{bmatrix} E_x \\ E_y \end{bmatrix} \tag{3-3}$$

Where E_x and E_y are the transverse electric fields, and P_{xx}, P_{xy}, P_{yx} and P_{yy} are square coefficient matrices.

Solving the above eigenvalue problem, the phase shift constant and the associated transverse fields can be calculated. Also, the axial fields can be calculated using Maxwell’s equations. The full details of the FDFD formulation and the coefficient matrices are provided in Appendix A.

3.2.1 The Multi-level meshing

To increase the accuracy of the FDFD method, a fine mesh is required, which needs more computational memory. To solve this problem, the multi-level mesh approach is proposed. Figure 3-2 shows the 2-to-1 multi level meshing. As the figure shows, the fine mesh was applied to the interface between different materials, while the coarse mesh was applied to other parts of the computational window. Since the number of points in the fine mesh is twice the number of points in the coarse mesh, the mesh is called the 2-to-1 multi level meshing.

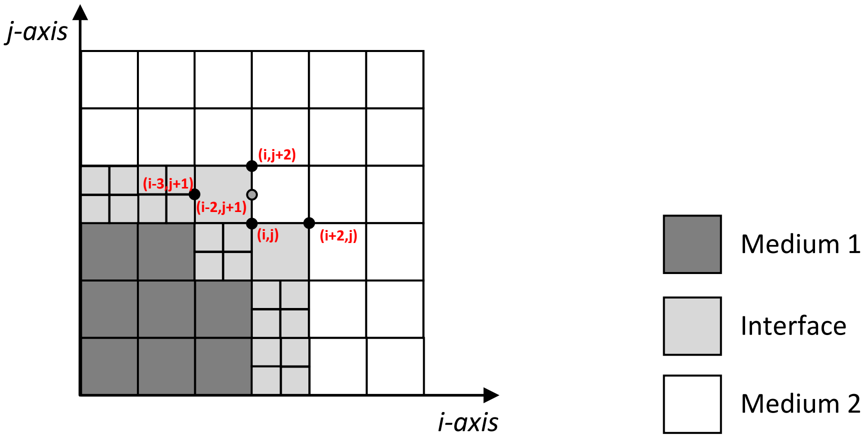

Figure 3-2 The grid distribution of the multi-level meshing

As an example of the above technique, the coefficient matrix of equation (3-2b) will be calculated. Using the Yee-discretized, the discretized equation can be re-write as;

$$jk_0 H_y\big|_{(i,j)} = j\beta E_x\big|_{(i,j)} - \frac{E_z\big|_{(i+1,j)} - E_z\big|_{(i,j)}}{\Delta x} \tag{3-4}$$

For a point in the coarse mesh, equation (3-4) becomes:

$$jk_0 H_y\big|_{(i,j)} = j\beta E_x\big|_{(i,j)} - \frac{E_z\big|_{(i+2,j)} - E_z\big|_{(i,j)}}{\Delta x} \tag{3-5}$$

While for a point at the fine mesh, the discretized equation turns to:

$$jk_0 H_y\big|_{(i-3,j+1)} = j\beta E_x\big|_{(i-3,j+1)} - \frac{E_z\big|_{(i-2,j+1)} - E_z\big|_{(i-3,j+1)}}{\Delta x/2} \tag{3-6}$$

For a point at the interface between two materials, first an interpolation process is used to calculate the field at this point:

$$E_z\big|_{interpolation} = \frac{1}{2}\left(E_z\big|_{(i,j)} + E_z\big|_{(i,j+1)}\right) \tag{3-7}$$

Then, substitute into equation (3-4), the equation becomes

$$jk_0 H_y\big|_{(i-2,j+1)} = j\beta E_x\big|_{(i-2,j+1)} - \frac{E_z\big|_{interpolation} - E_z\big|_{(i-2,j+1)}}{\Delta x} \tag{3-8}$$

Then the coefficient matrix A_x can be expressed as:

$$A_x = \frac{1}{\Delta x}\begin{pmatrix}
-2 & 2 & 0 & & & & & & & & & & & & \\
0 & \boxed{-2} & 2 & & & & & \cdots & & & & & & 0 & \\
0 & 0 & -1 & & & & & & & & & & & & \\
 & & & & \ddots & & & \ddots & & & \ddots & & & & \\
 & & & 0 & 0 & 0 & -1 & 1 & 0 & 0 & 0 & 0 & & & \\
 & \vdots & & 0 & \boxed{0.5} & 0 & 0 & -1 & 0 & 0 & \boxed{0.5} & 0 & & \vdots & \\
 & & & 0 & 0 & -1 & 0 & 0 & -1 & 0 & 0 & -1 & & & \\
 & & & & \ddots & & & \ddots & & & \ddots & & & & \\
 & & & & & & & & & & & & -1 & \boxed{0} & 0 \\
 & 0 & & & & & & \cdots & & & & & 0 & -1 & 1 \\
 & & & & & & & & & & & & 0 & 0 & -1
\end{pmatrix} \tag{3-9}$$

Some features in the above matrix worth mentioning. First, the highlighted zero in the above matrix represents the PEC boundary conditions. While the *"2"* in the coefficient matrix shows a field point located in the fine grid part. Finally, the "0.5" terms indicates the interpolation term for the points at the interface between the fine/coarse mesh.

3.2.2 The dielectric constant

The complex dielectric constant was used to analyze general guiding structure. The dielectric constant is defined as:

$$\varepsilon_r = \varepsilon' - j\varepsilon'' - j\frac{\sigma}{\omega\varepsilon_0} \tag{3-10}$$

where *"ε′"* is the dielectric constant, *"ε″"* is the dielectric losses, and *"σ"* is the conductivity.

By simply including the complex dielectric constant, the non-uniform FDFD method can be used to analyze lossless dielectric, lossy dielectric and lossy conductive materials.

3.2.3 Assessment of the non-uniform FDFD Method

In this section, the stability, accuracy and convergence of the non-uniform FDFD method will be investigated. The assessment was performed using the rib waveguide, further justifications are provided in Appendix A. For all the justifications, an electric wall – Perfect Electric Conductor (PEC) – boundary condition will be used to terminate the computational window. The simulation was performed using a personal computer with following specifications; dual-core CPU 2.6GHz and 4G RAM. A Matlab Code was used to implement the FDFD method.

3.2.3.1 The Rib Waveguide

To check the numerical precision of the non-uniform FDFD method in analyzing pure dielectric structures, the fundamental mode of a standard rid waveguide was selected as a test bench. A schematic diagram of the rib wave guide is shown in Figure 3-3, while a summary of the physical dimensions, the material properties and the operating wave length are listed in Table 3-I. Since the difference between the dielectric constant of the guiding layer and the substrate layer is very small ($\Delta n = 0.040$), the numerical method should be accurate enough to detect the waveguide parameters (up to the fourth decimal place at least).

Operating wavelength		1.15 µm
Physical Dimensions	Rib width (W)	3.00 µm
	Rib height (H)	0.20 µm
	Slab depth (D)	0.80 µm
Dielectric constant	Guide refractive index n_f	3.44
	substrate refractive index n_s	3.40
	Cladding refractive index n_c	1.00

Table 3-I The parameters of the Rib Waveguide

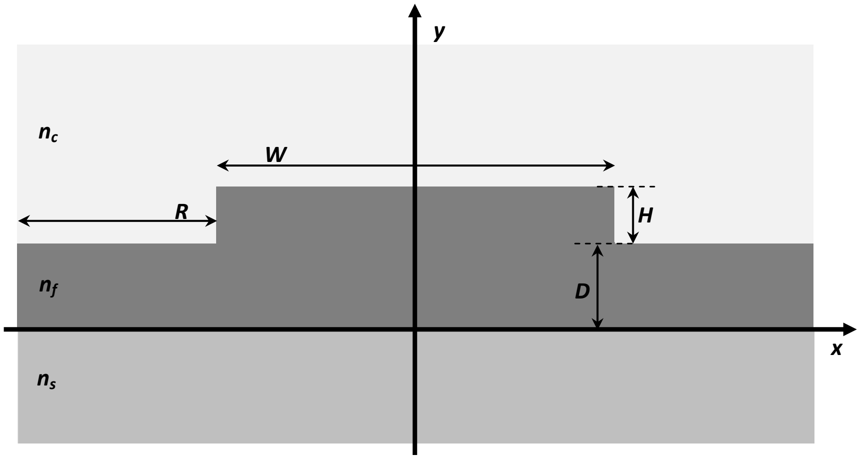

Figure 3-3 A schematic diagram of the Rib Waveguide

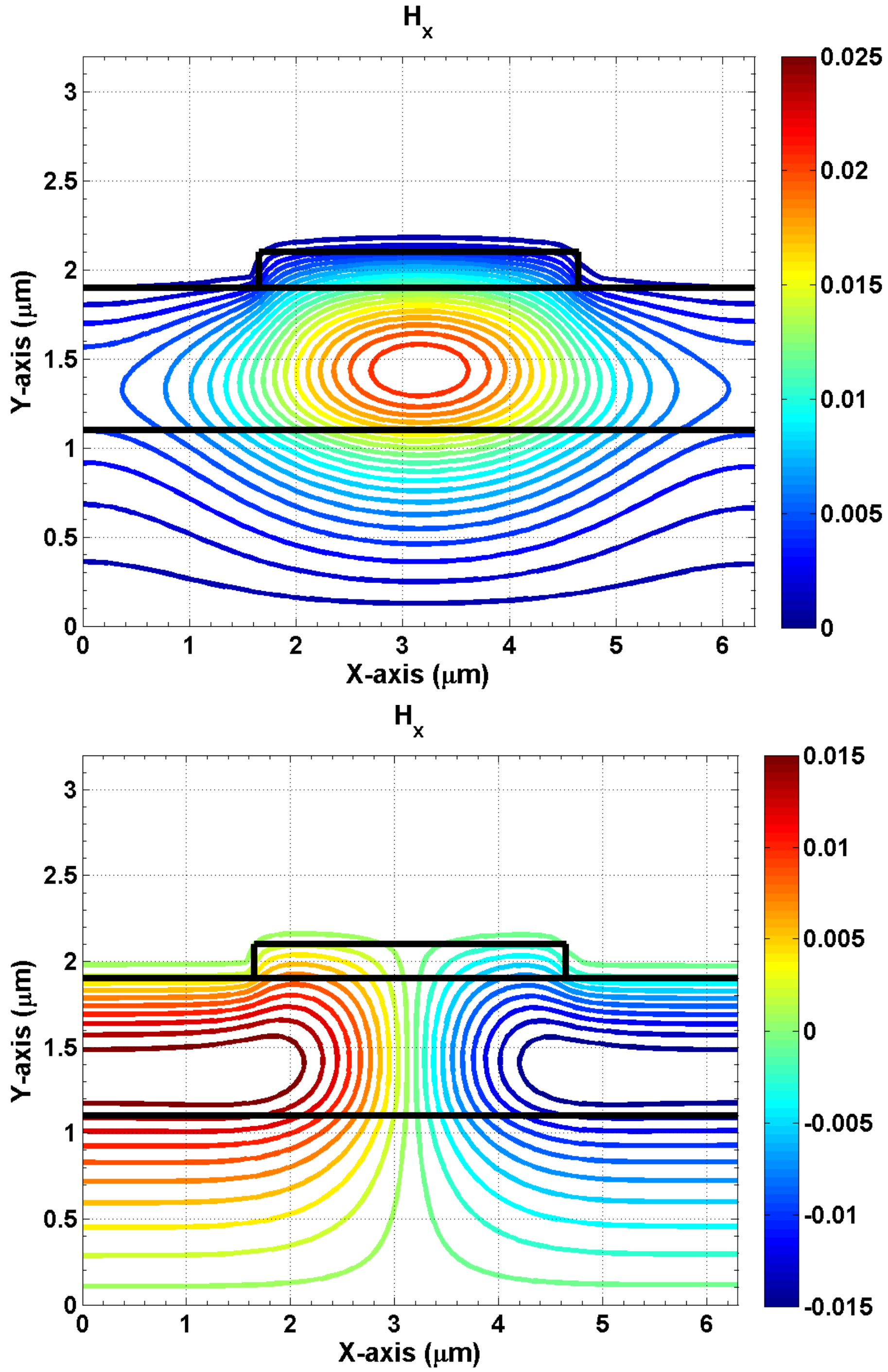

(a) (b)

Figure 3-4 Transverse magnetic field pattern of (a) dominant mode (b) next higher order mode

In this analysis, the discretization lengths in *x*- and *y*-directions were selected to be $0.183\lambda_0$ and $0.093\lambda_0$, respectively (which is equivalent to 1806 mesh points). The computational time was less than 5 seconds. The calculated effective refractive index (n_{eff}) was found to be 3.41424. Compared to the published Finite Element Method (FEA) a division of almost 0.0149% was detected [98]. Furthermore, the transverse magnetic field pattern (shown in Figure 3-4) shows a good agreement with the published one.

To show the robustness of the proposed non-uniform FDFD method, the variation of the effective refractive index of the fundamental mode at different rib height "*H*" is calculated (Table 3-II). The rib height was changed uniformly from *0.1μm* to *1.0μm*, while the slab depth "*D*" was selected such that *H+D=1μm*. The table also shows a comparison between the non-uniform FDFD method and different numerical methods (the Vector Finite Element Method (VFEM), Imaginary Distance full Vectorial Finite Element Beam Propagation Method (IDVFE-BPM) and the VFEM with higher order mixed-interpolation-type elements (Edge-FEM)). The results show that there is a good agreement between the non-uniform FDFD method and the different methods listed.

H (μm)	VFEM	IDVFE-BPM	Edge FEM	Non-uniform FDFD
1.0	3.41210	3.41202	3.41194	3.41163
0.9	3.41220	3.41213	3.41209	3.41174
0.8	3.41235	3.41229	3.41224	3.41190
0.7	3.41255	3.41250	3.41247	3.41214
0.6	3.41285	3.41279	3.41278	3.41242
0.5	3.41315	3.41314	3.41312	3.41277
0.4	3.41365	3.41358	3.41258	3.41332
0.3	3.41410	3.41410	3.41414	3.41383
0.2	3.41475	3.41473	3.41480	3.41424
0.1	3.41560	3.41558	3.41568	3.41569

Table 3-II Comparison between non-uniform FDFD and different FEM techniques at different values of rib heights *"H"*

The next test is the numerical convergence of the non-uniform FDFD method. In this test, the effective index of the rib waveguide, at a rib height H of 0.2μm, was calculated at different grid size.

Table 3-III presents the calculated effective index at different grid sizes. As expected, increasing the number of girds increases the number of elements at which the fields are calculated, and hence the computational time increases. The table shows that even for a coarse mesh, the variation of the effective index is small (within the fourth decimal place).

Mesh Size	Effective index (n_{eff})	No. of elements
30×30	3.4149	1806
50×50	3.4144	4834
70×70	3.4143	9310
85×85	3.4142	13463

Table 3-III Effect of changing the grid size

The final assessment of the non-uniform FDFD is the effect of the boundary separation *"R"* on the calculated effective index (Figure 3-3). The variation of the wall separation "*R*" on the effective index of the fundamental mode, is shown in Table 3-IV. The results indicate that only the fourth decimal place was affected by changing the separation *"R"*, thus the calculated effective index is independent on the wall separation.

R	n_{eff}
1.10	3.4144
1.65	3.4142
2.65	3.4141

Table 3-IV Effect of changing the structure size

3.3 The Photonic Crystal (PC) Structure

The Photonic Crystal (PC) structure consists of periodic materials (dielectric or conducting ones) placed in a periodic lattice structure [101-102]. The main feature of the PC structure is its ability to prevent certain electromagnetic wave – of a certain frequency bands – from propagation inside it. These bands of frequencies called the global band gaps. The PC structure can be formed by a one (1D) -, two (2D) - or three (3D) dimensions periodic lattice structure. For a 2D PC structures, there are two common lattice structures; the square lattice and the triangle lattice.

In this work, using both the good modal sensitivity of the 2D PC structure along with the power handling capabilities of the conducting structure, a metallic PC based SWS is introduced and analyzed. Since the TM-like mode is mainly responsible for the electron beam-wave interaction, only the triangle lattice will be considered in this work [102]. In this section, the design of the slow wave structure (also called the "*cold analysis"*) will be discussed in details.

3.3.1 The Photonic Crystal based Slow Wave Structure

The SWS is an electromagnetic structure that supports the propagation of an electromagnetic mode with a phase velocity lower that the speed of the light in the media. As discussed in *2.3 The Slow Wave Structure (SWS)*, the SWS is an essential part in the electron beam-wave interaction devices. According to Cerenkov condition, the slow wave mode can interact with an electron beam travelling with a velocity synchronized with the phase velocity of these modes. Thus, a narrow band of coherent electromagnetic radiation can be extracted from the beam. According to the literature review, there are some requirements for SWS design in the THz band. First, to have a high power source, the proposed SWS should be a metallic one. Furthermore, since the dimensions of the structure will be extremely small, the proposed SWS should have a simple cross section and compatible with the modern fabrication techniques. In addition, it will be better to have a separation between the generated THz signal and the electron beam to facilitate the extraction of the generated power.

To achieve these requirements; the metallic Double Defected-Photonic Crystal structure (DD-PC) was introduced. The DD-PC based SWS consists of three uniform layers of metallic rods, placed in a triangle lattice PC formation (Figure 3-5). The structure consists of two types of defects; a central defect (the air-core) and four slow wave defects. The central defect is obtained by removing the inner-most layer of the metallic rods, thus allowing the electron beam to move axially (longitudinally) inside the SWS structure. While, the slow wave defects or transverse-cavities, are formed by removing four additional rods as shown in the figure (numbered SW-1 to SW-4). These defects are used to support and extract the beam-wave interaction generated electromagnetic waves. In addition to its simplicity, the DD-PC SWS structure isolates the electron beam from the extracted electromagnetic wave, thereby potentially enabling simple extraction of the generated electromagnetic fields.

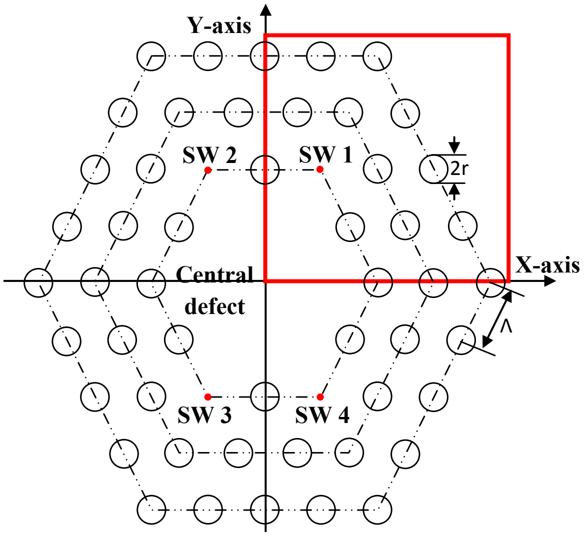

Figure 3-5 A cross section of the DD-PC based SWS

According to Maxwell's equations, in order to satisfy the wave equation, the wave number of the guided modes supported by the structure must satisfy the following dispersion equation [103-105]:

$$k^2 = \omega^2 \mu\varepsilon = k_{transverse}^2 + k_z^2 \tag{3-11}$$

where $k_{transverse}$ is the wavenumber in the transverse direction, and k_z is the wave number in the axial (z-) direction (i.e., the phase shift constant, β). The μ and ε are the intrinsic permeability and permittivity of the guiding medium (air in our case), and ω is the frequency of operation.

For a conventional closed metallic waveguide, the transverse wave number is always real. Therefore, the longitudinal wave number (k_z, or β) is always less than the wave number of the intrinsic medium (k). Thus, the guided modes can only be *"fast"* wave modes [103-105]. However, the proposed DD-PC structure has photonic band gap (PBG) like behavior in the transverse direction due to the periodic metallic electromagnetic boundary conditions. Thus, in such waveguide structure we can have an imaginary transverse wave number associated with a physically propagating mode in the z-direction. Therefore, as per (equation 3-11), the axial propagation constant (β) can be larger than the intrinsic wave number in the medium; hence the associated propagating wave is a *"slow"* wave, or the so called defect mode of the structure. This is the fundamental underlying principle behind the fact that the proposed structure can support axial slow wave propagation without any axial discontinuity. We believe that this is a very important observation for future technological development of the sub-mm/THz BWO devices.

Since the conductive rod is the building structure of the DD-PC structure, a full analytical analysis of the different modes propagation through such structure was performed in Appendix B [124]. The analysis also discusses several applications of the surface wave propagation along the conductive rod.

3.3.1.1 Design of the DD-PC based SWS

Starting from the band diagram of the triangle lattice metallic PC structure, the geometrical parameters of the DD-PC based SWS can be calculated [103]. Figure 3-6 shows the band diagram, with the black dot defines the operating point. This point was selected to allow the first mode to propagate with a frequency of 130GHz. From the operating point, the pitch size can be calculated ($\omega\Lambda/c = 5.4$, so at the operating frequency $\Lambda=2.00mm$). The rod radius is calculated from the same point ($r/\Lambda=0.4$, since pitch size was found to be 2.00mm, the rod radius equals 0.8mm).

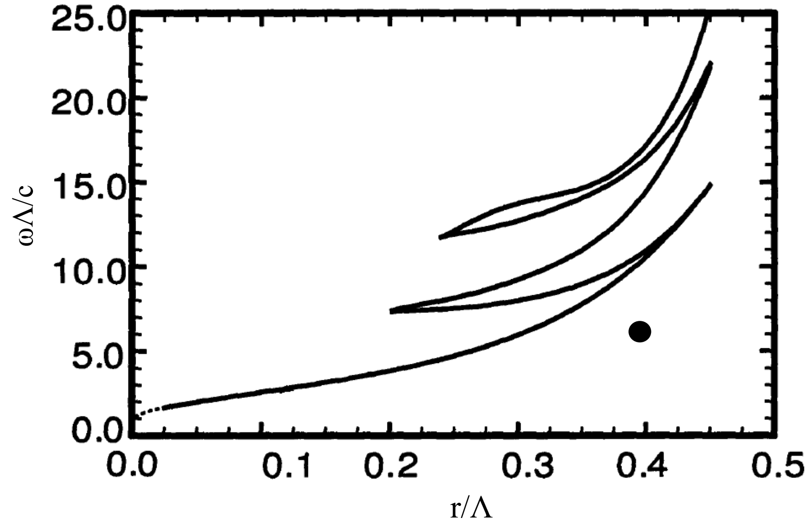

Figure 3-6 The band-diagram of the TM mode in a metallic triangle lattice PC, the solid dot represent the operating point at 130GHz

3.3.1.2 Analysis of the DD-PC based SWS

Since the structure doesn't have any axial discontinuity, the non-uniform FDFD method can be used to define the modes of the structure. Taking advantage of the structure symmetry, only a quarter of the structure was analyzed. The red square highlighted in the Figure 3-5 represents the computational window. The variation of the phase shift constant and the normalized phase velocity of the slow wave mode are plotted in Figure 3-7. The figure shows that for a frequency variation between 100 to 140GHz, the normalized phase velocity ($v_{ph}\big|_{norm} = v_{ph}/v_c$) varies between 0.2 and 0.6. This verifies that the propagating mode is a slow wave mode. Also the figure shows that for the same frequency range, the phase shift constant decreases with the increase of the frequency. This can be explained from the fact that as the frequency increases, the electrical dimensions of the structure expands. Therefore, the mode becomes less concentrated. And hence the phase shift constant decreases.

The transverse and the axial electric field components of the slow wave mode are plotted in Figure 3-8(a) and (b), respectively. The figure indicated that the field is localized at the entrances of the slow wave cavity. Thus, a good coupling between the electron beam fields and the slow wave modes can be achieved. Furthermore, since field is located at the air opening – away from the copper rods – the modal losses is minimized.

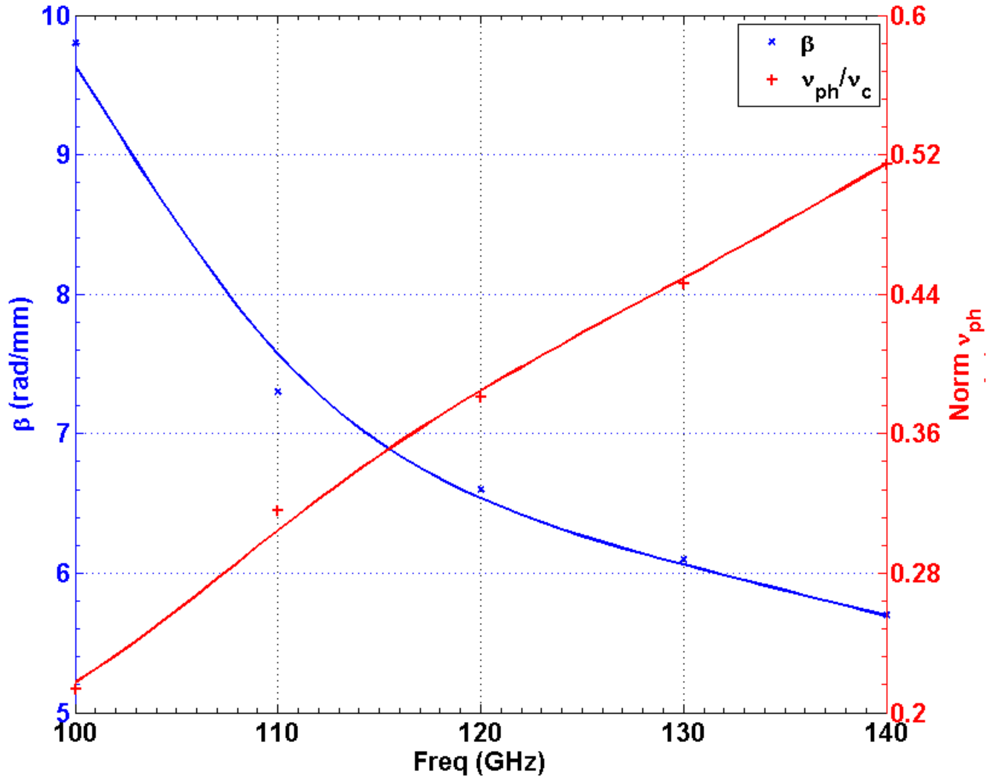

Figure 3-7 The dispersion curve of the DD-PC based SWS

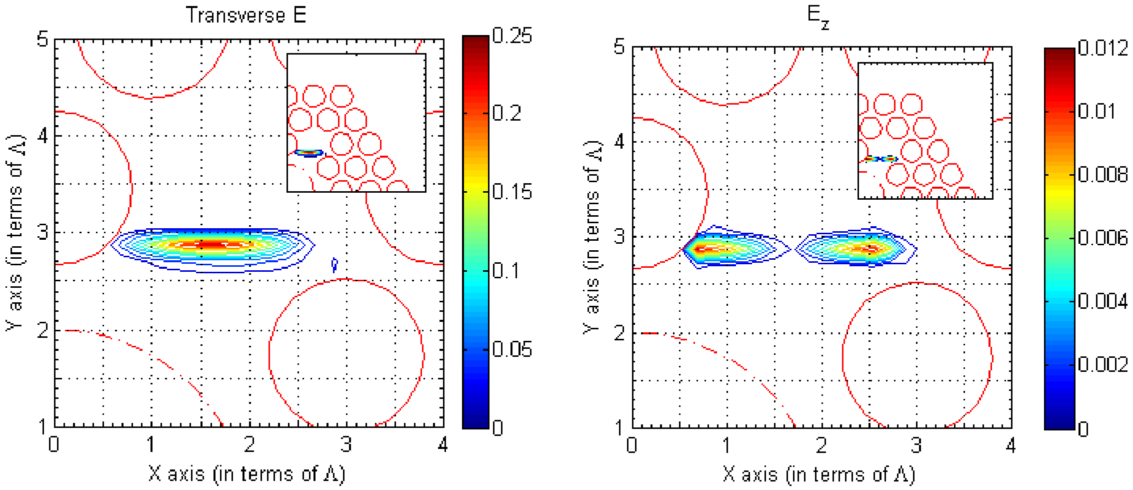

(a) (b)

Figure 3-8 A zoomed picture of (a) the transverse electric field and (b) the axial magnetic field calculated at 130GHz.

3.4 Verification of the slow wave mode in DD-PC based SWS

Since the proposed DD-PC based SWS is a novel structure, it is essential to prove the existence of the slow wave mode with other techniques. The verification is performed using both numerical analysis and simple experiments. As the structure was analyzed using a frequency domain method (non-uniform FDFD), the numerical verification was done using the Finite Difference Time Domain (FDTD) simulation. Furthermore, using the Computer Numerical Control (CNC) machinery, a scaled prototype of the SWS was fabricated and tested.

3.4.1 The numerical verification of the DD-PC based SWS

The FDTD method is a well know simulation tool used for analyzing electromagnetic structure. Taking advantage of the FDTD simple implementation, several complex and complicated problems can be tackled. Besides its simplicity, the FDTD method covers a wide band of frequencies in a single run [95], [106-107].

In the numerical verification, a multi-thread parallel FDTD code was designed to test the DD-PC based SWS. Using the parallel computing, a significant reduction in FDTD computational time was achieved. The flow chart of the FDTD method is presented in Figure 3-9. The chart shows the three main steps of FDTD simulation; problem initialization, the time loop, and the post processing. During the problem initialization, the following tasks were performed. First the different geometrical parameters are defined and allocated. Then different material parameters (dielectric constant (ε_r) and the conductivity (σ S/m)) are defined and assigned to different geometrical parts. The final part in the problem initialization is the discretization of the computational window, and defining the parameter of the applied Absorbing Boundary Conditions (ABCs). The next step – the time loop (Time marching) – is considered as the main bottle neck in the FDTD simulation. In each time step the value of the electric and magnetic fields are calculated / updated. For the post processing analysis, the electromagnetic fields are stored at different positions in the computational window. The time loop will continue until either the field values reaches a certain cut-off limit or till the time loop reaches a certain number of iterations. Finally, the post processing analysis is applied to the stored electromagnetic fields.

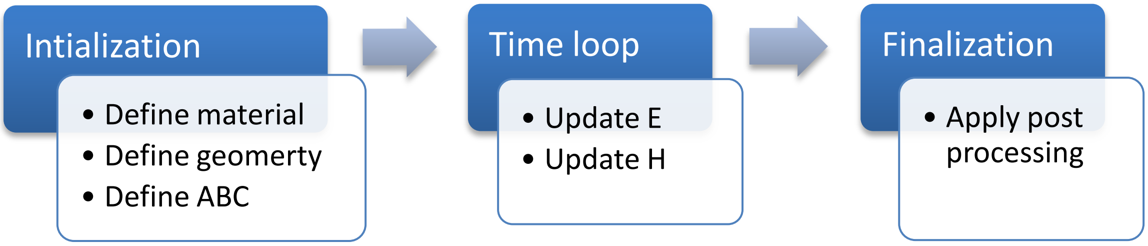

Figure 3-9 A flow chart of the FDTD

In a conventional (sequential) FDTD the field components are updated in a sequential pattern (Figure 3-10). Thus, within each time step, at least six calculations are performed one after the other. According to the Yee cell, updating of each magnetic (electric) field component depends only on electric (magnetic) field components and independent on the other magnetic (electric) field components. Therefore, all magnetic (electric) fields can be recalculated at the same time. A flow chart of the parallel FDTD is plotted in Figure 3-11. The figure indicates that the three electric (magnetic) field components are calculated at the same time step. Therefore, a time speed factor up to 3x can be achieved [108].

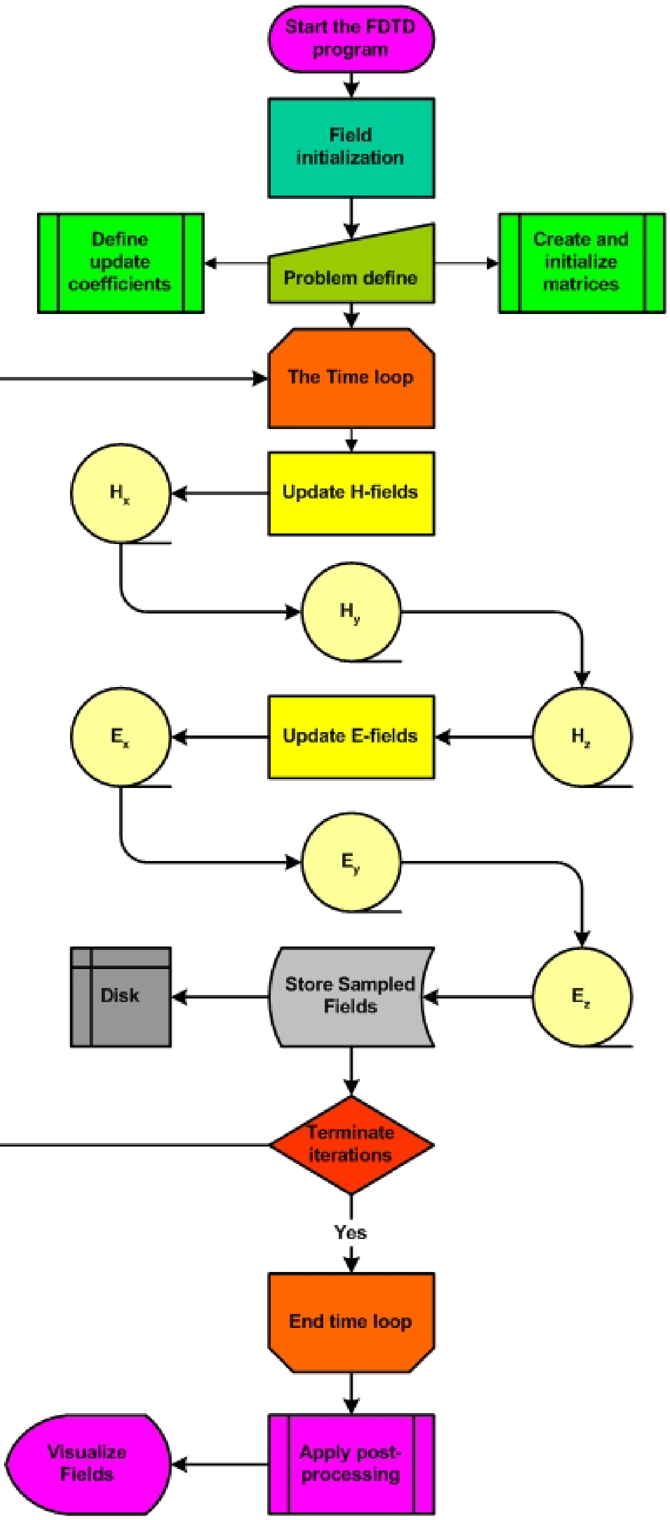

Figure 3-10 Sequential (conventional) representation of the FDTD simulation

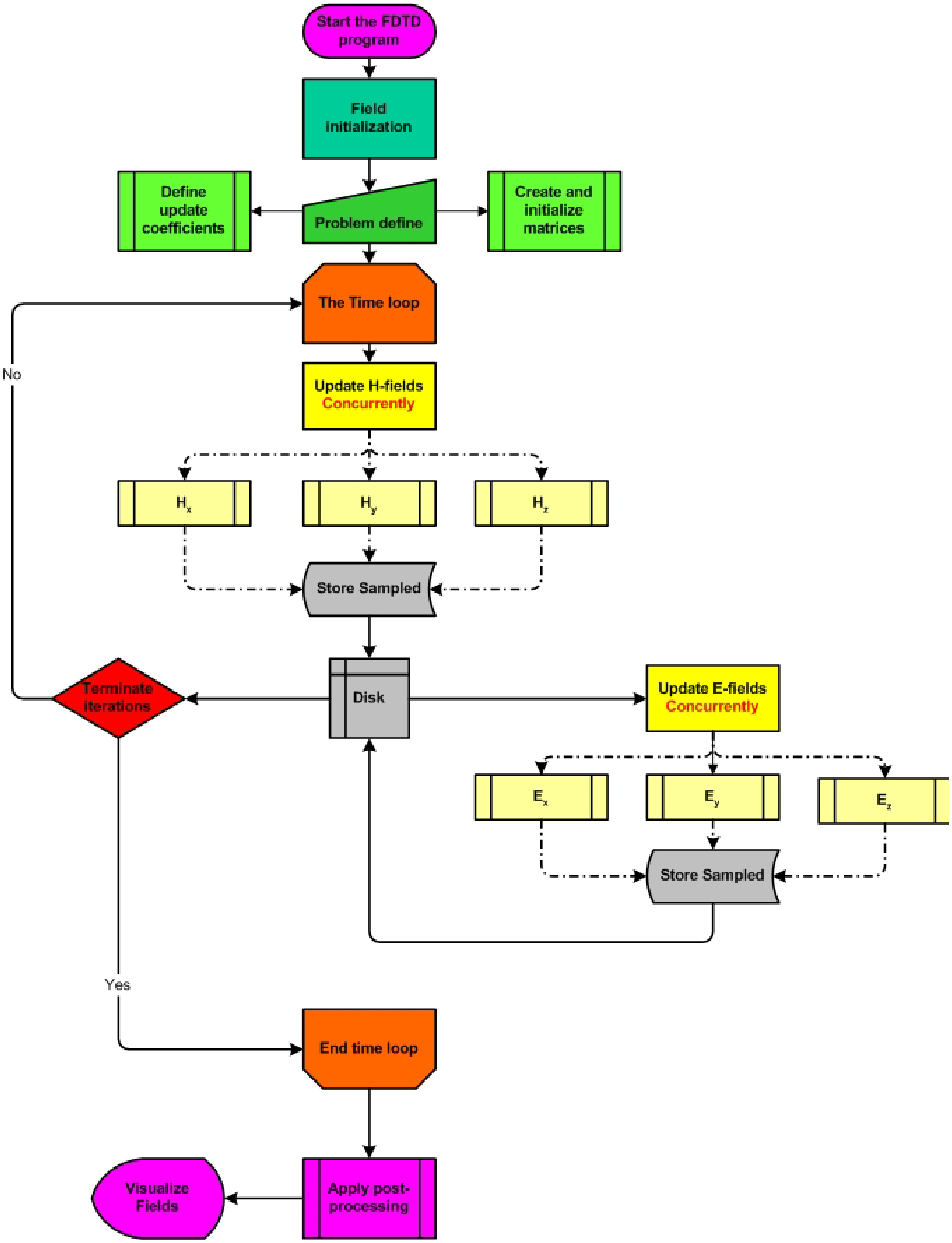

Figure 3-11 Parallel implementation of the FDTD simulation

The parallel FDTD is used to verify the slow wave mode existence in the DD-PC based SWS. A schematic diagram of the FDTD simulation window is plotted in Figure 3-12. The Device Under Test (DUT) consists of three parts; the DD-PC SWS, the input port, and the output port. The input/output ports are a coaxial feeder. The structure was excited with a Gaussian pulse. The center frequency (f_0) of the pulse is 150GHz, while the bandwidth (BW) of the pulse is almost 60GHz. The Perfectly Matched Layer (PML) was used as an ABC to terminate the FDTD computational window. To isolate the analyzed structure from the ABC-PML, a separation distance of $0.25\lambda_0$ (λ_0 is the wavelength at the center frequency f_0) was used to separate the structure from the PML-ABC terminations. Also, in the FDTD, all the metallic parts of the structure were defined as a copper ($\sigma = 5.6\times10^6\ S/m$).

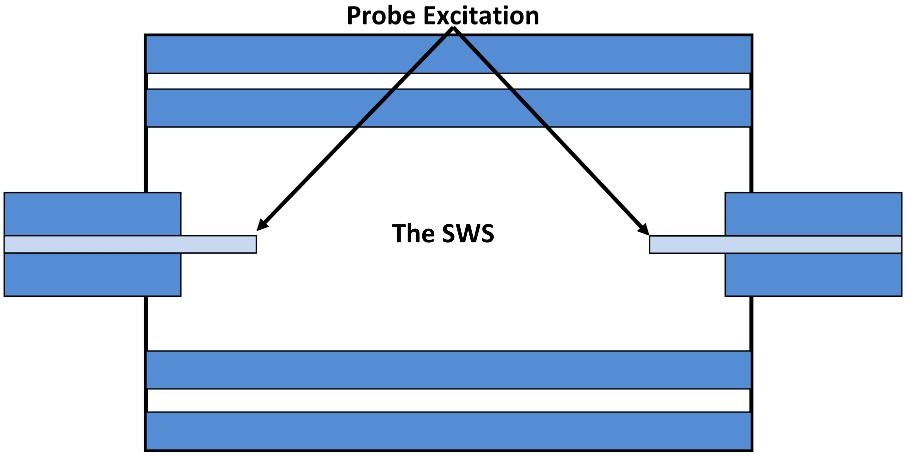

Figure 3-12 A schematic diagram of the FDTD computational window

The calculated return loss (S_{11}) of the FDTD code is plotted in Figure 3-13(a). The figure shows that at a frequency of around 120GHz, the reflection is minimized. Thus, most of the power incident at the input terminal propagates through the structure. Therefore, a propagating mode at this frequency can be detected. Similar result was obtained from the insertion losses (S_{12}) figure plotted in Figure 3-13(b). The figure shows that at the same frequency (120GHz) a limited bandwidth signal transmitted from one port to another. Also, the figure indicates that there is a noise signal detected around this frequency.

A conclusion from the S-parameters calculation indicates that at 120GHz a mode propagates inside the structure. The noise detected at the return losses is mainly due to the feeding network. According to the modal analysis, the slow wave mode located at the opening of the slow wave defect while the probe feeding network excited the field at the center of the SWS. Therefore, the probe-feeding network alone is not sufficient to excite the slow wave mode.

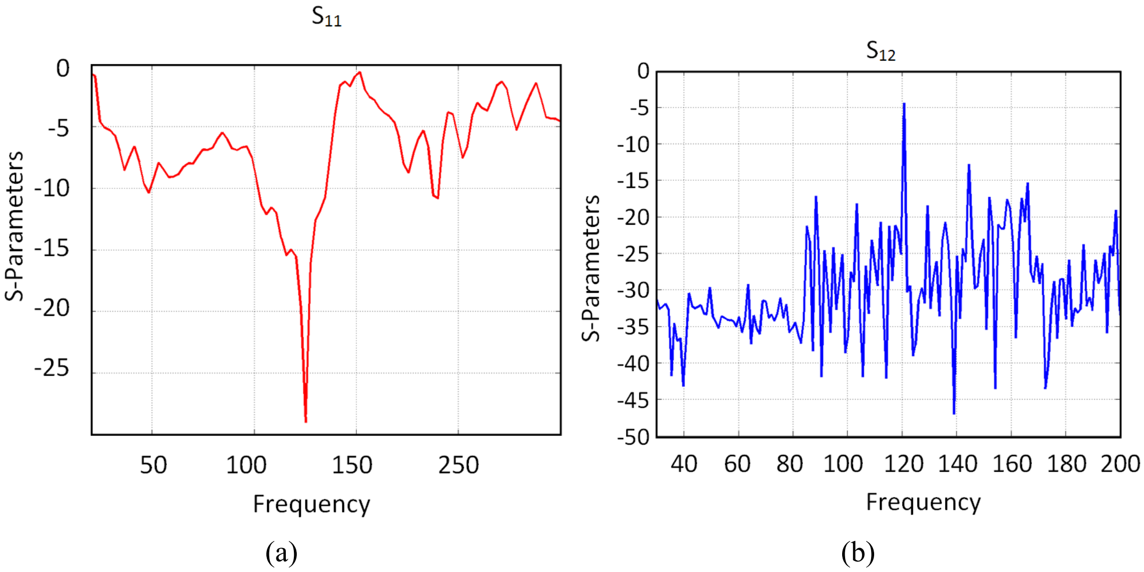

Figure 3-13 The calculated scattering parameters: (a) the return losses (S_{11}) and (b) the insertion losses (S_{12})

3.4.2 Analysis and measurement results of the DD-PC based SWS

In order to re-calculate the dispersion curve of the proposed DD-PC based SWS, the resonant method was used [109-110]. Figure 3-14(a) shows the HFSS model of the DD-PC based SWS with the probe-wheel radiator. The structure shows two main modifications in the DD-PC based SWS; the rod holders and the probe-wheel radiator. To provide a physical support to the SWS and to hold the metallic rod in its exact position, two rod holders were added at the top and bottom of the SWS. The rod holder is a metallic disk with multiple holes to allow the metallic rod to be installed inside it. The second modification is using the probe-wheel radiator to excite the slow wave mode. Since the conclusion from the previous section indicates that the probe-radiator cannot excite the slow wave mode. Therefore, a probe-wheel radiator was used (Figure 3-14 (b)) [109-110]. The probe-wheel radiator consists of two radiating parts; the wheel radiator and an axial probe radiator. The axial probe radiator is used to excite the waveguide modes, while the slow wave modes are launched using the wheel radiator.

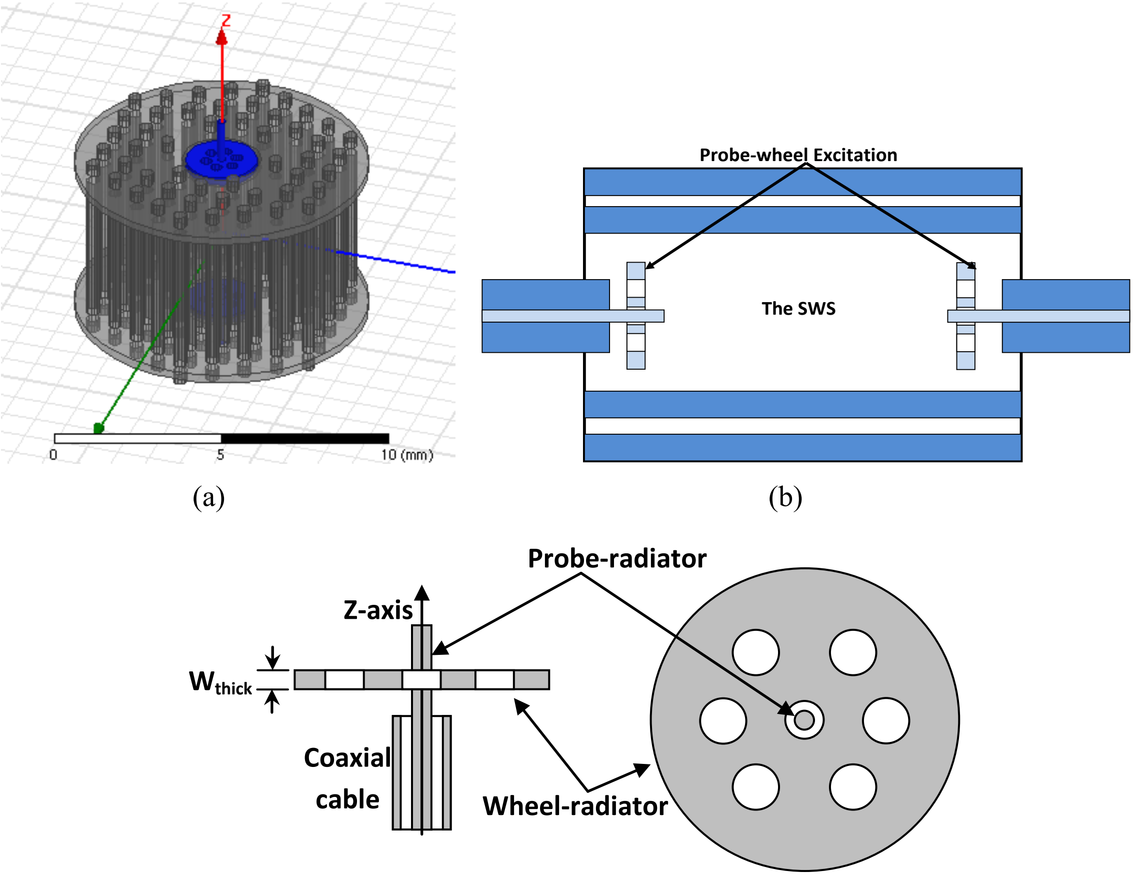

(a) (b)

(c)

Figure 3-14 (a) The DD-PC with the probe-wheel radiator, (b) a schematic diagram of the Device Under Test (DUT) and (c) the probe-wheel radiator

The wheel radiator consists of a conducting disk, with several axial symmetrical holes drilled inside it. There are two main features of the wheel radiator; first due to its axial symmetry, it excites axial symmetrical modes only. Second, it only excites the azimuthal component of the magnetic field (H_φ). Since it is a metallic wheel, the tangential electric field equals zero, therefore both cylindrical axial electric field (E_z) and the driven radial electric field (E_r) component will be excited along with the associated azimuthal magnetic field (H_φ). Thus, the slow wave mode (TM-like), located at the conducting plates can be excited. This conclusion was verified by the HFSS simulation of the current distribution over the wheel radiator itself, shown in Figure 3-15.

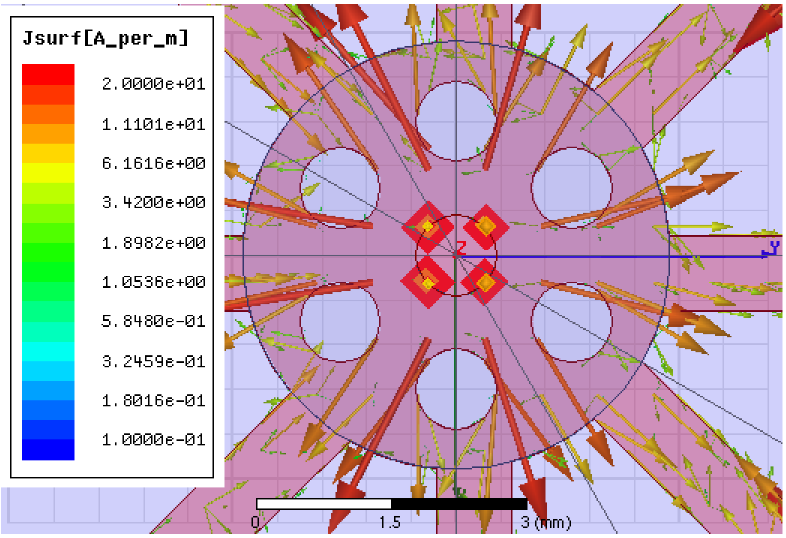

Figure 3-15 The current density over the probe-wheel radiator

3.4.2.1 Measurement results of the DD-PC based SWS with the probe-wheel radiator

To have an experimental verification for the existence of the slow wave modes in the DD-PC structure, a scaled prototype (5×) was fabricated. A picture of the assembly kit of the DD-PC based SWS is shown in Figure 3-16(a). The kit consists of several copper circular rods (42 rods are required to fully assemble the DD-PC structure), and the rod holder (2 required for provide physical stability for the rod). Figure 3-16(b) shows a picture of the assembled structure (without adding the probe-wheel radiator). Both the prototype fabrication and assembly were done in the machine shop using CNC machinery.

The S-parameters, return losses (S_{11}) and insertion losses (S_{12}), curve is presented in Figure 3-17. The figure shows that there are four spike frequencies observed in both return losses (nulls) and insertion losses (peaks).

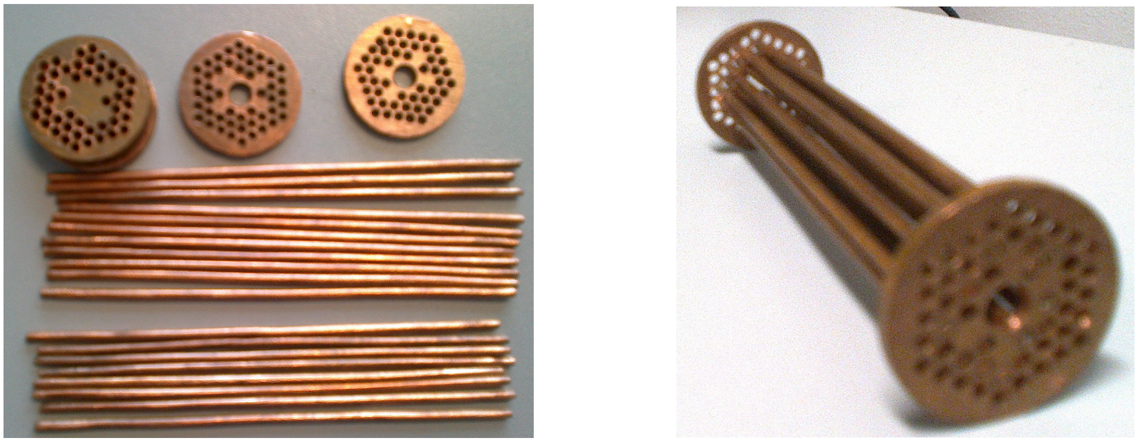

(a) (b)

Figure 3-16(a) The assembling rods and rod holder and (b) the assembled DD-PC based SWS

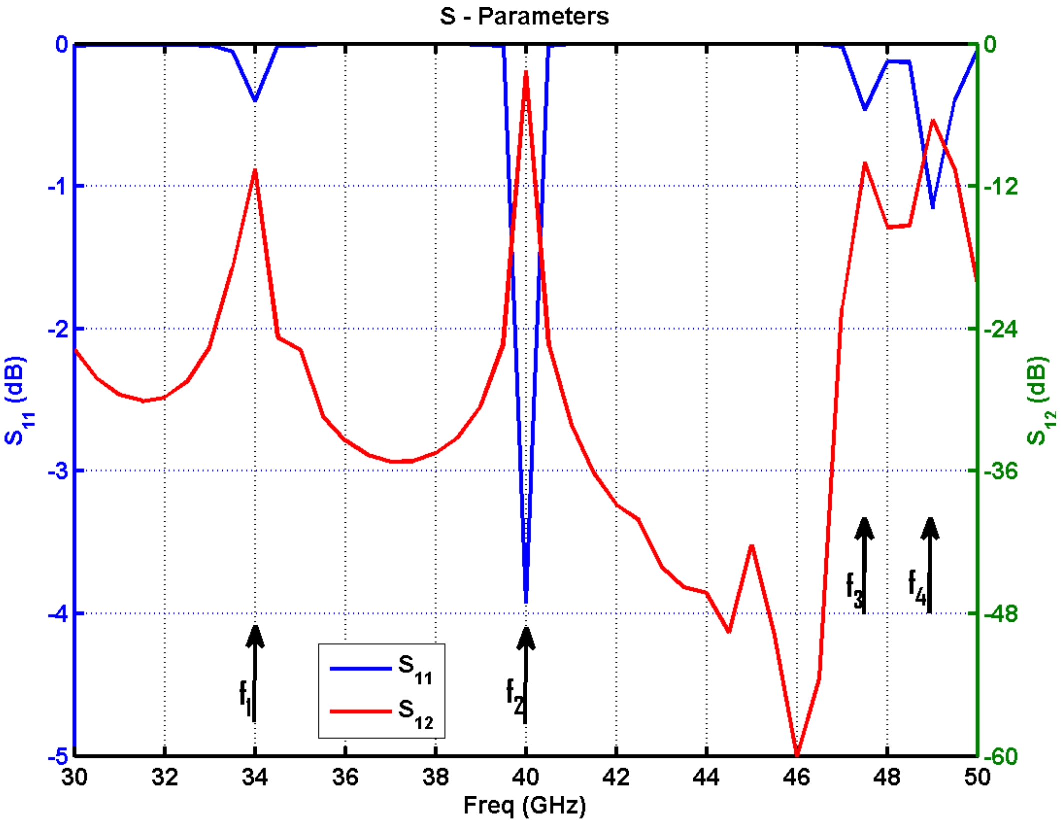

Figure 3-17 The Scattering parameters of the scaled ADD-PC based SWS

A comparison between the HFSS spike frequencies (of the scaled prototype), and the measures ones are presented in Table 3-V. The comparison indicates that there is a good correlation between the measured and HFSS predictions of the spike frequencies. Also, although the pure slow wave mode and pure waveguide mode could not be measured, they were detected using the HFSS simulation.

	HFSS probe wheel (GHz)	Measured (GHz)
f_0	33.9	--
f_1	35	33.6
f_2	38.5	34.4
f_3	42	39.3
f_4	42.8	41.2
f_5	44.2	--

Table 3-V Comparison between measured and HFSS resonance frequencies

3.5 Conclusion

At this point, the first phase of the project is completed. First, a metallic PC based SWS was introduced and analyzed. The proposed SWS satisfies the pre-defined requirements. First, the SWS is a copper based one. Thus, it can be used for high power applications. Replacing the axial discontinuity by radial ones has two advantages. First, it facilitates the fabrication of the proposed structure. Furthermore, it provides isolation between the electron beam and the generated electromagnetic fields. This will ease the extraction of the generated fields from the proposed VED device.

Using the CNC machinery, a scaled prototype of the proposed SWS was fabricated. Measurement results of the proposed DD-PC based SWS show a good correlation with the simulation ones. Although, the extraction of the dispersion curve is not shown here, it can be expressed as a summation of Fourier series (discussed later in section *5.5.1.1 The Dispersion Curve Extraction*).

Chapter 4

The Analysis of the Electron Beam-Wave Interaction Using the Finite Difference Time Domain / Particle In Cell Simulation

4.1 Introduction

Since the coherent radiation off the electron beam, as it travels through the SWS, is the main source of the generated electromagnetic wave, an accurate modelling of the electron beam-wave interaction is an essential part in the VED design. Due to the nonlinear behavior of the electron beam-wave interaction, it is extremely difficult to clarify all the details of the interaction between the electron beam and the electromagnetic field using theoretical models. Therefore, numerical simulation is considered as the main tool for studying the electron beam-wave interaction in VEDs (i.e. to perform the hot test simulation).

In this chapter the interaction between the electron beam and the electromagnetic wave inside the SWS is studied in detail. The numerical simulation can be divided into two main parts; the field simulation and the particle simulation. The field simulation is used to calculate and update the electromagnetic field components at the grid points at each time step. Since this simulation involves the update of magnetic and electric fields at every time step, the Finite Difference Time Domain (FDTD) simulation can be considered as a perfect candidate for this simulation. The particle simulation is responsible of calculating and updating the particle physical parameters (the particle position, velocity, acceleration and the applied electromagnetic forces) at each time step. In this simulation, the particle analysis was performed the Particle In Cell (PIC) analysis. Starting from the first principles concepts, the applied electromagnetic forces can be calculated, and then the particle velocity and position can be updated. The two way connection between the FDTD and the PIC are established using; the current density "***J***", and combination of electric field intensity "***E***" and magnetic flux density "***B***" (Figure 4-1) [21].

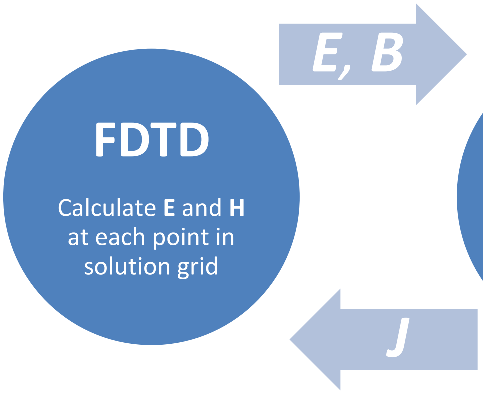

Figure 4-1 A schematic diagram of the electron beam-wave interaction simulation

In this chapter the following topics are covered. First the physical model, in which the basic physics of both the field analysis and the particle analysis are introduced. Then an introduction to the numerical simulation technique for both the field and particle and the post-processing analysis are provided. After that, the FDTD/PIC simulation was used to investigate the performance of the BWO using the DD-PC based SWS. The field and particle results of electron beam-wave interaction in the proposed BWO are presented. To optimize the BWO, the effect of varying both the beam current and the applied DC magnetic flux density on the performance of the BWO is investigated using the FDTD/PIC simulation.

4.2 The Physical Model

The electron beam-wave interaction simulation can be divided into two main sub-simulations; the field simulation and the particle simulation. Therefore, the physical model can be divided to the physics of the electromagnetic fields and the electron beam physics. The physics of the electromagnetic fields can be fully described using the Maxwell's equation;

$$\begin{aligned} \nabla\times\vec{\boldsymbol{E}} &= -\frac{\partial\vec{\boldsymbol{B}}}{\partial t} \\ \nabla\times\vec{\boldsymbol{H}} &= \frac{\partial\vec{\boldsymbol{D}}}{\partial t}+\vec{\boldsymbol{J}} \\ \nabla.\vec{\boldsymbol{E}} &= \frac{\rho_v}{\varepsilon} \\ \nabla.\vec{\boldsymbol{B}} &= 0 \end{aligned} \tag{4-1}$$

where "$\vec{\boldsymbol{E}}$" is the electric field intensity (V/m), "$\vec{\boldsymbol{H}}$" is the magnetic field intensity (A/m), "$\vec{\boldsymbol{D}}$" is the electric field density , "$\vec{\boldsymbol{B}}$" is the magnetic field density, "$\vec{\boldsymbol{J}}$" is the induced current (A/m^2), "ε" is the permittivity and "ρ_v" is the volume charge density (C/m^3).

Since the electron beam can be considered as a flow of charged particles traveling at a certain speed, the relativistic momentum equation is used to define the particle physics;

$$\begin{aligned}&\vec{\boldsymbol{F}} = m\vec{\boldsymbol{a}} = Q\vec{\boldsymbol{E}} + Q\frac{\vec{\boldsymbol{u}}}{\gamma}\times\vec{\boldsymbol{B}}\\&\vec{\boldsymbol{a}} = \frac{\partial\vec{\boldsymbol{u}}}{\partial t}\\&\vec{\boldsymbol{u}} = \frac{\partial\vec{\boldsymbol{R}}}{\partial t}\end{aligned}\tag{4-2}$$

And

$$\begin{aligned}&\vec{u} = \gamma.\vec{v}\\&\gamma = \frac{1}{\sqrt{1-\left(\left|\vec{v}\right|\big/ c\right)^2}}\end{aligned}\tag{4-3}$$

where "$\vec{\boldsymbol{F}}$" is the applied electromagnetic force (N), "Q" is the particle charge (C), "$\vec{\boldsymbol{u}}$" is the particle velocity (m/sec), "$\vec{\boldsymbol{a}}$" is the particle acceleration (m/sec^2), "$\vec{\boldsymbol{R}}$" is the particle position vector (m), and "γ" is the relativistic constant.

The interconnection between both the field simulation and the particle simulation is provided using both the current density and the electromagnetic force. The current density generated by the particle movement is defined as;

$$\vec{\boldsymbol{J}}(r,t) = \sum_i q_i \vec{v}_i \delta(r - r_i)\tag{4-4}$$

where "q_i" is the particle charge, "v_i" is the particle velocity, "r_i" is the particle position, and "δ" is a Dirac delta function.

The main difference between the particle and field simulation comes from the spatial representation. Since the field simulation was performed using the FDTD, it is a grid based simulation. All the fields are discretized in both space and time and allocated to the Yee-gird cells. Therefore, the electromagnetic fields are define and updated at fixed grid points. On the other hand, the PIC simulation is a grid-free (continuous) simulation. The particles are not aligned to grids. They can moves in anywhere inside the simulation domain. Connection between the FDTD (grid simulation) and the PIC (grid-free simulation) is considered as a source of the numerical error/noise in the FDTD/PIC simulation.

4.3 The FDTD/PIC simulation

In this section, both the particle simulation and the field simulation will be discussed in details. First the FDTD method, used for field simulation, is briefly introduced. Then a more detailed study of the particle analysis using the PIC simulation is discussed. The post processing analysis and the flow chart of the simulation procedures are provided at the end of this section.

4.3.1 The Field simulation (The FDTD algorithm)

In the FDTD/PIC code, the electromagnetic field simulation was carried out using the FDTD simulation [21-23]. In the FDTD method, the second-order finite difference approach is applied (in both time and space domains) to Maxwell's equations. Thus, a discretized form of Maxwell equation can be obtained. Then, using a leap-frog time marching technique, the electromagnetic fields can be updated at each time step. Besides its simplicity, FDTD covers a wide range of frequencies in a single run. The main limitation of the FDTD is the huge computational cost, in terms of computational time and memory requirements. With the advance of the modern computer hardware along with the proper implementation of the FDTD algorithm, the memory problem can be solved. Thus, the computational time can be considered as the main bottle neck in the FDTD method [106-107].

4.3.1.1 The Yee Algorithm

Yee algorithm, also called the Yee-Cell, has the following basic fundamentals [95]:

1. The Yee algorithms solves for both the electric and magnetic fields in time and space domains.
2. In space domain, each electric (magnetic) field component is surrounded by four circulating magnetic (electric) field components (Figure 4-2(a)).

3. In time domain, the leapfrog algorithm is used. The electric field components at time step "n+1" is calculated using the stored magnetic field and electric field components at time step "n+1/2" and "n", respectively (Figure 4-2(b)).

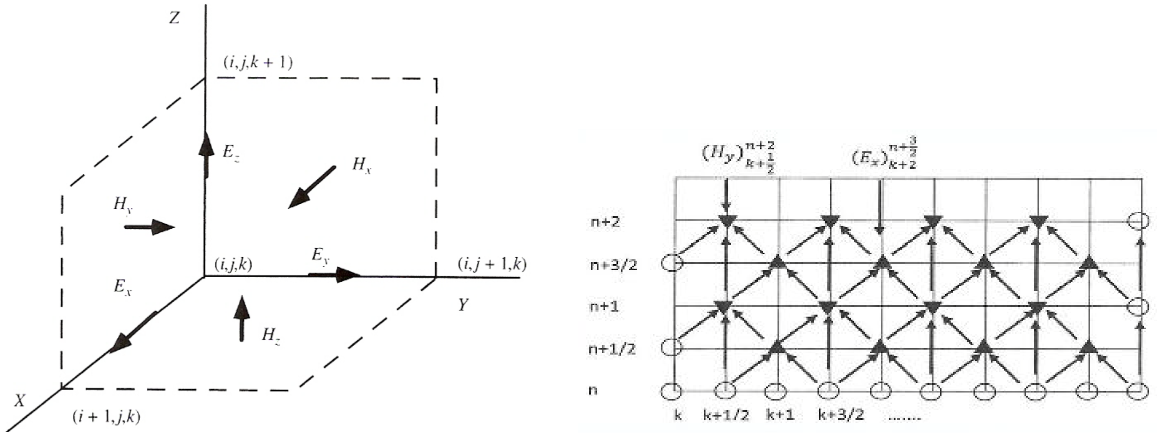

(a) (b)

Figure 4-2 (a) The Yee Cell in and (b) the leapfrog algorithm [106]

4.3.1.2 Discretization of Maxwell's Equations

Using the Yee algorithm, the Maxwell equation can be discretized in the following steps:

1- Convert Maxwell's equation from the vector form to the component form. For example, the electric field in z-direction:

$$\frac{\partial E_z}{\partial t} = \frac{1}{\varepsilon}\left[\frac{\partial H_y}{\partial x} - \frac{\partial H_x}{\partial y} - J_z\right] \tag{4-5}$$

2- Apply the finite difference approach:

$$\frac{E_z\Big|^{n+1}_{i,j,k+\frac{1}{2}} - E_z\Big|^{n}_{i,j,k+\frac{1}{2}}}{\Delta t} = \frac{1}{\varepsilon\Big|_{i,j,k+\frac{1}{2}}}\left\{\begin{array}{l} \dfrac{H_y\Big|^{n+\frac{1}{2}}_{i+\frac{1}{2},j,k+\frac{1}{2}} - H_y\Big|^{n+\frac{1}{2}}_{i-\frac{1}{2},j,k+\frac{1}{2}}}{\Delta x} - \dfrac{H_x\Big|^{n+\frac{1}{2}}_{i,j+\frac{1}{2},k+\frac{1}{2}} - H_x\Big|^{n+\frac{1}{2}}_{i,j-\frac{1}{2},k+\frac{1}{2}}}{\Delta y} \\ -\dfrac{J_z\Big|^{n+1}_{i,j,k+\frac{1}{2}} + J_z\Big|^{n}_{i,j,k+\frac{1}{2}}}{2} \end{array}\right\} \tag{4-6}$$

where $\boldsymbol{E}_z\big|^{n+1}_{i,j,k+\frac{1}{2}}$ is the discretized electric field in the z-direction at point *(iΔx, jΔy, (k+½)Δz)*, and at time step *(n+1)Δt*.

Then

$$\boldsymbol{E}_z\Big|^{n+1}_{i,j,k+\frac{1}{2}} = \boldsymbol{E}_z\Big|^{n}_{i,j,k+\frac{1}{2}} + \frac{\Delta t}{\varepsilon\big|_{i,j,k+\frac{1}{2}}}\left\{\begin{array}{l} \dfrac{\boldsymbol{H}_y\Big|^{n+\frac{1}{2}}_{i+\frac{1}{2},j,k+\frac{1}{2}} - \boldsymbol{H}_y\Big|^{n+\frac{1}{2}}_{i-\frac{1}{2},j,k+\frac{1}{2}}}{\Delta x} - \dfrac{\boldsymbol{H}_x\Big|^{n+\frac{1}{2}}_{i,j+\frac{1}{2},k+\frac{1}{2}} - \boldsymbol{H}_x\Big|^{n+\frac{1}{2}}_{i,j-\frac{1}{2},k+\frac{1}{2}}}{\Delta y} \\ -\dfrac{\boldsymbol{J}_z\Big|^{n+1}_{i,j,k+\frac{1}{2}} + \boldsymbol{J}_z\Big|^{n}_{i,j,k+\frac{1}{2}}}{2} \end{array}\right\}$$

(4-7)

Similar discretization can be applied to calculate other discretized electric and magnetic field components.

4.3.1.3 Termination of FDTD computational window

Since the FDTD problem is bounded in both space and time, a termination of the solution domain is required to remove any reflection from the boundaries. These termination boundaries are called the Absorbing Boundary Conditions (ABCs). Although several types of ABCs were reported [106], the Perfectly Matched Layer (PML) can be considered as the state-of-art for termination of the FDTD region. Therefore, a PML was used to terminate the boundaries of the FDTD problem.

4.3.2 The Particle Simulation (The PIC Simulation)

In the particle simulation, the electron beam is considered as a series of electrons, initially travels in the axial (z-) direction with an initial speed. To reduce the numerical error/noise, the macroscopic principle is used. In the macroscopic principle, each particle consists of a certain number of electrons:

$$\boldsymbol{Q}_{particle} = \boldsymbol{n}.\boldsymbol{Q}_e \tag{4-8a}$$

$$\boldsymbol{m}_{particle} = \boldsymbol{n}.\boldsymbol{m}_e \tag{4-8b}$$

Where “Q_e” is the charge of electron (1.6×10^{-19}C), “m_e” is the mass of the electron (9.1×10^{-31}kg), and “n” is the number of electrons in a particle.

Therefore, the particle mass-to-charge ratio is equal to the electron mass-to-charge ratio. Furthermore in the macroscopic scheme, the particle-particle interaction is not considered. And, the interaction between the particle and electromagnetic fields is the only interaction allowed in this simulation. Physically, this condition can be imposed by adding a limitation on the initial electron beam current density [21-23], [111].

There are two main problems in linking between the FDTD and PIC simulation; the spatial simulation conversion and the numerical error/noise reduction. The first problem – the spatial simulation conversion – arises mainly from the difference between the spatial FDTD and PIC simulation. The FDTD is a grid based simulation, while the PIC simulation is a continuous one. So to couple between these two spatial-different simulations the weighting function is used twice every time step. First, the weighting function is used to estimate the value of the electric and magnetic fields (grid-value simulation) exerted on the electron beam (continuous-value simulation). The second use of the weighting function is to find the value of the current density (continuous-value simulation) at each grid point (grid-value simulation), such that it can be used to update the electromagnetic fields in the FDTD simulation.

The second problem is related to both the reduction of numerical noise and stability of the simulation. In order to enforce the satiability of the FDTD/PIC simulation, It was found by applying the Courant stability condition the FDTD/PIC simulation is stable [21]. For a stable FDTD simulation, the time step used must satisfy the Courant stability condition:

$$c.\Delta t < \left[\frac{1}{(\Delta x)^2} + \frac{1}{(\Delta y)^2} + \frac{1}{(\Delta z)^2} \right]^{-\frac{1}{2}} \tag{4-9}$$

To reduce the numerical noise, the Gauss's law is used. Since in the FDTD simulation only the first two Maxwell's equations are used (Equation 4-1), by using the Gauss's law an estimation of the error can be defined as

$$\boldsymbol{Error}\Big|_{(r,t)} = \nabla.\vec{\boldsymbol{E}} - \frac{\rho(r,t)}{\varepsilon} \tag{4-10}$$

4.3.2.1 The analysis of the PIC simulation

The analysis of the PIC simulation is discussed from the first principles. Since there is no limitation on the particle speed in the PIC simulation, the general relativistic equation of motion was used. Starting from the relativistic equation of motion;

$$\vec{a} = \frac{\vec{F}}{m} = \frac{\partial \vec{u}}{\partial t} \tag{4-11}$$

Then, the finite difference approach can be used to update the particle velocity as;

$$\frac{\left.\vec{u}\right|_{par}^{n+1} - \left.\vec{u}\right|_{par}^{n}}{\Delta t} = \frac{\left.\vec{F}\right|_{par}^{n+\frac{1}{2}}}{m}$$

$$\left.\vec{u}\right|_{par}^{n+1} = \left.\vec{u}\right|_{par}^{n} + \frac{\Delta t}{m}\left.\vec{F}\right|_{par}^{n+\frac{1}{2}} \tag{4-12}$$

Using the updated velocity, the particle position can be updated as;

$$\left.\vec{u}\right|_{par}^{n+1} = \frac{\left.\vec{R}\right|_{par}^{n+\frac{1}{2}} - \left.\vec{R}\right|_{par}^{n-\frac{1}{2}}}{\Delta t}$$

$$\left.\vec{R}\right|_{par}^{n+\frac{1}{2}} = \left.\vec{R}\right|_{par}^{n-\frac{1}{2}} + \Delta t.\left.\vec{u}\right|_{par}^{n+1} \tag{4-13}$$

Then using the relativistic constant

$$\left.\vec{v}\right|_{par}^{n+1} = \frac{\left.\vec{u}\right|_{par}^{n+1}}{\gamma_{par}^{n+1}}$$

$$\gamma_{par}^{n+1} = 1 \Bigg/ \sqrt{\left(1 - \left(\left|\vec{v}_{par}^{\,n}\right| \big/ c\right)^{2}\right)} \tag{4-14}$$

To link between the FDTD and the PIC simulation, the current density is defined as:

$$\vec{J}_{par} = Q_{par}\vec{v}_{par} \tag{4-15}$$

4.3.2.2 The Weighting function (δ)

As discussed above, it is required to have a spatial conversion between the FDTD (grid based simulation) and the PIC (continuous based simulation). The weighting function is used to provide such conversion. For example a first order weighting function (δ) is defined as:

$$\delta = \begin{cases} 1 - \left|\dfrac{r}{\Delta}\right| & |r| < \Delta \\ 0 & else \end{cases} \tag{4-16}$$

Where "δ" is the weighting function, "r" is the relative position of the particle with respect to the Yee grid and "Δ" is the space discretization.

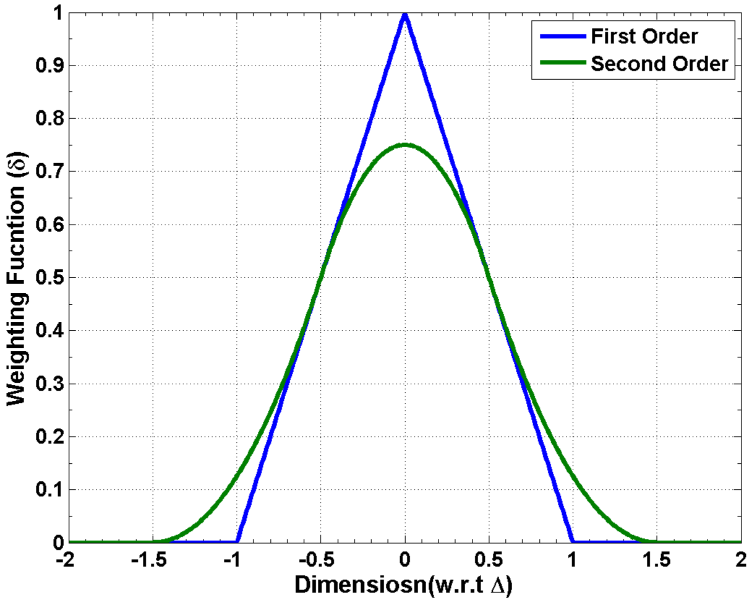

Figure 4-3 The weighting function of the first and second order

A graphical representation of the first order weighting function is plotted in Figure 4-3. To reduce the conversion error, higher order weighting functions can be used. A comparison between the first order weighting function and the second order weighting is plotted in Figure 4-3.

4.3.2.2.1 The current density weighting

Using the weighting function, the continuous-value current density – calculated for the PIC simulation – is converted to a gridded-value. Thus it can be used in the FDTD simulation. The gridded-value of the current density is expressed as:

$$\vec{\boldsymbol{J}}\Big|_{(r_i,t)}=\vec{\boldsymbol{J}}\Big|_{(r,t)}\cdot\delta(\boldsymbol{r}-\boldsymbol{r_i}) \tag{4-17}$$

Where $\vec{\boldsymbol{J}}\Big|_{(r_i,t)}$ is the current density vector at the grid point (r_i), and $\vec{\boldsymbol{J}}\Big|_{(r,t)}$ is the continuous current density vector.

4.3.2.2.2 The Electromagnetic wave weighting

Using the same procedure described above, the electromagnetic field applied on each particle can be define as the weighted fields at the surrounded grids;

$$\boldsymbol{E}(r)\Big|_{par}=\boldsymbol{E}(r_i)\Big|_{grid}\delta(\boldsymbol{r}-\boldsymbol{r_i}) \tag{4-18}$$

where "$\boldsymbol{E}(r)\Big|_{par}$" is the electromagnetic field on the particle, "$\boldsymbol{E}(r_i)\Big|_{grid}$" is the field at the Yee grid, "r_i" is the position of the grid, and the "r" is the actual position of the particle.

4.3.2.3 The termination of the PIC simulation

In the real application, the electron beam is terminated by a collector, at which the kinetic energy of the electron beam is converted to thermal energy. Since the analysis of the thermal energy is not included in this work, a simple replacement of particle was introduced. When the particle reaches the end of the structure, the particle is extracted and a fresh particle enters the structure from the other end.

4.3.3 The Post-processing Analysis

In the post-processing section, the analysis of the generated electromagnetic fields and the particle's physical parameters are performed. Taking advantage of the DD-PC based SWS designed in *3.3.1.1*

Design of the DD-PC based SWS, the FDTD/PIC simulation was used to analyze the BWO operating at 130 GHz.

4.3.3.1 Electromagnetic Field Simulation

A cross sectional view of the DD-PC based SWS is shown in Figure 4-4. As the figure shows, the structure consists of a three layers of metallic rods, placed in a triangle lattice PC structure with two types of defects; the central defect and the slow wave defect. The central defect is formed by removing inner most rods. It is designed to allow the electron beams to travel axially through the structure. The slow wave defects are formed by removing extra four rods; numbered SW1 to SW4.

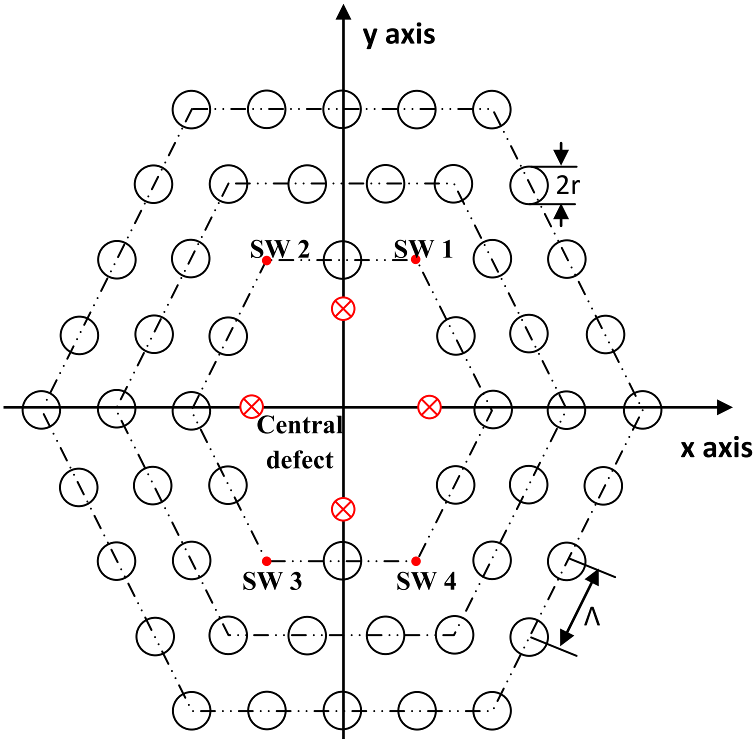

Figure 4-4 A cross-sectional view of the DD-PC based SWS showing the initial location of the electron beams

In order to sample the generated fields, the fields at the center of each slow wave defect (shown as red dots in Figure 4-4) are stored through the entire time simulation for the post-possessing analysis. The fields are stored at three axial locations; at $0.25L_z$ (where L_z is the axial length of the structure), 0.50L_z and 0.75L_z. Furthermore, to calculate the generated electromagnetic power, the transverse fields are stored at seven axial locations; 0.25L_z, 0.30L_z, 0.40L_z, 0.50L_z, 0.60L_z, 0.70L_z and 0.75L_z.

4.3.3.2 The Particle Physical Parameters

Since there are four slow wave defects used to collect the electromagnetic fields, four initial electron beams were implemented in the DD-PC based SWS. The exact location of these beams are; (0, 0.5Λ), (0.5Λ, 0), (0, -0.5Λ) and (-0.5Λ, 0). A graphical representation of the exact position of the electron beams are presented in the cross sectional view of the DD-PC based SWS as a red "×" plotted in Figure 4-4. For the post processing analysis, all the physical parameters of the particles are stored at each time step. These physical parameters include; the particle position, velocity, acceleration, electromagnetic fields applied on each particle and electromagnetic force applied on each particle.

4.3.4 The Computational Procedure

The computational steps of the FDTD/PIC simulation are summarized in the flow chart (Figure 4-5). As the figure shows, the program starts with zero-initialization of the electromagnetic fields and particle stored fields. Then within the time marching loop, both the field (FDTD), and the particle (PIC) simulations are excluded. During the PIC simulation, the particle physical parameters are update, and then these parameters are used to find the current density "J". The current density "J" is used to excite the electromagnetic fields in the FDTD simulation. Finally, the generated electromagnetic fields are used to calculate the electromagnetic forces on the particles. Since both the field and the particle simulations are independent; then a parallel approach can be applied to speed-up the simulation. Taking advantage of the multiple cores (available in all the modern CPUs), in each time step, different cores can be assigned to the FDTD, and PIC simulation.

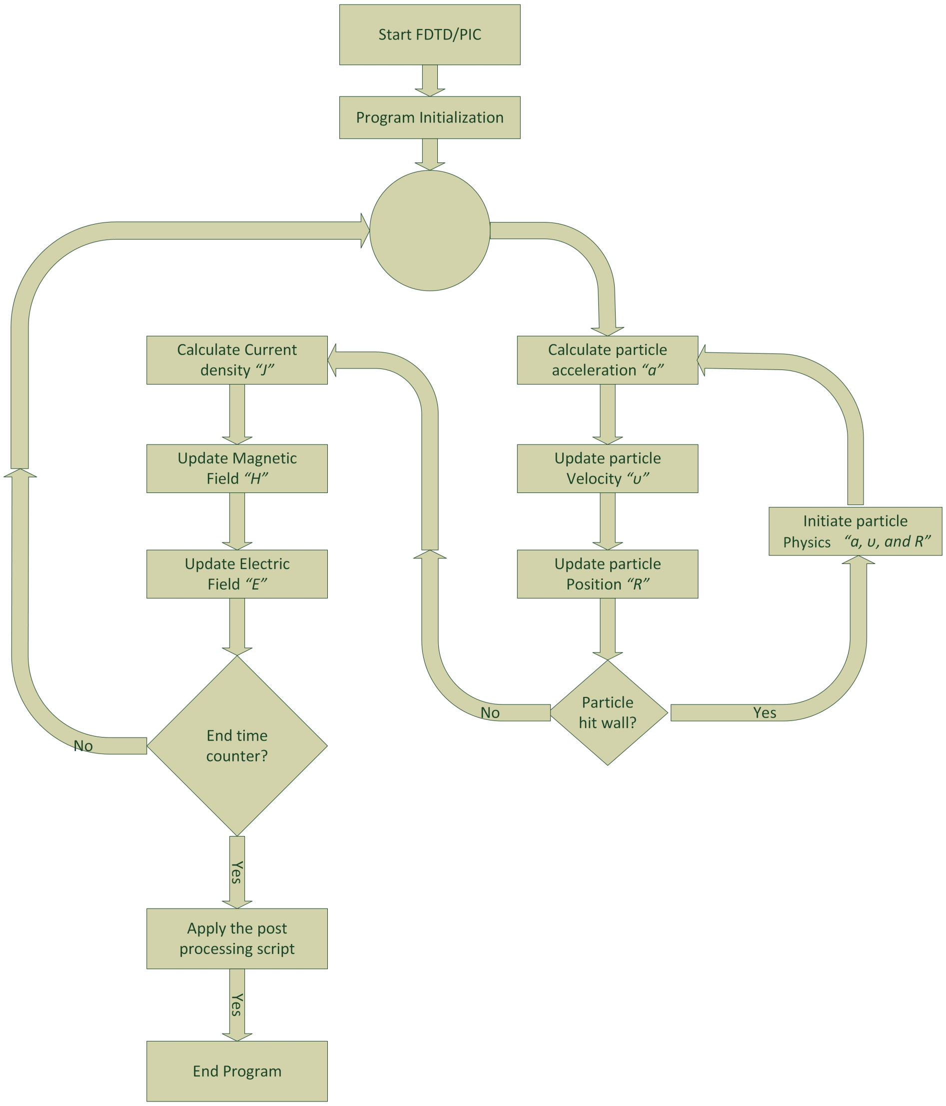

Figure 4-5 A flow chart of the FDTD/PIC simulation

4.4 The analysis of 130GHz BWO using the FDTD/PIC simulation

The FDTD/PIC simulation discussed above is used to analyze the electromagnetic beam-wave interaction within the DD-PC based SWS. Using the Open Multi-Processing (OpenMP), a multithreading parallel implementation of the FDTD/PIC simulation was realized [112].

Starting from the non-uniform FDFD analysis, discussed in *3.2 3.2 The non-uniform FDFD method*, the modal parameters of the SWS was analyzed. The dispersion diagram along with the modal analysis of the DD-PC based SWS is presented in Figure 3-7. The modal analysis indicates that with a frequency band extending from 100 – 140GHz, a slow wave mode is supported by the DD-PC based SWS. The corresponding phase velocity of the slow wave mode changes between 0.25vc – 0.55vc. Then, a BWO was designed, at 130GHz, using the DD-PC based SWS. At the design frequency (130GHz), a slow wave mode has a propagation constant of $\beta = 6.05\ rad/mm$ and the associated phase velocity $v_{ph} = 0.45v_c$. A summary of the parameters of the BWO using the DD-PC based SWS, is listed in Table 4-I.

Structure Parameters	$\Lambda = 2.0$ mm r = 0.8 mm Air-core radius = 1.5 Λ
Structure material	Perfect conductor
Electron beam	$\nu_{int}=0.45\nu_c$ ν_c : Free space light speed
Beam current	$850mA$
FDTD/PIC window	$20 \times 20 \times 60mm$
DC magnetic flux	$0.5T$

Table 4-I A summary of the BWO parameters

4.4.1 The Electromagnetic Field Simulation Results

This section investigates the sampled electric and the magnetic fields, considering specifically the time domain analysis and frequency domain analysis. The time domain sampled electric and magnetic fields inside the first cavity, at the first plane $0.25L_z$, are shown in Figure 4-6(a) top and bottom figures, respectively. The figure shows that the E_z field dominates E_x and E_y fields, while H_z field is almost zero. Therefore, the generated mode is a TM-like mode. Since the electron beam is travelling in the longitudinal (*z*-) direction, the current density will have a strong z-component. Thus in order to have a strong electron wave-beam interaction, the propagating electromagnetic mode should be TM-mode type in nature, as verified by our simulation.

To study the frequency response spectrum of the electromagnetic fields, the Fast Fourier Transform (FFT) is applied to the sampled time domain fields. Figure 4-6(b) provides the FFT results of the sampled fields shown in Figure 4-6(a). The FFT analysis confirms our desired results. First, all four cavities are dominated by fields over a very narrow frequency band (≈130GHz). Second, the frequency response of the E-fields and H-fields is almost the same in all the cavities, indicating symmetrical beam-wave interactions. Finally, although FFT results show some noise the structure has good frequency selectivity. Similar time-domain and frequency-domain results were obtained inside the slow wave cavities at other longitudinal locations consistently.

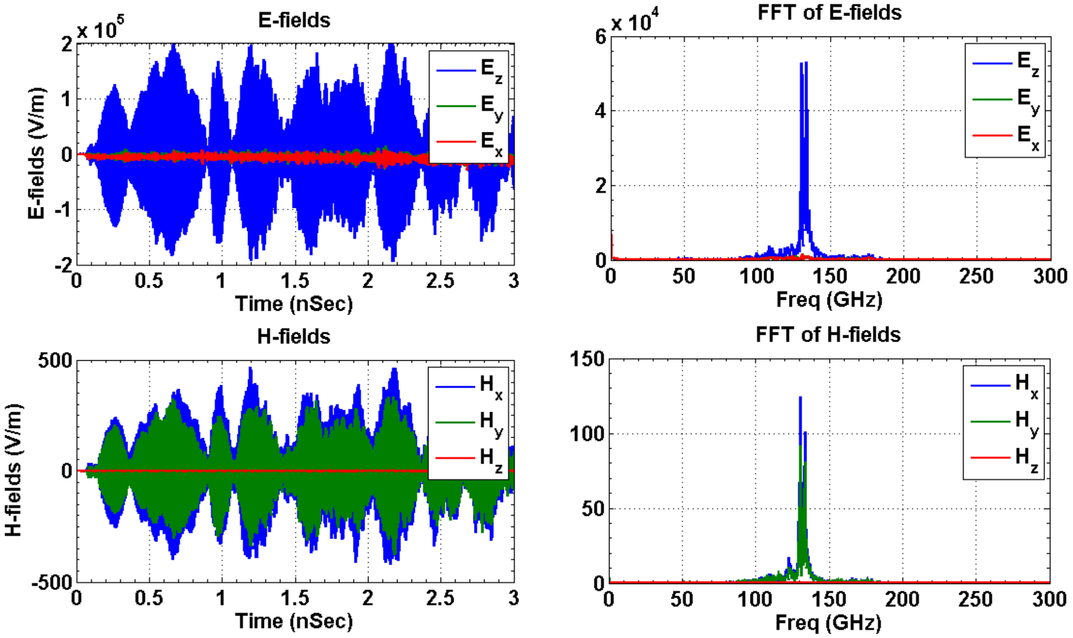

(a) (b)

Figure 4-6 (a) The Time domain electric (top) and magnetic (down) fields inside the first slow wave cavity and (b) the corresponding FFT response of electric (top) and magnetic (bottom) fields

Further insight to the nature of the generated fields can be gained by time-zooming the FDTD generated time-domain electromagnetic fields. This can be done by plotting the fields over a short time period. A typical zoomed-in electric and magnetic fields (between 0.55 – 0.57 nsec) inside the first cavity at the first longitudinal sampling plane, i.e. at $z = 0.25L_z$, is plotted in Figure 4-7. The transverse electric and magnetic fields are shown in Figure 4-7(top). As the plots show E_x and H_y, are sinusoidal in nature (with some noise and a small bandwidth – see Figure 4-6), and in-phase, while E_y and Hx are out of phase. Therefore, the two terms of the Poynting vector, $S_z = E_xH_y - E_yH_x$ in the longitudinal (z-) direction are always constructively. Figure 4-7 (bottom) also presents the time-zoomed E_z and H_z fields. As discussed later, the H_z field component is zero while the E_z field is dominate, compared to E_x and E_y field components. This confirms the TM-like modal nature of the generated fields as expected from the theory [111], [113].

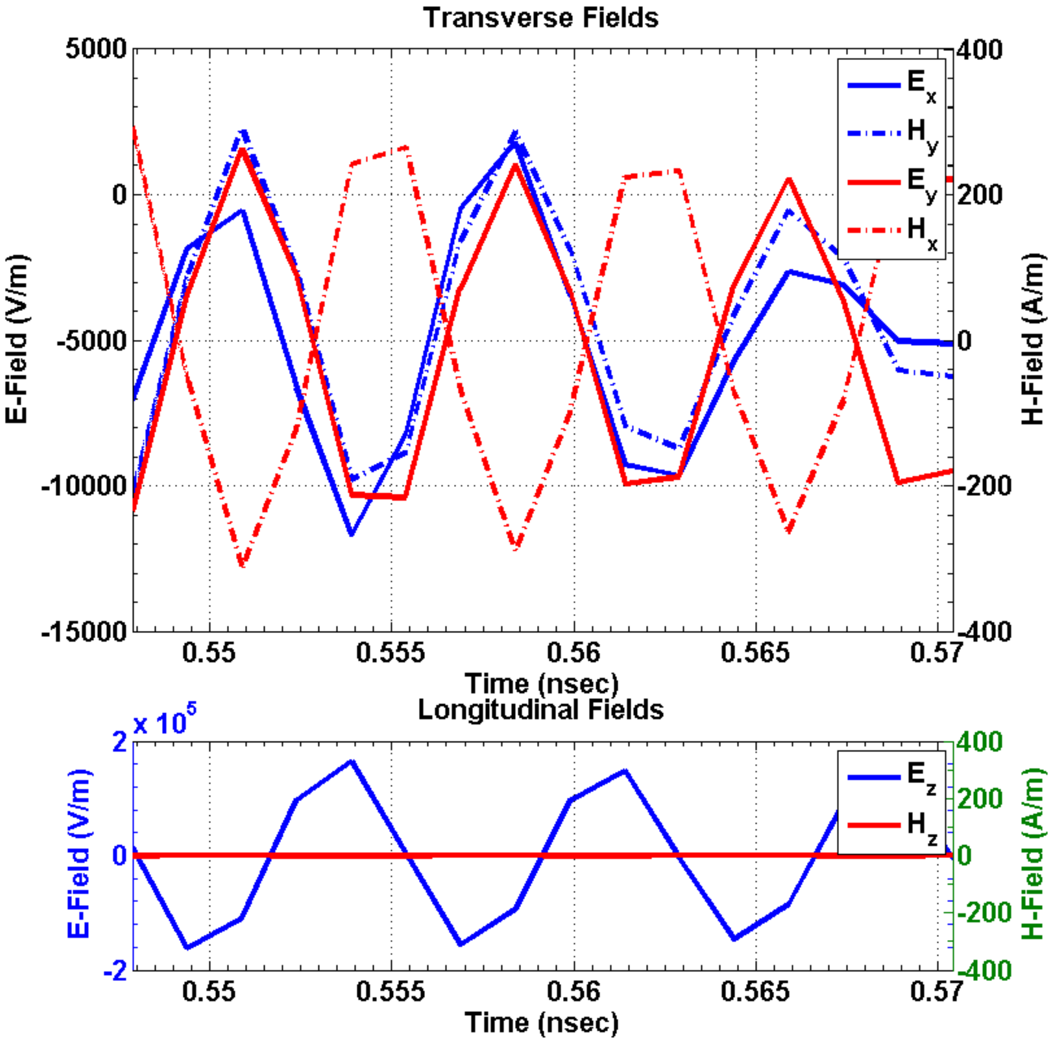

Figure 4-7 Time-zoomed electromagnetic fields inside the first cavity at 0.25Lz

The last analysis in this section is the electromagnetic wave classification. The propagating electromagnetic mode can be sorted into two categories; the forward wave and backward wave, based on the propagation direction. A forward wave propagates in the $+z$ direction, while the wave that propagates in the $-z$ direction is called a backward travelling wave. In order to study the nature of the generated wave, the electric field is sampled at three different incremental planes: $0.5L_z - \delta z$, $0.5L_z$, and $0.5L_z + \delta z$, where δz is a very small displacement in z-direction. Then the FFT is applied to the sampled fields at the three planes to calculate the corresponding frequency responses. The phases of the electric field at these three locations, at 130GHz (the peak of the spectrum), are equal to: -2.87°,

-2.74°, and -2.70°, respectively. Therefore, we conclude that the propagating wave is a backward wave in nature, since the differential phase has a positive slope along the z-direction ($+j\omega t$ convention).

4.4.2 Tunability of the BWO

According to the dispersion diagram of the DD-PC based SWS (Figure 3-7) the frequency of the generated fields can be changed by varying the velocity of the electron beam, which can be done by varying the voltage applied to the electron beam source. To show the tunability of the proposed BWO, the applied electron beam velocity was changed. Then using the FDTD/PIC simulation, the BWO was analyzed with the following electron beam parameters; initial particle velocity $0.50v_c$ and a beam current density of almost $50mA/m^2$. The applied magnetic flux was set to be $0.1T$. According to the dispersion diagram, there is an electromagnet wave propagating at a frequency of almost 140GHz. The sampled electric and magnetic fields, at longitudinal distance of $0.25L_z$, inside the first slow wave defect (SW1), in both time domain and frequency domain are shown in Figure 4-8(a). The Frequency response of the sampled fields indicates that the generated electromagnetic wave has a frequency of 137GHz, which is less than 3% shift compared to the theoretical expectation.

A time-zoomed version of the sampled electric and magnetic fields are plotted in Figure 4-8(b). The axial electric and magnetic fields are plotted in the top figure. As the figure indicates, the axial magnetic fields is almost zero, thus the propagation mode is a TM-like mode. From the transverse electromagnetic fields Figure 4-8(b-bottom) the axial power density is adding-up (as explained in the previous section).

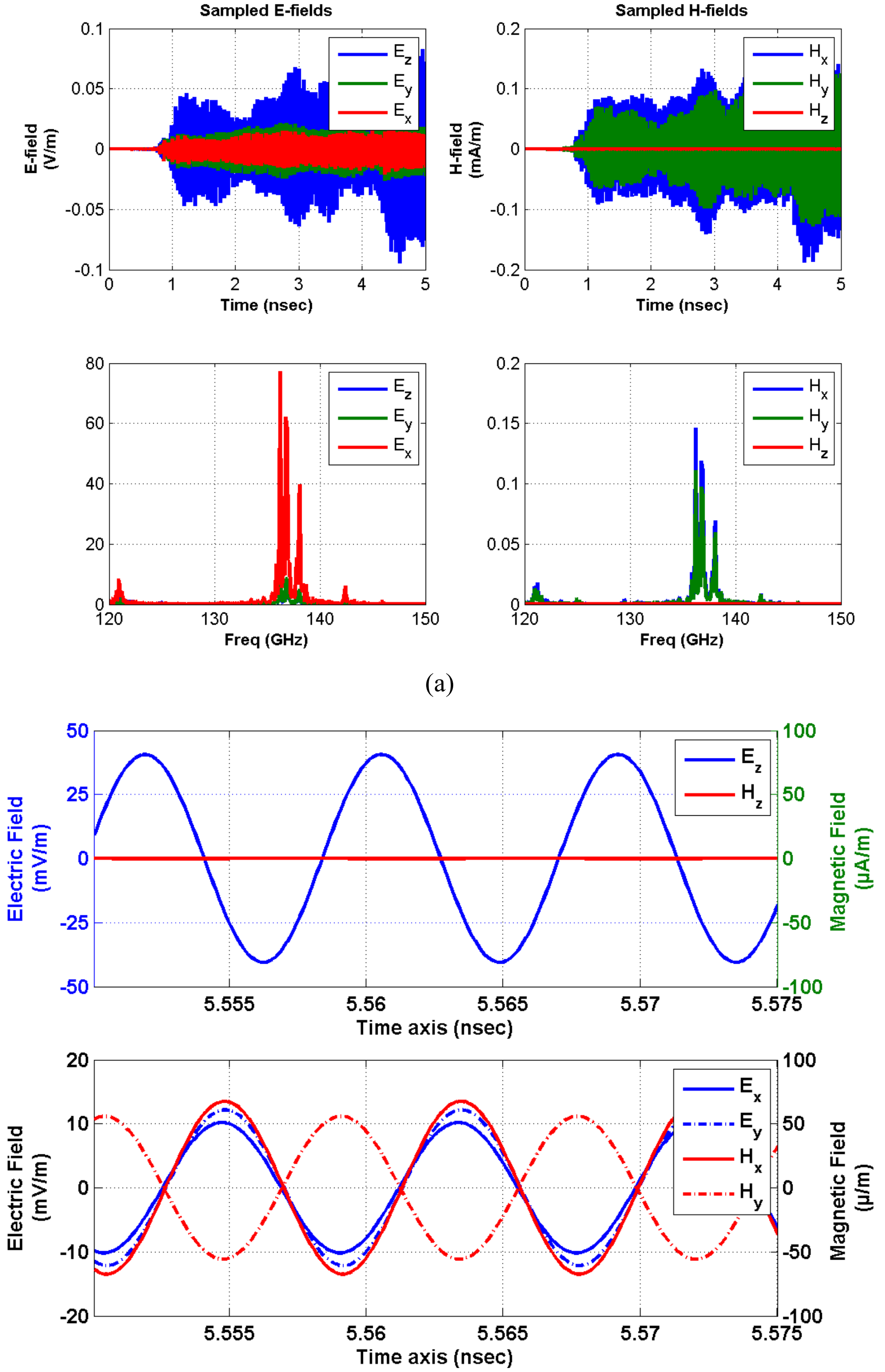

(a)

(b)

Figure 4-8 (a) The sampled electric and magnetic fields in time and frequency domains, and (b) zoomed version of the fields

4.4.3 The Particle Simulation Result

Next, we explore the time evolution of the particle dynamics. The phase space diagram is used to define the electron beam modulation and electron energy lost. It expresses the relation between the position of the particle and the associated longitudinal velocity of the particle (v_z) at that given point. A sample phase space diagram, obtained through the FDTD/PIC simulation, is presented in Figure 4-9(top) shortly after the launching of the electron beam, and Figure 4-9(bottom) at the end of time simulation. In this figure the four dotted lines represent the normalized longitudinal particle velocity of the four beams. The particle velocity is normalized with the initial particle velocity.

At the beginning of the time evolution, the generated field is small. Therefore, the electron beam-wave interaction is very weak. Thus, the particle velocity remains almost constant as it transverses the interaction length (Figure 4-9 (top)). Toward the end of the simulation time span (steady-state), the electron beam-wave interaction is strong. Hence, the beam velocity is expected to be strongly modulated. This electron beam modulation is shown in Figure 4-9(bottom). The figure shows that the particles have lost almost 15% of its initial velocity.

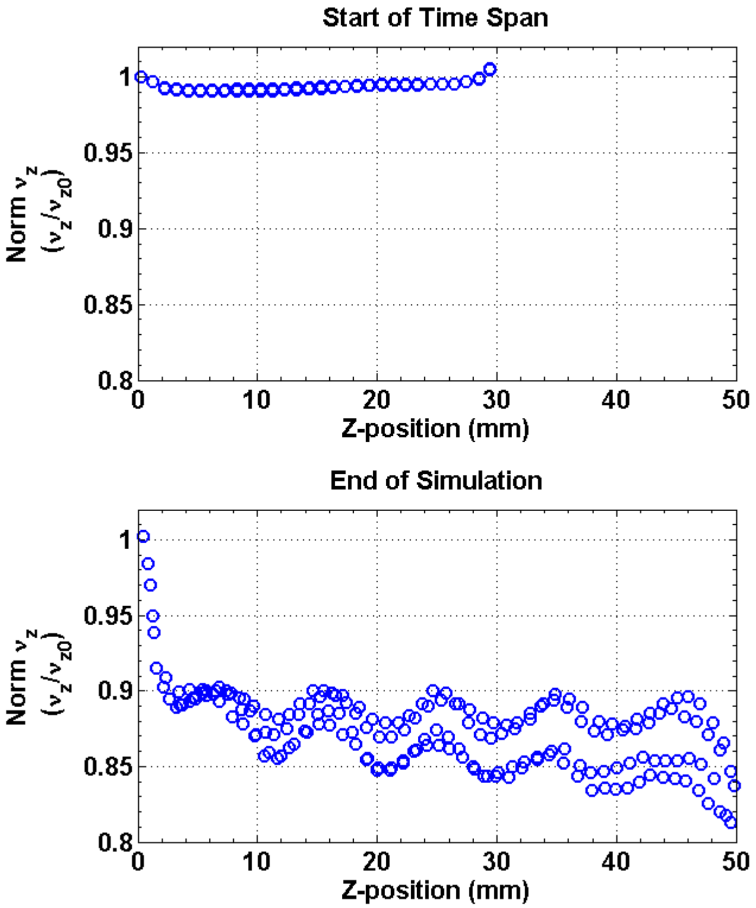

Figure 4-9 The Phase Space diagram at (top) beginning of time domain simulation and (bottom) at end of time domain simulation.

The calculated normalized particle's Kinetic Energy ($KE_{norm} = KE / KE_0$, $KE=0.5mv^2$, KE_0 is the initial KE) at the beginning of the time evolution and at the steady-state are presented in Figure 4-10(top) and (bottom), respectively. Several insights about the particle physics can be explained from the figure. Since the *KE* behavior is similar to the behavior of the particle velocity in the *z*-direction, this indicates that the main component of the velocity is the longitudinal (*z*-) component. This can be explained from the time domain generated fields plotted in Figure 4-7 and Figure 4-8. These figures show that the main electric field component is the axial components, which interacts with the axial velocity component, furthermore the initial transverse components of the velocity equals zero; this explains the dominance of the axial velocity over the transverse components. Besides, the figure indicates that the beam has lost almost *25%* of its KE energy through the beam-wave interaction process. The velocity reduction and power/energy losses of the electron beam are good indicators of the device efficiency [10], [111], [113-114].

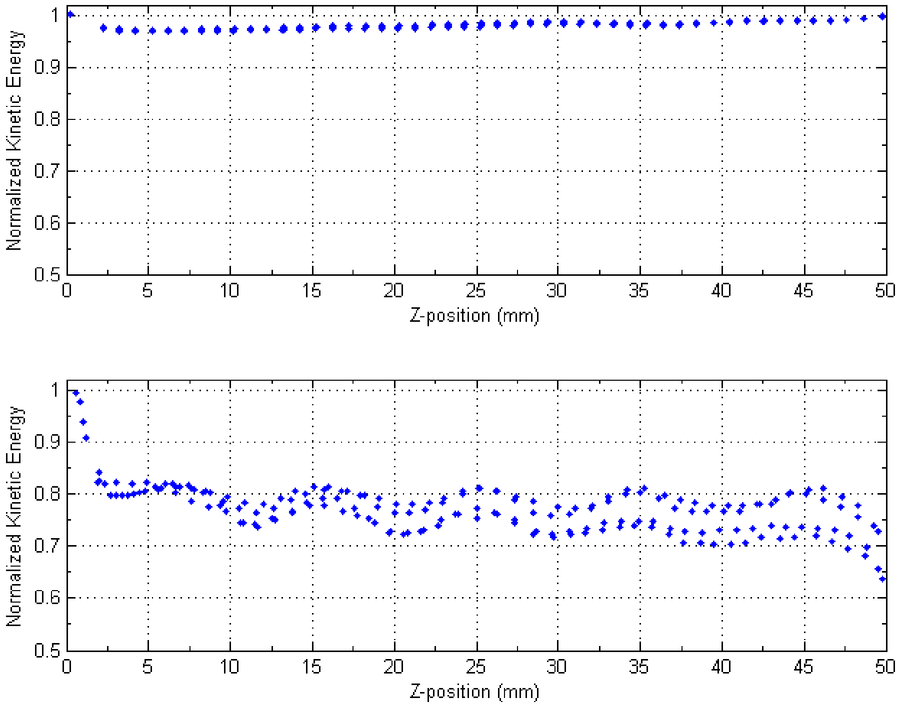

Figure 4-10 The variation of the KE at (top) beginning of time domain simulation and (bottom) at end of time domain simulation

A picture of the particles velocity trace is plotted in Figure Figure 4-11. The figure shows that the electron beams have a semi-circular trance, of radius 0.5Λ, in the transverse plane. Therefore, the electron beams particles interact with the slow electromagnetic wave located at the entrance of four slow wave defects. Furthermore, due to the axial velocity component, the particles travels in a helical path through the DD-PC based SWS. Thus, the interaction length is significantly increased compared to linear beam movement. The figure indicates that the transverse velocity changes between $+1.5\times10^{6}$ to -1.5×10^{6} m/sec, which is almost 1% of the initial axial velocity. Which confirm the behavior of both the particle velocity and the Kinetic Energy shown and explained in Figure 4-9 and Figure 4-10.

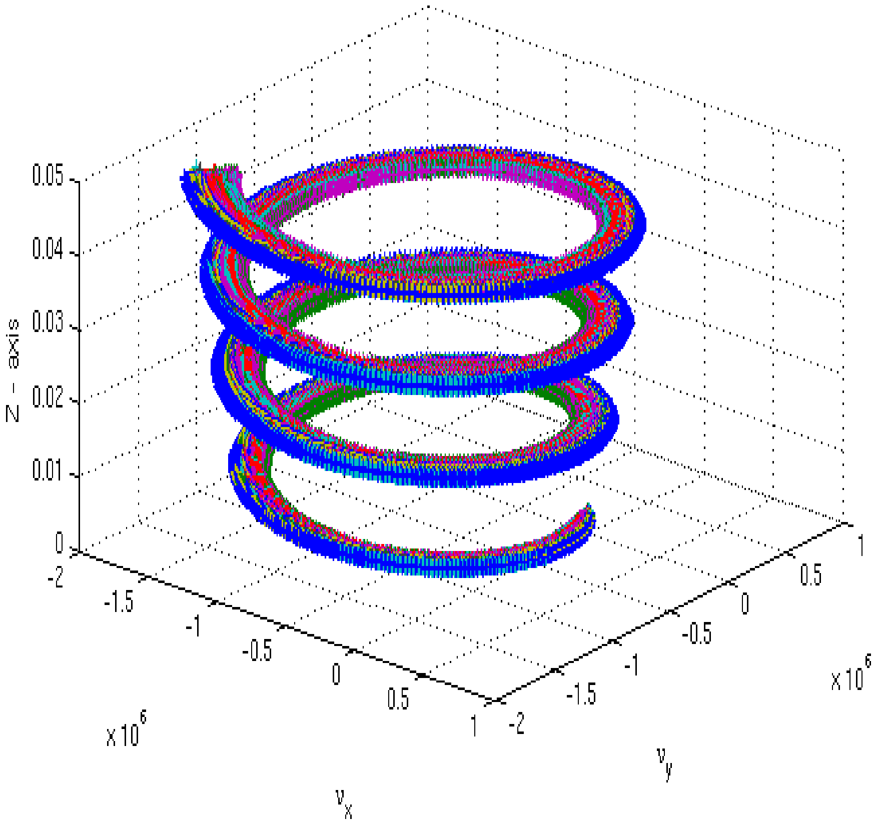

Figure 4-11 A 3D velocity trace of the electron beams showing the helical movement behavior of the electron beam particles

4.4.4 The Electromagnetic Power Density

Starting from the Poynting theorem, the average electromagnetic power flow in frequency domain can be defined as:

$$\vec{S} = \vec{E} \times \vec{H}' \tag{4-19a}$$

$$P_d\big|_z = E_x . H_y' - E_y . H_x' \tag{4-19b}$$

where, $\vec{S}$ is the Poynting vector, $\vec{H}'$ is the complex conjugate of magnetic field $\vec{H}$, and $P_d\big|_z$ is the average power density flow in the z-direction.

To apply the Poynting theorem, the time domain transverse fields (E_x, E_y, H_x, and H_y) obtained from the FDTD simulations stored at different transverse planes. Then, the FFT is applied to these fields to calculate the frequency response. In order to reduce the noise, the frequency domain signals are numerically filtered using a Gaussian filter with the following parameters: the center frequency equals the resonance frequency (130GHz in this case) and the filter bandwidth is 10% around the center frequency. After filtering, the Poynting vector in the z-direction (S_z) is calculated using the filtered fields. Finally, the calculated Poynting vector is integrated over the cross-sectional area to obtain the average power flow in z-direction. A summary of the power calculation processes is plotted in Figure 4-12.

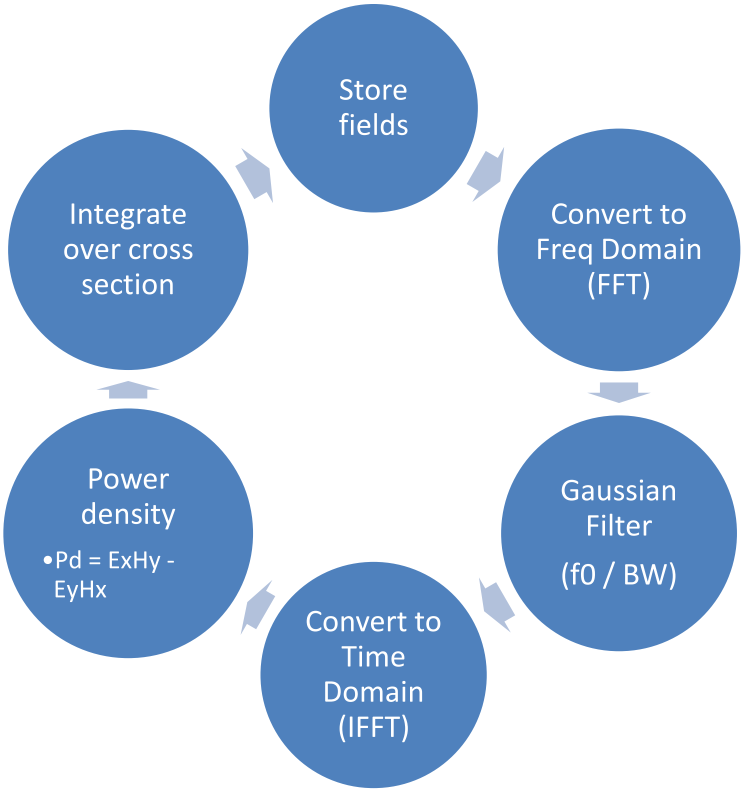

Figure 4-12 A flow chart of the power calculation process

The transverse fields are stored at 7 transverse planes, at $0.25L_z$, $0.30L_z$, $0.40L_z$, $0.50L_z$, $0.60L_z$, $0.70L_z$, and $0.75L_z$. The power flow calculation process is applied at each one of these planes. The cross sectional magnitude of the Poynting vector in z-direction, at $0.50L_z$, is plotted in Figure 4-13. The calculation was done at a frequency of 130GHz. The figure indicates that there is a significant amount of the power located inside the central defect; this can be clarified since the electron beams travel through the central defect. Furthermore, since the slow wave mode is located at the opening of the slow wave defects, the power is extracted from the central defect to the slow wave defect. The figure shows that the strength of the power inside the slow wave defects is almost half the strength of the power at the central defect; thus the power extraction can be verified.

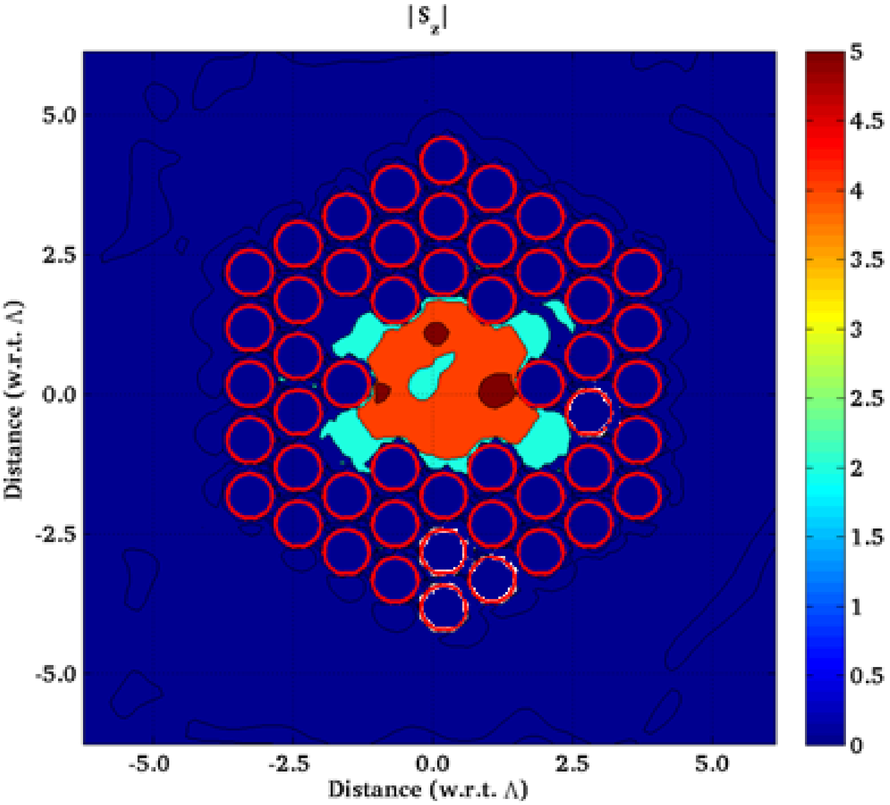

Figure 4-13 The magnitude of the z-component of the Poynting vector (logarithmic scale)

The electromagnetic power is calculated by integrating the power density over a circular cross-sectional area (Figure 4-12), at the pre-determined seven axial planes. The power distribution is plotted in Figure 4-14. The figure shows that the maximum generated electromagnetic power is located next to the terminal at which the electron beam entranced the SWS. Since the proposed device is a BWO, as explained in *4.4.1 The Electromagnetic Field Simulation Results*, it is expected to have the maximum power location at the entrance point of the electron beam. Thus the generated electromagnetic power plotted in Figure 4-14 is justified. Furthermore, to acquire a close approach about the power distribution inside the DD-PC based SWS, the power distribution across the cross-section is calculated between two segments; the core power and defect strip power. The core power is defined as the power within the radius $r < 1.5\Lambda$, while the defect strip power is defined as the power between $1.5\Lambda < r < 2.5\Lambda$ (the slow wave cavities ring). The core power and the defect strip power, along with the overall power distribution are plotted in Figure 4-14. The figure illustrates that the core power and the defect strip power are almost the same. Also, both of them equal -approximately- half of the overall calculated power (which calculated with a circle of a radius $r < 5\Lambda$).

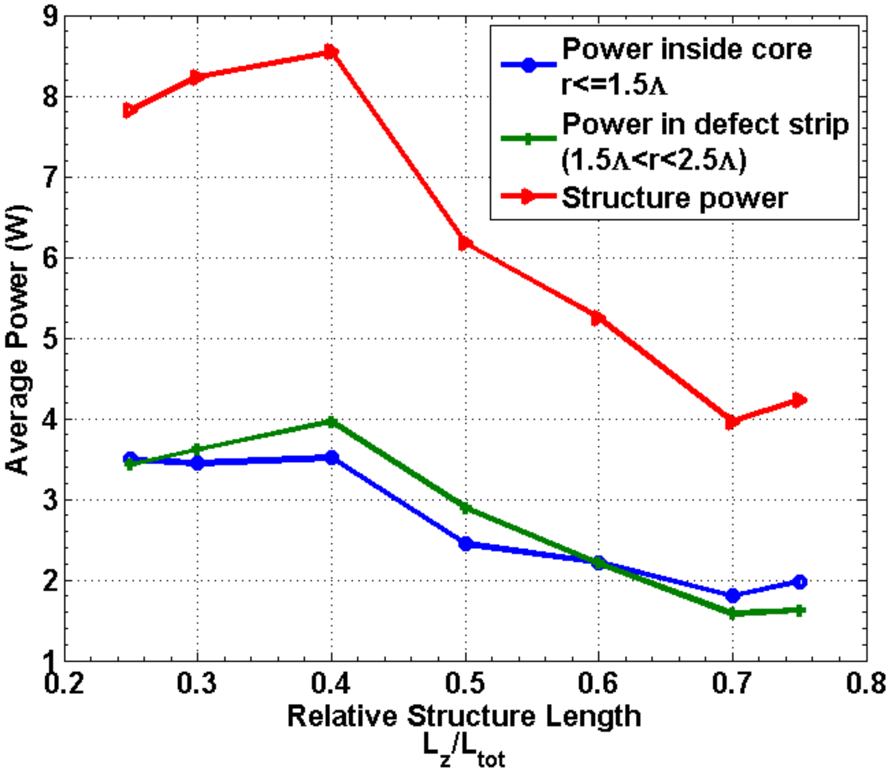

Figure 4-14 The axial power distribution

Figure 4-15 presents the time integration of the Poynting vector, in the axial direction, inside the center of the first slow wave cavity (SW-1). The integration was done at three different longitudinal locations $0.25L_z$, $0.50L_z$, and $0.75L_z$. As shown in the figure, the integration of the Poynting vector increases with time which indicates power build up inside the slow wave cavity. Moreover, the integration inside the cavity decreases while moving towards the end of the structure, thus verifies the backward wave behavior of the slow wave mode.

One of the drawbacks of the BWO is the location of maximum electromagnetic power density and maximum charged particle modulation. Since the maximum charged particle modulation is located at the minimum electromagnetic field location, the overall efficiency of the BWO is limited [10].

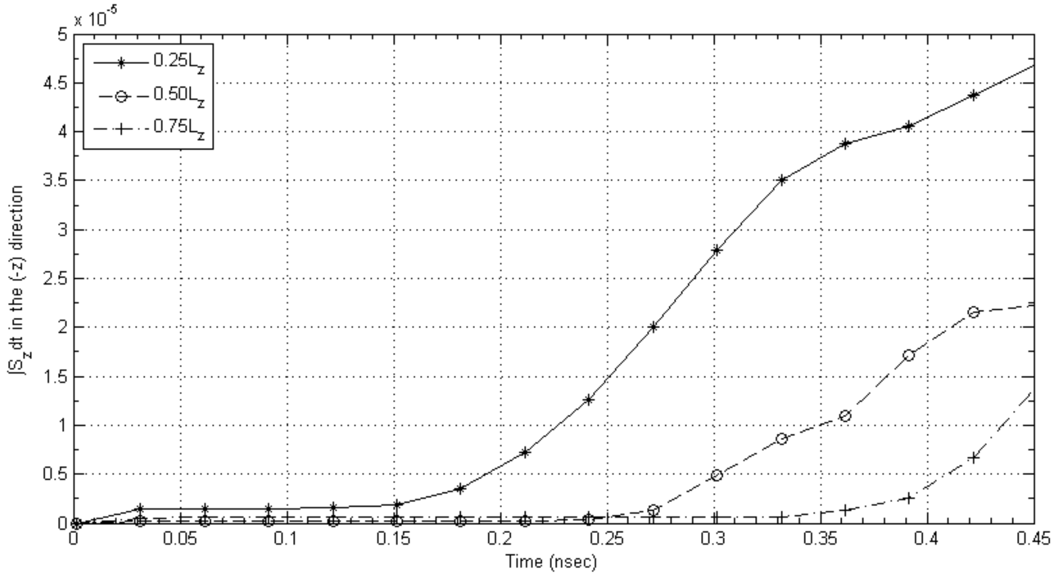

Figure 4-15 Time integration of S_z inside first slow wave cavity

4.4.4.1 Sector and Sectional Power Analysis

More information about the power distribution over the cross-sectional area inside the proposed DD-PC based SWS can be obtained from the sector power and the sectional power analysis. The sector power is defined as electromagnetic power calculated over certain sector (of predefined angle Figure 4-16(a)). In this work, four sector regions were defined, each sector extends for 30˚. The start and end angles of each sector are defined as 45˚-75˚, 105˚-135˚, 225˚ - 255˚, and 285˚ - 315˚, respectively.

The calculated power over these sectors is plotted in Figure 4-17. The figure indicates that the electromagnetic field power is equally distributed over the four sectors. Additionally, the summation of the four sector powers equals half of the overall structure power. This verifies that the generated electromagnetic power migrates to the slow wave cavities.

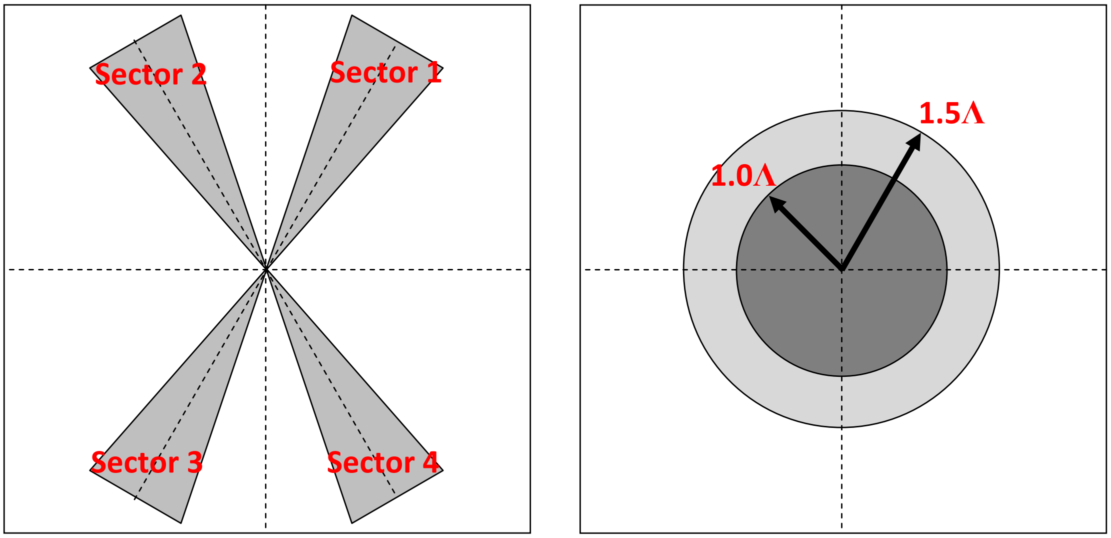

(a) (b)

Figure 4-16 (a) The Sector Power and (b) the Sectional Power

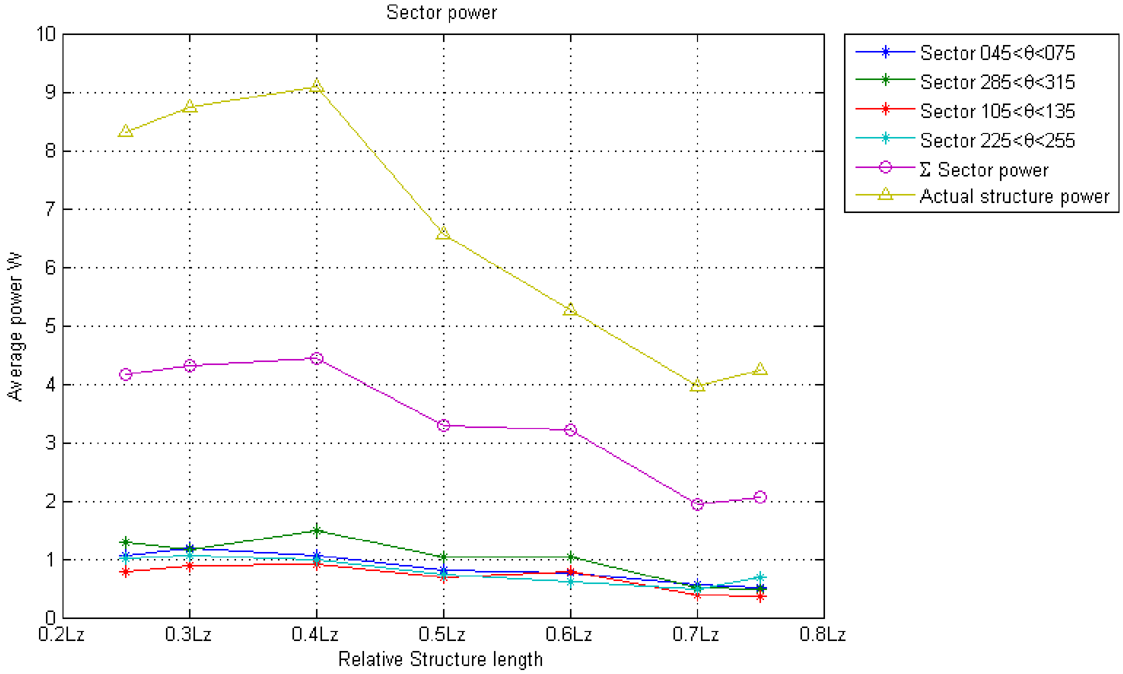

Figure 4-17 The Sector Power

More detailed analysis of the power distribution can be studied by the determination of the power located between two radii (strip power). Figure 4-16(b) displays an example of two strips; the inner strip which define as a circular area of radius $r < \Lambda$, and the second strip, which described as a disk of radius r extended between $\Lambda < r < 1.5\Lambda$. The calculated power over five different strips is plotted in Figure 4-18. In the first strip ($r = 0$ to 0.5Λ) the maximum generated power is less than 1W. Since the electron beams are located at a radius 0.5Λ, the generated electromagnetic power inside the second strip $(0.5\Lambda - 1.0\Lambda)$ is almost twice the generated power within the first strip. The last strip is the defect strip, which has a radius extend between 1.5Λ to 2.5Λ, has a maximum power of 3.75W. This can be explained from the cross sectional power density plot shown in Figure 4-14. Since this strip has the slow wave defects located inside it (at which half of the generated electromagnetic power is located) this explains the high power level located in this strip.

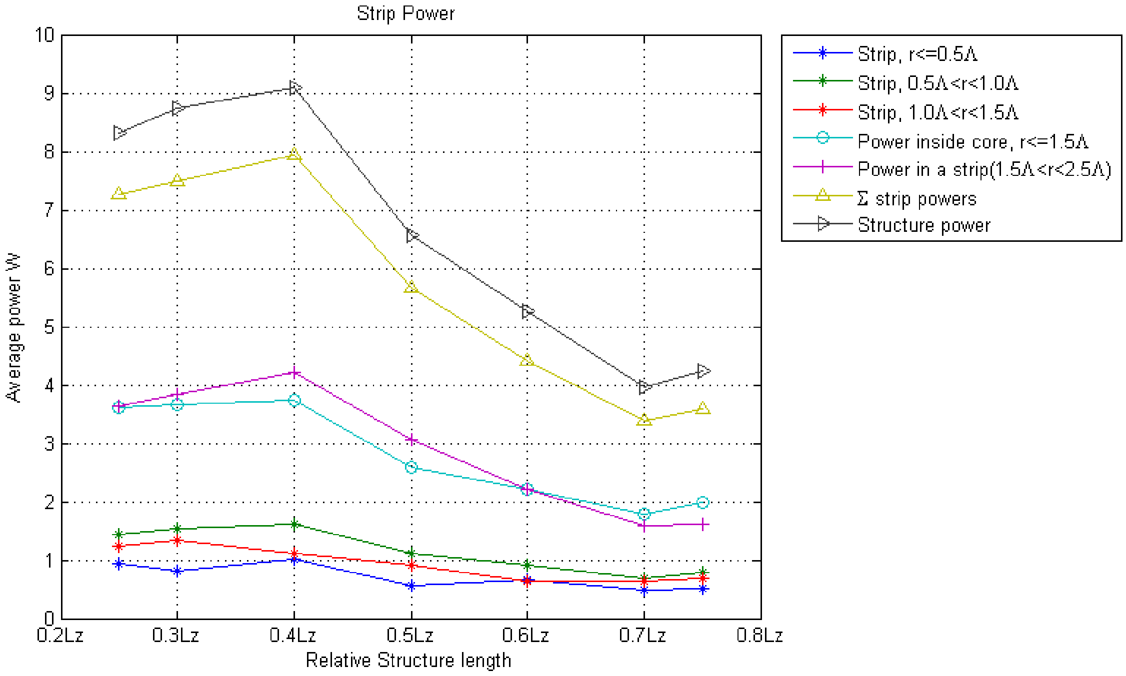

Figure 4-18 The Strip Power

4.5 Variation of the BWO parameters

In the last part of the BWO analysis, the effect of changing both the beam current and the applied axial magnetic flux density on the generated electromagnetic power is investigated. The analysis was performed using the FDTD/PIC CAD tool.

4.5.1 The Electron Beam Current

The electron beam power can be defined based on two parameters: the beam current and the beam voltage. The initial velocity of the electron beam particles is defined by the beam voltage. While the operating frequency (and bandwidth) of the BWO is directly related to the beam voltage (and beam velocity –as discussed in *4.4.2 Tunability of the BWO*-), changing the beam current affects the generated electromagnetic power. The particle charge is used to calculate the beam current. In this section, the effect of changing the electron beam current on the generated power, at a constant beam velocity, is investigated. This was done by change the number of electron in each particle ("*n*" in Equation (4-8)).

The upper limit of the electron beam current was defined such that the particles remain in the space-charge limited region – such that the effect of the particle-particle interaction remains negligible – (Figure 4-19). This assumption is justified as long as the *Preveance Number* ($PN = I/V^{3/2}$, where I the beam current and V is the beam voltage) is less than 2.5×10^{-6}. Furthermore, increasing the beam current may cause the particles to hits the structure walls before the extraction point. Therefore, the maximum beam current was selected such that at least *90%* of the particles can travel through the DD-PC based SWS without hitting its walls. Increasing the beam current has two main effects on both the generated electromagnetic power and the spectral purity of the electromagnetic fields. As the beam current increases, the electron beam-wave interaction enhanced. Thus, the generated electromagnetic power is also increased [32]. On the other side, increasing the electron beam current affected the spectral purity of the generated electromagnetic signal.

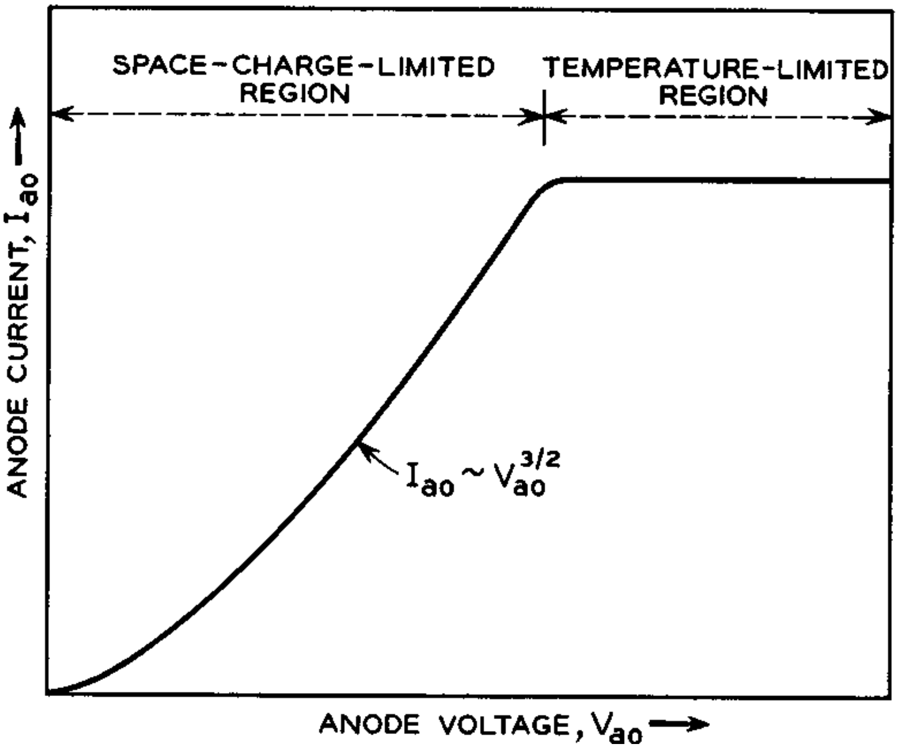

Figure 4-19 The Space Charge Limit [32]

A plot of the effect of changing the beam current on the calculated maximum generated power is plotted in Figure 4-20. As expected, increasing electron beam current enhances the electron beam-wave interaction, thus the generated electromagnetic power is also increased. Figure 4-20 also shows the power within the slow wave cavity ring. The figure indicates that almost half of the structure power is within the slow wave cavities ring

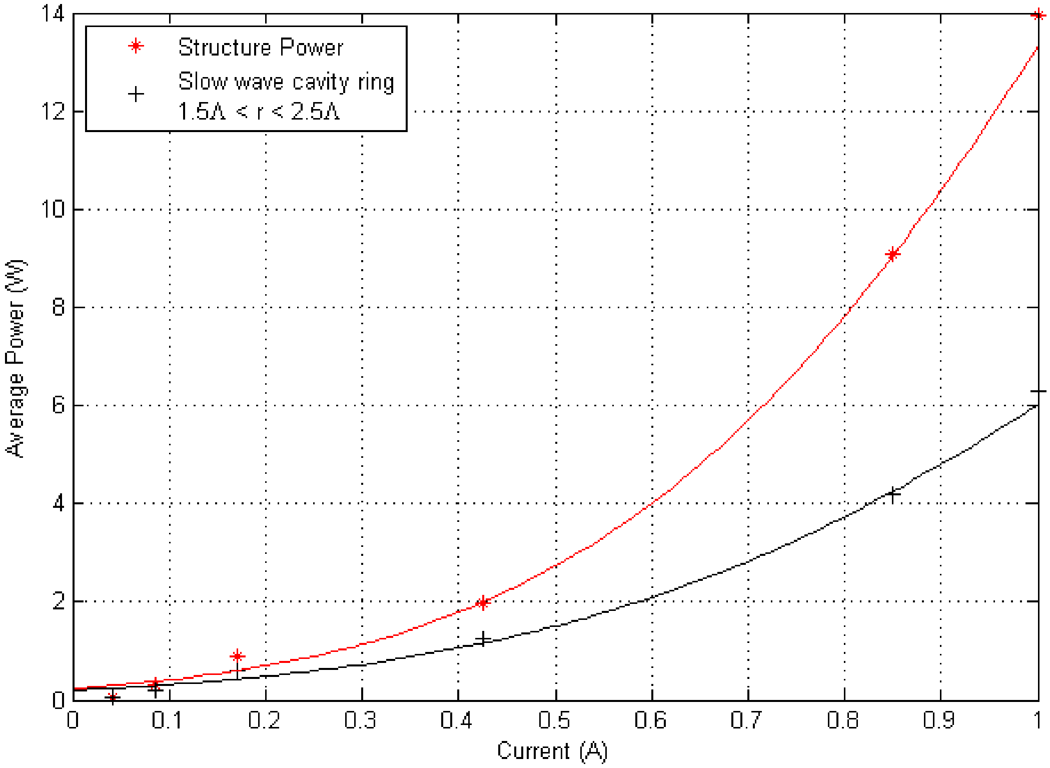

Figure 4-20 The Effect of changing the beam current

As the value of the beam current is boosted, the electron beam-wave interaction is enhanced. Also, the kinetic energy lost by the electron beam increases as well;

$$\boldsymbol{KE_{lost} = KE_{Steady\ State} - KE_0} \qquad (4\text{-}20)$$

where KE_{lost} is the changing in the particle KE, $KE_{steady\ state}$ is the particle KE at the steady state and KE_0 is the initial value of the particle KE.

Figure 4-21 shows both the change in the electron beam kinetic energy and the lost electron beam power (with respect to its initial value) as it travels through the BWO. The reduction in electron beam kinetic energy and electron beam power can be used as a measure of conversion efficiency [10],[24].

The effect of changing the beam current on the lost beam power ($\Delta P_{beam}=P_{beam}|_{enter.point}$ - $P_{beam}|_{extract.point}$). The electron beam power can be defined as:

$$P_{beam} = V_{beam} . I_{beam} \tag{4-21}$$

where V_{beam} is the beam voltage and I_{beam} is the beam current.

Since increasing the beam current enhances electron beam-wave interaction. Therefore, the electron beam velocity decreases, and hence both the lost beam power and the change in the particle KE increases.

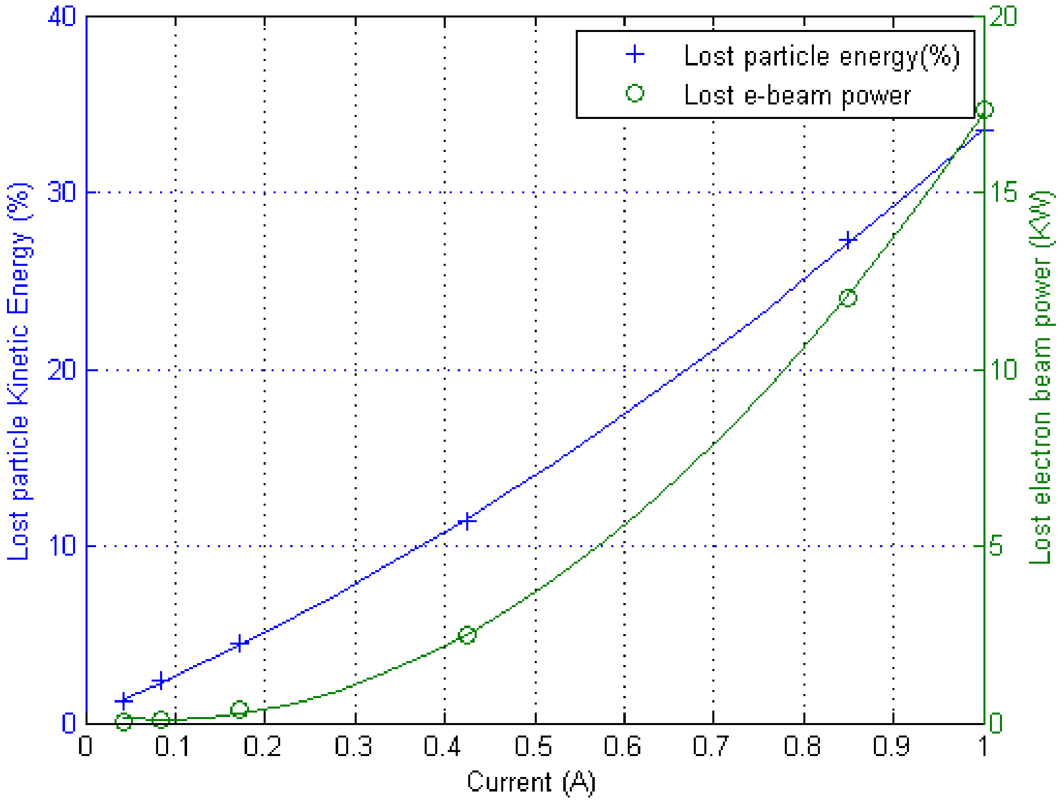

Figure 4-21 The effect of changing beam current on the kinetic energy and the electron beam power

4.5.2 The Applied DC Magnetic Flux Density

One of the advantages of slow wave devices is the lower DC magnetic flux density requirements, compared to the fast wave devices requirements. For fast wave devices, the resonance condition is defined as:

$$\boldsymbol{\omega = s\omega_c} \tag{4-22}$$

where "ω" is the operating frequency, "s" is the cyclotron harmonics number (for the fundamental mode, s is selected to be 1) and "ω_c" is the cyclotron frequency.

Using the above equation, it was found that the resonance condition indicates that the emission frequency is *29GHz/T*. Therefore, in order to generate an electromagnetic field of 130 GHz, a DC magnetic flux of *4.5T* would be required. Compared to the proposed BWO, which typically needs *0.5T*, the required DC magnetic field for the fast-wave devices is very high [10], [16-17].

This section investigates the effect of the applied DC magnetic flux on the electron beam energy. It can be preserved from Figure 4-22 that for an applied DC magnetic flux in the range of 0.4 – 0.5T, the reduction in electron beam energy is almost 27%. For the particular structure here, the application of more magnetic flux reduces the losses in the electron beam, which indicates lower extracted power. As the DC axial magnetic flux increases, above a certain limit, the transverse particle acceleration increases, and the particles start to hit the walls of the SWS. Hence, the FDTD/PIC code will generate a new particle entering the structure with the initial electron beam velocity. This explains the decrease of the reduction of the electron beam energy.

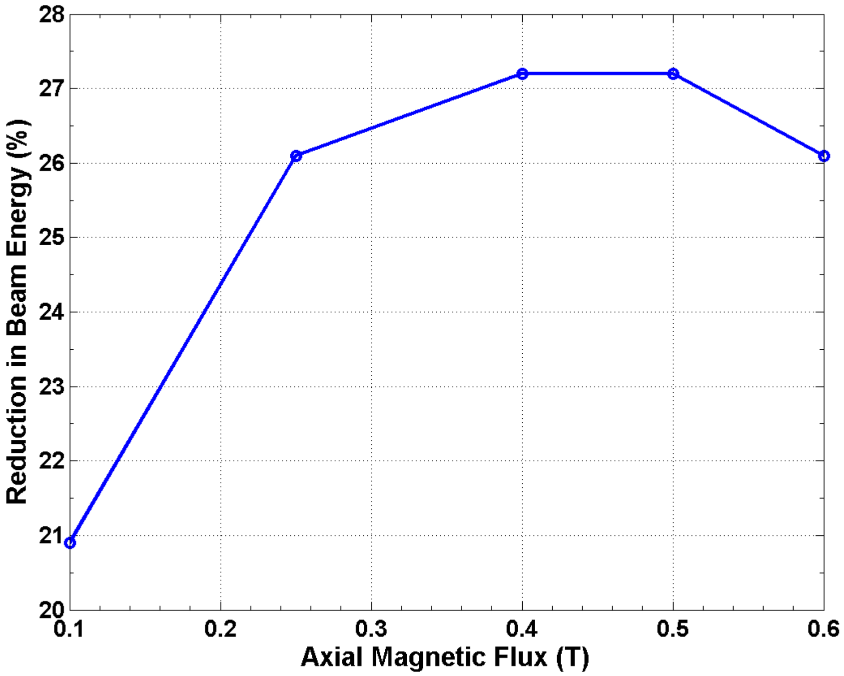

Figure 4-22 The effect of changing DC axial magnetic flux density on the beam energy

4.6 Conclusion

Thus far, the second part of the project – the analysis of the electron beam-wave interaction in the SWS – is completed. First, the physical model of both the electromagnetic waves and the particle parameters is introduced. Then, using the FDTD simulation and the PIC simulation, the numerical analysis of the electron beam-wave interaction was performed. A full discussion of the different aspects of the FDTD/PIC simulation was studied in details.

Taking advantage of the DD-PC based SWS proposed in the previous chapter (3.3.1.1 Design of the DD-PC based SWS), a BWO operating at 130GHz was proposed. The performance analysis of the BWO was carried-out using the FDTD/PIC simulation. The field simulation results were consistent with the SWS analysis (performed in the previous chapter). The power simulation results showed that the BWO capable of delivering up to 9W with an electron beam efficiency of 33%. The effect of the electron beam current variation was analyzed using the FDTD/PIC simulation. As expected form the theoretical discussion, the electron beam-wave interaction was significantly enhanced as the electron beam current increased. Similarly, the optimum value of the applied magnetic flux was found to be 0.4 – 0.5T.

Chapter 5

Design and Analysis of a Cherenkov-radiation based BWO

5.1 Introduction

In order to increase the bandwidth and reduce the size of the modern communication devices and to fulfill the modern application requirements in terms of power and frequency, the communication frequency has been pushed to the sub-mm/THz frequency band. The propagation characteristics and the operating bandwidth of the THz frequency band make them an excellent choice for the modern wireless communicating system [3-5], [7]. The atmospheric attenuation diagram, presented in Figure 5-1, shows that there are four frequencies; 35GHz, 94GHz, 140GHz and 220GHz, at which the atmospheric attenuation is considerably reduced. Thus, these frequencies were defined as an operational window for communication systems. Within this work, a detailed analysis of a BWO, using the DD-PC based SWS, operates at the third window was proposed, analyzed and tested in the previous two chapters.

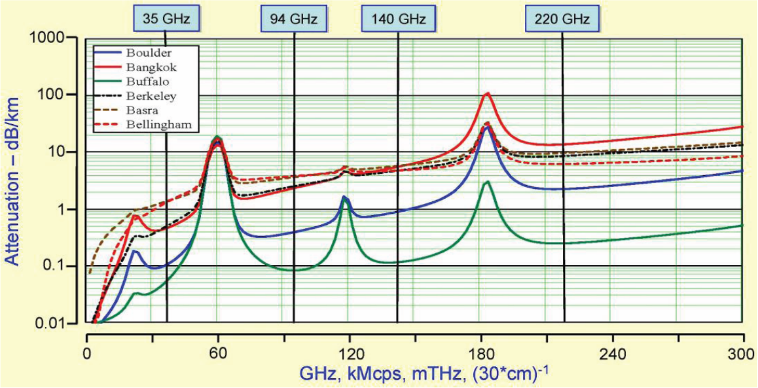

Figure 5-1 Atmospheric attenuation for different weather conditions [7]

In this chapter, a BWO (operates at 200 GHz) is introduced using two different SWSs. The first SWS is designed using a DD-PC structure. To enhance the efficiency and to reduce the electron beam requirements of the DD-PC based SWS, an Axial loaded Double Defected Photonic Crystal (ADD-PC) structure is used as a SWS. The modal analysis of the proposed structures is performed using both non-uniform FDFD and High Frequency Structure Simulator (HFSS), while the electron beam-wave interaction is carried out using FDTD/PIC simulation. To show the potential of the ADD-PC based SWS, the same design methodology was used to extend the operation of the BWO to 650GHz.

The ADD-PC based SWS has lower electron beam requirements. Thus, the efficiency of the BWO using this SWS is enhanced. However, the main drawback of the ADD-PC based SWS is the complex fabrication requirements. The axial discontinuity and the small structure dimensions of the 650GHz design, places limitation with respect to its fabrication using the current fabrication techniques.

5.2 The Physical Model

A two dimension (2D) cross-section of the triangle lattice cylindrical PC structure is shown Figure 5-2(a). It consists of several metallic rods, each of radius "*r*", placed in a triangle lattice structure. The distance between the centers of any two adjacent rods is the pitch size "*Λ*". The band diagram of the first three TM-modes to axial direction of the PC structure is plotted in Figure 5-2(b) [103]. As the figure indicates, the condition for a single mode operation is $r/\Lambda < 0.2$.

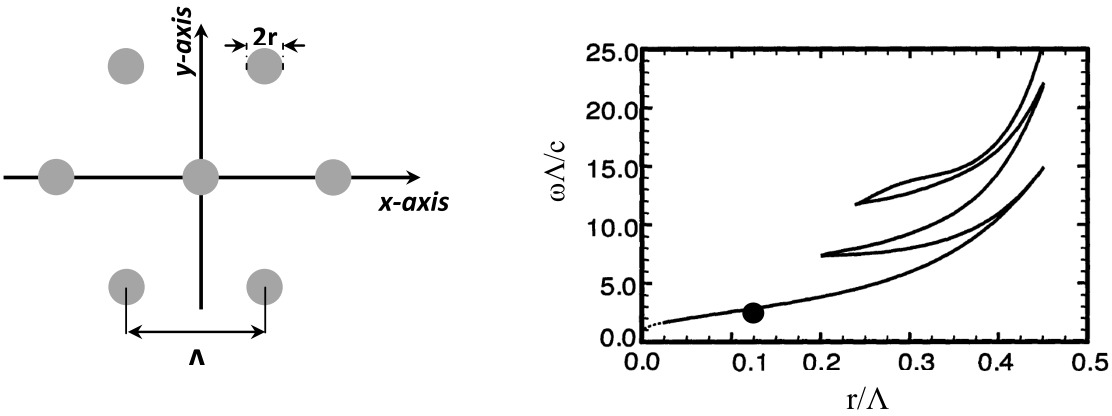

(a) (b)

Figure 5-2 (a) The triangle lattice, and (b) the band diagram of a triangle lattice for TM-modes

To design SWS operates at 200GHz; the first step is to design a single mode PC waveguide structure at the specified operating frequency. Thus, an operating point that matches the above condition was selected (shown as a black dot in the band diagram figure). For a single mode operation, the rod radius to pitch size ration (r/Λ), and the normalized pitch size (ωΛ/c) were selected to be 0.125 and 3.0, respectively. Thus, a single mode waveguide can be designed by creating a central defect (created by removing the two inner most layers of rods (Figure 5-3(a)). On the other hand, the DD-PC based SWS can be designed by introducing two types of defects; the central defect and the slow wave defects (Figure 5-3).

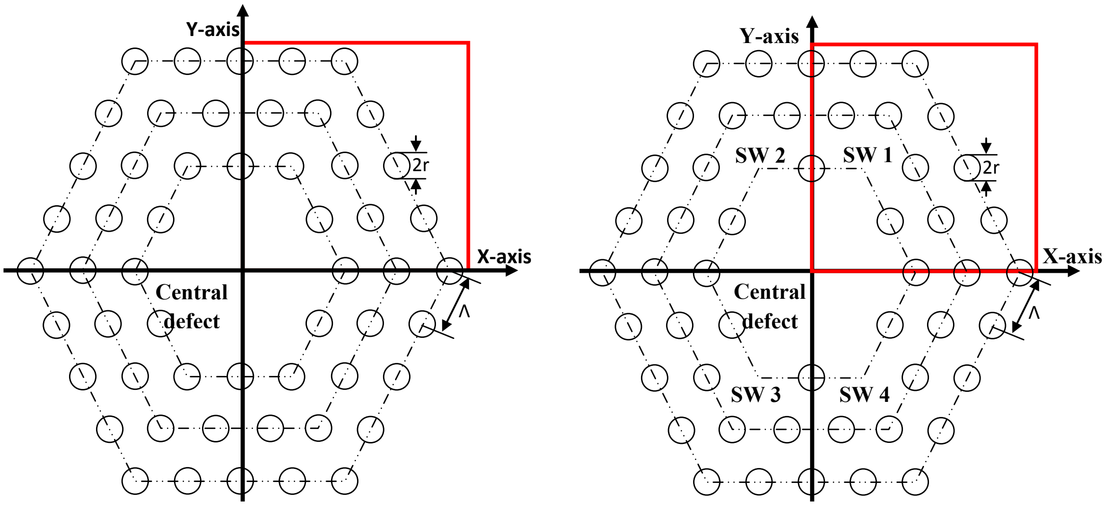

(a) (b)

Figure 5-3 The schematic diagram of (a) the PC waveguide, (b) the DD-PC based SWS

5.3 The Modal Analysis

The modal analysis of both the PC waveguide and the DD-PC was performed using the non-uniform FDFD developed in *3.2 The non-uniform FDFD method*. In the FDFD analysis, copper metallic rods, with a conductivity of $\sigma = 5.96\times107$ S/m, were used. Taking advantage of the structure symmetry, only quarter of the structure was analyzed (represented as a solid square in Figure 5-3)

5.3.1 The Photonic Crystal Waveguide

The field profile of the waveguide mode at 200GHz is shown in Figure 5-4. The figure shows that the axial electric field is concentrated at the center of the waveguide. The calculated modal phase shift of the TM-like mode $\beta = 3.887 - 2.1\times10^{-6}$ *rad/m.*

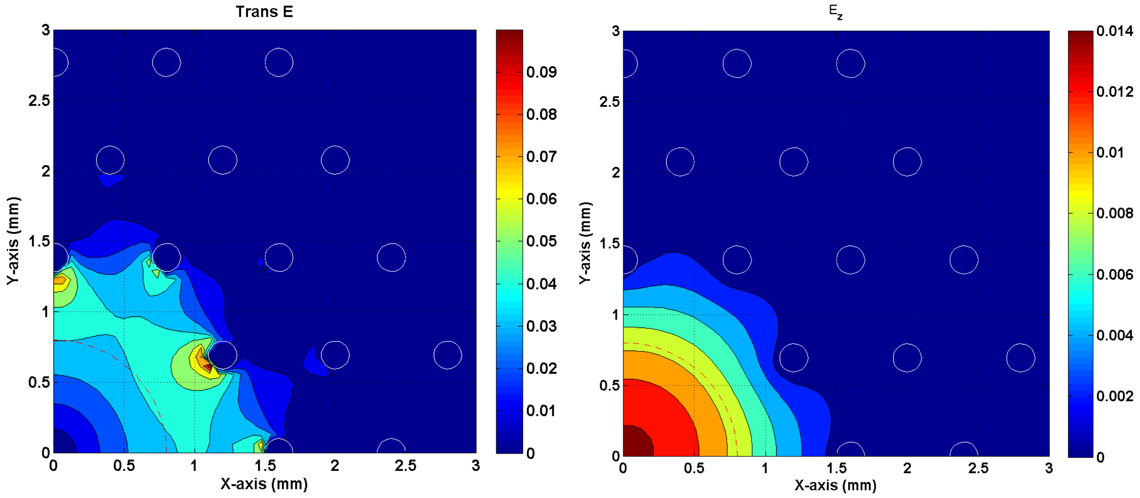

Figure 5-4 The waveguide modal fields (a) transverse E-fields and (b) E_z field

5.3.2 The Double Defected Photonic Crystal (DD-PC) Structure

For the DD-PC structure, the axial electric field profile of both the slow wave mode and the waveguide mode are shown in Figure 5-5. The axial electric field of the TM_{01}-like waveguide mode (Figure 5-5(a)), is concentrated at the central defect. Figure 5-5(b) shows the axial electric field of the slow wave mode in the DD-PC. A zoomed version of the same figure is presented in Figure 5-5(c). The slow wave mode is located in the slow wave defect and concentrated next to the metallic conductors. The modal parameters of the waveguide mode and the slow wave mode are given in Table 5-I. Due to the finite conductivity of the copper conductor used, both the slow wave mode and the waveguide mode have some losses (imaginary part in the phase shift constant).

In Cherenkov's radiation, an electromagnetic wave is excited if an electron beam travels through medium with a speed that matches the phase velocity of this electromagnetic mode [33]. Since the proposed SWS supports a mode with a phase velocity of almost $0.70v_c$, then Cherenkov's radiation can be generated within this structure if electrons beam of speed $0.70v_c$ travel through it. The main problem in this device is the high acceleration voltage required. It required almost 125KV to accelerate the particles to $0.70v_c$. Therefore, the electron beam source will require a high operating power. Hence, the conversion efficiency of an oscillator using the proposed SWS is expected to be low.

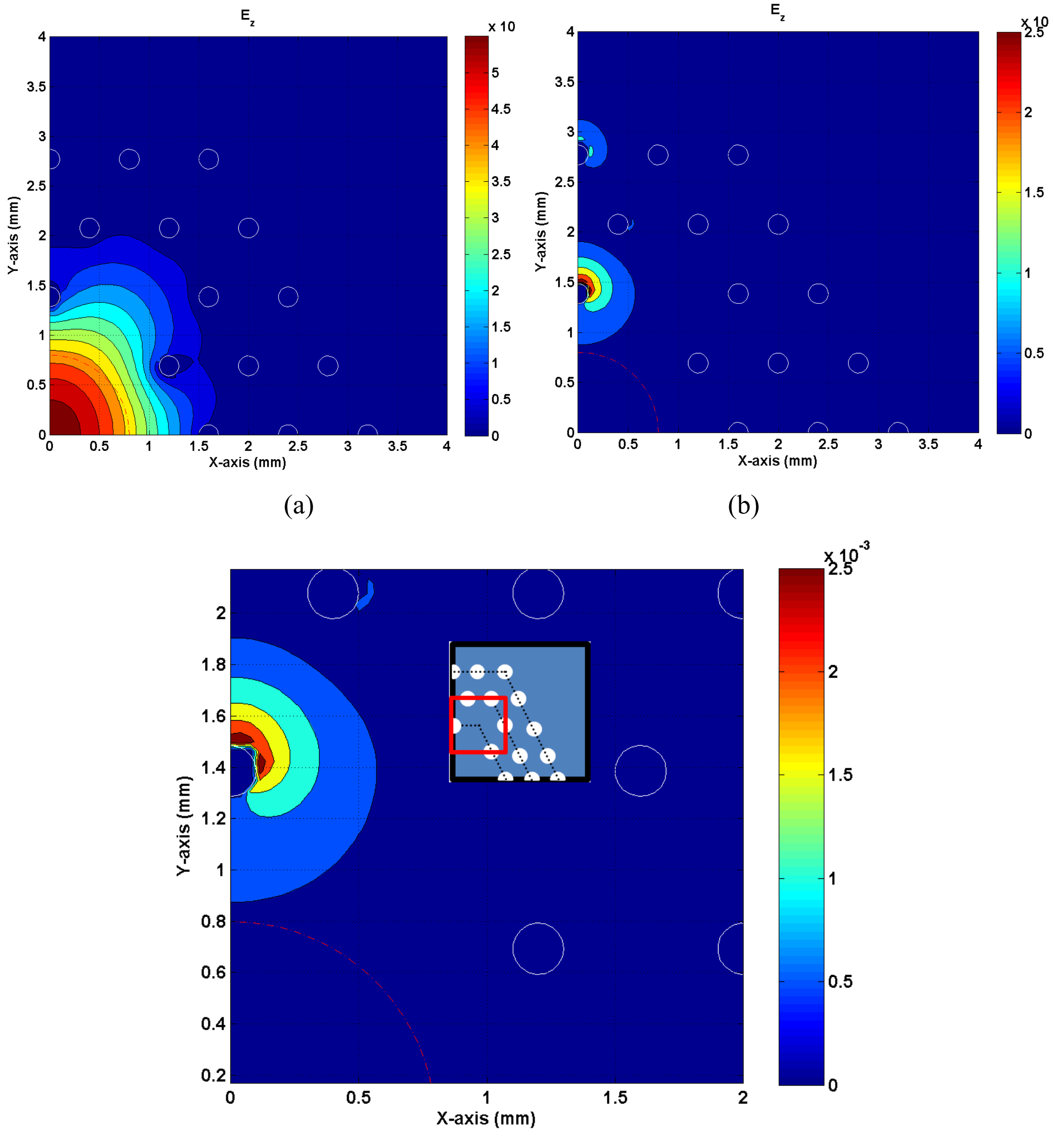

(a) (b)

(c)

Figure 5-5 The operating modes of the structure, (a) the waveguide mode and (b) the SWS mode, and (c) Zoomed SWS mode

	Waveguide mode	***Slow wave mode***
Operating frequency (f)	200GHz	200GHz
The phase shift (β – rad/mm)	$3.91682733 - j4.57\times10^{-6}$	$5.984 - j9.96\times10^{-6}$
The Normalized phase velocity (v_{ph}/v_c)	1.07016348	0.70
Wavelength (λ mm)	1.6	1.0
Impedance (η)	352.5228	538.5727

Table 5-I The modal parameters of the waveguide mode and the slow wave mode

5.4 Analysis of the 200GHz BWO using the DD-PC based SWS

Using the predesigned DD-PC based SWS, a BWO operates at 200GHz was proposed. The analysis of the electron beam-wave interaction was done using the FDTD/PIC CAD tool introduced in the previous chapter (*4.3 The FDTD/PIC simulation*). For the electron beam-wave interaction, a circular electron beam is used to excite the structure. The main parameters of the BWO are listed in Table 5-II

Parameter	Value
Beam voltage	125KV
Beam current	17.71 mA
Beam radius	80 μm
Applied DC magnetic field	1.5 T
The structure dimensions	100 × 100 × 4500 μm

Table 5-II Summary of the BWO parameters

The maximum beam current limit was defined such that the particles remain in the space-charge limited region (Figure 4-19) [32]. Moreover, the value of the starting current defines the minimum electron beam current applied to achieve a particle/field interaction. In the current simulation, the electron beam current and the axial magnetic field were selected such that at least 90% of the particles reach the end of the structure.

5.4.1 The Field Simulation Results

The time domain sampled electric and magnetic fields, at the center of the first slow wave defect “SW-1”, are shown in Figure 5-6(a), and (b). The figure shows that the axial electric field dominates the transverse fields. Also, the axial magnetic field can be neglected compared to the transverse magnetic fields. Therefore, the generated fields are TM-like mode, which concurs with the predicted from the FDFD modal analysis. The frequency response of the electric and magnetic fields are shown in Figure 5-6(c) and (d), respectively. The figure shows that both the electric and magnetic fields have the same frequency response (214 GHz).

Since the FDTD/PIC simulation was performed on a perfect conductor; while the modal analysis, performed by FDFD, was done using a copper conductor; it is expected to have a slight frequency shift between the modal FDFD and FDTD/PIC results.

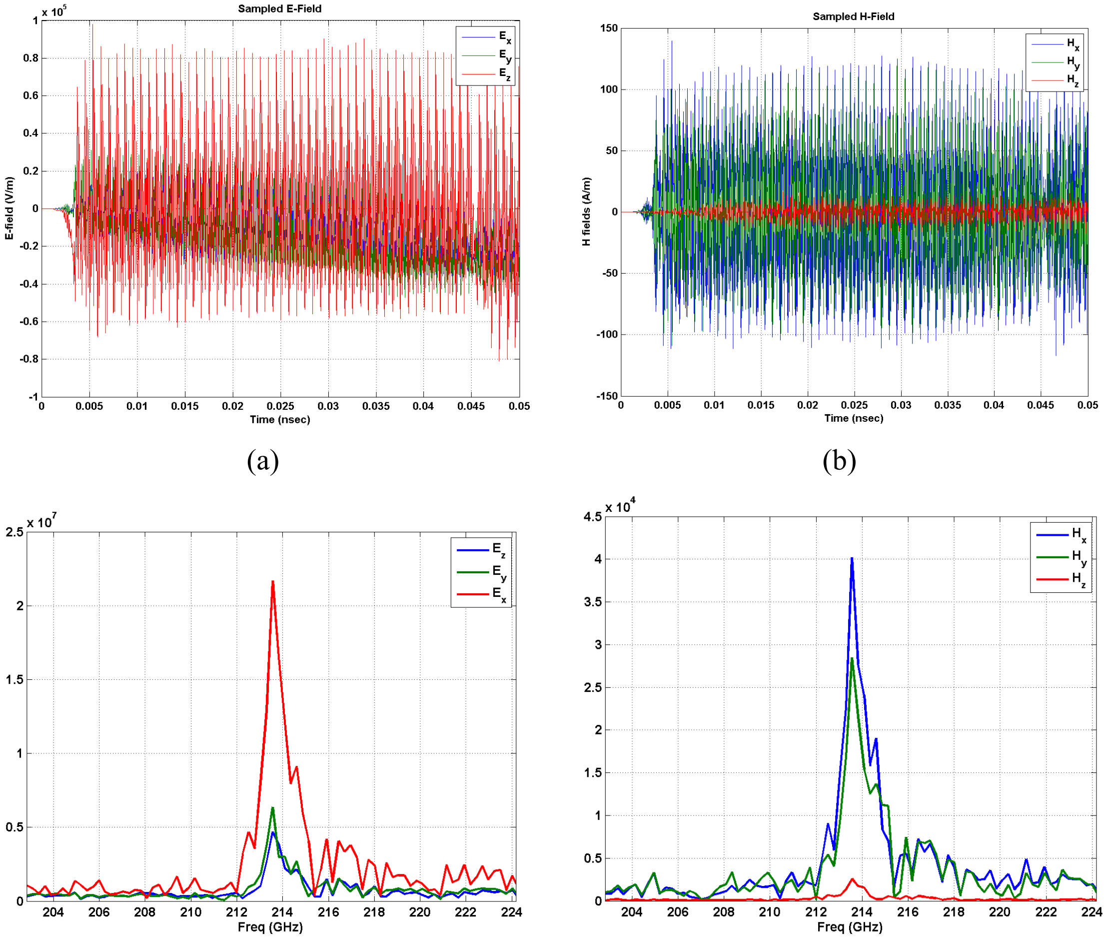

(a)

(b)

(c)

(d)

Figure 5-6 The time domain sampled (a) electric and (b) magnetic fields and the corresponding FFT response of (c) electric and (d) magnetic fields

The time-zoomed sampled transverse electric and magnetic field are shown in Figure 5-7(a) and (b), respectively. It is clear from the figure that the transverse electric field components are in-phase, while the transverse magnetic field components are out of phase. Therefore we have a constructive summation in the power density equations ($Power\ density = E_xH_y - E_yH_x$).

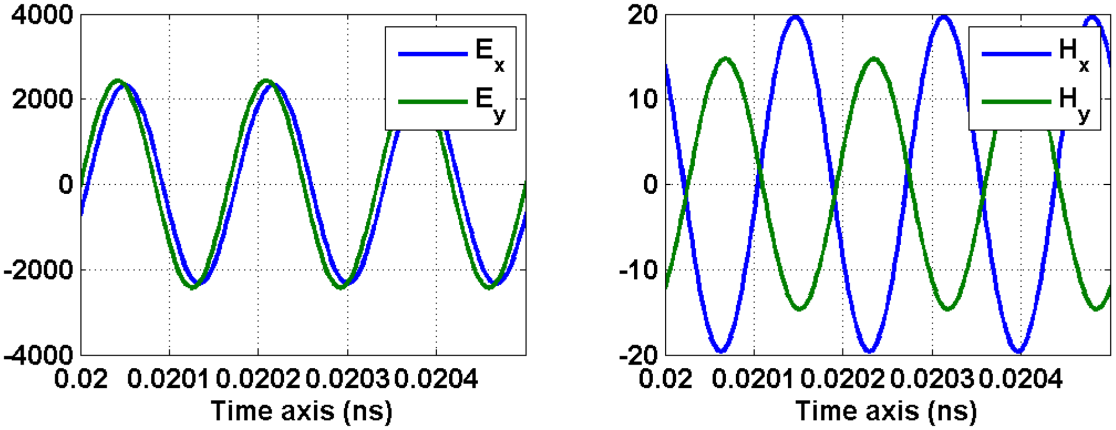

(a) (b)

Figure 5-7 A time-zooming of both (a) transverse electric fields and (b) transverse magnetic fields

5.4.2 The Electromagnetic Power Analysis

Using the Poynting theorem (*4.4.4 The Electromagnetic Power Density*), the generated electromagnetic power is calculated. Figure 5-8(a) presents the normalized power density, while a time-zoomed version of the same calculation is shown in Figure 5-8(b). The power density calculation was performed at a frequency of 214GHz. The zoomed figure shows that the two terms of the power density ($Pd = Pd_1 - Pd_2 = E_xH_y - E_yH_x$) have opposite signs, thus the power density calculation is always a cumulative summation.

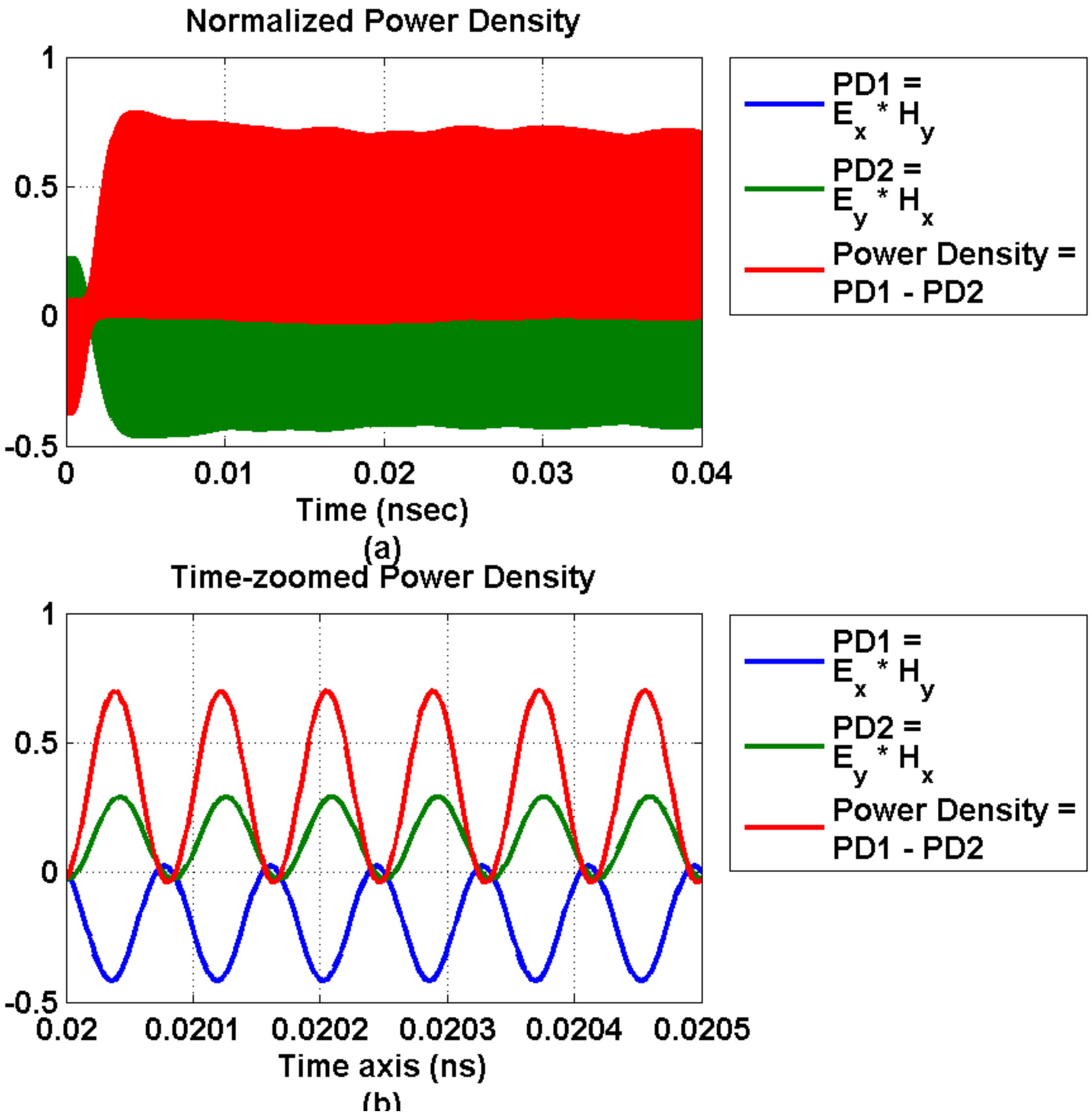

Figure 5-8 (a) The power density analysis and (b) time-zoomed figure for the power density

5.5 The Axial loaded Double Defected Photonic Crystal Structure

The main problem of the slow wave mode in the DD-PC is its high phase velocity. Therefore, the required electron beam velocity is high. To reduce the phase velocity, an axial discontinuity is introduced (similar to the *2.3.5 The Periodic Loaded Waveguide (PLW)*). The axial discontinuity was formed by adding metallic disks each of thickness "*t*" at a certain axial distance "*L* – cell size". The Axial loaded Double Defected Photonic Crystal guide (ADD-PC) is shown in Figure 5 6(a), while a cross section of the axial discontinuity is shown in Figure 5 6(b). The analysis of the ADD-PC was done using HFSS Floquet's mode solver. In the HFSS solver, the metallic parts of the structure were selected to be perfect conductors.

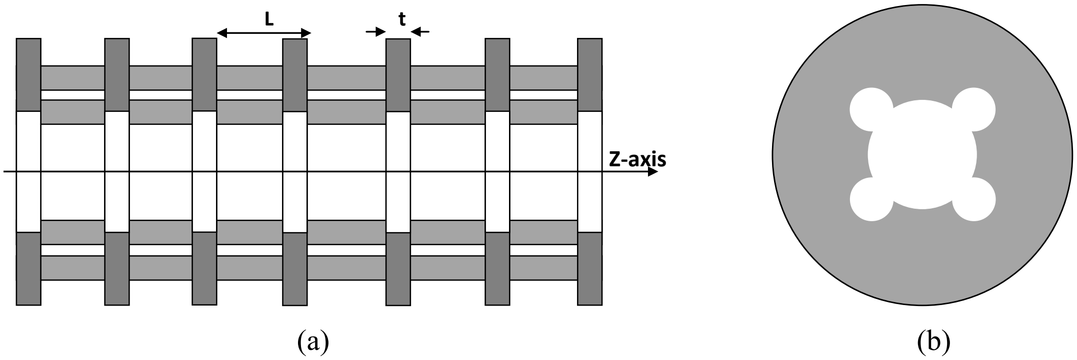

(a) (b)

Figure 5-9 (a) A schematic diagram of the ADD-PCF, (b) a cross sectional diagram of the axial discontinuity

The initial values of the cell size (*L*) and the thickness of the discontinuity disk (*t*) were selected to be $\lambda_0/2$ and *L/3*, respectively. To optimize the selected values, an optimization analysis was run on the HFSS Floquet's mode solver to find the optimum "*L*" and "*t*" values. The optimization is run based on the electromagnetic field pattern. For the waveguide mode (also known as the "0-mode" which equivalent to a 0° phase shift between the master and slave boundary conditions), the fields should be concentrated at the center of the structure. On the other hand, the slow wave mode (also called *π*-mode or 180° phase shift between the master and slave boundary condition), the electric field migrates to the walls of the metallic structure. The optimized values of cell size and the discontinuity thickness were found to be 0.75mm and 0.1875mm respectively.

The HFSS Floquet's mode setup is shown in Figure 5-10(a). The setup consists of the single cell of the ADD-PC terminated with both master and slave boundary conditions. The resonance frequencies are calculated at phase difference of 0, $\pi/6$, $\pi/3$, $\pi/2$, $2\pi/3$, $5\pi/6$, and π between the master/slave boundary condition. The field pattern of the 0-mode and the π-mode are shown in Figure 5-10(b) and (c), respectively. The 0-mode, which is a waveguide mode, is concentrated at the center of the SWS. Alternatively, the slow wave mode is located near the copper conductors.

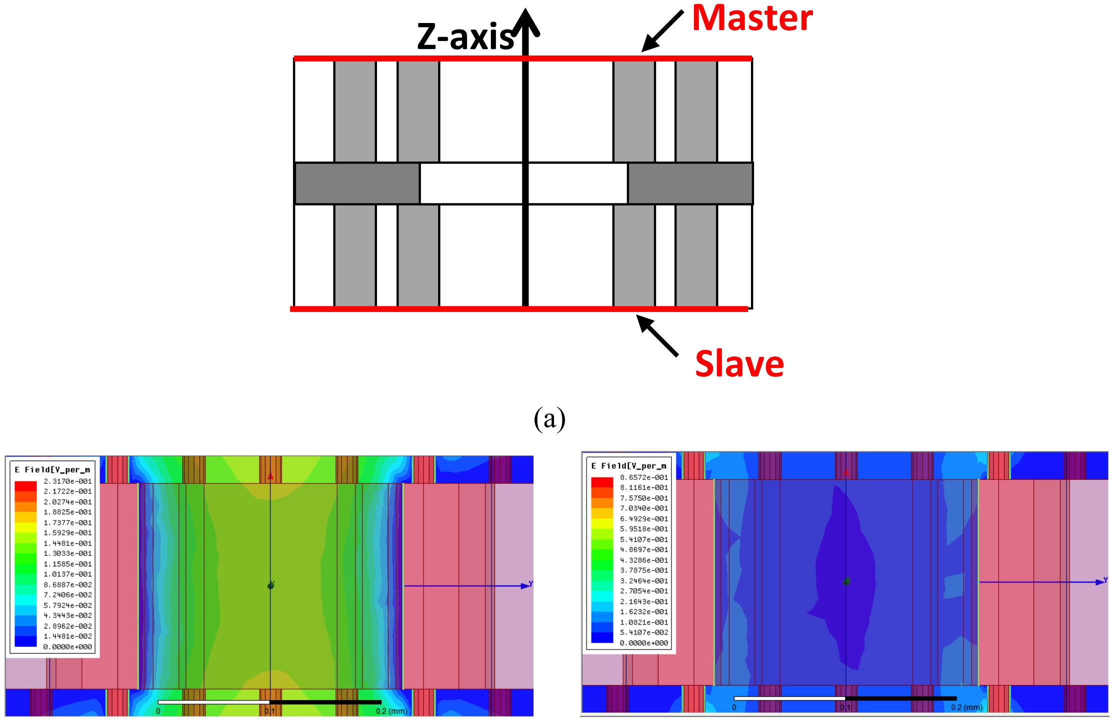

(a)

(b) (c)

Figure 5-10 (a) A unit cell of the ADD-PC model (analyzed using the HFSS Floquet's mode), (b) The 0-phase shift mode, and (c) the π-phase shift mode

5.5.1 Analysis of the ADD-PC based SWS

Taking advantage of the Floquet's mode analysis, the modal parameters of the ADD-PC are calculated. These modal parameters are; the dispersion curve, the normalized phase velocity and the Beam Interaction Impedance (BII).

5.5.1.1 The Dispersion Curve Extraction

Using the resonance frequency data obtained from HFSS Floquet's mode, the dispersion curve can be expanded as [115]:

$$f = function(cos(\beta L), G) \tag{5-1}$$

where, "β" is the phase shift constant, "L" is the cell size, "G" represents geometrical parameters (usually selected to be 1.0) and "f" is the frequency of the Floquet's mode.

Since the dispersion relation is an even function of β, and the dependence of frequency on βL is periodic with the period of 2π, so it can be expressed as:

$$f = \sum a_m cos(m\beta L) \tag{5-2}$$

where "a_m" is the expansion coefficients.

Using the Floquet's frequencies calculated from HFSS Floquet's at different phase difference values, the unknown expansion coefficients "a_m" can be calculated. Thus, a dispersion curve can be extracted as well as other modal parameters. Using the pre-calculated expansion coefficient, a plot of the dispersion curve, of the TM-like mode, propagates in the ADD-PC based SWS is shown in Figure 5-11. The figure also presents the normalized phase velocity (with respect to the light speed in vacuum) for the same mode.

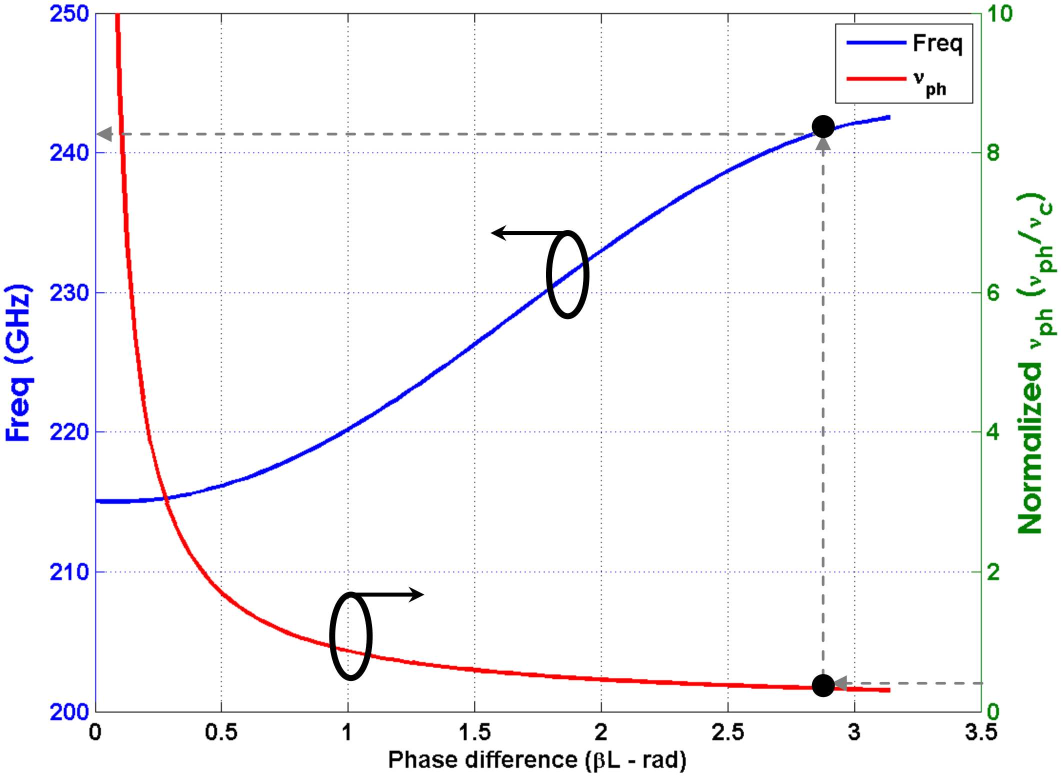

Figure 5-11 The dispersion curve for TM-like mode of the ADD-PC based SWS, and the associated normalized phase velocity curve

5.5.2 The Beam Interaction Impedance

To estimate the amount of energy transferred from the electron beam to the electromagnetic mode, the Beam Interaction Impedance (BII) is calculated [32]. The BII is defined as:

$$BII = \frac{\int |E_z|^2 dS}{2\beta^2 PS} \tag{5-3}$$

where "E_z" is the axial electromagnetic field, "β" is the phase shift constant, "P" is the electromagnetic power transmitted by the slow-wave electromagnetic mode, "S" is the beam cross-sectional area, and the integration is done over the cross section of the beam.

The normalized BII of the first slow wave mode in the ADD-PC is plotted in Figure 5-12. The figure shows that the BII is significantly reduced with the increase of the phase difference. The reduction of the BII is due to two factors; the excitation of higher order modes, and the field profile. AS the phase difference increases higher order modes can propagate through the structure. Therefore, the electromagnetic power will be divided between multiple modes. Moreover, as the phase difference increases, the field migrates to the conducting rods. Thus, the integration term is significantly reduced. This explains the decrease of the BII with the increase of frequency.

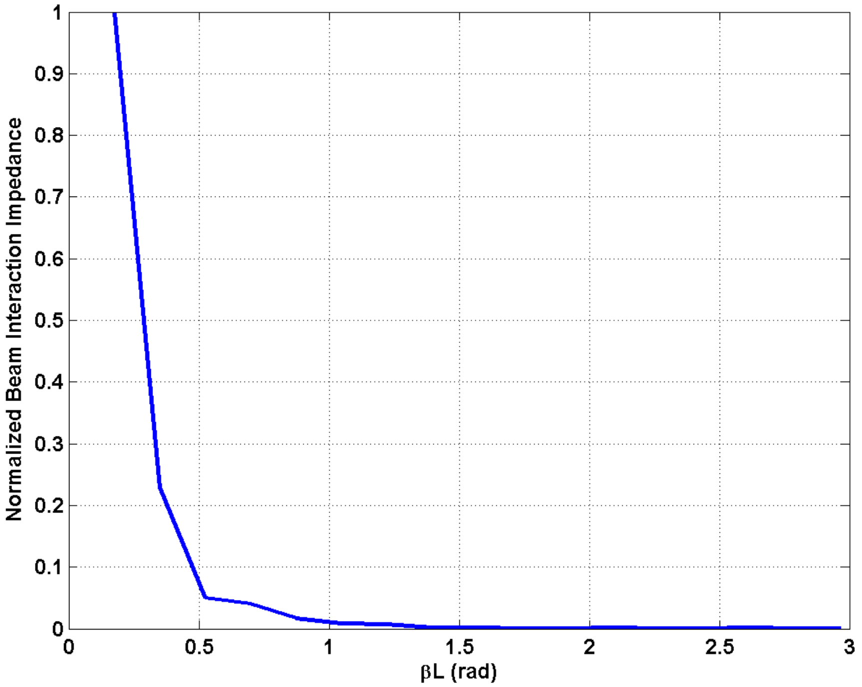

Figure 5-12 The normalized Beam Interaction Impedance (BII)

5.6 Analysis of the 200GHz BWO using the ADD-PC based SWS

In this section the analysis of the 200GHz BWO using the ADD-PC based SWS is performed. The simulation was done using the FDTD/PIC CAD tool. For the electron beam-wave interaction, a circular electron beam is used to excite the structure.

To define the lower limit of the electron beam current, the starting current –for an axial periodic structure- is defined as [116].

$$I_{st} = \frac{I_A}{4\pi}\left(\frac{p}{L}\right)^3 \frac{\gamma_i^3 \upsilon_{zn}^2}{k_* P} \frac{\upsilon_{gr}(\omega)}{C_c} \tilde{I}_{st} \tag{5-4}$$

where “I_A” is a constant ($mc^3/q=1.7\times10^4$A), “p” is the period length, “L” is the total length of the structure, “γ_i” is the relativistic Lorentz factor, “υ_{zn}” is the normalized axial velocity of the electron beam, “ω” is the operating frequency, “υ_{gr}” is the group velocity at the operating frequency, “C_c” is the coupling factor at the resonance frequency, “$k= \omega/\upsilon_{zn}$” is the wavenumber at the operating frequency, and “$\tilde{I}_{st}$” is a dimensionless number called the universal starting current ($\tilde{I}_{st}$ =7.7).

Using the above equation, a starting current of almost 4.2mA was calculated for the particular structure under consideration. The beam current is usually selected to be less than three times the starting current. Although increasing the beam current increases both the generated electromagnetic power and efficiency, it affects the spectral purity of the generated electromagnetic wave [37].

	DD-PC based BWO	ADD-PC based BWO
Beam voltage	125KV	31.3 KV
Beam current	17.71 mA	9.2 mA
Applied DC magnetic field	1.5 T	
Beam radius	80 µm	
The structure dimensions	100 × 100 × 4500 µm	

Table 5-III Comparison between the electron beam requirements of two BWO

A comparison between the main parameters of the BWO using both the DD-PC based SWS and the ADD-PC based SWS is listed in Table 5-III. The table shows that using the ADD-PC based SWS reduced the beam voltage from 125KV to 31.3KV. Therefore, there is a significant reduction in the electron beam power.

5.6.1 The Field Simulation Results

The time domain sampled electric and magnetic fields are shown in Figure 5-13(a), and (b). The figure shows that the axial electric field dominates the transverse fields. Also, the axial magnetic field is neglected compared to the transverse magnetic fields. Therefore, the generated fields are TM-like mode, which verifies the prediction of the HFSS modal analysis. The frequency response of the electric and magnetic fields are shown in Figure 5-13(c) and (d), respectively. The figure shows that both the electric and magnetic fields have the same frequency response (247 GHz). Compared to the DD-PC, the ADD-PC is more selective in the generated frequencies.

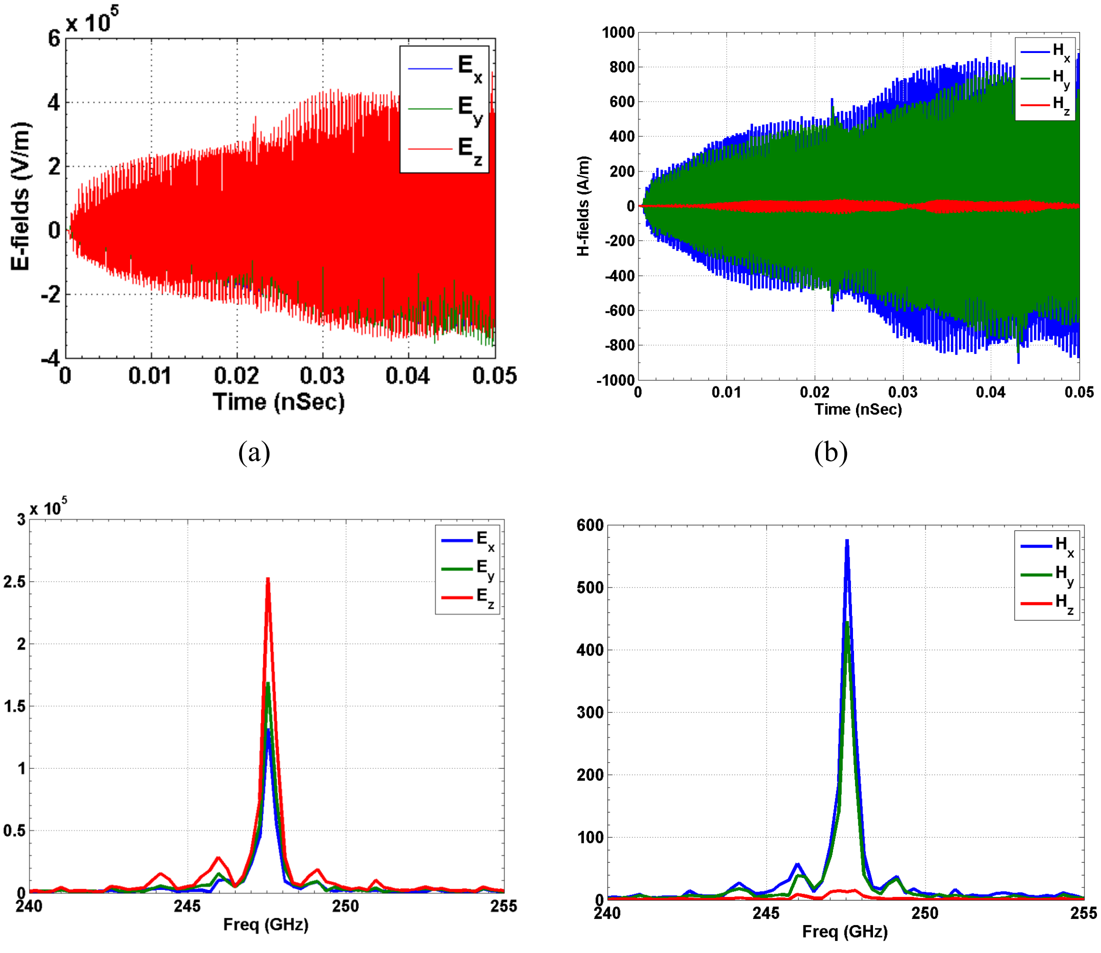

(a)

(b)

(c)

(d)

Figure 5-13 The time domain sampled (a) electric and (b) magnetic fields and the corresponding FFT response of (c) electric and (d) magnetic fields

The time-zoomed sampled transverse electric and magnetic field are shown in Figure 5-14(a) and (b), respectively. It is clear from the figure that the transverse E-field components are in-phase, while the transverse magnetic field components are out of phase. Therefore we have a constructive summation in the power density equations (*Power density* = $E_xH_y - E_yH_x$).

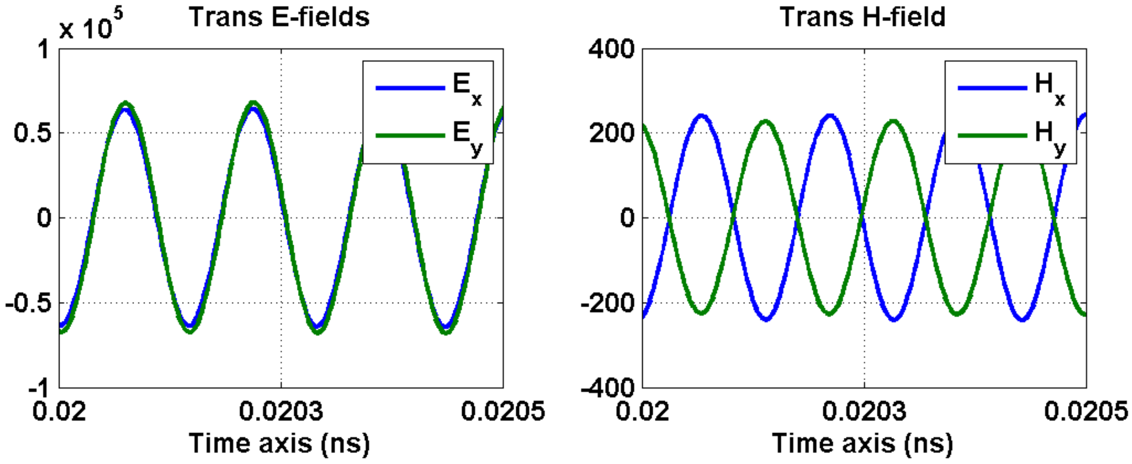

(a) (b)

Figure 5-14 A time-zooming of both (a) transverse electric fields and (b) transverse magnetic fields

5.6.2 The Power Analysis

Figure 5-15(a) presents the normalized power density, and a time-zoomed version of the same figure is shown in Figure 5-15(b). The power density calculation was performed at a frequency of 247GHz. The zoomed figure shows that the two terms of the power density ($Pd = Pd_1 - Pd_2 = E_xH_y - E_yH_x$) have opposite signs, thus the power density calculation always add-up.

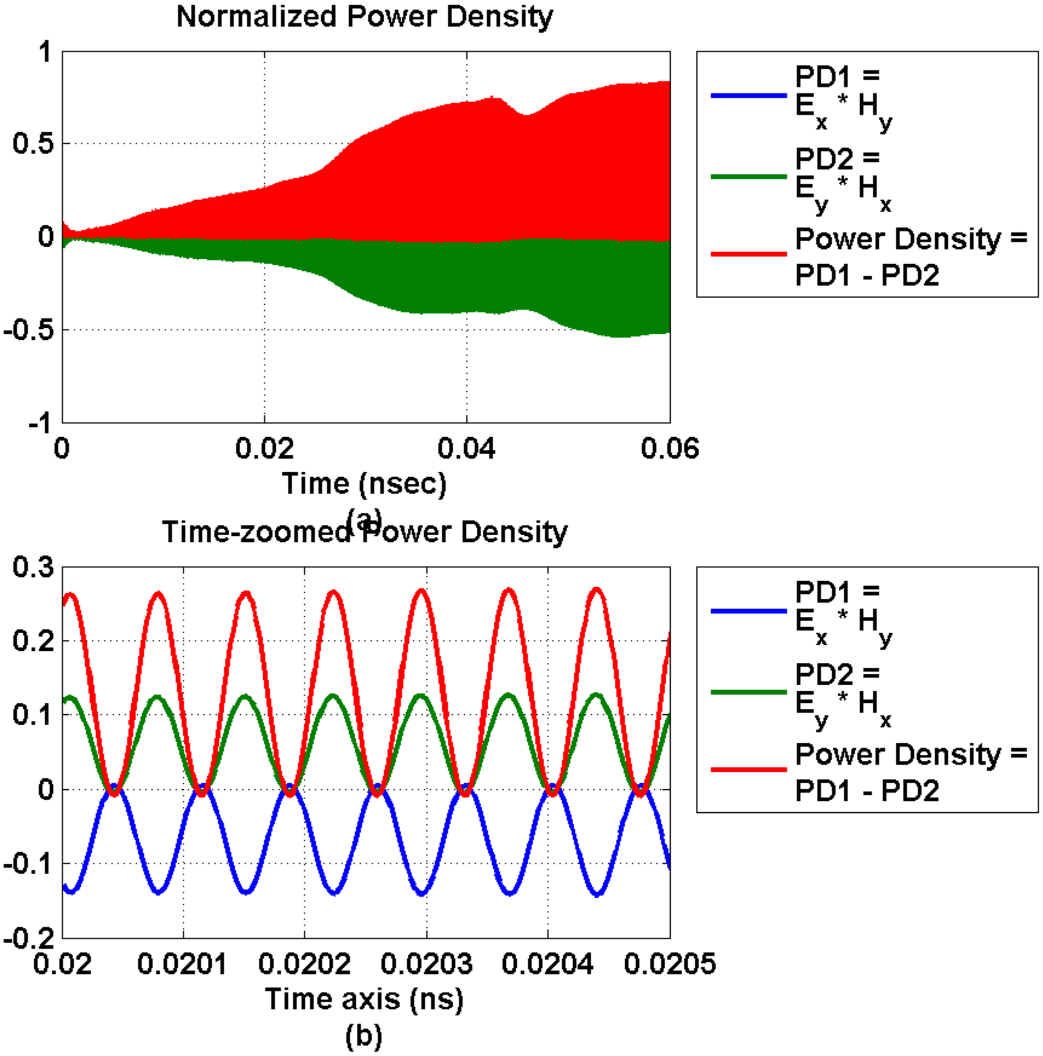

Figure 5-15 (a) The power density analysis, (b) time-zoomed figure for the power density

5.6.3 The tunability of the BWO

Taking advantage of the dispersion curve, the ADD-PC can be used as a tunable BWO. To demonstrate the tunability of the ADD-PC structure, two operating points were selected on the dispersion curve, and the normalized velocity curve, shown in Figure 5-16. The first operating point is for an electromagnetic mode with a phase velocity of around $0.35v_c$. This point has a resonance frequency approximately 242GHz. The second operating point defined an electromagnetic mode operating at 218GHz with a phase velocity of nearly $0.90v_c$.

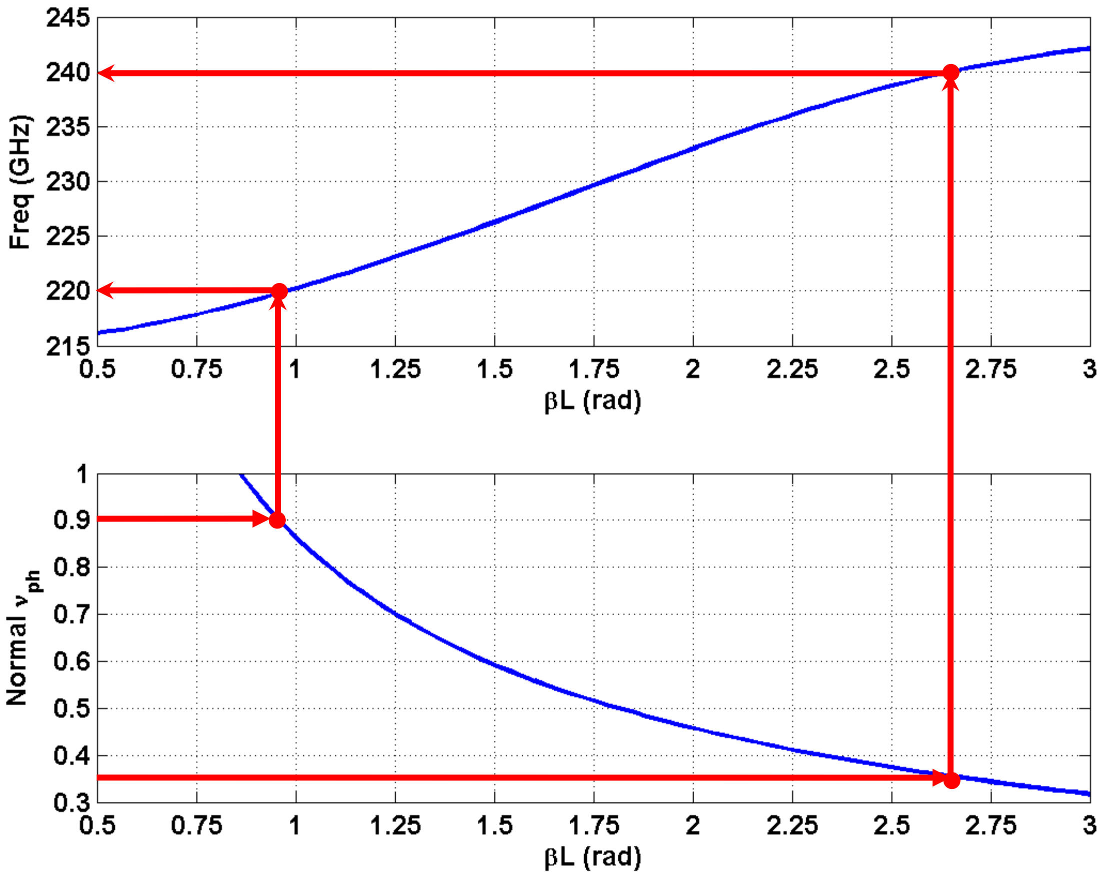

Figure 5-16 The dispersion curve of the ADD-PC based SWS and the normalized phase velocity

Using the FDTD/PIC CAD tool, the BWO was simulated at these two operation points. A summary of the FDTD/PIC simulation parameters are listed in Table 5-IV. The electron beam parameters were selected as discussed in *5.6 Analysis of the 200GHz BWO using the ADD-PC based SWS*.

		Operating Point 1	Operating Point 2
v_{beam}		0.35 v_c	0.90 v_c
I_{beam}		17mA	23mA
B_z		1.5	1.5
Frequency response	Theoretical – expected	242GHz	218GHz
	Actual – FFT response	247GHz	214GHz

Table 5-IV The parameters of BWO for two operating points

5.6.3.1 Field Simulation Results of the First Operating Point

The time domain sampled electric and magnetic fields and their corresponding frequency domain response are shown in Figure 5-17. Similar to the previous analysis, the simulation shows that the mode is a TM-like mode. Also, the FFT response of the sampled electric and magnetic fields, shown in Figure 5-17(c) and (d) respectively, indicates that fields resonate at the same frequency (247 GHz), which is shifted by almost 0.8% compared to the HFSS simulation.

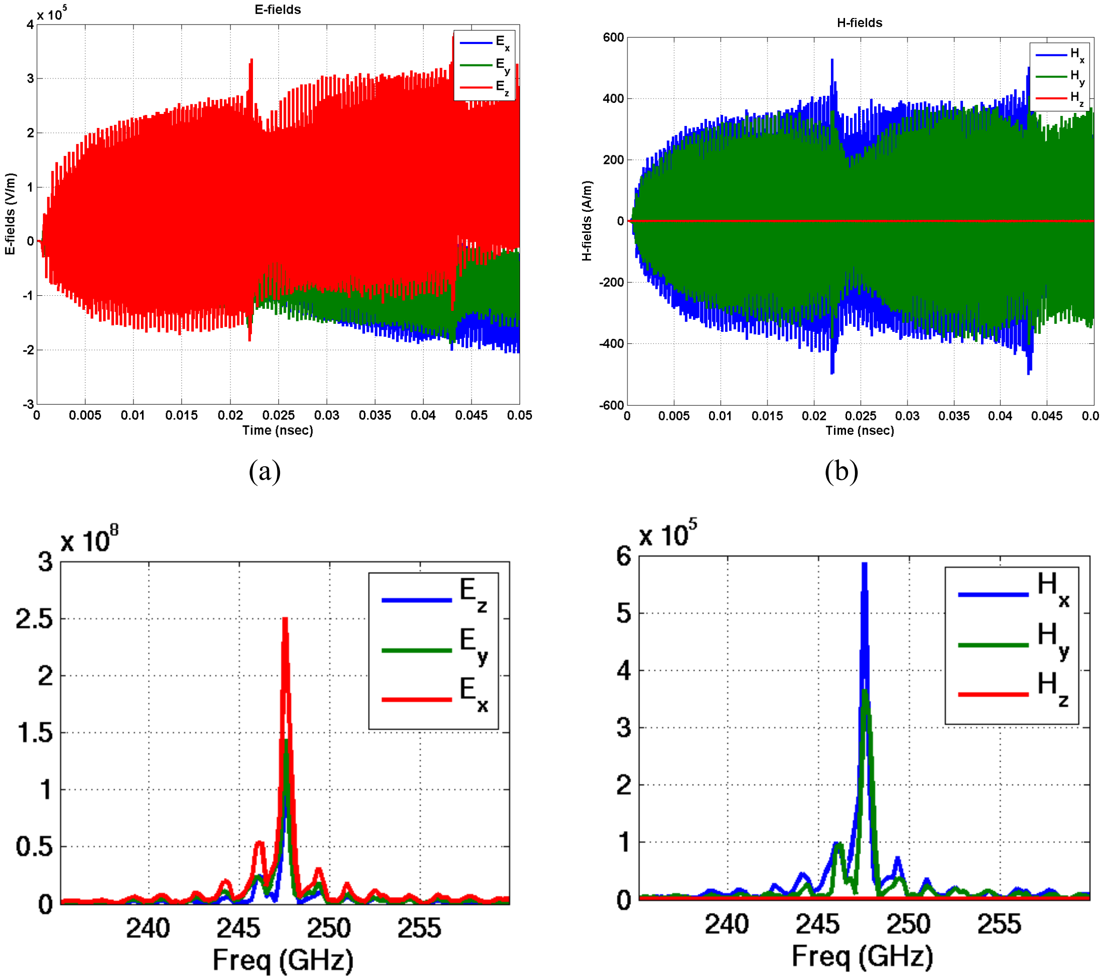

(a) (b)

(c) (d)

Figure 5-17 The time domain sampled (a) electric and (b) magnetic fields, and the corresponding FFT response of (c) electric and (d) magnetic fields

A zoom plot of the transverse electric and magnetic fields are shown in Figure 5-18. The figure shows that both the transverse electric field components are in-phase, while, the transverse magnetic field components are out of phase. Therefore, the power density (*Power Density* = $E_xH_y - E_yH_x$) is always adding-up.

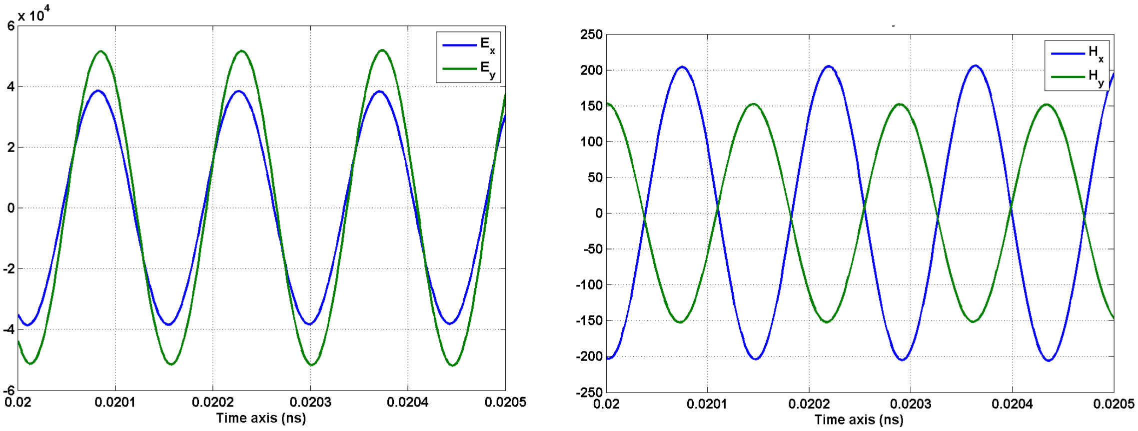

(a) (b)

Figure 5-18 A zoomed plot of the transverse (a) electric and (b) magnetic fields

5.6.3.2 Field Simulation Results of the Second Operating Point

The time domain sampled electric and magnetic fields and their corresponding frequency domain response are shown in Figure 5-19. Similar to the previous analysis, the simulation shows that the mode is a TM-like mode. Also, the FFT response of the sampled electric and magnetic fields, shown in Figure 5-19(c) and (d) respectively, indicates that fields resonate at the same frequency (214 GHz). Also, the zoomed version of the transverse fields (Figure 5-20) indicates that the power density terms are constructively adding-up.

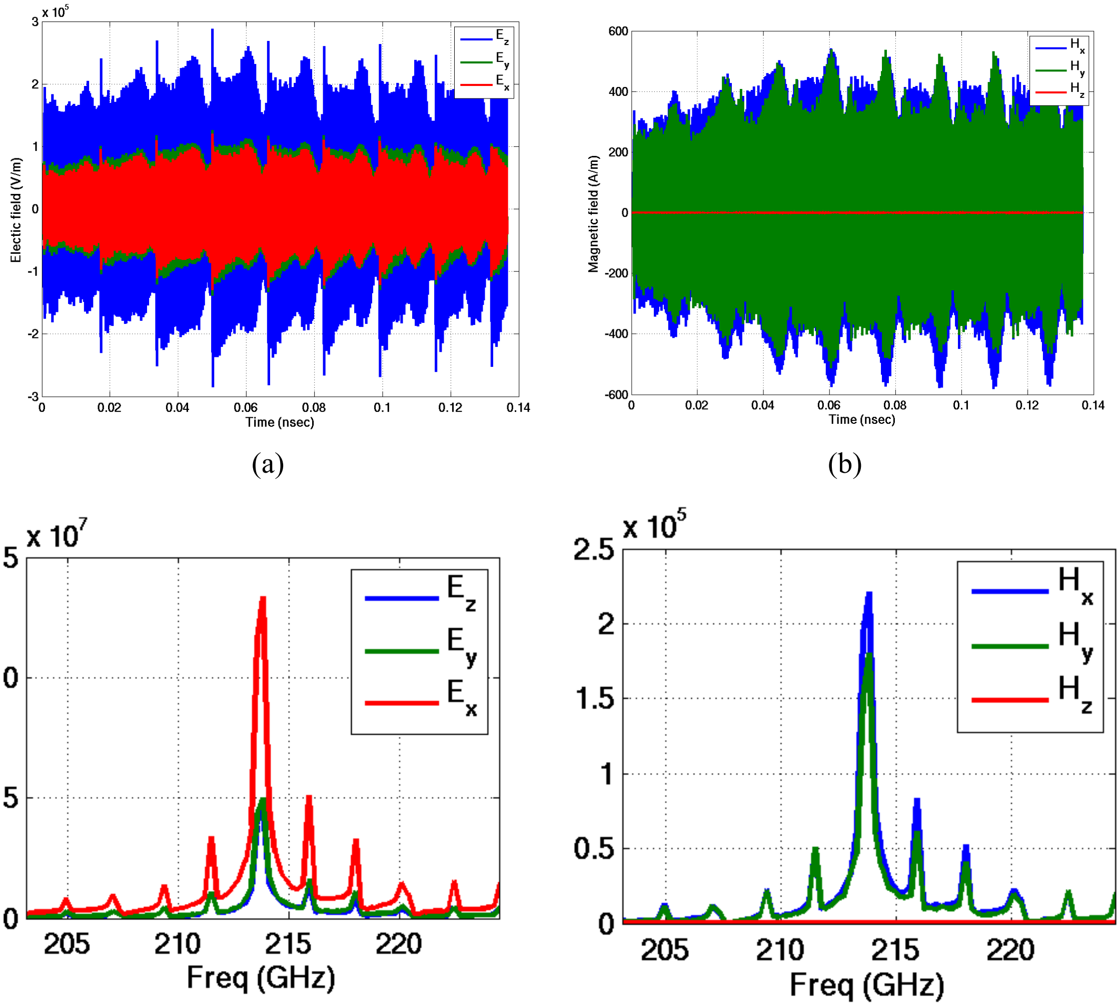

(a) (b)

(c) (d)

Figure 5-19 The time domain sampled (a) electric and (b) magnetic fields, and the corresponding FFT response of (c) electric and (d) magnetic fields

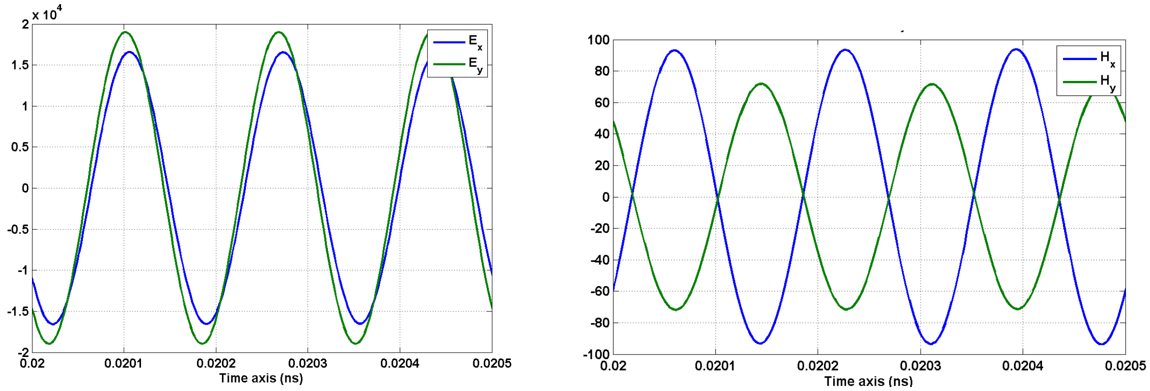

(a) (b)

Figure 5-20 The time domain zoomed of (c) electric and (d) magnetic fields

5.6.4 Optimization of the ADD-PC Oscillator

As discussed above, The ADD-PC resonates at 247GHz (at beam velocity of $0.35v_c$) which is 25% higher than the desired operating frequency. To overcome this frequency overshot, the axial disk of the ADD-PC was fine-tuned to operate at 200GHz. A schematic of the optimized ADD-PC is shown in Figure 5-21. A summary of the starting point values of the ADD-PC structure parameters are given in Table 5-V.

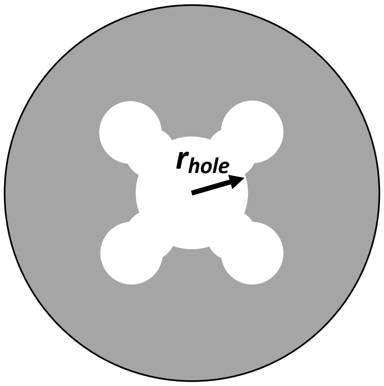

Figure 5-21 A cross sectional view of the axial load disk

Parameter	Value
Λ	0.40 mm
r	0.05 mm
t	0.50 * L
r_{hole}	Variable
L	Variable

Table 5-V The Optimized ADD-PCF structure parameters

Using the HFSS Floquet's mode analysis, followed by a dispersion curve extraction (equation and procedure explained in *5.5.1.1 The Dispersion Curve Extraction*), the dispersion curve can be calculated. The main optimization parameters in these simulations are; the period length "*L*" and the inner radius of the iris "r_{hole}".

5.6.4.1 The Optimization of the period length "L"

In this section the inner radius of the iris "r_{hole}" is kept constant at *1.2Λ*, while the period length "*L*" is changed from 0.05 – 0.5mm with a step of 0.05mm. The dispersion curves of the ADD-PC for several period lengths "L" are shown in Figure 5-22(a); and the corresponding phase velocities are shown in Figure 5-22(b).

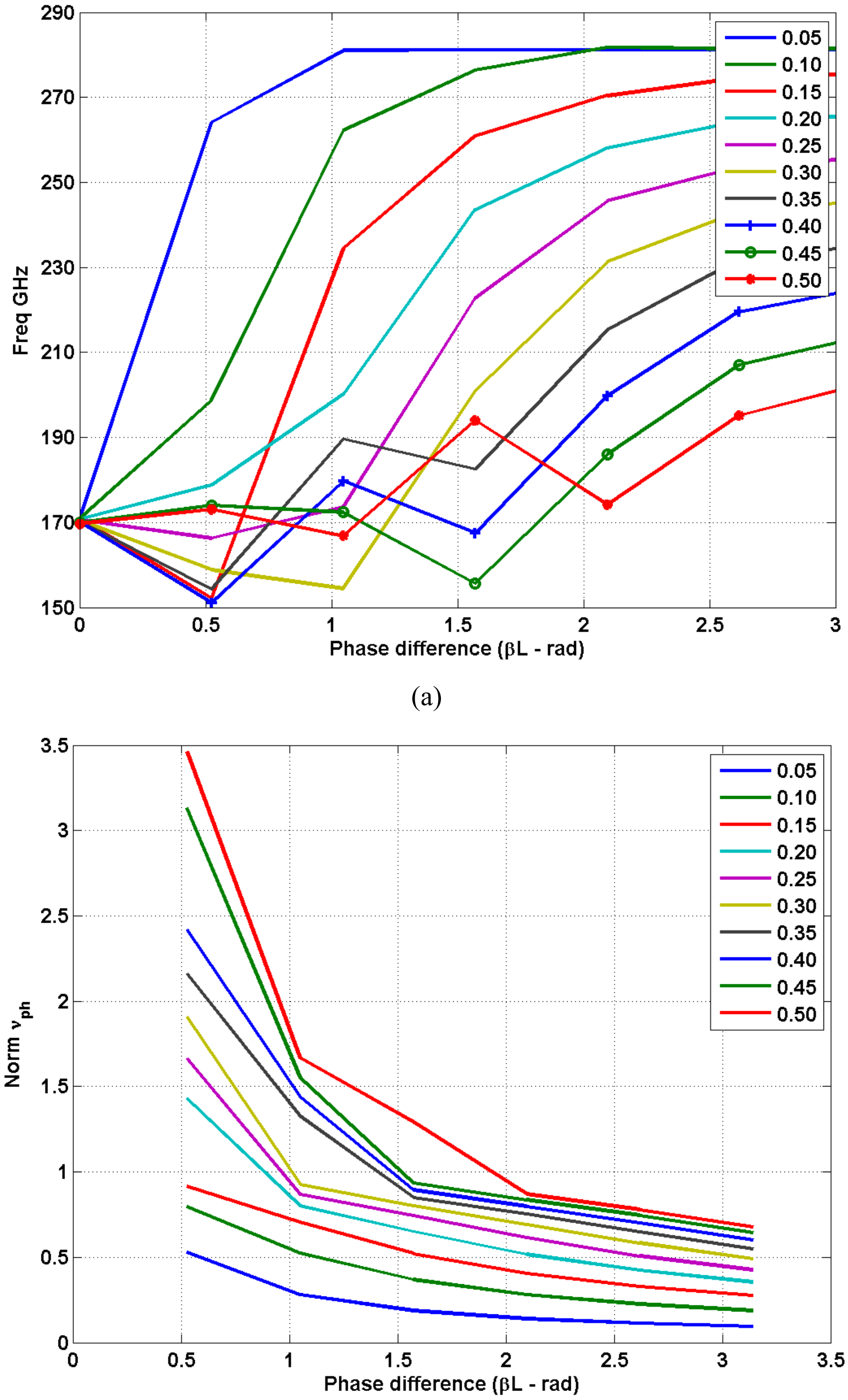

(a)

(b)

Figure 5-22 Optimization curves of the ADD-PCF for (a) the dispersion curve, and (b) the phase velocity

Using the FDTD/PIC CAD simulation tool, it was found the changing the cell length “*L*” has a minor effect on the frequency of the generated electromagnetic wave.

5.6.4.2 The Optimization of the Inner Radius of the iris “r_{hole}”

In this part, an optimization of the inner radius of the iris (Figure 5-21) is performed. The period length “*L*” is kept constant at 0.2mm. Figure 5-23 presents both the dispersion and the phase velocity curves at two different inner radius of the iris; 0.90Λ, and 0.95Λ. The figure indicates that using an inner radius of 0.95Λ, the structure is able to generate an electromagnetic field of a frequency of almost 200GHz.

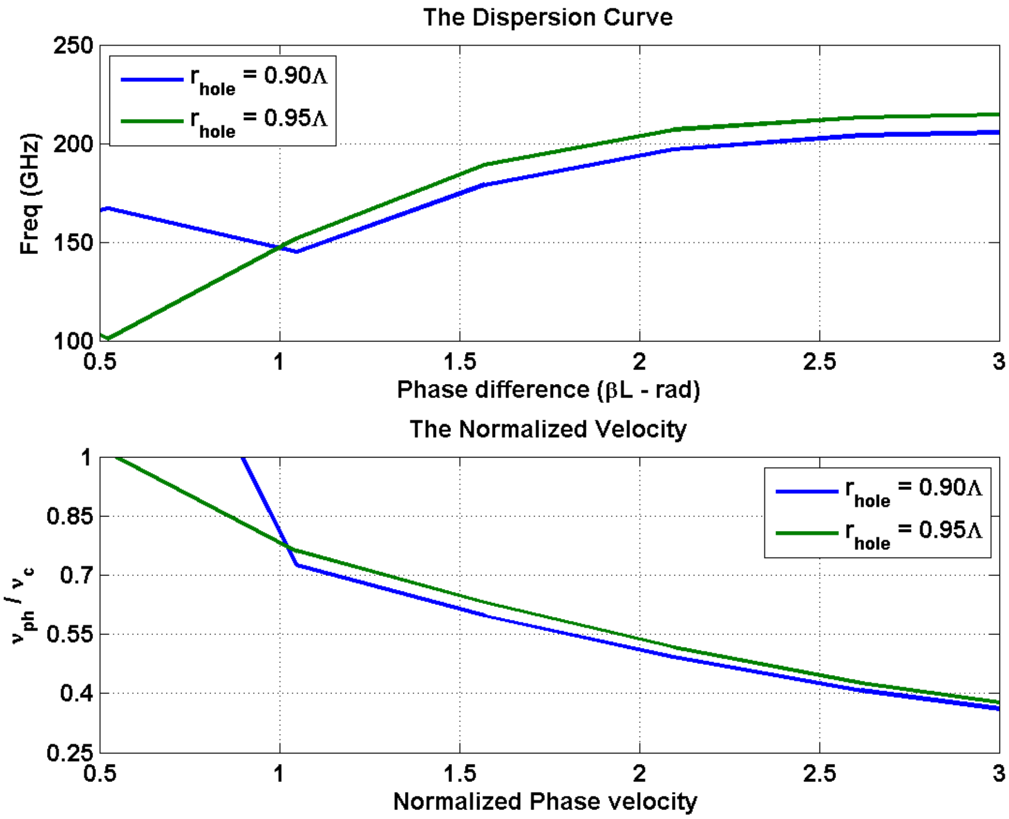

Figure 5-23 The dispersion curve and the corresponding phase velocity of the optimized r_{hole}

5.6.4.2.1 The FDTD/PIC Simulation of the Optimized Structure

In this part the results of the FDTD/PIC simulation of the optimized structure are presented. Using the same analysis described previous in *5.6 Analysis of the 200GHz BWO using the ADD-PC based*

SWS, the upper and lower limits of the beam currents was set to be 0.5mA and 5.0mA, respectively. Therefore, the electron beam operation point was set to be; electron beam current I_{beam} of 3.8mA, and beam accelerating voltage of 41KV (which equivalent to beam velocity of 0.40c).

5.6.4.2.1.1 The Field Simulation Results

The time domain sampled electric and magnetic field inside the first slow wave cavity (SW-1) is plotted in Figure 5-23(a) and (b), respectively. The corresponding FFT response of the time domain fields is shown in Figure 5-23(c) and (d). The frequency domain analysis indicates that both the electric and magnetic fields resonates at almost 199GHz which is very close to the required operating point.

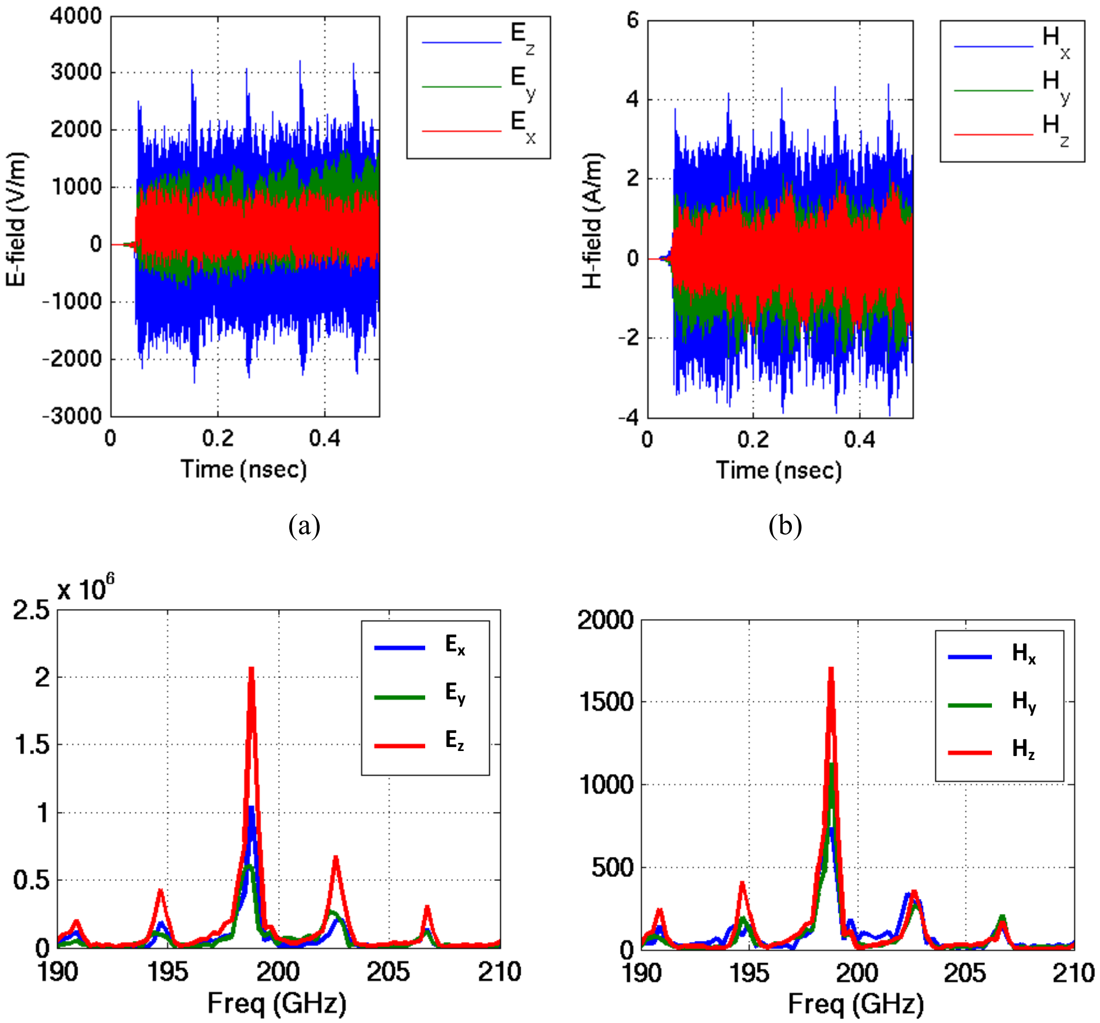

(a) (b)

(c) (d)

Figure 5-24 The time domain sampled (a) electric and (b) magnetic fields, and the corresponding FFT response of (c) electric and (d) magnetic fields

The power density figure, at 0.10Lz, is plotted in Figure Figure 5-25(a). The figure shows that the maximum power is located at the center of the structure. This is expected, since the electron beam travels through the center of the structure. Also, the figure shows that there is a significant amount of the power is located inside the slow wave cavities. The axial power distribution is plotted in Figure 5-25(b). Since the structure is a BWO, it is expected to have the maximum power at the input terminal of the structure. The figure shows that the structure could be able to deliver up-to 30dBm of power.

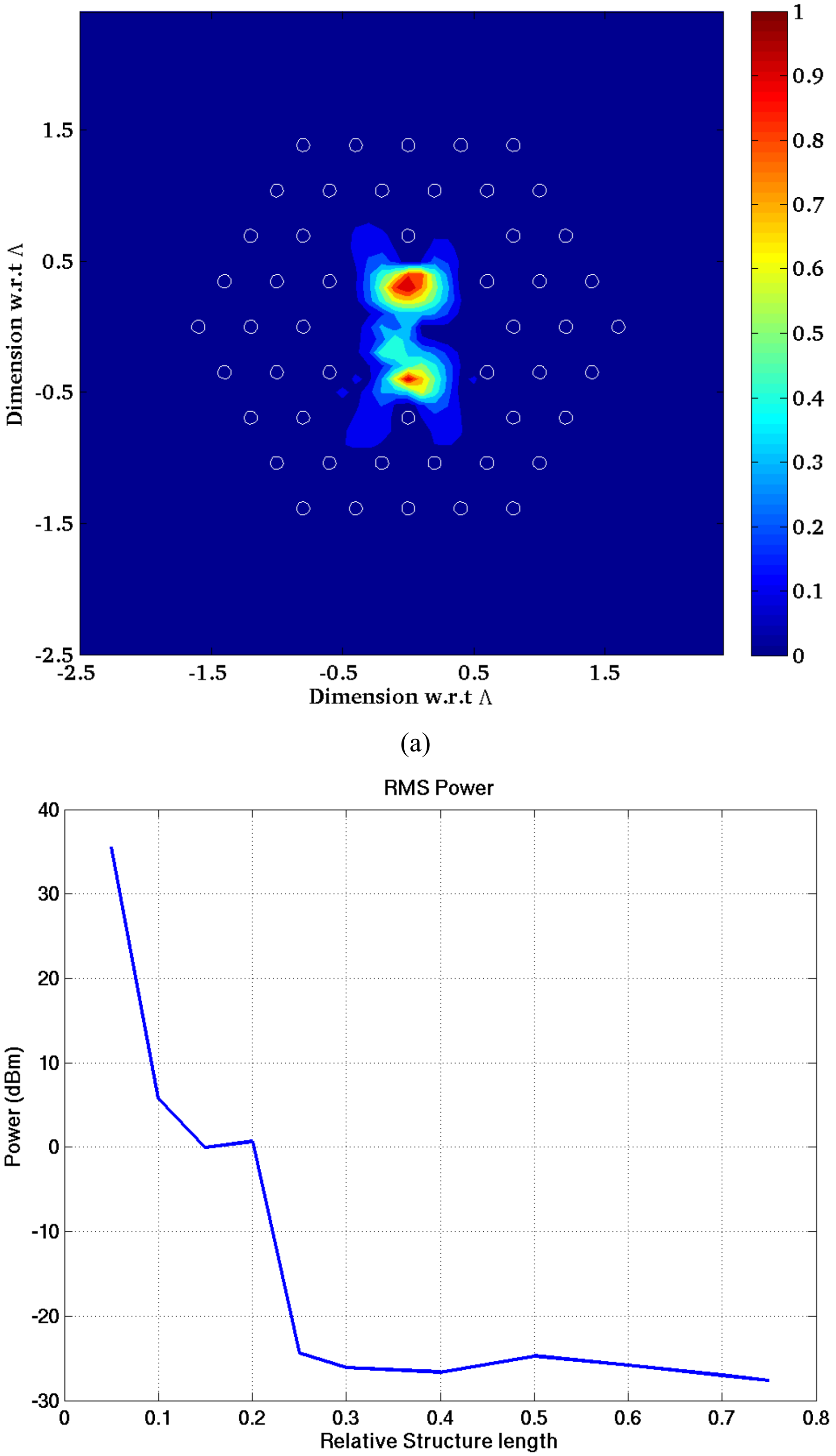

(a)

(b)

Figure 5-25 (a) The Power density distribution and (b) The Power distribution

5.7 Verification of the Modal Analysis of the ADD-PC Structure

In order to prove the existence of the slow mode in the ADD-PC structure proposed here, the resonant method is used to accurately re-calculate the dispersion curve [109-110]. As shown in the dispersion analysis *5.5.1.1 The Dispersion Curve Extraction,* the SWS supports both fast waves (the 0-mode is a normal waveguide mode), and slow wave mode (π-mode). Therefore, it is required to excite both modes. For exciting the waveguide mode, the axial probe is a common excitation method. Since the slow wave mode is located at the conducting walls and inside the SW-defects, it cannot be excited efficiently using the axial probe. Therefore, a probe-wheel radiator is used to excite these two modes together [110]. Figure 5-26(a) shows a schematic diagram of the probe-wheel radiator. The probe-wheel radiator consists of two parts; the wheel itself and an axial probe. The axial probe is used to launch the waveguide mode (TM_{01}-like mode), while the slow wave mode is excited using the wheel radiator.

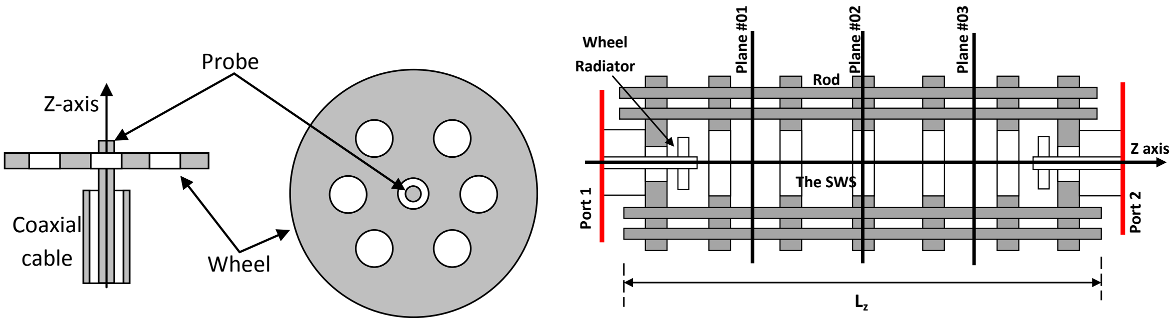

(a) (b)

Figure 5-26 The resonant method; Schematic of (a) The probe-wheel radiator and (b) The ADD-PC structure with the radiator

The wheel radiator consists of a conducting disk, with several axial symmetrical holes drilled inside it (Figure 5-26(a)). There are two main features of the wheel radiator; first due to its axial symmetry, it only excites axial symmetrical modes. Second, it only excites the azimuthal component of the magnetic field (H_φ). Since it is a metallic wheel, the tangential electric field equals zero, therefore both cylindrical axial electric field (E_z) and the driven radial electric field (E_r) component will be excited along with the associated azimuthal magnetic field (H_φ). Thus, the slow wave mode (TM-like), located at the conducting plates can be excited. This conjecture was verified by the HFSS simulation of the current distribution over the wheel radiator itself, shown in Figure 5-27. As expected, the current distribution is in the radial direction, which will only excite the azimuthal magnetic field (H_φ).

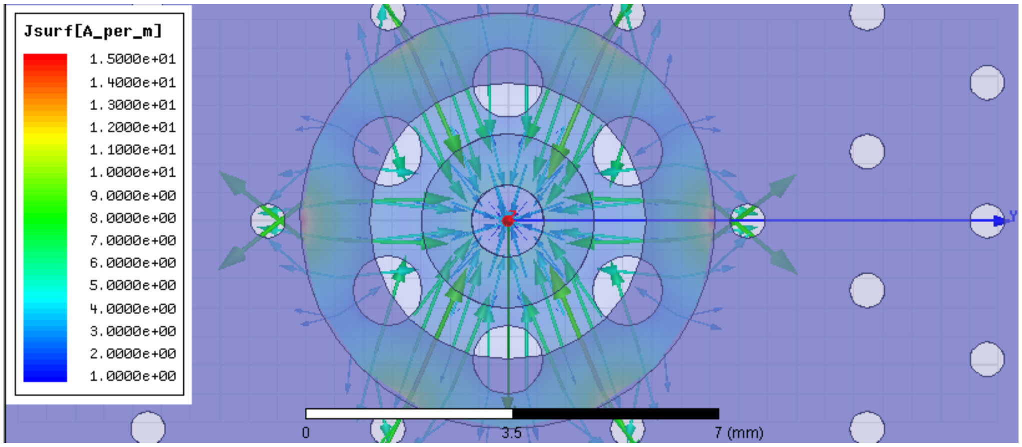

Figure 5-27: HFSS simulation of the current distribution on the wheel

To validate the existence of the slow wave mode, a scaled model of the proposed SWS was fabricated. The dispersion characteristic of the SWS was measured using the resonant method. The structure was fabricated using a 3D-printer, and then it was coated with a metallic conductive layer. A picture of the fabricated structure is shown in Figure 5-28(a), while a schematic of the Device Under Test (DUT) is shown in Figure 5-28(b). The DUT is a scaled model of the ADD-PC shown in Figure 5-9. In order to support the structure, an extra six thick rods were placed at the corners of the fabricated structure (Figure 5-28(b)).

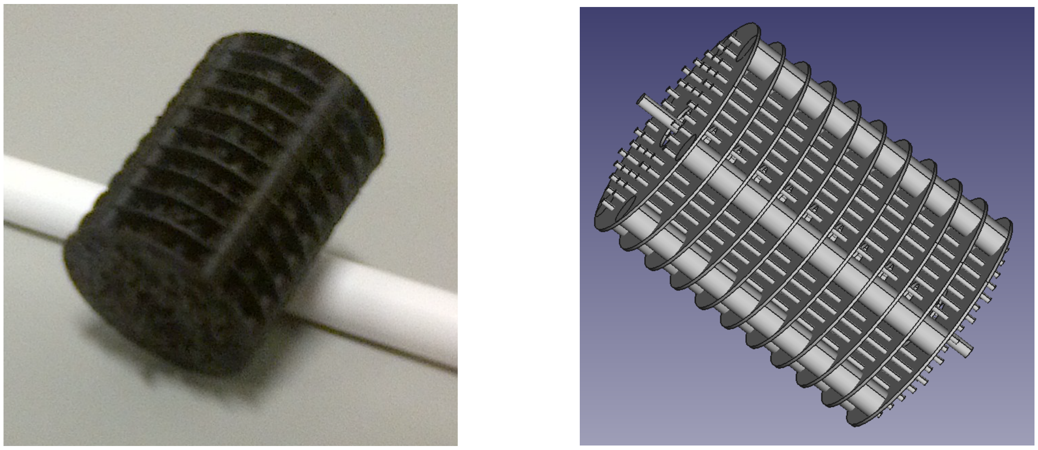

(a) (b)

Figure 5-28: (a) The scaled fabricated ADD-PC SWS, (b) Schematic of the ADD-PC

The return losses (S_{11}) and insertion losses (S_{12}) curve are plotted in Figure 5-29. The figure shows that there are four resonant frequencies –corresponding to π/5-mode, 2π/5-mode, 3π/5-mode and 4π/5-mode– are observed in both S_{11} (nulls) and S_{12} (peaks). These frequencies are corresponding to a phase shift "βL" of π/5, 2π/5, 3π/5 and 4π/5, respectively

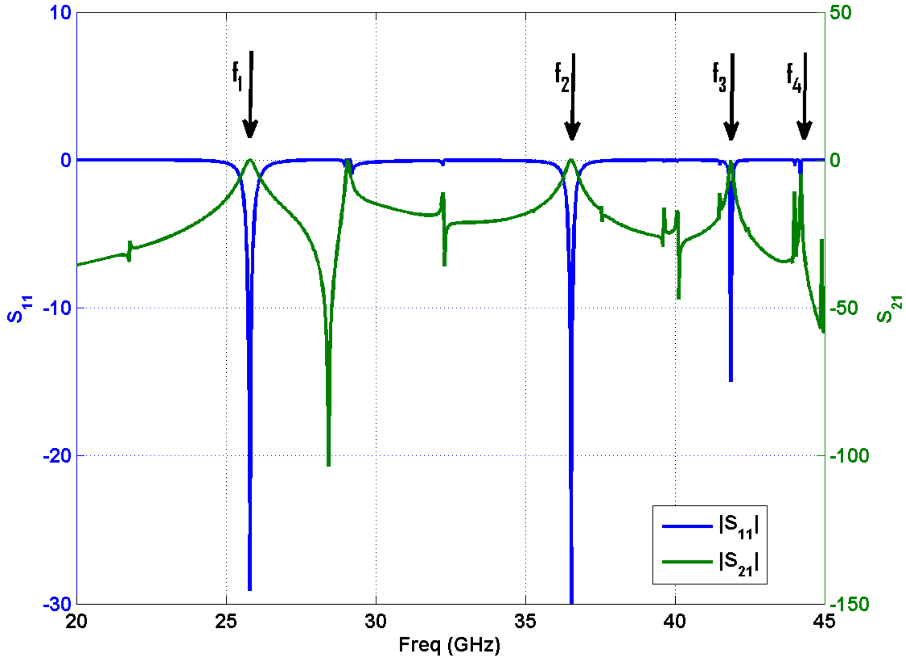

Figure 5-29 The S-parameters

A comparison between the HFSS resonance frequencies and the measures ones is plotted in Figure 5-30. The comparison indicates that there is a good correlation between the measures and HFSS resonance frequencies. Moreover, although the pure slow wave mode and waveguide mode couldn't be measures, the comparison indicates that as there is a good agreement between the calculated resonance frequency and the dispersion curve, thus verifies the successfully launching of both the slow wave mode and the fast wave mode.

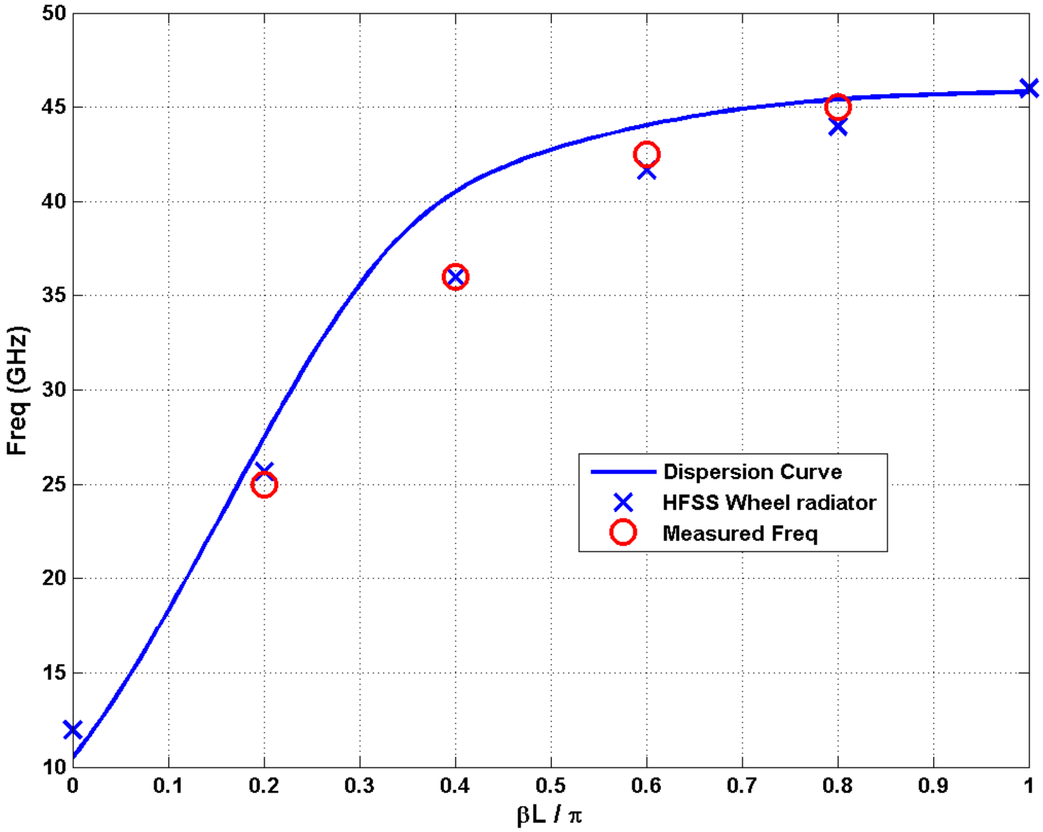

Figure 5-30 The dispersion curve of the scaled ADD-PC SWS, showing ccomparison between the measured and calculated resonance frequencies

5.8 Extend the operating frequency of the BWO

To show the potential of the proposed ADD-PC based SWS, It was used to design BWO operating at 650GHz. As it will be shown later, the realization/fabrication of the ADD-PC based SWS at this frequency is challenging. Due to the small dimensions of the SWS (at this frequency range) and the existence of the axial discontinuity, an accurate fabrication is required.

5.8.1 The ADD-PC based SWS

Starting from the band gap diagram, the geometrical parameters of the ADD-PC based SWS can be calculated (as done in *5.3.1 The Photonic Crystal Waveguide*). To accommodate the frequency drop due to numerical modelling, the geometrical parameters were selected to operate at 110% of the designed frequency (650GHz). A summary of the structural parameters are listed in Table 5-VI.

Parameter	Value
Rod Radius "r"	15 µm
Pitch Size "Λ"	100 µm
Period Length "L"	42 µm
Inner disk radius "R_{in}"	100 µm
Outer disk radius "R_{out}"	450 µm
Disk thickness "t"	14 µm

Table 5-VI The ADD-PC structure parameters

5.8.1.1 The Dispersion Analysis

Using the same approach presented in section *5.5.1.1 The Dispersion Curve Extraction*, the HFSS Floquet's mode analysis was used to calculate the dispersion curve. The extracted dispersion curve of the ADD-PC based SWS and the corresponding phase velocity (normalized with respect to the speed of the light in the vacuum) are plotted in Figure 5-31. The phase velocity curve indicates that the structure can support a slow wave mode of phase velocity as low as $0.20v_c$. Using an electron beam with a variable beam velocity, obtained by changing the beam acceleration voltage, a continuous tuning – over certain band of frequency – of the generated electromagnetic radiation can be achieved.

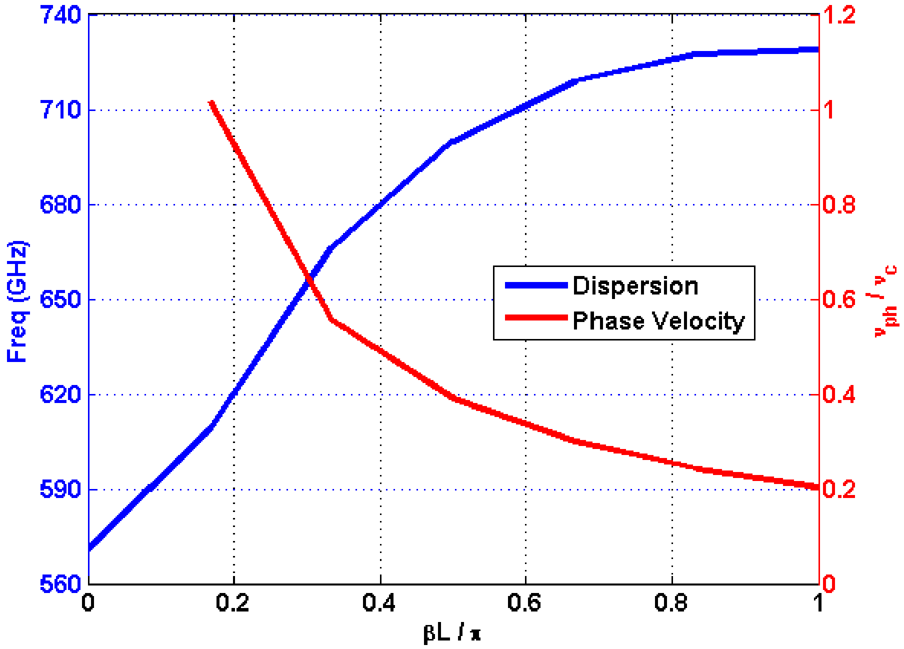

Figure 5-31 The dispersion curve and the corresponding normalized phase velocity

5.8.1.2 The Beam Interaction Impedance

To estimate the amount of energy that can transferred between the electron beam and the electromagnetic wave, the beam interaction impedance is introduced [32]. Following the same procedure explained in *5.5.2 The Beam Interaction Impedance*, the beam interaction impedance was calculated (Figure 5-32).

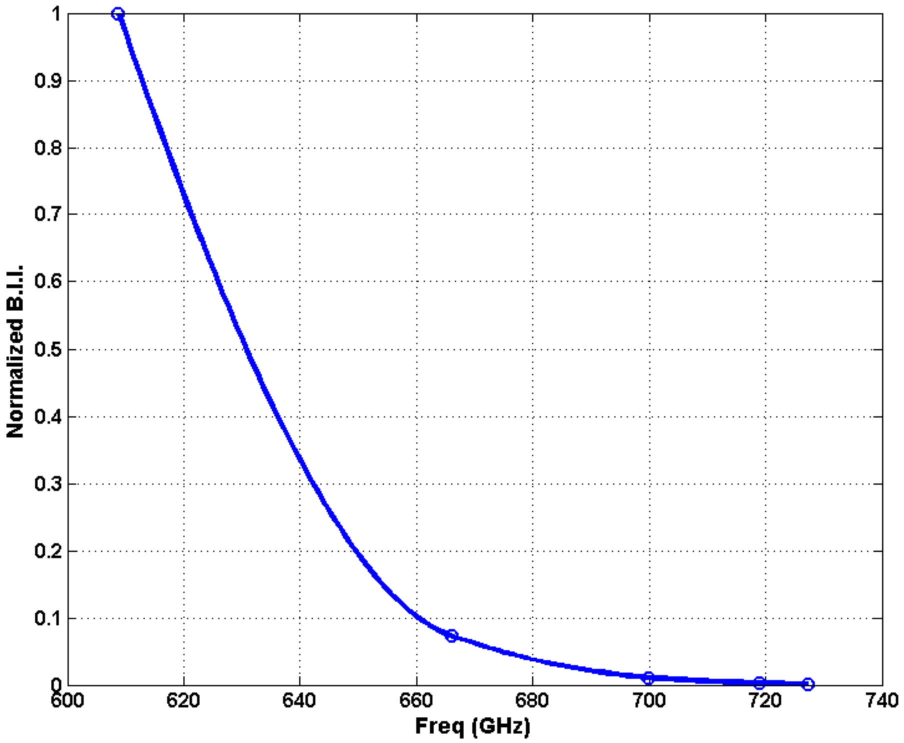

Figure 5-32 The normalized Beam Interaction Impedance

5.8.2 The BWO Performance

Using the FDTD/PIC CAD tool, the performance of a typical designed BWO will be investigated. In the simulation, all the metallic surfaces are considered to be flat and smooth, and made of highly conductive copper ($\sigma = 5.99\times10^{7}\Omega^{-1}.m^{-1}$). A summary of the BWO and electron beam parameters are listed in Table 5-VII.

Electron beam	Beam current	13.8 mA
	Beam Voltage	40.9 KV
	Beam radius	50 μm
	Number of particles	2840
	Electrons per particle	100
DC - B_z		1.5 T
FDTD window		113×113×60 cells Uniform cell, 14 μm side

Table 5-VII The BWO parameters

5.8.2.1 Electromagnetic Field Results

A typical time-zoomed view of the time sampled fields is presented in Figure 5-33. The transverse electric fields and magnetic fields are shown in Figure 5-33(a) and Figure 5-33(b) respectively, while the longitudinal fields are plotted in Figure 5-33(c). Although the fields have some noise, the figure shows the sinusoidal nature of the generated fields. Moreover, the figure indicates that both the transverse electric fields are in-phase while the transverse magnetic fields are out of phase; therefore the Poynting vector pointing in the z-direction always has a constructive summation. Furthermore, the longitudinal fields plot (Figure 5-33(c)) shows that the longitudinal electric field dominates the transverse ones, and the longitudinal magnetic fields is almost zero compared to the transverse ones, thus the mode is a TM-like mode (as expected from the modal analysis).

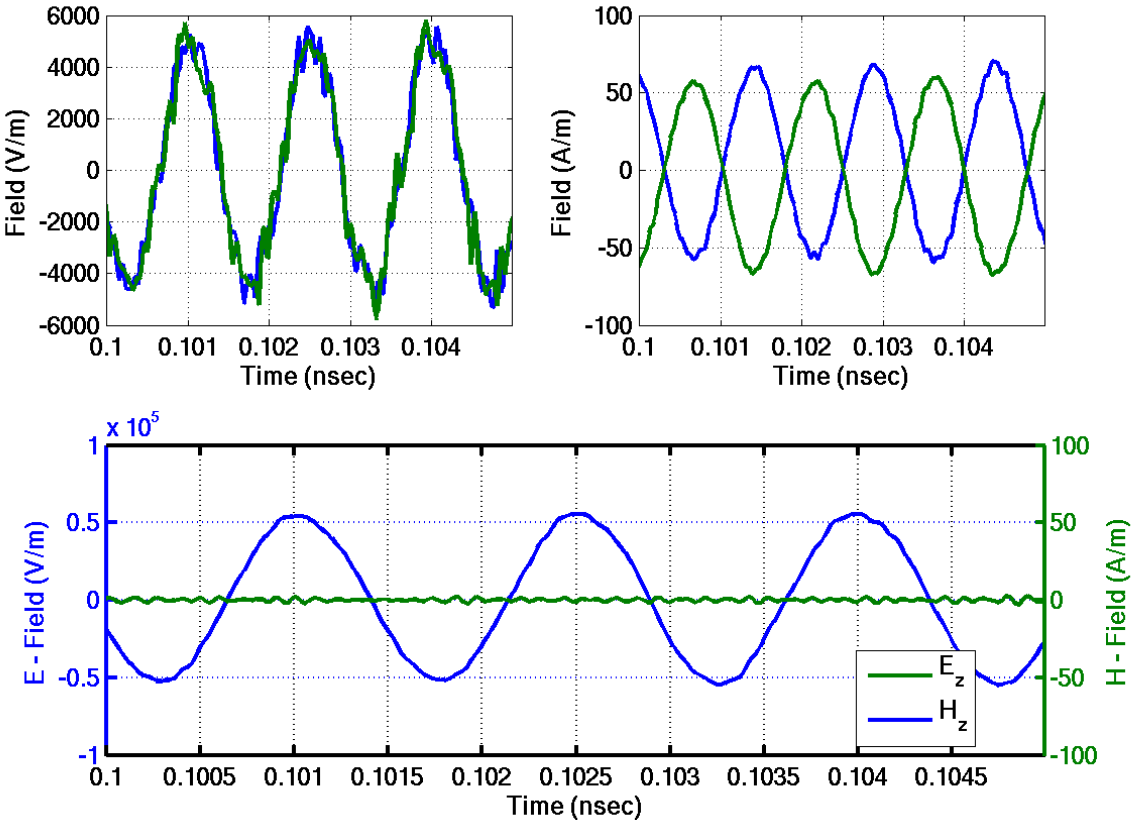

Figure 5-33 Time domain Field, (a) transverse electric fields, (b) transverse magnetic fields and (c) axial fields

A further verification of the field generation can be obtained from the frequency response of the time sampled fields. The FFT analysis of the time sampled transverse electric and magnetic fields in the second cavity (SW-2) is shown in Figure 5-34(a) and (b), respectively. The figure shows that both the eclectic and magnetic fields are resonating at the same frequency (670 GHz). Although it is not shown here, all the fields at the other SW-defects resonate at the same frequency. The shift between the HFSS resonance frequency predication and the FDTD results is mainly due to both numerical errors and the material used. In the FDTD analysis, the SWS consists of a highly conductive copper, while in the HFSS analysis the SWS was assumed to be a perfect conductor.

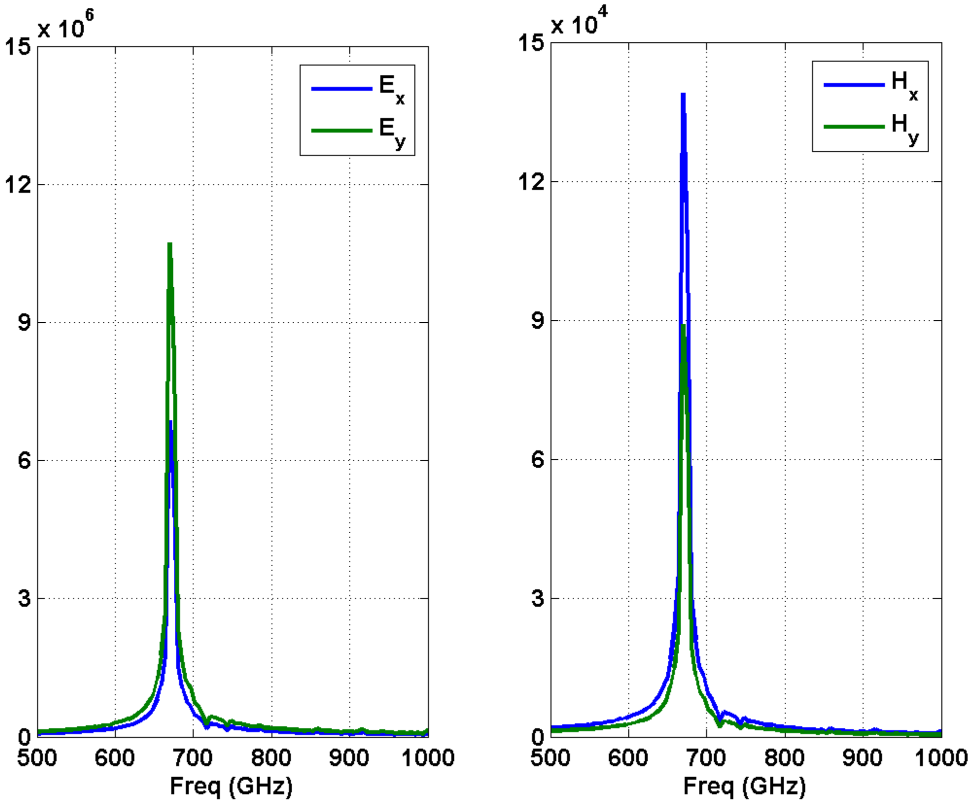

(a) (b)

Figure 5-34 Frequency domain Fields, transverse (a) electric and (b) magnetic fields

Using the Poynting theorem, the average electromagnetic power was calculated. A logarithmic scale of the cross sectional power density at $0.50L_z$, in the longitudinal (z-) direction, calculated at a frequency of 670 GHz is presented in Figure 5-35(a). The figure shows that maximum of the generated power is located at the central defect. Since the electron beam travels through the beam tunnel, it is expected to have a large amount of the power in the central defect. Moreover, the figure also shows that a significant amount of the generated power has been migrated to the slow wave defects.

A plot of the variation of the generated electromagnetic power in the axial direction is plotted in Figure 5-35(b). Since the proposed structure is a BWO, it is expected to have the maximum power at the electron gun end. Furthermore, the maximum generated power is almost 8W. Compared to the electron beam power, the overall conversion efficiency of the proposed BWO (efficiency = maximum generated power / electron beam power) is almost 1.8%.

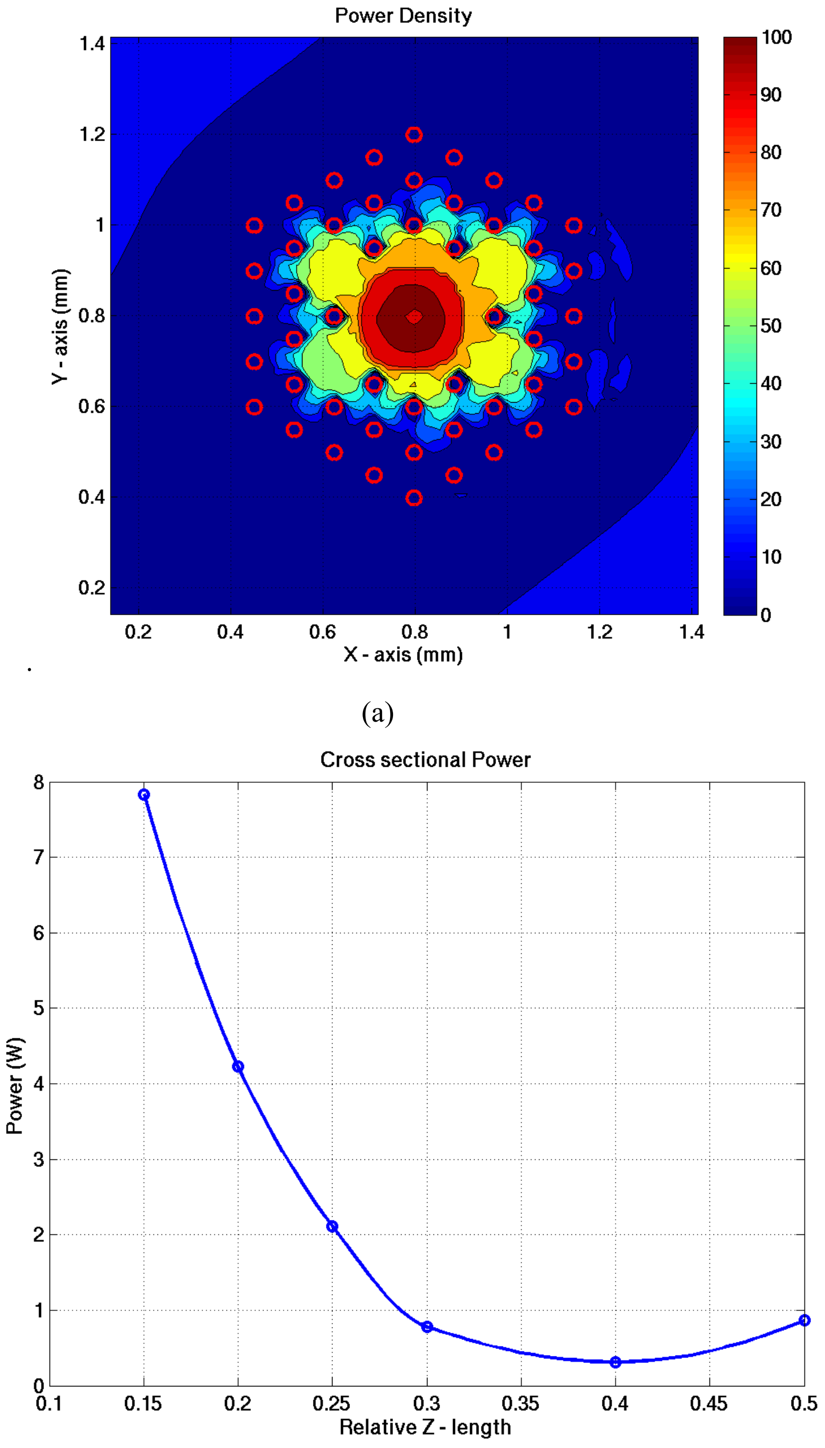

(a)

(b)

Figure 5-35 The generated power; (a) the power density (dB), and (b) the structure power

5.8.2.2 The Particle Analysis

The variation of the normalized z-component of the particle velocity, at the axis of the SWS, at two different time steps (at 0.03 nsec and 0.20 nsec) is plotted in Figure 5-36. Initially (at 0.03 nsec), the generated electromagnetic fields are weak. Thus, the electron beam-wave interaction and the particle velocity modulation are small (Figure 5-36(a)). While, at 0.20 nsec, the generated waves become more robust and the electron beam-wave interaction increases, hence the particle velocity modulation is heightened (Figure 5-36(b)). The physics of the particle dynamic can be explained from this figure. Initially, there is no electromagnetic wave generated, and the electron beam travels along in the SWS, and it initiates the electromagnetic wave excitation. As the generated wave gains strength, the beam-wave interaction becomes substantial, and some of the particles get trapped in the electric field of the electromagnetic fields (deceleration phase). As the electromagnetic wave reaches a saturation point, most of the particles are trapped and the particle velocity reaches a minimum. After that the particle moves from a deceleration phase to acceleration region, hence the electron velocity begins to increase again. Thus the energy is transferring between the electromagnetic fields and the particles [32].

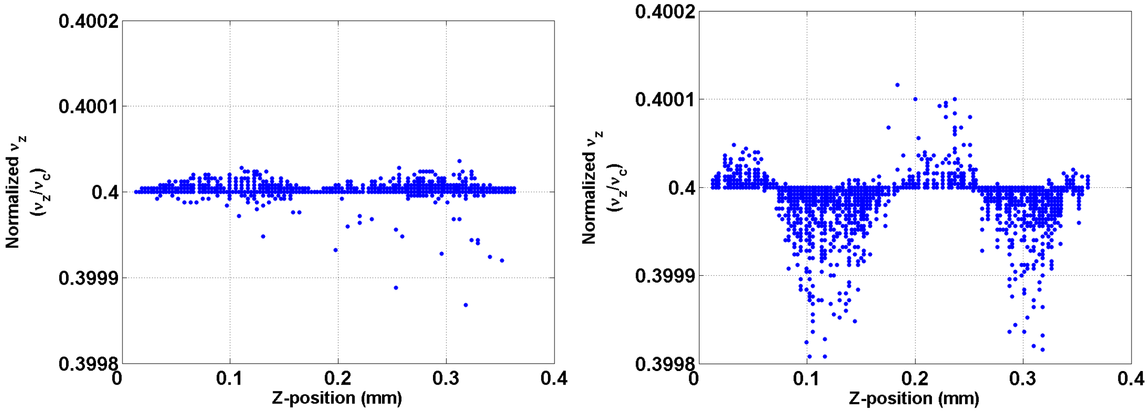

(a) (b)

Figure 5-36 Particle velocity at (a) 0.03nsec, and (b) 0.20 nsec

The phase space diagram and the Kinetic Energy (K.E. = $mv^2/2$, $v=\sqrt{v_x^2+v_y^2+v_z^2}$) variations are presented in Figure 5-37. The z-component of the particle velocity variation, normalized with respect to the speed of light in the vacuum, across the SWS length at the beginning of the time simulation and at the saturation is plotted in Figure 5-37(a) and (c), respectively. Initially the particles are entering the structure so they have not reached the end of the structure. Since initially the SWS is empty and the generated fields are weak at this stage, the beam-wave interaction is almost zero. This explains the constant electron beam velocity shown in Figure 5-37(a). While at the saturation case, there is a strong generated electromagnetic wave, thus the beam-wave interaction is maximized, and the particle velocity is modulated causing bunching (Figure 5-37(c)). Similar behavior was observed in the normalized K.E. ($K.E._{norm} = K.E. / K.E._{initial}$) as show in Figure 5-37(b) and Figure 5-37(d).

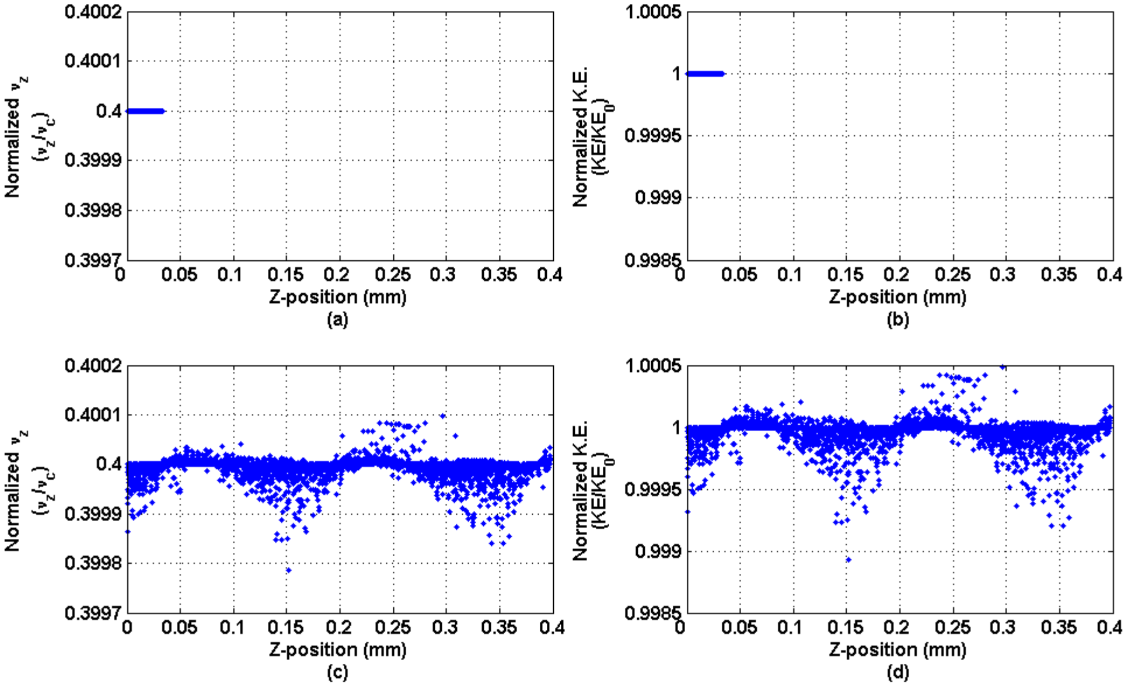

Figure 5-37 The phase space diagram, at (a) starting of the simulation and at (c) the saturation case, and the normalized K.E. at (b) starting of the simulation and at (d) the saturation case

5.9 Conclusion

Driven by the modern technology requirements, the operating frequency of the “electromagnetic devices” is extending toward sub-mm/THz regime. For several reasons, the generation of high power sub-mm/THz electromagnetic wave is always a problematic issue. A key objective of this work was to investigate and open the potential extensions of the VED approach for the source technology in this frequency regime. The choice of VED strategy (electron beam-wave interaction) is based on their impressive record of success at millimeter and microwave frequency range in the recent past. Since most of the VED parameters are determine by the SWS parameters, the design of a SWS operating at this frequency range is considered as the key stone part in this work.

To address this objective, both the DD-PC based SWS and the ADD-PC based SWS suitable for high power Cherenkov radiation-based VEDs were introduced and analyzed. While the DD-PC based SWS has no axial discontinuity, the high electron beam requirements limit its efficiency. On the other hand, while the ADD-PC based SWS has a lower electron beam requirements, it requires a complex fabrication technique.

To provide a comparison between these two SWSs, two BWOs operating at 200GHz were designed using both of them. While, the DD-PC based SWS was analyzed using the non-uniform FDFD method, the dispersion curve and modal analysis of the ADD-PC based SWS were carried-out using the HFSS Floquet's mode solver and the resonance method. The electron beam-wave interaction was performed using the FDTD/PIC simulation. The simulation result shows the potential of the ADD-PC based SWS as an efficient and a powerful source in sub-mm/THz band. Furthermore, another BWO operating at 650GHz was proposed using the ADD-PC based SWS. While, the realization of such device faces different challenges, the simulation results showed an excellent power and efficiency results.

Although the design and analysis of both the SWS and the BWO were discussed in details, other aspects need further investigation. For extracting the generated electromagnetic fields, special input/output ports are required. Although a preliminary coaxial cable was proposed (as will be shown in chapter 6 – *6.5 Extraction of the generated wave* –), further investigation is required to design optimum input/output ports. Furthermore for the BWO realization, although the electroforming technique – in which the whole structure is grown as a single unit and therefore the connection between the rods and the axial discontinuity can be ensured – is considered as the most promising fabrication technique for this type of structures, other fabrication techniques – such as; the 3D printing and the high precision micromachining – are considered as possible alternative fabrication methods.

Chapter 6

Summary and Conclusion

6.1 Summary

The main focus of this thesis was the design of a PC based SWS suitable for table-top and high power BWO operating in sub-mm/THz regime. A summary of the key objectives achieved are highlighted below:

- A full vectorial FDFD method was implemented. The FDFD method can investigate both dielectric and conductor structure. Using a primitive adaptive (multi-level) meshing, the FDFD method can determine the propagating modes properties both efficiently and accurately. The accuracy of the FDFD method was tested and verified via different examples.
- A simple outline of the physics of the surface wave propagation over a conducting rod, which is considered as the building block of the proposed DD-PC based SWS, is introduced.
- The proposed FDFD method is used to analyze a novel DD-PC based SWS. In order to verify the existence of the slow wave mode, further study of the structure was performed using both the FDTD and HFSS code. Both methods prove the existence of the slow wave mode at the defined frequency.
- A custom FDTD/PIC CAD tool was developed to analyze the performance and the physics of the THz radiation. Both 2D and 3D versions of the FDTD/PIC simulation were first implemented, and then a more efficient multithread 3D version of the code was realized using the OpenMP.
- The FDTD/PIC tool was used to investigate the performance of a BWO – designed using the DD-PC based SWS – operating at 130GHz. The investigation includes the generated electromagnetic field, the average generated power and the electron beam physical parameters. Also, the effect of changing the applied magnetic flux and the electron beam current on the performance of the BWO was conducted.

- To reduce the electron beam requirements and enhance the efficiency of the BWO, the Axial loaded Double Defected PC (ADD-PC) SWS was introduced. Both the ADD-PC based SWS and the DD-PC based SWS were used to design BWO operating at 200GHz.
- The design of a BWO operating at 650GHz was performed using the ADD-PC based SWS. The simulation results showed a power conversion efficiency of 1.8%. Due to the small dimensions and the geometry of the SWS, the fabrication and assembly of the BWO is complicated at present.
- Several scaled prototypes were fabricated and tested. Two main techniques were used in the fabrication; the CNC machinery and the 3D printing technology. Using the CNC machining a full cupper metallic structure was fabricated. Using the 3D printer, the ADD-PC structure was realized. Then, using the conductive coating, a metallization layer was added to the structure.

6.2 Ongoing Work

Along with the presented work here, the following work is still on-going:

- Using the CNC machining, along with the vacuum enclosure technology, another prototype of the cold structure is currently under fabrication.
- With collaboration with another colleague, the fabrication and the testing of the Field Emitting Array (FEA) is currently under development.
- Other fabrication technology, such as the electroforming technique –in which all the structure parts are grown together as a single component or simply an 3D printing using copper material–, is considered as an efficient and accurate manufacturing technique that can be used to realize the proposed SWS. This fabrication technique is provided from Custom Microwave Inc. [117]
- The last on-going part in this project is the assembly of the SWS, the FEA, and the supporting parts inside a vacuum media.

6.3 Future Work

At this point, we have found some areas that are worth further investigation:

- Design and implement a wave absorber at the end of the BWO to prevent the forward wave from propagation through the structure. Thus, the generated THz radiation power can be enhanced and noise level can be significantly reduced.
- It was found that the FDTD/PIC simulation was very expensive in terms of computational resources (time and memory). Since, the computational memory required for FDTD is not as critical as the computational time. A parallel implementation of the FDTD/PIC will reduce the computational time required for the FDTD/PIC simulation.
    - The first step towards parallelization is to implement the code in a multi-threading scheme. Using this approach a speed up factor of $\approx n$ (where n is the number of the available processors) can be achieved.
    - Moreover, using an efficient scheme to implement the FDTD/PIC on a Graphical Processing Unit (GPU) should provide further reduction in the simulation time.
- Using both HFSS and the FDTD/PIC CAD tools, a more extensive optimization can be performed.

6.4 Parallel Implementation of the FDTD/PIC

Another ongoing project here is the realization of the parallel FDTD/PIC algorithm. In order to show the speed-up gained from the parallelization, a comparison between the parallel FDTD/PIC and the sequential FDTD/PIC is provided.

In a conventional FDTD, the field components are updated sequentially. In every time step, all field components are updated. Then the particles physical parameters (position, velocity and acceleration) are recalculated. After that, the equivalent particle current components are computed. Instead of calculate each field component in a single processer, a speed gain can be obtained by dividing the problem over multiple processors (Figure 6-1) [118-120].

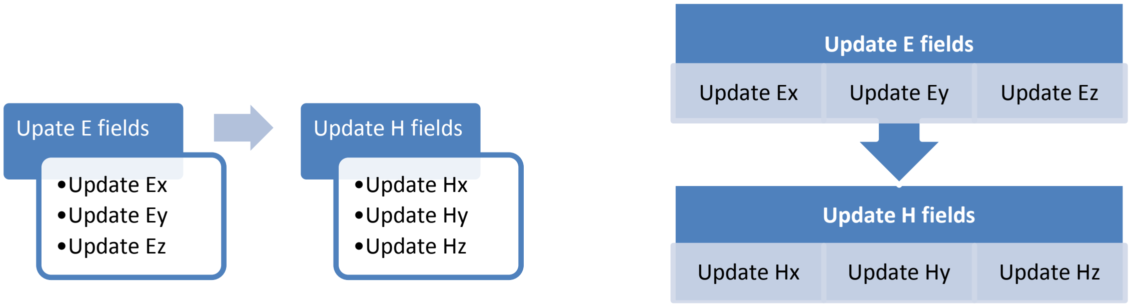

(a) (b)

Figure 6-1 The Time loop, (a) sequential and (b) parallel FDTD

A schematic diagram of the OpenMP implementation of the FDTD/PIC is shown in Figure 6-2. As indicated previously, the FDTD/PIC was implemented in three main steps; FDTD/PIC initialization, the time loop and the post processing. First, initial tasks such as the initialization of the field/particle matrices, define the update matrices and discretization of the computational window are completed.

In each time step the following tasks are preformed; the parallel magnetic field calculation is performed, particles physical parameters are defined, the associated current densities are calculated, parallel electric field updated occurred, and finally a snapshot of the sampled electromagnetic fields and particles parameters are saved to external files.

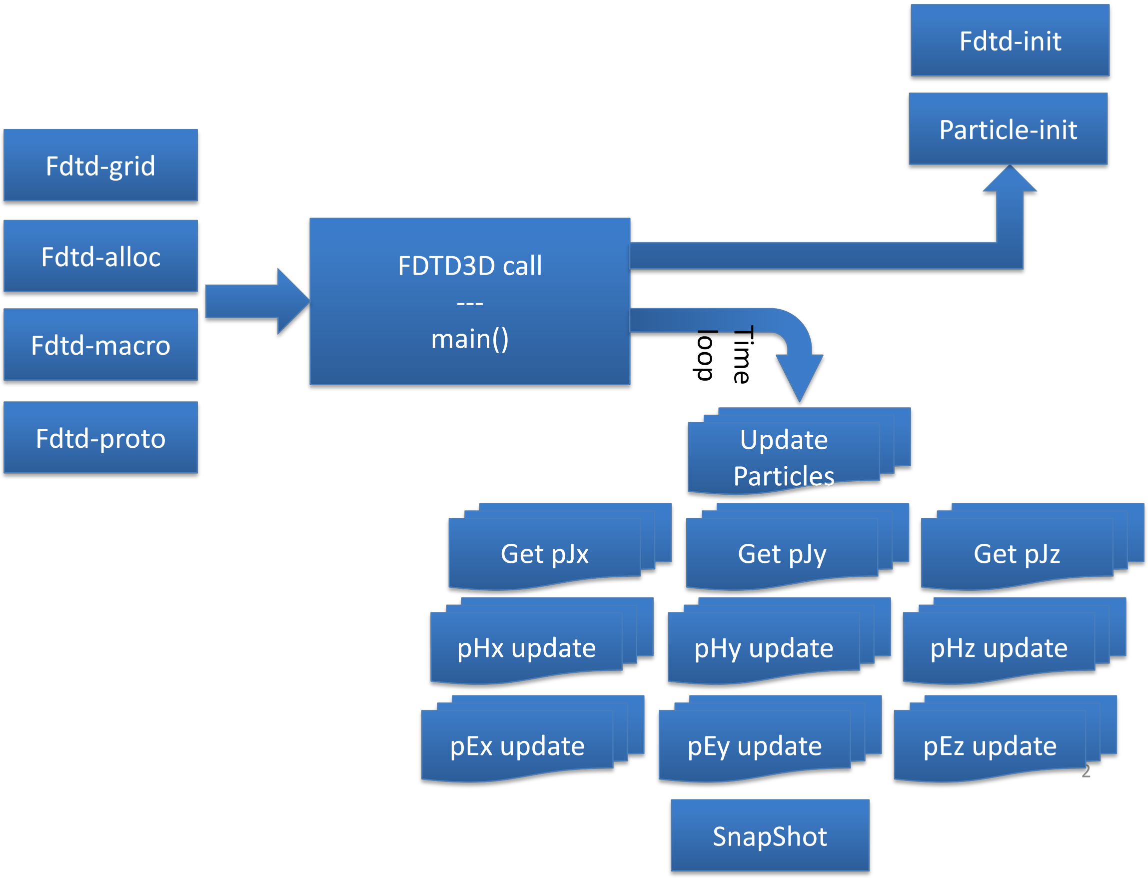

Figure 6-2 The Parallel implementation of the FDTD/PIC

Using the previous schematic, the parallel FDTD/PIC CAD tool can be realized. Other topics such as spaced discretization and GPU implementation need further analysis.

6.5 Extraction of the generated wave

To extract the generated electromagnetic fields, a coaxial cable was added at the point of maximum generated power. Since the structure is a BWO, the extraction point was placed at the electron beam entrance port. The coaxial transmission line was implemented in the main FDTD using the thin wire model [121-123]. Using Faraday's law the current was extracted at the output coaxial cable. The coaxial cable placed, such that the inner conductor is placed inside the first slow wave defect, and the outer conductor placed on the rods. The coaxial cable was terminated with Perfectly Matched Layer (PML) boundary conditions to simulate a matched absorbing load.

6.5.1 The Coaxial Cable Model

The field extraction/excitation is performed using a simple coaxial cable model, which was configured in the FDTD code using the thin wire model [121-123]. The thin wire approach is used to handle the fields around the inner wire inserted into the FDTD structure. Assuming the wire is a perfect conductor, and its radius is smaller than half the cell size ($r_{in} < \frac{dx}{2}$), the electric field inside the wire equals zero, and the integral Maxwell's equations are used to analyze the fields.

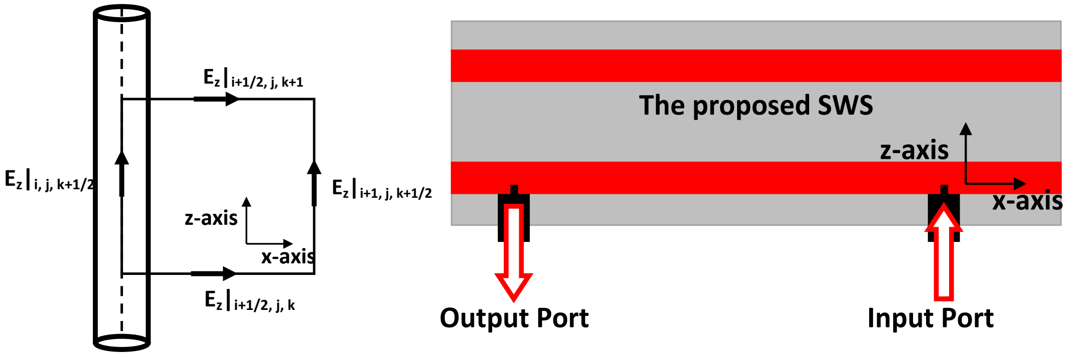

(a) (b)

Figure 6-3 (a) The FDTD thin wire model and (b) a schematic diagram of the proposed BWO with the coaxial cable model

Starting from Ampere's law and Faraday's law:

$$\int_{S_d} \frac{\partial}{\partial t}\left(\varepsilon\vec{E}\right).d\vec{S}_d = \oint_{C_d} H.d\vec{l}_d \qquad (6\text{-}1a)$$

$$-\int_{S_p} \frac{\partial}{\partial t}\left(\mu\vec{H}\right).d\vec{S}_p = \oint_{C_p} \vec{E}.d\vec{l}_p \qquad (6\text{-}1b)$$

where "S_d" is the dual grid cell facet bounded by contour "C_d" formed by dual-grid cell edges and "S_p" is the primary grid cell facet bounded by contour "C_p" formed by primary grid cell edges.

Using the thin wire model, the FDTD/PIC discretization equation can be updated. For example, the x-component of Faraday law can re-write as:

$$\mu\int\frac{\partial \boldsymbol{H}_y}{\partial \boldsymbol{t}}\boldsymbol{dS} = -\int \boldsymbol{E.dl} \qquad (6\text{-}2)$$

Then by applying the discretization, the update equation of the H_y field component becomes:

$$H_y\Big|^{n+1/2}_{i+1/2,j,k+1/2} = H_y\Big|^{n-1/2}_{i+1/2,j,k+1/2} + \frac{\Delta t}{\mu}\left(-\frac{E_x|^{n}_{i+1/2,j,k} - E_x|^{n}_{i+1/2,j,k+1}}{\Delta z} - \frac{E_z|^{n}_{i+1,j,k+1/2} - E_z|^{n}_{i,j,k+1/2}}{\Delta x}\right)$$

(6-3)

Since the thin wire is located at the grid *(i+1, j, k+½)*, and assuming the coaxial cable consists of a perfect conducting material, then H_y –on grid *(i+½, j, k+½)* – becomes:

$$H_y\Big|^{n+1/2}_{i+1/2,j,k+1/2} = H_y\Big|^{n-1/2}_{i+1/2,j,k+1/2} + \frac{\Delta t}{\mu}\left(-\frac{E_x|^{n}_{i+1/2,j,k} - E_x|^{n}_{i+1/2,j,k+1}}{\Delta z} + \frac{E_z|^{n}_{i,j,k+1/2}}{\Delta x}\right)$$

(6-4)

On the other side –on grid *(i+3/2, j, k+½)* – of the thin wire H_y becomes:

$$H_y\Big|^{n+1/2}_{i+3/2,j,k+1/2} = H_y\Big|^{n-1/2}_{i+3/2,j,k+1/2} + \frac{\Delta t}{\mu}\left(-\frac{E_x|^{n}_{i+3/2,j,k} - E_x|^{n}_{i+3/2,j,k+1}}{\Delta z} - \frac{E_z|^{n}_{i+2,j,k+1/2}}{\Delta x}\right)$$

(6-5)

6.5.2 The Amplifier Analysis

In this section, the DD-PC based SWS, is used as an amplifier. Therefore, two coaxial cables were added to the SWS, as shown in schematic diagram presented in Figure 6-3(b). As the figure shows, the input signal is placed at next to the electron beam exit end, while the output signal was extracted at a point next to the electron beam entrance point. In the input, a ramped modulated Gaussian signal was used as an input. The signal has a center frequency of 150GHz. Figure 6-4 shows the input signal in both time and frequency domains.

$$\boldsymbol{V_{input}} = \begin{cases} \mathbf{sin}(\boldsymbol{\omega t})\,.\,\boldsymbol{e}^{-0.5(\frac{t_0-t}{\tau})^2} & \boldsymbol{t < t_0} \\ \mathbf{sin}(\boldsymbol{\omega t}) & \boldsymbol{t > t_0} \end{cases} \qquad (6\text{-}6)$$

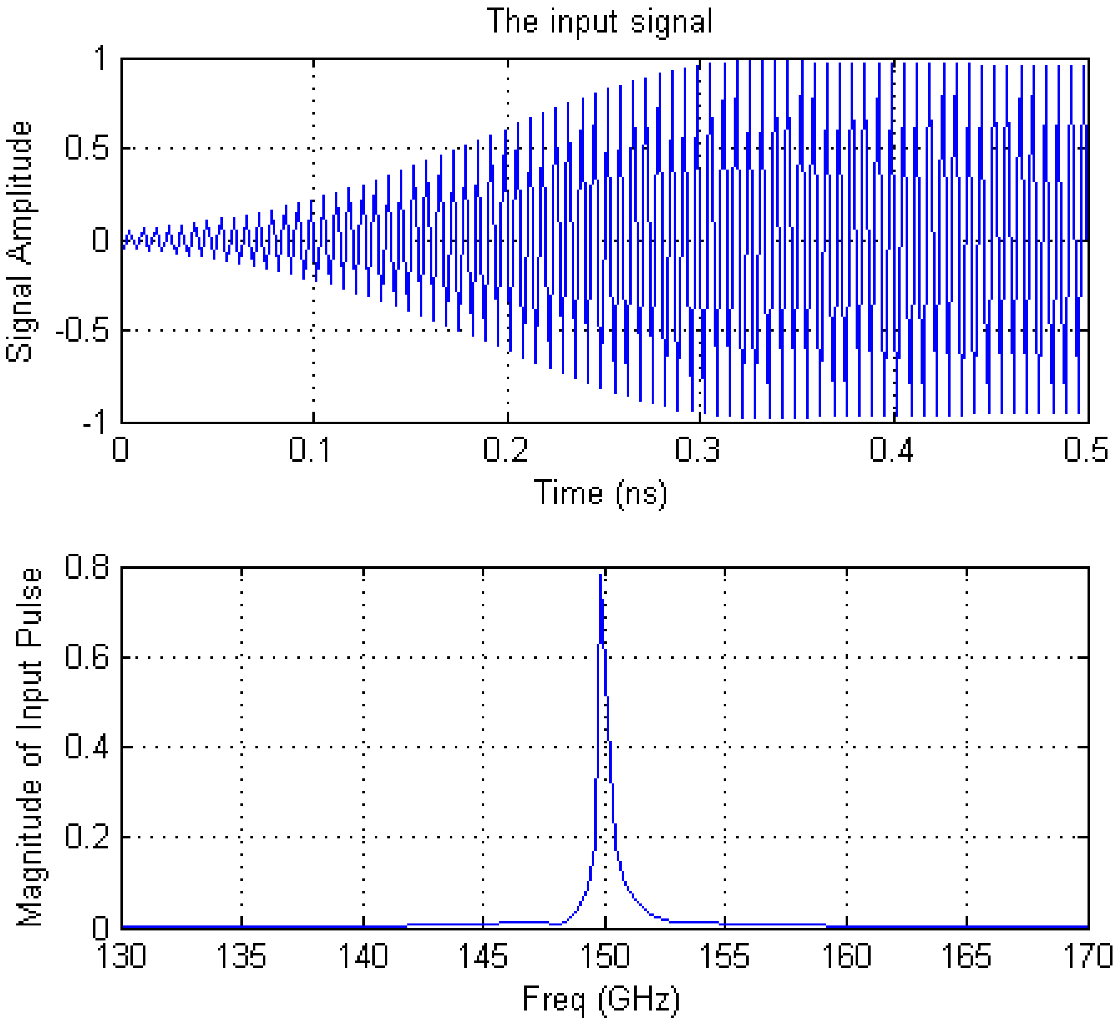

Figure 6-4: The input signal in (upper) time-domain and (lower) the frequency domain

Figure 6-5 shows the voltage and current signals, in both time and frequency domains, captured at the extraction coaxial cable. The frequency domain analysis shows that both the voltage and current signals oscillates at the center frequency of 150GHz. Also, the time domain voltage signal has a span variation between +10μV and -10μV, and the time domain current signal varies between ±3A.

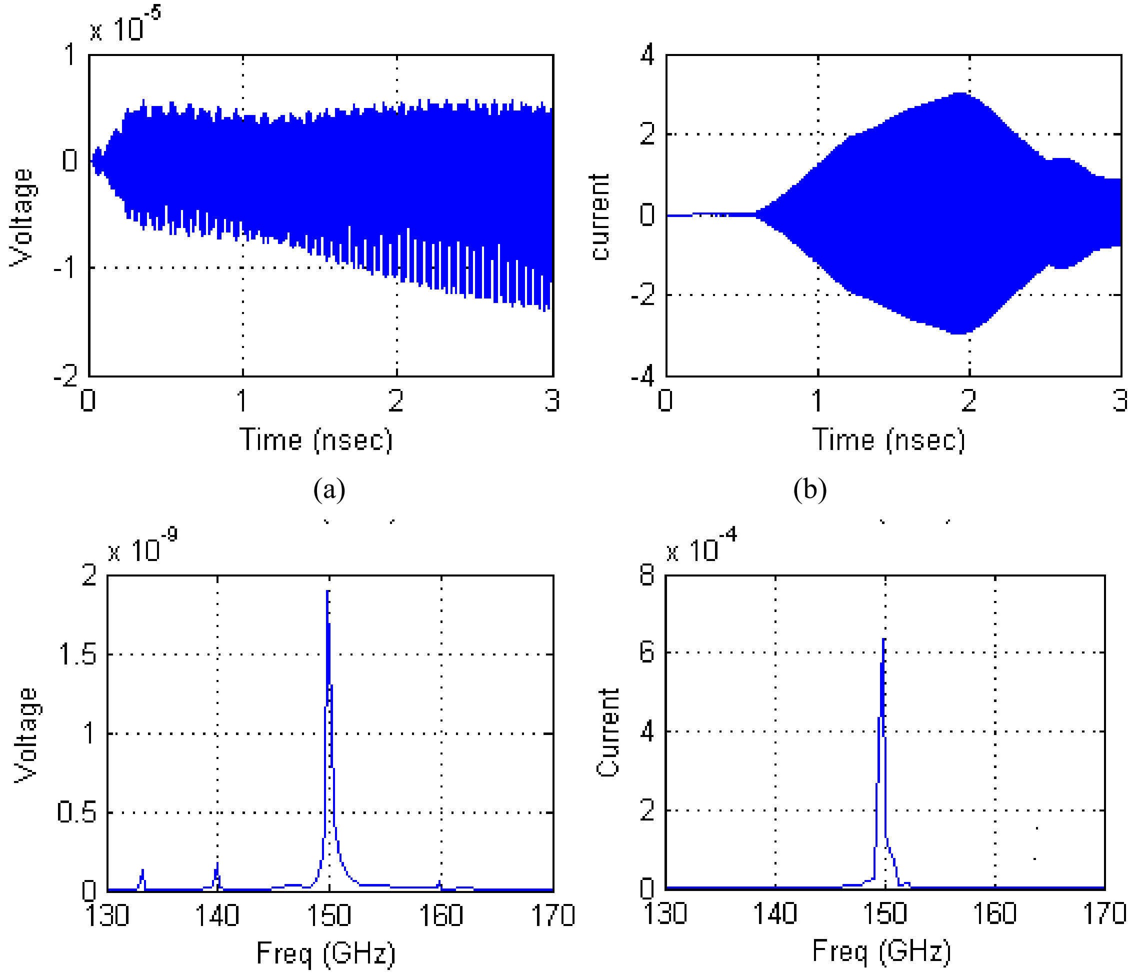

(a) (b)

(c) (d)

Figure 6-5 The extracted voltage wave in (a) Time domain and (c) frequency domain; and current wave in (b) Time domain and (d) frequency domain.

Appendix A
The Finite Difference Frequency Domain (FDFD) method

In this appendix, the formulation of non-uniform FDFD method will be described in details. Starting from Maxwell equation, a derivation of eigenvalue problem will be presented. As it will be shown, there are two eigenvalue problems. For the transverse electric field (E_x and E_y), a *P*-based eigenvalue problem was established, while for the transverse magnetic field (H_x and H_y) a *Q*-based eigenvalue problem was introduced.

A. 1. Formulation

Starting from Maxwell's equations

$$\boldsymbol{\nabla} \times \boldsymbol{E} = -\frac{\boldsymbol{\partial B}}{\boldsymbol{\partial t}} \tag{A1.a}$$

$$\boldsymbol{\nabla} \times \boldsymbol{H} = \frac{\boldsymbol{\partial D}}{\boldsymbol{\partial t}} \tag{A1.b}$$

Assume that all fields propagate in the axial (z-) direction, and all the field component has a variation with time and propagation direction in the form of $e^{j(\omega t-\beta z)}$. Where ω represents the angular frequency and β is phase constant. Then Maxwell equations become:

$$\nabla \times E = -j\omega B \tag{A 2.a}$$

$$\nabla \times H = -j\omega D \tag{A2.b}$$

After scaling electric field by free space impedance ($Z_0 = \sqrt{\mu_0 \epsilon_0}$), the Maxwell's equation in the component form can be expressed as:

$$jk_0 H_x = \frac{\partial E_z}{\partial y} - j\beta E_y \tag{A3.a}$$

$$jk_0 H_y = -\frac{\partial E_z}{\partial x} + j\beta E_x \tag{A3.b}$$

$$jk_0 H_z = \frac{\partial E_y}{\partial x} - \frac{\partial E_x}{\partial y} \tag{A3.c}$$

and,

$$-jk_0 \epsilon_r E_x = \frac{\partial H_z}{\partial y} - j\beta H_y \tag{A4.a}$$

$$-jk_0 \epsilon_r E_y = -\frac{\partial E_z}{\partial x} + j\beta H_x \tag{A4.b}$$

$$jk_0 \epsilon_r E_z = \frac{\partial H_y}{\partial x} - \frac{\partial H_x}{\partial y} \tag{A4.c}$$

The above equations were applied to 2D Yee discretization, shown in Figure A-1, to get;

$$jk_0 H_x(i,j) = \frac{E_z(i,j+1)-E_z(i,j)}{\Delta y} - j\beta E_y(i,j) \qquad \text{(A5.a)}$$

$$jk_0 H_y(i,j) = -\frac{E_z(i+1,j)-E_z(i,j)}{\Delta x} + j\beta E_x(i,j) \qquad \text{(A5.b)}$$

$$jk_0 H_z(i,j) = \frac{E_y(i+1,j)-E_y(i,j)}{\Delta x} - \frac{E_x(i,j+1)-E_x(i,j)}{\Delta y} \qquad \text{(A5.c)}$$

and,

$$-jk_0 \epsilon_{rx}(i,j) E_x(i,j) = \frac{H_z(i,j+1)-H_z(i,j)}{\Delta y} - j\beta H_y(i,j) \qquad \text{(A6.a)}$$

$$-jk_0 \epsilon_{ry}(i,j) E_y(i,j) = -\frac{H_z(i+1,j)-H_z(i,j)}{\Delta x} + j\beta H_x(i,j) \qquad \text{(A6.b)}$$

$$-jk_0 \epsilon_{rz}(i,j) E_z(i,j) = \frac{H_y(i+1,j)-H_y(i,j)}{\Delta x} - \frac{H_x(i,j+1)-H_x(i,j)}{\Delta y} \qquad \text{(A6.c)}$$

where,

$$\epsilon_{rx}(i,j) = \frac{\epsilon_r(i,j)+\epsilon_r(i,j-1)}{2} \qquad \text{(A7.a)}$$

$$\epsilon_{ry}(i,j) = \frac{\epsilon_r(i,j)+\epsilon_r(i-1,j)}{2} \qquad \text{(A7.b)}$$

$$\epsilon_{rz}(i,j) = \frac{\epsilon_r(i,j)+\epsilon_r(i-1,j)+\epsilon_r(i,j-1)+\epsilon_r(i-1,j-1)}{4} \qquad \text{(A7.c)}$$

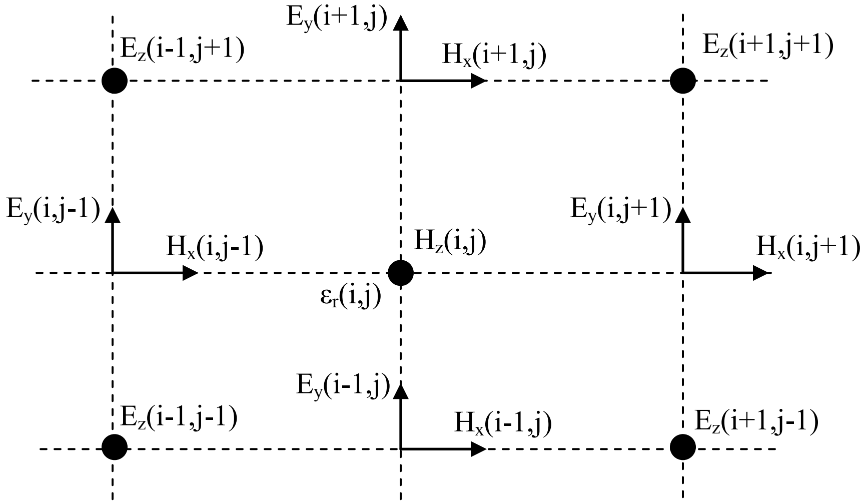

Figure A-1, 2-D Yee mesh based

By applying the above equations (Equation A5 and Equation A6) to every point in the mesh grid, a system of linear equations can be formed in terms of the unknown field profile and the phase constant. These equations can be expressed in matrix form as:

$$jk_0[H_x] = [A_y][E_z] - j\beta[E_y] \tag{A8.a}$$

$$jk_0[H_y] = -[A_x][E_z] + j\beta[E_x] \tag{A8.b}$$

$$jk_0[H_z] = [B_x][E_y] - [B_y][E_x] \tag{A8.c}$$

and,

$$-jk_0[\epsilon_{rx}][E_x] = [C_y][H_z] - j\beta[H_y] \tag{A9.a}$$

$$-jk_0[\epsilon_{ry}][E_y] = -[C_x][H_z] + j\beta[H_x] \tag{A9.b}$$

$$-jk_0[\epsilon_{rz}][E_z] = [D_x][H_y] - [D_y][H_x] \tag{A9.c}$$

Where A_x, A_y, B_x, B_y, C_x, C_y, D_x, and D_y are coefficient matrices. These matrices depend on the discretization distance, material constants and the applied boundary conditions. It was found that these matrices are sparse matrices.

A. 2. Derivation of eigenvalue problem

The derivation of the eigenvalue problem is performed by converting the above system of equations, Equation A8 and A9, to two equations. This procedure is performed in the following steps. First, get the axial field components (E_z and H_z) and substitute in the above equations. For example, The E_z and H_z can be obtained from (A8.c) and (A9.c) as;

$$[H_z] = \frac{1}{jk_0}[B_x][E_y] - \frac{1}{jk_0}[B_y][E_x] \tag{A10.a}$$

$$[E_z] = \frac{1}{-jk_0}[\epsilon_{rz}]^{-1}[D_x][H_y] + \frac{1}{jk_0}[\epsilon_{rz}]^{-1}[D_y][H_x] \tag{A10.b}$$

Then, Substitute in (A7.a) to get;

$$jk_0[H_x] = [A_y]\left(\frac{1}{-jk_0}[\epsilon_{rz}]^{-1}[D_x][H_y] + \frac{1}{jk_0}[\epsilon_{rz}]^{-1}[D_y][H_x]\right) - j\beta[E_y]$$

$$\left(jk_0 - \frac{1}{jk_0}[A_y][\epsilon_{rz}]^{-1}[D_y]\right)[H_x] = \frac{1}{-jk_0}[A_y][\epsilon_{rz}]^{-1}[D_x][H_y] - j\beta[E_y]$$

$$j\beta[E_y] = \frac{1}{-jk_0}[A_y][\epsilon_{rz}]^{-1}[D_x][H_y] - \left(jk_0 - \frac{1}{jk_0}[A_y][\epsilon_{rz}]^{-1}[D_y]\right)[H_x]$$

$$[E_y] = \frac{1}{j\beta k_0}[A_y][\epsilon_{rz}]^{-1}[D_x][H_y] - \left(\frac{k_0}{\beta} + \frac{1}{\beta k_0}[A_y][\epsilon_{rz}]^{-1}[D_y]\right)[H_x] \tag{A11.a}$$

Similarly, the other field components can be define as;

$$[E_x] = -\frac{1}{\beta k_0}[A_x][\epsilon_{rz}]^{-1}[D_y][H_x] - \left(\frac{k_0}{-\beta} - \frac{1}{\beta k_0}[A_x][\epsilon_{rz}]^{-1}[D_x]\right)[H_y] \tag{A11.b}$$

$$[H_y] = \frac{1}{-\beta k_0}[C_y][B_x][E_y] - \left(-\frac{k_0}{\beta}[\epsilon_{rx}] - \frac{1}{\beta k_0}[C_y][B_y]\right)[E_x] \tag{A12.a}$$

$$[H_x] = \frac{1}{\beta k_0}\left[B_y\right][C_x][E_x] - \left(\frac{k_0}{\beta}\left[\epsilon_{ry}\right] + \frac{1}{\beta k_0}[B_x][C_x]\right)\left[E_y\right] \qquad \text{(A12.b)}$$

Then the above equations (Equation A11 and A12) are coupled to either transverse electric fields components (E_x and E_y) or transverse magnetic fields components (H_x and H_y). For the transverse electric field case, the eigenvalue problem is:

$$\beta^2 E_x = \left((k_0^2 I + A_x \epsilon_{rz}^{-1} D_x)\left(\epsilon_x + k_0^{-2} C_y B_y\right) - k_0^{-2} A_x \epsilon_{rz}^{-1} D_y B_y\right) E_x$$
$$+\left(A_x \epsilon_{rz}^{-1} D_y\left(\epsilon_y + k_0^{-2} C_x B_x\right) - (I + k_0^{-2} A_x \epsilon_{rz}^{-1} D_x) C_y B_x\right) E_y$$

(A13.a)

and,

$$\beta^2 E_y = \left((k_0^2 I + A_y \epsilon_{rz}^{-1} D_y)\left(\epsilon_y + k_0^{-2} C_x B_x\right) - k_0^{-2} A_y \epsilon_{rz}^{-1} D_x B_x\right) E_y +$$
$$\left(A_y \epsilon_{rz}^{-1} D_x\left(\epsilon_x + k_0^{-2} C_y B_y\right) - \left(I + k_0^{-2} A_y \epsilon_{rz}^{-1} D_y\right) C_x B_y\right) E_x$$

(A13.b)

Which can summarized as,

$$\beta^2 \begin{bmatrix} E_x \\ E_y \end{bmatrix} = \begin{bmatrix} P_{xx} & P_{xy} \\ P_{yx} & P_{yy} \end{bmatrix} \begin{bmatrix} E_x \\ E_y \end{bmatrix} \qquad \text{(A14)}$$

Similar equations can be obtained for transverse magnetic field as;

$$\beta^2 H_x = \left((k_0^2 I + A_x \epsilon_{rz}^{-1} D_x)\left(\epsilon_x + k_0^{-2} C_y B_y\right) - k_0^{-2} A_x \epsilon_{rz}^{-1} D_y B_y\right) E_x +$$
$$\left(A_x \epsilon_{rz}^{-1} D_y\left(\epsilon_y + k_0^{-2} C_x B_x\right) - (I + k_0^{-2} A_x \epsilon_{rz}^{-1} D_x) C_y B_x\right) E_y$$

(A15.a)

and,

$$\beta^2 H_y = \left((k_0^2 I + A_y \epsilon_{rz}^{-1} D_y)\left(\epsilon_y + k_0^{-2} C_x B_x\right) - k_0^{-2} A_y \epsilon_{rz}^{-1} D_x B_x\right) E_y +$$
$$\left(A_y \epsilon_{rz}^{-1} D_x\left(\epsilon_x + k_0^{-2} C_y B_y\right) - \left(I + k_0^{-2} A_y \epsilon_{rz}^{-1} D_y\right) C_x B_y\right) E_x$$

(A15.b)

This also can be expressed in the matrix form:

$$\beta^2 \begin{bmatrix} H_x \\ H_y \end{bmatrix} = \begin{bmatrix} Q_{xx} & Q_{xy} \\ Q_{yx} & Q_{yy} \end{bmatrix} \begin{bmatrix} H_x \\ H_y \end{bmatrix} \qquad \text{(A16)}$$

Solving the above eigenvalue problem (Equation A14 and A16), a solution for wave-equation can be obtained. Furthermore, the longitudinal field components can be calculated from Maxwell's equations (A8.c) and (A9.c).

A. 3. Assessment Examples

In this section, further justifications for the non-uniform FDFD method are provided. For all the justifications, an electric wall – or simply a Perfect Electric Conductor (PEC) – boundary condition will be used to terminate the computational window. The simulation was done on a personal computer with following specifications; dual-core CPU 2.6GHz and 4G RAM. A Matlab Code was used to implement the FDFD method.

A. 3. 1. The Circular Waveguide

In this part, the performance of the non-uniform FDFD method in analyzing metallic structures is evaluated. The copper circular waveguide, with conductivity of $\sigma = 5.8\times10^7$ s/m, inner radius of 3mm and outer radius of 3.6mm, was analyzed at 80GHz. Taking advantage of the structure symmetry, only a quarter of the structure was analyzed. For the dominant mode (TM_{01}), the phase shit constant "β" was calculated to be:

$$\beta_{FDFD} = 1.466 \; - 0.18 \times 10^{-6}\mathrm{i} \;\; \mathrm{rad/mm}$$

$$\beta_{Theoritiacal} = 1.472 \; \mathrm{rad/mm}$$

The longitudinal electric field is shown in Figure A-2(a). Both the propagation constant value and the field pattern are in a good agreement with the theoretical results [99].

Figure A-2 (b) presents the transverse field distribution of the TE_{11} mode, obtained from the non-uniform FDFD method. The transverse modal field pattern is in a good agreement with the published one [99]. The phase constant of this mode was found to be 1.5586 rad/mm, which has less than 0.2% error compared to the theoretical results.

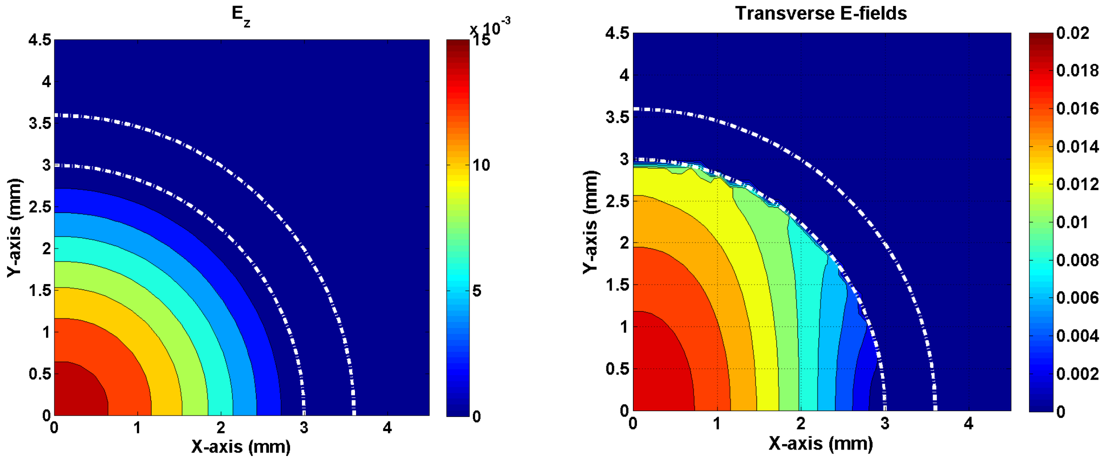

(a)

(b)

Figure A-2 (a)The E_z field of the dominant mode (TM_{01}), (b) The Transverse field of TE_{11} mode.

A. 3. 2. The Terahertz Air-core Microstructure Fiber (TAMF)

For the final assessment, the non-uniform FDFD method was used to analyze the terahertz air-core microstructure fiber (TAMF). The TAMF is a low loss waveguide for THz band, It consists of a hollow core and a cladding layer formed by periodic arrangement of flexible and commercial available polytetrafluorethylene (Teflon, refractive index of 2.1) plastic tubes [100]. A summary of the parameters of the TAMF is listed in Table A-I.

Geometrical parameters	Pitch Size (Λ)	2.08 mm
	Inner tube radius	0.84 mm
	Outer tube radius	1.04 mm
Dielectric constant	Teflon	2.1
	Air	1.0

Table A-I The Parameters of the TAMF waveguide

Using non-uniform FDFD, the structure was analyzed at a frequency of 637GHz. Figure A-3(a) shows the dominant modal electric field of the waveguide. The figure shows that the field is concentrated inside the core of the waveguide. Moreover, the modal field is an ARROW-like mode from the anti-resonance of the Teflon tubes. Compared to the published field pattern, there is a perfect correlation between both field patterns. The variation of the effective refractive index (n_{eff}) of the TAMF with the frequency is presented in Figure A-3 (b). The figure also shows a good agreement between the results obtained from both normal FDFD and non-uniform FDFD method.

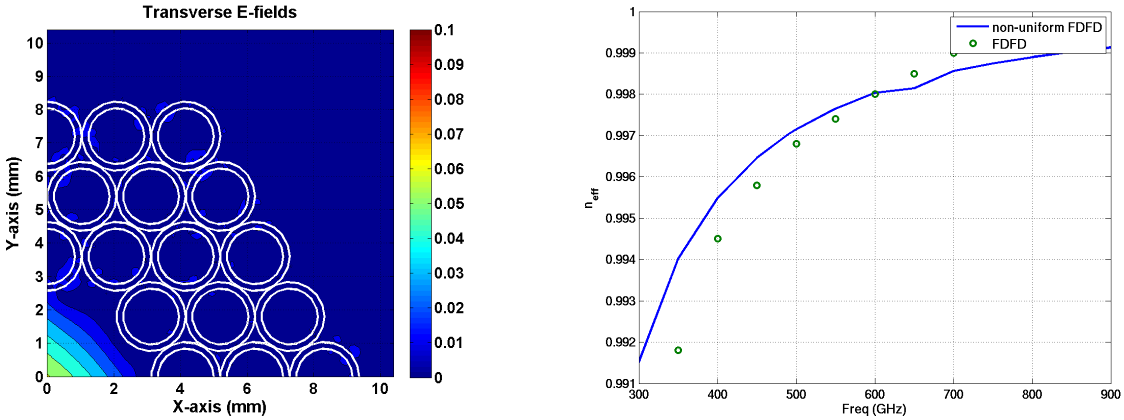

(a) (b)

Figure A-3 (a) E modal pattern and (b) The dispersion relation of the TAMF

Appendix B

Analysis of Surface Wave along conductive wire

In this appendix, a verification of the existence of the surface wave along a conductive rod is investigated using the HFSS. Within the following analysis, the properties of the surface waves along the conductive wire are calculated, and the accuracy of the HFSS model is investigated. Furthermore, some primitive application of the surface wave in material sensing.

B.1. Propagation of Surface Wave along Copper Rod

In this part, the propagation of an electromagnetic wave along a copper conductive wire is investigated using the HFSS analysis. A schematic diagram of the HFSS model is presented in Figure B-1. It consists of conductive rod of radius 0.45mm, and a delta-gap source for excitation [125]. The separation between the rod tip and the coaxial excitation was selected to be 2.5mm. The rod was terminated using a tapered section, of length 2.5mm, to facilitate the field coupling to the wire.

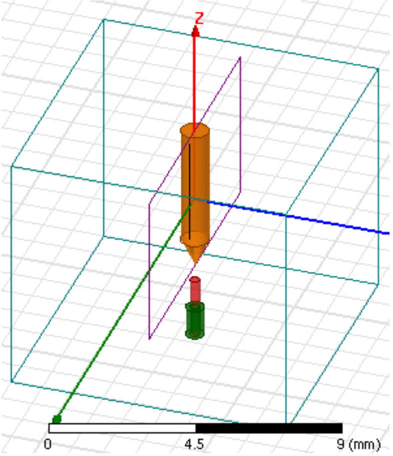

Figure B-1 HFSS model of a single conductive rod with delta-gap excitation.

B.1.1. Single Rod Analysis

Using the predefined HFSS model, the reflection analysis (S_{11} return losses) along the excitation probe is plotted in Figure B-2(a). The figure indicates that the delta-gap excitation coupled the electromagnetic fields to the rod at two frequencies; 100GHz and 240GHz. The axial field distribution along the rod at 100GHz is plotted in Figure B-2(b), while the same electric field at

240GHz is presented in Figure B-(c). The figure shows that both fields are slowly decaying along the surface of the conductive rod.

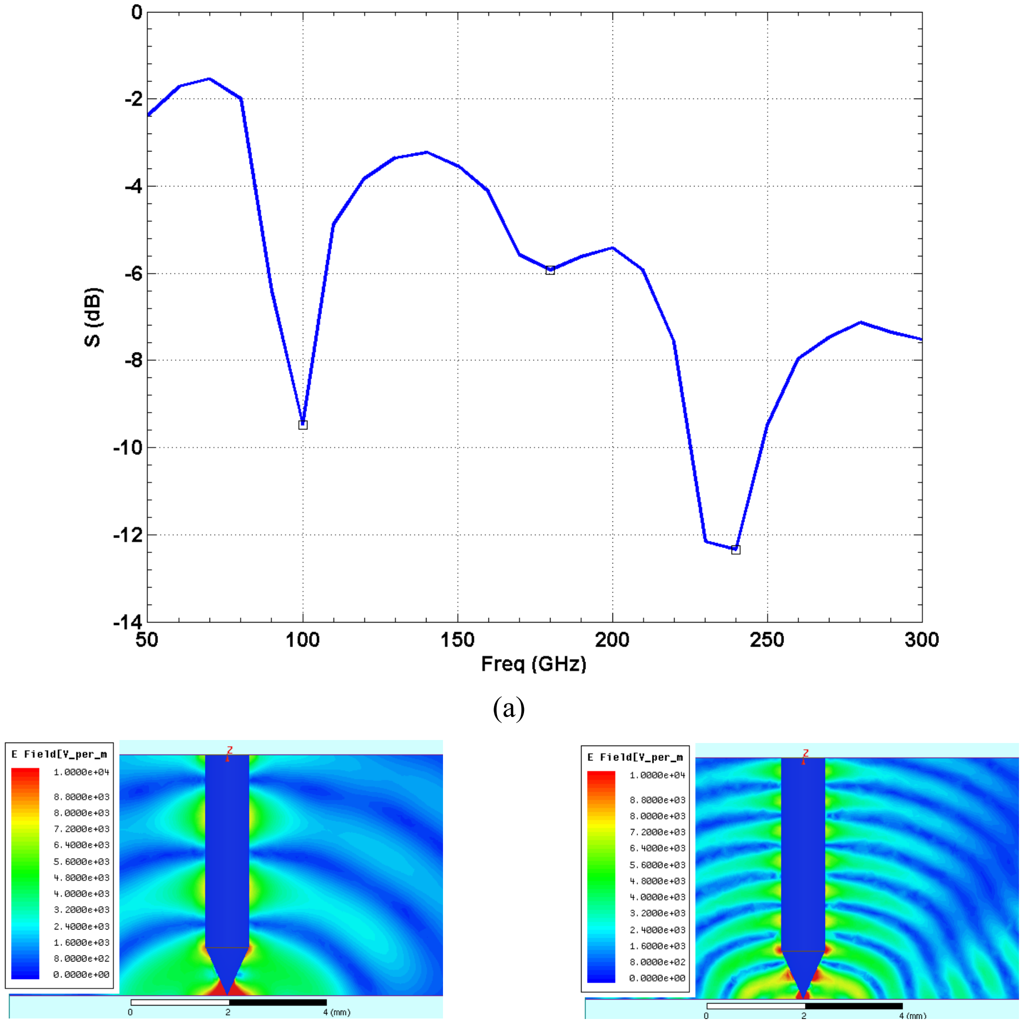

(a)

(b)

(c)

Figure B-2 (a) The Return losses, cross-sectional field at (b) 100GHz and (c) 240GHz

More detailed analysis can be obtained from the field at the surface of the conductive wire. A plot of the amplitude of the normalized (with respect to the excitation value) surface field is shown in Figure B-3(a). The figure shows that as the field propagates along the wire, the field amplitude is slowly decaying. Although it is not shown here, the same decay observation was spotted in the 100GHz case

B.1.1.1. Attenuation factor analysis

In order to investigate the accuracy of the HFSS simulation, the curve fitting technique is used to extract the attenuation factor of the HFSS field. Since the electric field at the surface of the conducting rod is exponential decay (Figure B-2(a)), an exponential decay fit can be used to calculate the attenuation factor:

$$E_{Surface} = E_0 e^{-\alpha . z} \tag{B-1}$$

Where E_0 is the maximum field value, α is the attenuation factor and the z is the propagation distance.

Using the exponential decay curve fitting, both the decay for the 100GHz and the 240 GHz surface fields were calculated and plotted in Figure B-3(b). The figure shows that both the surface waves are attenuated. Furthermore, the effect of the attenuation is increased as the frequency increases.

For the wave operates at the 240GHz, the curve fitting attenuation factor was found to be 86.31 Nb/mm. Using the theoretical analysis, the attenuation factor was calculated to be 95.16 Nb/mm, which is 9.3% shifted from the curve fitting approximation. Since only two full waves were used to extrapolate the attenuation factor, the error between the theoretical and extrapolated values can be justified.

Furthermore, for the 100GHz case the extracted and the theoretical values of the attenuation was calculated to be 78.4 Nb/mm and 51.8Nb/mm respectively. As shown in Figure B-3(b), almost one full wave of the field was calculated on the rod at 100GHz. Therefore it is expected to have higher error values for the surface wave operates at the 100GHz compared to the 240GHz case.

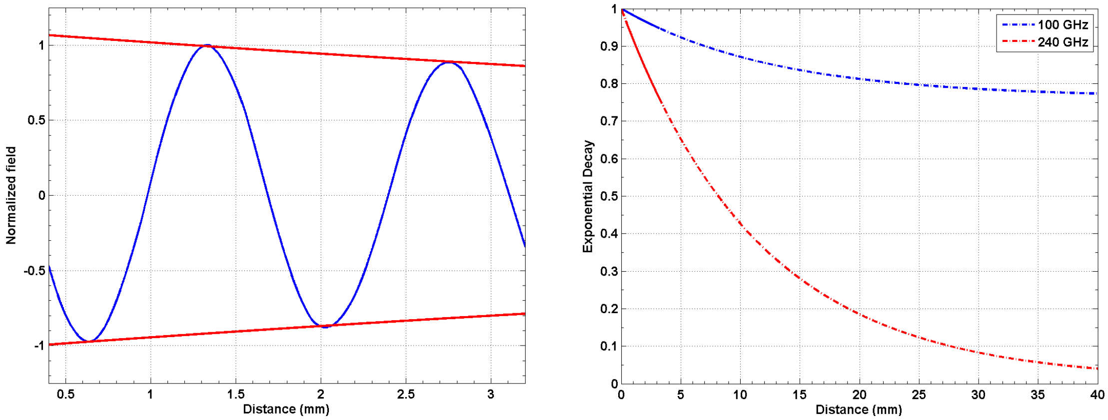

(a) (b)

Figure B-3 (a) The Surface Field at 240GHz and (b) the extracted exponential decay of the field at 100GHz and 240GHz

The last section in this part is the effect of surrounding medium perturbation. The analysis was performed with the same configuration as shown in Figure B-1, with a material box (2.7×2.7×2mm of relative permittivity ε_r=1.5, Figure B-4).

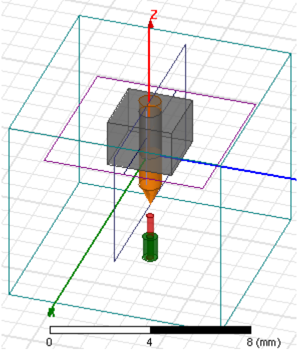

Figure B-4 Schematic diagram of the single rod with a material box

Since the same excitation is used, the insertion losses will be the same and hence the analysis will be applied on 100GHz and 240GHz. The cross sectional field at these two frequencies is presented in Figure B-5(a) and Figure B-5(b), respectively. For both figures, the field propagates, with attenuation, along the rod surface.

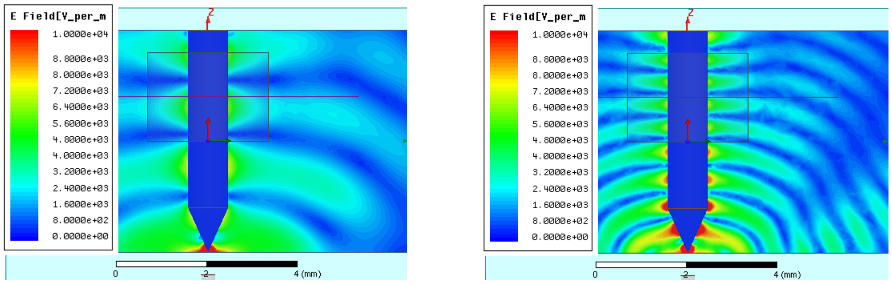

(a) (b)

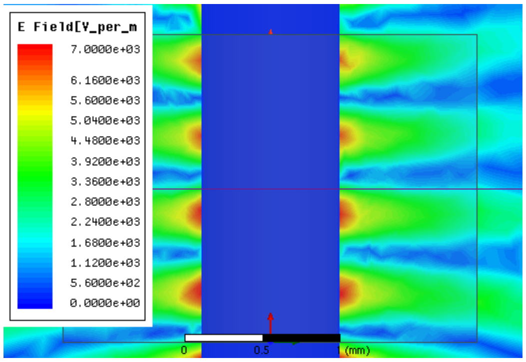

Figure B-5 The cross-sectional field at (a) 100GHz and (b) 240GHz, and (c) a zoomed picture of the fields inside the material box.

B.1.2. Two Balanced Rods

Alike the previous section, the coupling analysis between two similar rods is investigated. Figure B-6(a) shows the schematic diagram of two similar rods, with 1.8mm separation between the axes of the rods. Similar to the single rod analysis, a delta-gap excitation technique –with the same excitation parameters– will be used. Therefore the fields are coupled to the rod at the same resonance frequencies. The axial cross section of the fields at 100GHz and 240GHz (resonance frequencies) is plotted in Figure B-6(b) and (c) respectively. For the 100GHz case, the fields at the first rod is decaying as it propagates along the rod. The figure also shows that a significant amount of the EM-fields are coupled to the second rod. Furthermore, the figure shows that the separation between the rods provides a guiding mechanism to the fields. The same field behavior is observed in the 240GHz resonance. Similarly, the axial cross section at the 240GHz shows that most of the fields are coupled in the separation between the two rods.

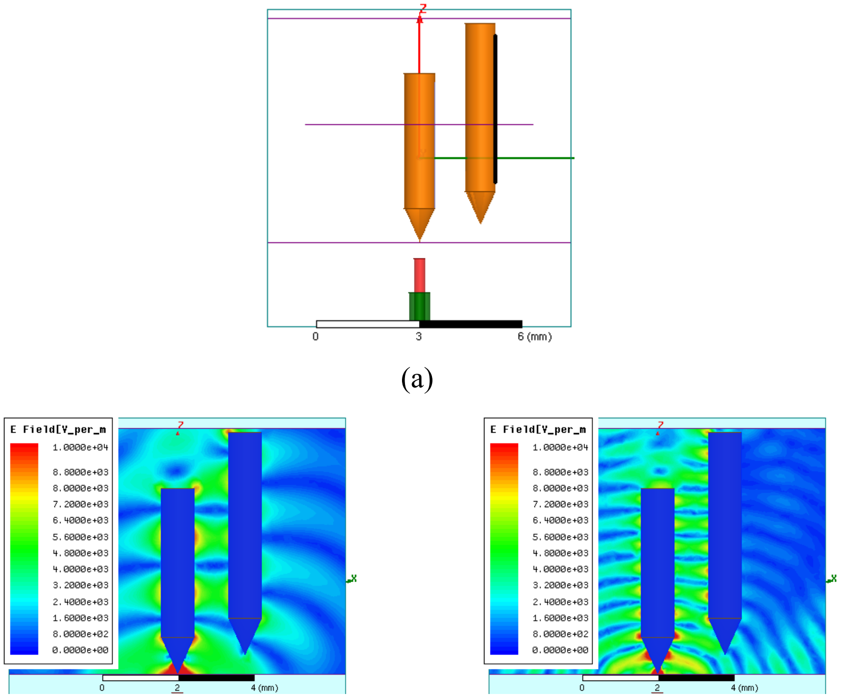

(a)

(b)

(c)

Figure B-6 (a) Schematic diagram of the two rods analysis, and cross-sectional field at (b) 100GHz and (c) 240GHz

More insight information can be obtained from the surface wave analysis. The electromagnetic fields at the surface of the second rod (the extracted field line is shown as a black line in Figure B-6(a)) were extracted from the HFSS file. A plot of the surface field is plotted in Figure B-7. The figure indicates that the surface wave is a sinusoidal decaying field. The attenuation factor was found to be 311.3 Nb/mm, which is greater than single rod placed in homogeneous medium.

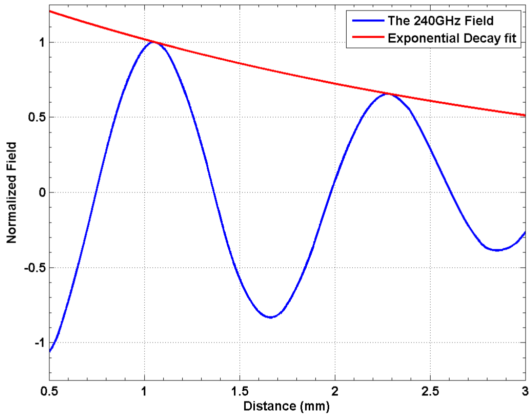

Figure B-7 The field propagation along the surface of the rod

B.1.3 Two Unbalanced Rods

Within this section, the effect of unbalanced rod is investigated. Alike the balanced rod case, the radius of the first is kept constant at 0.450mm while the radius of the second rod increased to 0.675mm (1.5x times the first rod). All other geometrical parameters; excitation network and rod separation, are kept constant.

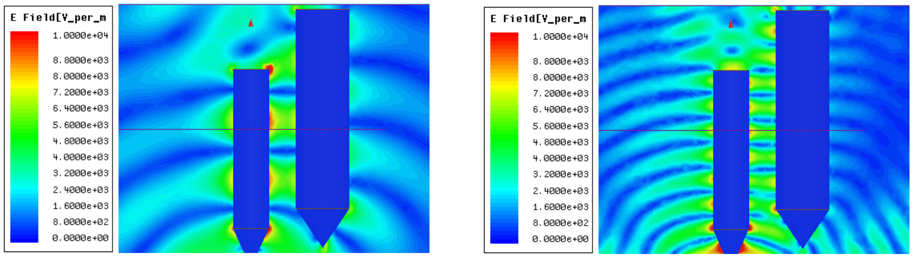

(a) (b)

Figure B-8 The axial field pattern at (a) 100GHz and (b) 240GHz

Since the excitation is kept constant, the delta gap-excitation resonates at 100GHz and 240GHz. The axial field across the metallic rods, at 100GHz and 240GHz, is plotted in Figure B-8(a) and Figure B-8(b), respectively. Both figures show the fields are concentrated at the surface of the rod. Since the theoretical analysis indicates that the surface fields are lossy fields, the fields slowly decays as it propagate across the rods.

B.2 Application of Surface Wave along Conductive Rods

Taking advantage of the sensitivity of the surface wave to the surrounding medium, it can be used to detect different surrounding medium. In this section, a primitive analysis of the potential of the surface wave applications in sensing is introduced. The analysis is performed on two coupled rods using the HFSS model in two modes; the balanced mode and the unbalanced mode. In the balanced case, both the rods have the same radius (0.45mm), and the distance between the centers of the rods was selected to be 1.8mm. While in the unbalanced case, the radius of the first rod is 0.45mm and the radius of the other rod is increased to 0.675mm. Within both cases, the geometrical parameters and the excitation are kept constant.

Instead of using the delta-gap excitation –as used in the previous section–, the excitation is performed by direct connection between the rods and the inner conductor of a coaxial cable. Taking advantage of the radius matching between the rod and the "2.92 mm (K) Connectors", an efficient contact between them can be achieved (Figure B-9). The figure also shows a dielectric box placed, in which the electromagnetic coupling is performed. Within the following sections, the effect of changing the box material on S-parameters is investigated.

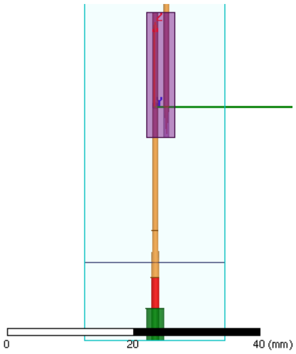

Figure B-9 A schematic diagram of the excitation

B.2.1 Air Dielectric Box

The first step in this analysis is to define the return losses (S_{11}) without any dielectric box added. This is performed in the HFSS by assigning Air properties to the dielectric box. The return losses at the excitation port, with the two rods placed in the vacuum is plotted in Figure B-10(a). The figure shows that the electromagnetic fields are coupled to the rods at three coupling frequencies; 23.75, 27, and 29.75GHz. The cross sectional field at 23.75 and 29.75GHz is plotted in Figure B-10(b) and (c) respectively. Both figures shows that the fields are coupled between the two rods.

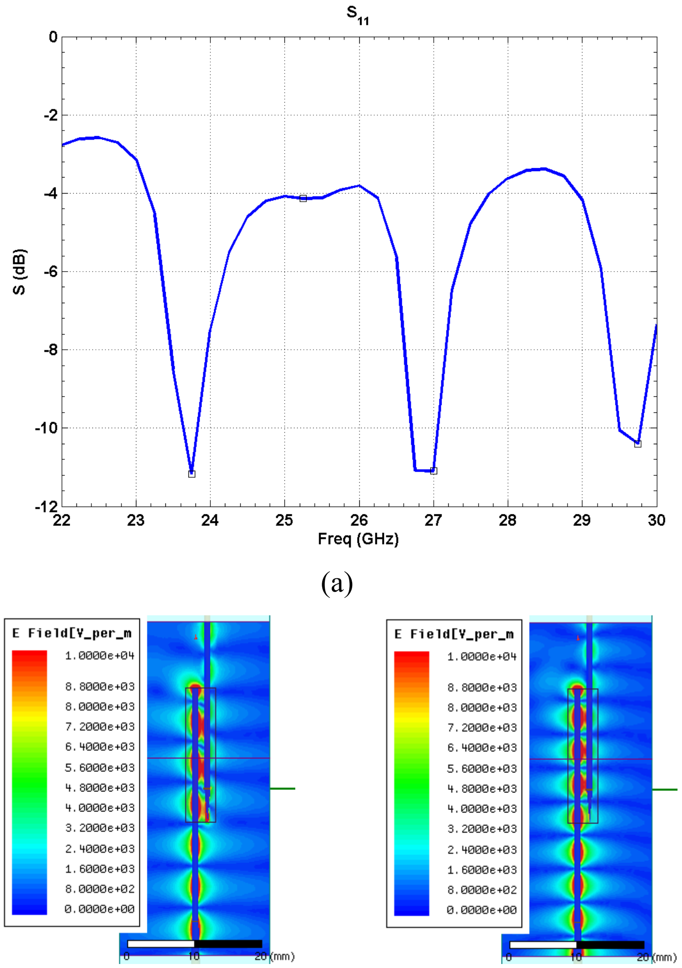

(a)

(b) (c)

Figure B-10 (a) The return losses of the coupled two rods placed in the vacuum, and The cross axial field at (b) 23.75GHz and (c) 29.75GHz

B.2.2 The Dielectric Box

To demonstrate the effect of the surrounding medium on the return losses of the surface wave modes, a dielectric box, with relative permittivity ($\varepsilon_r = 1.25$), is used to replace the air box. The calculated return loss is plotted in Figure B-11(a). The figure shows that the resonance frequencies are 23, 25.75, and 29GHz. The cross sectional field at 23 and 29 GHz is presented in Figure B-11(b) and (c) respectively. Compared to the previous section, the resonance frequency and amplitude is shifted due to the dielectric box added. Therefore the surface wave propagation along the conductive rod can be used in sensing applications.

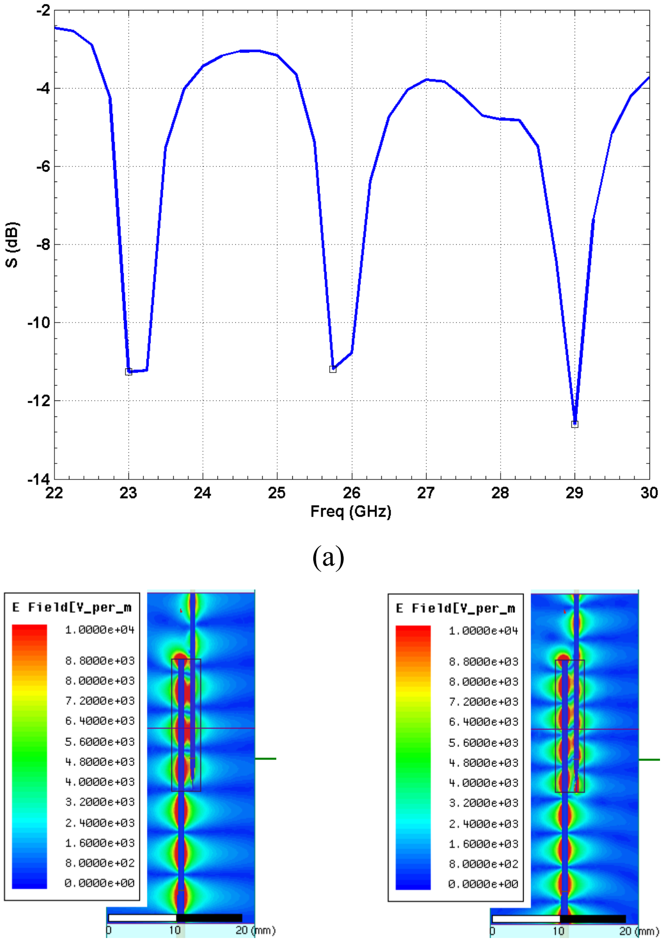

(a)

(b) (c)

Figure B-11 (a) The return losses of the coupled two rods placed in the vacuum, and The cross axial field at (b) 23GHz and (c) 29GHz

The sensitivity of the surface wave to different dielectric materials is presented by changing the dielectric box materials. A plot of the corresponding return losses of these dielectric boxes, calculated around 23GHz and 27GHz, is plotted in Figure B-12(a) and Figure B-12(b), respectively. In both figures the resonance frequency and the amplitude of the resonance frequency is affected by the dielectric material assigned to the material box. In both figures, as the relative permittivity (ε_r) of the dielectric box increases, a slight reduction of the resonance frequency is noticed. For example, the resonance frequency in the first frequency window (around 23GHz) changed from 23.75GHz to 23.50 when the dielectric box material changed from air to another material with relative permittivity of 1.05. Replacing the air box with another dialectic box of relative permittivity of 1.25 shifts the resonance frequency to 23.0GHz, while placing a Teflon box reduces the resonance frequency to 22.5GHz. Similar behavior was observed in the second frequency window (around 27GHz).

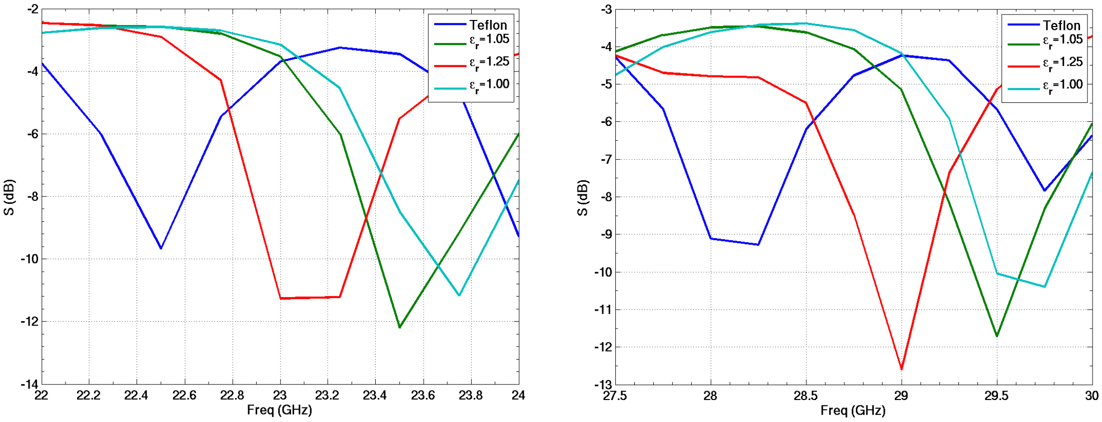

(a) (b)

Figure B-12 The return losses at (a) the first frequency window, and (b) the second frequency window

Bibliography

[1] Yun-Shik Lee, “*Principles of Terahertz Science and Technology*”, Springer (2009).

[2] Matteo Perenzoni, and Douglas Paul, “*Physics and Applications of Terahertz Radiation*”, Springer (2014).

[3] D. M. Pozer, “Consideration for Millimetre Wave Printed Antennas,” IEEE Trans. Antennas and Propagation, vol. 31, no.5, pp.740-747, Sep 1983.

[4] H. LiQuan, “Some Advances In Millimeter Wave Application Systems”, Proc. IEEE Asia Pacific Microwave, pp. 749-752, Dec 1997.

[5] Adel S. Emhemmed, Ian McGregor, Khaled Elgaid, “200 GHz Broadband Proximity Coupled Patch Antenna”, Proc. IEEE Ultra-Wideband, ICUWB, pp.404-407, Sept. 2009.

[6] R A Lewis, “A review of terahertz sources,” J. Phys. D, Appl. Phys. 47, 374001, 2014.

[7] M. J. Rosker, H.B. Wallace, “Vacuum electronics and the world above 100 GHz,” Proc. IEEE Vacuum Electronics (IVEC), pp.5-7, April 2008.

[8] P. H. Siegel, “Terahertz technology,” IEEE Trans. Microwave Theory Tech., vol. 50, no. 3, pp. 910–928, Mar. 2002.

[9] H. B. Wallace, “Analysis of RF imaging applications at frequencies over 100 GHz,” Appl. Opt., vol. 49, no. 19, pp. E38–E47, Jul. 2010.

[10] J. H. Booske, R. J. Dobbs, C. D. Joye, C. L. Kory, G. R. Neil, G. S. Park, et al., “Vacuum electronic high power terahertz sources,” IEEE Trans. Terahertz Sci. Technol., Vol. 1, No. 1, PP. 54–75, Sep. 2011.

[11] Goutam Chattopadhyay, "Technology, Capabilities, and Performance of Low Power Terahertz Sources, " IEEE Trans. Terahertz Science and Technology, vol.1, no.1, pp.33-53, Sept. 2011.

[12] L. A. Samoska, "An Overview of Solid-State Integrated Circuit Amplifiers in the Submillimeter-Wave and THz Regime," IEEE Trans Terahertz Science and Technology, vol.1, no.1, pp.9-24, Sept. 2011.

[13] M. S. Vitiello, A. Tredicucci, "Tunable Emission in THz Quantum Cascade Lasers," IEEE Trans Terahertz Science and Technology, vol.1, no.1, pp.76-84, Sept. 2011.

[14] Jerome V. Moloney, Joe M. Yarborough, Mahmoud Fallahi, Maik Scheller, Stephan W. Koch and Martin Koc, "Compact, high-power, room-temperature, narrow-line terahertz source," SPIE Newsroom, March 2011.

[15] R. Kompfner, "The Invention of Travelling Wave Tubes," IEEE Trans. Electron Devices, vol. 23, no. 7, pp. 730-738, July 1976.

[16] R. J. Barker, J. H. Booske, N. C. Luhmann, and G. S. Nusinovich, "Modern Microwave and Millimeter-Wave Power Electron", Piscataway, NJ: IEEE, 2005.

[17] T. Idehara, T. Saito, H. Mori, H. Tsuchiya, L. Agusu and S. Mitsudo, "Long pulse operation of the THz gyrotron with a pulse magnet," Int. J. Infrared Millim. Waves, vol. 29, no. 2, pp. 131-141, 2008.

[18] R. Kompfner and N. T. Williams, "Backward wave tubes," Proc. IRE, vol. 41, no. 11, pp. 1602–1611, Nov. 1953.

[19] R. J. Barker, J. H. Booske, N. C. Luhmann, and G. S. Nusinovich, Modern Microwave and Millimeter-Wave Power Electron.. Piscataway, NJ: IEEE, 2005.

[20] A. I. Nashed, S. K. Chaudhuri, and S. Safavi-Naeini, "A cylindrical metallic photonic crystal waveguide—Design and analysis," in IEEE AP-S/URSI Int. Conf. Proc., pp. 2495–2498, 2010.

[21] Toshiyuki Shiozawa and Akimasa Hirata, "Analysis of Free-Electron Lasers via FDTD Method," Electronics and Communications in Japan, Part 2, Vol. 86, No. 5, 2003.

[22] A. I. Nashed, S. K. Chaudhuri, and S. Safavi-Naeini "THz Wave Generation via Electron Beam-Wave interaction in Cylindrical Photonic Crystal Waveguide," IEEE AP-S/URSI International Conf., proceedings 2011, pp. 2354 – 2357.

[23] A. I. Nashed, S. K. Chaudhuri, and S. Safavi-Naeini, "Analysis and Design of a Novel Photonic Crystal-based sub-mm/THz Backward Wave Oscillator," IEEE THz Sci. and Techn., pp. 642 – 651, Nov. 2012.

[24] J. D. Jackson, Classical Electrodynamics, 3rd ed. New York: Wiley, 1999.

[25] R.H. Abrams, B. Levush, et al., "Vacuum electronics in the 21st centuries," IEEE Microwave Mag. 2, 61, Sept. 2001.

[26] Joseph A. Eichmeier, Manfred K. Thumm*, Vacuum Electronics - Components and Devices*, Springer, New Yourk, 2008.

[27] N.E. Lindenblad, U.S. Patent 2,300,052, filed May 4, 1940, issued October 27, 1942.

[28] Sudeep Bhattacharjee, John H. Booske, Carol L. Kory, Dan W. van der Weide, Steve Limbach, S. Gallagher, John D. Welter, Mike R. Lopez, Ronald M. Gilgenbach, R. Lawrence Ives, Michael E. Read, Ralu Divan, and D. C. Mancini, "Folded Waveguide Traveling-Wave Tube Sources for Terahertz Radiation," IEEE Tarns. Plasma Sci., Vol. 32, No. 3, June 2004.

[29] S. Millmann, "A spatial harmonics amplifier for 6 mm wavelength," Proc. IRE 39, 1035 (Sept.) (1951).

[30] A. M. Elfrgani, S. Prasad, M. I. Fuks, E. Schamiloglu, "Relativistic BWO with linearly polarized Gaussian radiation pattern," IEEE Trans. Plasma Science, vol.42, no.8, pp.2135-2140, Aug. 2014.

[31] A. M. Elfrgani, S. Prasad, M. I. Fuks, E. Schamiloglu, "Dual-band operation of relativistic BWO with linearly polarized Gaussian output," IEEE Trans. Plasma Science, vol.42, no.8, pp.2141-2145, Aug. 2014.

[32] J. W. Gewartowski and H. A. Watson, Principles of Electron Tubes, Van Nostrand, Princeton, N.J., 1965.

[33] Robert K. Parker, Richard H. Abrams, Bruce G. Danly, and Baruch Levush, "Vacuum Electronics," IEEE MTT, Vol. 50, No. 3, March 2002.

[34] www.brittanica.com last visit 24 February 2015.

[35] Sudeep Bhattacharjee, John H. Booske, Carol L. Kory, Dan W. van der Weide, Steve Limbach, S. Gallagher, John D. Welter, Mike R. Lopez, Ronald M. Gilgenbach, R. Lawrence Ives, Michael E. Read, Ralu Divan, and D. C. Mancini, "Folded Waveguide Traveling-Wave Tube Sources for Terahertz Radiation," IEEE Tarns. Plasma Sci., Vol. 32, No. 3, June 2004.

[36] Robert K. Parker, Richard H. Abrams, Bruce G. Danly, and Baruch Levush, "Vacuum Electronics," IEEE MTT, Vol. 50, No. 3, March 2002.

[37] George Caryotakis, "The Klystron: A Microwave Source of Surprising Range and Endurance," The American Phys Soc., Division of Plasma Phys Conf., Pittsburgh, PA, Nov 1997.

[38] M. Hyttinen, P. Horoyski, and A. Roitman, “Ka-band extended interaction klystrons (EIKs) for satellite communication equipment,” Proc. 3rd IEEE Int. Vacuum Electron., Monterey, CA, pp. 320–321, April 2002.

[39] R. Dobbs, M. Hyttinen, B. Steer, and A. Soukhov, “Rugged and efficient Ka-band extended interaction klystrons for satellite communication systems,” in Proc. 8th IEEE Internationl Vacuum Electron., Kitakyushu, Japan, pp. 107–108, May 2007.

[40] S. Millmann, “A spatial harmonics amplifier for 6 mm wavelength,” Proceedings of the IRE , vol.39, no.9, pp.1035-1043, Sept. 1951.

[41] http://www.insight-product.com/index.htm last visit 24 February 2015.

[42] http://www.mtinstruments.com/ last visit 24 February 2015.

[43] http://www.l-3com.com/ last visit 24 February 2015.

[44] A. M. Elfrgani, S. Prasad, M. I. Fuks, E. Schamiloglu, “Relativistic BWO with linearly polarized Gaussian radiation pattern,” IEEE Trans. Plasma Science, vol.42, no.8, pp.2135-2140, Aug. 2014.

[45] A. M. Elfrgani, S. Prasad, M. I. Fuks, E. Schamiloglu, “Dual-band operation of relativistic BWO with linearly polarized Gaussian output,” IEEE Trans. Plasma Science, vol.42, no.8, pp.2141-2145, Aug. 2014.

[46] Albert W. Hull, “The effect of Uniform magnetic field on the motion of the electrons between coaxial cylinders,” Physics Rev., vol. 18, no. 1, 1921.

[47] Gun-Sik Park, Yong Hyup Kim, Haewook Han, Joon Koo Han, Jaewook Ahn, Joo-Hiuk Son, Woong-Yang Park, Young Uk Jeong, Convergence of Terahertz Sciences in Biomedical Systems, Springer, 2012.

[48] V. D. Yeryomka, M. A. Kopot, O. P. Kulagin, and V. D. Naumenko, “Spatial-harmonic magnetrons – THz electromagnetic radiation oscillators,” Proc. ICMMT, pp 1199 – 1201, 2008.

[49] Andres Larraza , Davud M. Wolfe, Jeffery K. Catterlin, “Terahertz (THZ) reverse magnetron,” US patent, Sep. 30, 2010.

[50] Vasily Naumenko, Alexander Suvorov, and Alexey Sirov, “Tunable magnetron of a two-millimeter-wavelength band,” Microwave and Optical Technology Letters, Volume 12, Issue 3, pages 129–131, June 1996.

[51] Lester M. Field, “Some Slow-Wave Structures for Traveling-Wave Tubes,” Proceeding of IRE, vol. 37, no. 1, pp 34-40, 1949.

[52] Yanyu Wei, Wenxiang Wang, Baoh Jia, A.K.Sinha, Sheng-gang Liu and Gun-Sik Park, “An Ultra Wideband Helical Groove Waveguide TWT,” Proc. 3rd International Microwave Millimeter Wave Technology, pp. 82 - 85, 2002.

[53] Wenxiang Wang, Yanyu Wei, Guofen Yu, Yubin Gong, Minzhi Huang, and Guoqing Zhao, “Review of the Novel Slow Wave Structures For High Power Travelling Wave Tube,” International Journal of Infrared and Millimeter Waves, Vol. 24, No. 9, September 2003.

[54] C. Liss, R. Harper, M.P.Puri, “Helical waveguide millimeter wave TWT,” International Electron Devices Meeting (IEDM), pp.374-377, Dec. 1988.

[55] Gregory G. Denisov, Vladimir L. Bratman, Alan D. R. Phelps, and Sergei V. Samsonov, “Gyro-TWT with a Helical Operating Waveguide: New Possibilities to Enhance Efficiency and Frequency Bandwidth,” IEEE Trans. Plasma Sci., Vol. 26, No. 3, June 1998.

[56] S. Ahn, and A. K. Ganguly, “Analysis of Helical Waveguide,” IEEE Trans. Electron Devices, Vol. ED33, No.9, Sept. 1986.

[57] J. A. Dayton, C. L. Kory, G. T. Mearini, D. Malta, M. Lueck, C. A. Bower, “A 650 GHz helical BWO,” Proceeding International Vacuum Electronics Conference (IVEC), pp.396 - 397, April 2008.

[58] J. A. Dayton, C. L. Kory, G. T. Mearini, D. Malta, M. Lueck, B. Vancil, “Fabrication and testing of the 0.650 THz helical BWO,” Proceeding International Vacuum Electronics Conference (IVEC), pp.33 - 34, April 2012.

[59] C. L .Kory, J. A. Dayton, G. T. Mearini, D. Malta, M. Lueck, K. Gilchrist, B. Vancil, “95 GHz helical TWT design,” Proceeding International Vacuum Electronics Conference (IVEC), pp.125 - 126, 28-30 April 2009.

[60] M. C. Balk, C. L. Kory, J. A. Dayton, “Investigation of a 95GHz helical TWT with CST STUDIO SUITE™,” Proceeding International Vacuum Electronics Conference (IVEC), pp.505 - 506, 28-30 April 2009.

[61] D. G. Zhang, Edward K. N. Yung, and H. Y. Ding, “Dispersion Characteristics of a Novel Shielded Periodic Meander Line,” Microwave and Optical Technology Letter, vol. 12, no. 1, May 1996.

[62] S. Sengele, Jiang Hongrui, J. H. Booske, C. L. Kory, D. W. van der Weide, R. L. Ives, “Microfabrication and Characterization of a Selectively Metallized W-Band Meander-Line TWT Circuit,” IEEE Trans. Electron Devices, Vol.56, No.5, pp.730 - 737, May 2009.

[63] Shen Fei, Wei Yanyu, Yin Hairong, Gong Yubin, Xu Xiong, Wang Shaomeng, Wang Wenxiang, Feng Jinjun, “A Novel V-Shaped Microstrip Meander-Line Slow-Wave Structure for W-band MMPM,” IEEE Trans. Plasma Science, Vol.40, No. 2, pp.463 - 469, Feb. 2012.

[64] G. Dohler, D. Gagne, D. Gallagher, R. Moats, “Serpentine Waveguide TWT”, Proc. International Electron Device Meeting, pp. 485 - 488, 1987.

[65] S. T. Han, K. H. Jang, J. K. So, J. I. Kim, and Y. M. Shin, “Low-voltage operation of Ka-band folded waveguide traveling-wave tube,” IEEE Trans. Plasma Sci., Vol. 32, No. 1, pp. 60–66, Feb. 2004.

[66] Ke Li, Wenxin Liu, Yong Wang, and Miaomiao Cao, “Dispersion Characteristics of Two-Beam Folded Waveguide for Terahertz Radiation”, IEEE Trans. Electron Devices, Vol. 60, No. 12, Dec. 2013.

[67] H. Gong, Y. Gong, T. Tang, J. Xu, and W. Wang, “Experimental investigation of a high-power Ka-band folded waveguide traveling-wave tube,” IEEE Trans. Electron Device, Vol. 58, No. 7, pp. 2159–2163, Jul. 2011.

[68] Sudeep Bhattacharjee, John H. Booske, Carol L. Kory, Dan W. van der Weide, Steve Limbach, S. Gallagher, John D. Welter, Mike R. Lopez, Ronald M. Gilgenbach, R. Lawrence Ives, Michael E. Read, Ralu Divan, and D. C. Mancini, “Folded Waveguide Traveling-Wave Tube Sources for Terahertz Radiation”, IEEE Trans. Plasma Sci., Vol. 32, No. 3, June 2004.

[69] Huarong Gong, Jin Xu, Tao Tang, Yanyu Wei, Yubin Gong, Changqing Zhang, Xiaogang Su, Shaolun Cai, Gang Wu, and Jinjun Feng, "A 1-kW 32–34-GHz Folded Waveguide Traveling Wave Tube", IEEE Trans. Plasma Sci., pp. 8 – 12, Jan. 2014.

[70] G. Dohler, D. Gallagher, and J. Richards, "Millimeter wave folded waveguide TWTs", Vacuum Electronics Annual Review Proceedings (Crystal City, VA), pp. V15-V20, 1993.

[71] J. J. Choi, C. M. Armstrong, A. K. Ganguly, and F. Calise, "Folded waveguide gyrotron traveling wave tube amplifier," Phys. of Plasmas 2, 915 (1995).

[72] Guo Guo, Yanyu Wei, Minghao Zhang, Gil Travish, Lingna Yue, Jin Xu, Hairong Yin, Minzhi Huang, Yubin Gong, and Wenxiang Wang, "Novel Folded Frame Slow-Wave Structure for Millimeter-Wave Traveling-Wave Tube," IEEE Trans. Electron Device, Vol. 60, No. 11, Nov. 2013.

[73] Ciersiang Chua and Sheel Aditya, "A 3-D U-Shaped Meander-Line Slow-Wave Structure for Traveling-Wave-Tube Applications," IEEE Trans. Electron Devices, Vol. 60, No. 3, March 2013.

[74] Young-Min Shin, Jin-Kyu So, Seong-Tae Han, Kyu-Ha Jang, Gun-Sik Park, Jong-Hyun Kim, and Suk-Sang Chang, "Microfabrication of millimeter wave vacuum electron devices by two-step deep-etch xray lithography," Applied Phys. Letter 88, 091916 (2006).

[75] Ruilin Zheng,Wei Sunand Xuyuan Chen, "Characterizing and smoothing of striated sidewall morphology on UV-exposed thick SU-8 structures for micromachining millimeter wave circuits," J. Micromech. Microeng. 20 (2010).

[76] M. A. Nwachuku, The Helical Waveguide as a Periodic Structure for Millimeter Wave Ph.D. dissertation, Univ. London, London, U.K., 1961.

[77] V. Paramonov, "Parameters of the Disk Loaded Waveguide structure for intermediate particles acceleration in the intermediate energy range"

[78] Vishal Kesari and Baidyanath Basu, "Analysis of Beam and Magnetic Field Parameter Sensitivity of a Disc-Loaded Wideband Gyro-TWT," IEEE Trans Plasma Sci., Vol. 41, No. 5, pp1557 - 1563 May 2013.

[79] Robert J. Barker, Edt Schamitogtu, "High-Power Microwave Source and Technologies", IEEE press, NY 2001.

[80] Xu Xiong, Wei Yan-Yu, Shen Fei, Huang Min-Zhi, Tang Tao, Duan Zhao-Yun, and Gong Yu-Bin, “Research of sine waveguide slow-wave structure for a 220-GHz backward wave oscillator,” Chin. Phys. B Vol. 21, No. 6 (2012) 068402.

[81] Xiong Xu, Yanyu Wei, Fei Shen, Hairong Yin, Jin Xu, Yubin Gong, and Wenxiang Wang, “A watt-class 1-THz backward-wave oscillator based on sine waveguide,” Phys. Plasma 19, 013113 (2012).

[82] W. C. Turner, Y.-I. Chen, W. E. Nexsen, M. C. Green, G. Miram, and A. V. Nordquist, “High brightness, high current density cathode for induction LINAC FELs,” Proc. Linear Accel., Williamsburg, Virginia, USA, 1988.

[83] J. Gao, “Microwave electron gun theory and experiments,” Review of Scientific Instruments, 63, 64 (1992).

[84] David B. Williams, C. Barry Carter, Transmission Electron microscopy, Springer 2009.

[85] J. D. Jarvis, H. L. Andrews, B. Ivanov, C. L. Stewart, N. de Jonge, E. C. Heeres, W.-P. Kang, Y.-M. Wong, J. L. Davidson, and C. A. Brau “Resonant tunneling and extreme brightness from diamond field emitters and carbon nanotubes,” J. Appl. Phys. 108, 094322 (2010).

[86] K. J. Sankaran, K. Srinivasu, K. C. Leou, N. H. Tai, and I. N. Lin “High stability electron field emitters made of nanocrystalline diamond coated carbon nanotubes,” J. Appl. Phys. Let. 103, 251601 (2013).

[87] J. D. Jarvis, B. K. Choi, A. B. Hmelo, B. Ivanov, C. A. Brau, “Emittance measurements of electron beams from diamond field emitter arrays,” J. Vac. Sci. Technol. B 30 , 042201 (2012).

[88] Masayuki Nakamoto, and Jonghyun Moon, “Extremely environment-hard and low work function transfer-mold field emitter arrays,” Applied Surface Science 275 (2013): 178-184.

[89] Masayuki Nakamoto, et al., “Low operation voltage field emitter arrays using low work function materials fabricated by transfer mold technique,” IEDM, PP.297-300, Dec 1998.

[90] Masayuki Nakamoto, Toshimichi Hasegawa, and Katsuyoshi Fukuda, “Uniform, stable and high integrated field emitter arrays for high performance displays and vacuum microelectronic switching devices,” IEDM, PP717-720, Dec 1997.

[91] Masayuki Nakamoto, et al., “Low operation voltage field emitter arrays using low work function materials fabricated by transfer mold technique,” IEDM, PP.297-300, Dec 1998.

[92] Masayuki Nakamoto, Toshimichi Hasegawa, and Katsuyoshi Fukuda, "Uniform, stable and high integrated field emitter arrays for high performance displays and vacuum microelectronic switching devices," IEDM, PP717-720, Dec 1997.

[93] W. C. Turner, Y.-I. Chen, W. E. Nexsen, M. C. Green, G. Miram, and A. V. Nordquist, "High brightness, high current density cathode for induction LINAC FELs," Proc. Linear Accel., Williamsburg, Virginia, USA, 1988.

[94] J. Gao, "Microwave electron gun theory and experiments," Review of Scientific Instruments, 63, 64 (1992).

[95] Kane Yee, "Numerical solution of initial boundary value problems involving Maxwell's equations in isotropic media", IEEE Trans. Antenna Propagat. Vol.14 (1966).

[96] T. Hasegawa, E. Sasaoka, M. Onishi, M. Nishimura, Y. Tsuji, and M. Koshiba, "Hole-assisted light guide fiber for large anomalous dispersion and low optical loss", Opt. Express Vol. 9 (2001).

[97] Chin-Ping Yu and Hung-Chun Chang, "Yee-mesh-based finite difference eigenmode solver with PML absorbing boundary conditions for optical waveguides and photonic crystal fibers", Opt. Express Vol. 12 (2004).

[98] S. S. A. Obayya, B. M. Azizur Rahman, Kenneth T. V. Grattan, and H. A. El-Mikati, "Full Vectorial Finite-Element-Based Imaginary Distance Beam Propagation Solution of Complex Modes in Optical Waveguides," J. Lightwave Technol., vol.20, no. 6, pp. 1054-1060, June 2002.

[99] C. S. Lee, S. W. Lee, and S. L. Chuang, "Plot of Modal Field Distribution in Rectangular and Circular Waveguides," IEEE Trans. MTT, vol.33, 1985.

[100] Ja-Yu Lu, Chin-Ping Yu, Hung-Chung Chang, Hung-Wen Chen, Yu-Tai Li, Ci-Ling Pan, and Chi-Kuang Sun "Terahertz air-core microstructure fiber", App. Phys. Let. Vol. 92, 2008.

[101] Eli Yablonovitch, "Inhibited Spontaneous Emission in Solid-State Physics and Electronics," Phys. Rev. Lett., Vol.58, No. 20, May 1987.

[102] John D. Joannopoulos, Steven G. Johnson, Joshua N. Winn, and Robert D. Meade, Photonic Crystals: Molding the flow of light, Princeton University Press, Princeton, Second edition, 2008.

[103] E. I. Smirnova, C. Chen, M. A. Shapiro, J. R. Sirigiri, and R. J. Temkin, “Simulation of photonic band gaps in metal rod lattices for microwave applications”, Journal of Applied Physics Vol. 91, pp. 960 , 2002.

[104] D. M. Pozar, Microwave Engineering, Wiley, 1998.

[105] R. E. Collin, Foundations for Microwave Engineering, Wiley 2001.

[106] A. Taflove and Susan C. Hagness, Computational electrodynamics: The finite-difference time-domain method, Artech House; 2000.

[107] Dennis Sullivan, “Electromagnetic simulation using the FDTD method”, IEEE press, Piscataway, NJ.

[108] T. M. Millington, N. J. Cassidy “Optimizing GPR modelling: A practical, multi-threaded approach to 3D-FDTD numerical modelling,” Computers & Geosciences, Vol.36, 1135–1144, 2010.

[109] Hezhong Guo, Yuval Cannel, Weiran R. Lou, Leemian Chen, John Rodgers, David K. Abe, A. Bromborsky, William Destler, and Victor L. Granatstein, “A Novel Highly Accurate Synthetic Technique for Determination of the Dispersive Characteristics in Periodic Slow Wave Circuits,” IEEE Trans. Micro. Theory Tech., Vol. 40. No. 11, Nov. 1992.

[110] Xi Gao, Ziqiang Yang, Yong Xu, Limei Qi, Dazhi Li, Zongjun Shi, Feng Lan, Zheng Liang, “Dispersion characteristics of a slow wave structure with metal photonic band gap cells,” Nuclear Instruments and Methods in Physics Research A 592 (2008) 292– 296.

[111] J. R. Pierce, “Theory of the Beam-Type Traveling Wave Tube”, Proceedings of the IRE, 1947.

[112] https://msdn.microsoft.com/en-us/magazine/cc163717.aspx last visited 05 February 2015.

[113] J. R. Pierce and Lester M. Field, “Traveling-wave Tubes,” Proc. IRE, Vol. 35, pp. 108, 1947.

[114] L. J. Chu, D. Jackson, “Field Theory of Travelling Wave Tubes,” Research Laboratory of Electronics, MIT, April 1947.

[115] Hezhong Guo, Yuval Cannel, Weiran R. Lou, Leemian Chen, John Rodgers, David K. Abe, A. Bromborsky, William Destler, and Victor L. Granatstein, "A Novel Highly Accurate Synthetic Technique for Determination of the Dispersive Characteristics in Periodic Slow Wave Circuits," IEEE Trans. Micro. Theory Tech., Vol. 40. No. 11, Nov. 1992.

[116] Qing-Lun Liu, Zi-Cheng Wang, Pu-Kun Liu, Chao-Hai Du, Hai-Qiang Li, and An-Yu Xu, "A THz Backward-Wave Oscillator Based on a Double-Grating Rectangular Waveguide," IEEE Trans Electon Devices, Vol. 60, No. 4, April 2013.

[117] http://custommicrowave.com/index.html, last visited 04 February, 2015.

[118] T. M. Millington, N. J. Cassidy "Optimising GPR modelling: A practical, multi-threaded approach to 3DFDTD numerical modelling," Computers & Geosciences, Vol.36, 1135–1144, 2010.

[119] William Buchanan, Analysis of Electromagnetic Wave propagation using the 3D Finite Difference Time Domain Method with Parallel processing, PhD Thesis, 2007.

[120] M. Inman, A. Elsherbeni, Optimizing Multiple GPU FDTD Simulations in CUDA, Proc. Parallel and Hardware Acceleration for Computational Electromagnetics, 2011

[121] Riku M. Mäkinen, Jaakko S. Juntunen, and Markku A. Kivikoski, "An Improved Thin-Wire Model for FDTD," IEEE Trans MTT, Vol. 50, No. 5, May 2002.

[122] Riku Makinen, Ville Kangas, Janne Lahtinen, and Markku Kivikoski1, "A Coaxial Probe Feed Model for FDTD," Micro. and Optical Lett., Vol. 34, No. 3, August 2002.

[123] Seung-Yeup Hyun and Se-Yun Kim, "3-D Thin-Wire FDTD Analysis of Coaxial Probe Fed in Asymmetric Microwave Components," IEEE Trans MTT, Vol. 59, No. 11, Nov. 2011.

[124] J A Stratton, Electromagnetic Theory, McGraw-Hill, 1941

[125] C. Balanis, Antenna Theory Analysis and Design, Wiley 1997.